

LOCAL SIMULATIONS OF MAGNETIZED ACCRETION DISKS

Jacob Bernhard Simon  
Collinsville, IL

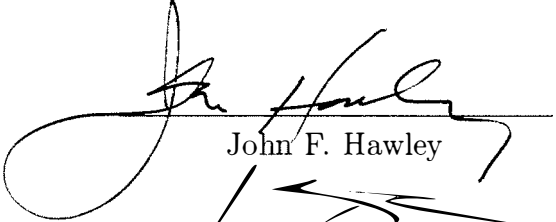
B.S. in Physics, University of Illinois, 2004

M.S. in Astronomy, University of Virginia, 2006

A Dissertation Presented to the Graduate  
Faculty of the University of Virginia  
in Candidacy for the Degree of  
Doctor of Philosophy

Department of Astronomy

University of Virginia  
July, 2010



---

John F. Hawley



---

Zhi-Yun Li



---

Phillip L. Arras



---

Andrew S. Grimshaw

©Copyright by  
Jacob B. Simon  
All rights reserved  
August, 2010

*To my grandfather, who inspired me to become a scientist through our many  
conversations about the Universe.*

## ABSTRACT

We present local shearing box simulations with the Athena code in order to study angular momentum transport in magnetized accretion disks via the magnetorotational instability (MRI). Parameterizing dissipation in the form of shear viscosity,  $\nu$ , Ohmic resistivity,  $\eta$ , and the magnetic Prandtl number,  $P_m = \nu/\eta$ , we examine the role of these parameters in setting the MRI-turbulent angular momentum transport rate. Through a series of simulations without physical dissipation or vertical gravity, we characterize numerical dissipation as a function of length scale and resolution, quantified in terms of effective  $\nu$ ,  $\eta$ , and  $P_m$ . The resulting effective  $P_m \sim 2$ , independent of resolution and initial field geometry, and we find that MRI simulations with effective  $\nu$ ,  $\eta$ , and  $P_m$  determined by numerical dissipation are not equivalent to those where these numbers are set by actual physical dissipation. We also determine that energy injected into turbulent fluctuations from differential rotation dissipates on a timescale of much less than an orbital time; turbulent stress and disk heating are locally correlated.

We then study the effect of physical dissipation on the MRI, but without vertical gravity. In agreement with a previous study performed with the ZEUS code, we find that turbulence dies out for values of  $P_m \lesssim 1$  if there is no net magnetic flux through the domain. With a net toroidal magnetic flux, however, turbulence can be sustained even when  $P_m < 1$ ; only a sufficiently large resistivity can quench the turbulence. In both cases, volume-averaged stress levels increase with  $P_m$  when turbulence is sustained.

Finally, we examine the  $P_m$  effect with vertical gravity. Again, increasing  $P_m$  leads to enhanced turbulence, but with a shallower dependence on  $P_m$  and with considerably more temporal variability in the turbulent stress levels. Resistivity is

again the critical parameter; if  $\eta$  is sufficiently large, the turbulence decays, leaving a remnant weak radial field. This radial field then shears into toroidal field that eventually reaches sufficient strength to reactivate the MRI. The result is episodic outbursts of turbulence occurring on timescales ranging from tens to hundreds of orbits.

## Acknowledgments

The past six years have been some of the best in my entire life. From the sunny Saturdays spent cooped up in my office debugging code to the numerous wine festivals I've gone to with my friends (these were on the other sunny Saturdays; they weren't all wasted inside!), these years have had it all: tons of hard work and hair-pulling along with the parties and good times to make it all worth while. So, I'd like to take a few pages of my thesis to thank some of the people that have made my experience here as productive, insightful, and fun as it was.

The first person to mention should definitely be my research advisor, John Hawley, as he has taught me how to be a theorist, the value of carefully constructed numerical simulations, and the importance of understanding the “nitty-gritty” details of numerical algorithms. And perhaps most importantly, he trained me to always treat my simulation results with an educated skepticism, an essential skill for any numericist. I would also like to thank Jim Stone for all the questions that he's answered about the Athena code over the years as well as his input on various numerical methods and tests to use in developing Athena. My friend, colleague, and collaborator Kris Beckwith was always around when I needed to ask a question, vent about my code crashing, or bounce an idea off of someone. Also, thanks go to Kris for inviting me to the disk conference in England last September as well as to Boulder in November. And a big thank you to Megan who walked at least 8 miles with me around London and also showed me (the other) Cambridge! And of course, thanks go to all the other scientists who have helped me in my work along the way. Starting with my thesis committee: Phil Arras, Zhi-Yun Li, and Andrew Grimshaw. And my collaborators and fellow disk theorists, with whom I've consulted over the years: Sebastien Fromang, Xiaoyue Guan, Charles Gammie, Steve Balbus, Jeremy Goodman, Omer

Blaes, Julian Krolik, Pierre-Yves Longaretti, Martin Pessah, Shane Davis, and Tom Gardiner.

Of course, without the comforting presence of some of the best friends that I have ever had, grad school would not have been nearly as much fun, nor as productive. Thank you to all of my friends at UVA, but special thanks go out to some people in particular. My roommates over the years, Dan, Ori, Jarron (and Steph), Guillermo, and Andre - thanks for putting up with me for so long and tolerating my OCD tendencies. Also, thank you Dan for immortalizing me in your living room coasters and pretending to not see me when I eat yogurt and stare at you. Ori, thanks for the shared gripe fest in the fall about how we were all doomed and wouldn't get any jobs even though we all got great ones! Jarron and Steph, thank you for the cats, aioli, and the Wii (before I got my own Wii). Gail, you have listened to so many of my worries and anxieties over the years and you've always been there for me - I won't ever forget that. Also, thank you for organizing so many fun nights and weekends!!! I will miss them! Genevieve, you've been a great officemate and an even better friend, as you have always been willing to talk with me about anything and you don't mind that I put salt on your bathroom floor. I will also miss our airport ride exchange program. Paul, I've enjoyed sharing many things with you, in particular our love for sci-fi, getting sloshed at wine festivals, and countless lunch time discussions about anything we could think of. (Oh, and DS9 is better than Bab 5). Joleen, you were one of the first friends that I made here as we bonded over our similar interests, our long-distance relationships with the S.O.'s, and our love for Star Wars. Meeting you at the prospective weekend six years ago certainly helped make my decision to come to UVA. To my fellow obsessor/worrier/overthinker, Greg: you have given me so much good advice over the years, but I especially thank you for giving us all the

non-sugar-coated truth about a career in astronomy. Lisa May, thank you for your company (and your cats' company!) over the past few years. I've enjoyed just hanging out with you, especially when I needed a friend (moo point). Nicole, I've had so much fun with you over the years - you definitely know how to party! And I am glad you finally saw the light and became a Star Trek fan. (Live long and prosper). Howard, thank you for fixing the cluster every time I broke it and not being too annoyed at me when I came into your office with a computer problem. Oh, and the trips to Short Pump were always a blast! And Cheng-Yu, I thank you for educating me in the ways of Buddhism and meditation and mindfulness. I have learned a lot from you, and you have always been so generous in everything. (Also, thank you for the books!!).

Finally, where would I be without the support of my other close friends and my family back home. A special thanks to my parents, Pat and Craig, for helping me to get this far by paying for my undergraduate education (which certainly made this career possible), moving me out to Charlottesville, and just being there for me during my rough days. And I have to acknowledge my dad for his contribution to my thesis: tying my tie on my defense day when I was too nervous and wound up to do it myself. Thanks also go to my best friend of more than a decade, Chris. You've always just been a phone call away, and that'll never change, no matter where our lives take us. Go Cardinals!!! Last but most certainly not least is my wonderful wife Angela. We've shared so much together, and we have come such a long way since we first met nearly 10 years ago. I am so lucky to have a wife that speaks my language (I mean science... not English... well, English too of course) and with whom I can discuss fluid dynamics over Ethiopian food!

This work was supported by NASA Headquarters under the NASA Earth and Space Science Fellowship Program - Grant NNX08AX06H; a Virginia Space Grant Consortium fellowship; NASA grants NNX09AD14G, NNG04GK77G, and NAG5-13288; and NSF grant AST-0908869. The simulations were run on the Mercury system at NCSA and the Ranger system at TACC, both of which are part of TeraGrid and are supported by the National Science Foundation.

*“Nothing Happens Unless First a Dream”*

*Carl Sandburg*

# Table of Contents

|  |              |
|--|--------------|
| <b>ABSTRACT</b>  | <b>iv</b>    |
| <b>Acknowledgments</b>   | <b>vi</b>    |
| <b>List of Figures</b>   | <b>xxvi</b>  |
| <b>List of Tables</b>  | <b>xxvii</b> |
| <b>1 Introduction</b>  | <b>1</b>     |
| 1.1 The $\alpha$ Model for Accretion Disks . . . . .                 | 3            |
| 1.2 The Magnetorotational Instability (MRI) . . . . .                | 5            |
| 1.2.1 MHD Equations . . . . .  | 6            |
| 1.2.2 The Linear MRI . . . . .                                       | 8            |
| 1.2.3 Hydrodynamic Transport? . . . . .                              | 13           |
| 1.2.4 The Nonlinear Regime . . . . .                                 | 15           |
| 1.3 Motivation: Connecting MRI Transport to Disk Phenomenology . . . | 18           |
| 1.4 Thesis Structure . . . . .                                       | 23           |
| <b>2 Numerical Methods</b>   | <b>24</b>    |
| 2.1 Athena . . . . .   | 24           |
| 2.2 The Local Shearing Box Approximation . . . . .                   | 27           |
| <b>3 Local Simulations with Numerical Dissipation</b>                | <b>31</b>    |
| 3.1 Introduction . . . . .   | 32           |
| 3.2 Numerical Simulations . . . . .                                  | 34           |
| 3.3 General Properties of MRI Turbulence . . . . .                   | 38           |
| 3.3.1 Characteristics of Saturation . . . . .                        | 39           |
| 3.3.2 Channel Solution . . . . .                                     | 45           |
| 3.3.3 Energy Power Spectra . . . . .                                 | 48           |
| 3.4 Locality of Turbulence . . . . .                                 | 50           |
| 3.4.1 Sustained Turbulence . . . . .                                 | 52           |
| 3.4.2 Decaying Turbulence . . . . .                                  | 63           |
| 3.5 Measuring Numerical Dissipation . . . . .                        | 64           |

|          |  |            |
|----------|--|------------|
| 3.5.1    | Zero Net Magnetic Flux . . . . .                               | 70         |
| 3.5.2    | Net Vertical Magnetic Flux . . . . .                           | 82         |
| 3.6      | Summary and Discussion . . . . .                               | 87         |
| <b>4</b> | <b>Prandtl Number Effects on Unstratified Disks</b>            | <b>96</b>  |
| 4.1      | Introduction . . . . .   | 97         |
| 4.2      | Numerical Simulations . . . . .                                | 98         |
| 4.2.1    | Tests of Physical Dissipation . . . . .                        | 101        |
| 4.2.2    | Shearing Box Parameters . . . . .                              | 103        |
| 4.3      | Zero Net Flux Simulations . . . . .                            | 104        |
| 4.4      | Toroidal Field Simulations . . . . .                           | 109        |
| 4.4.1    | The Linear Regime . . . . .                                    | 110        |
| 4.4.2    | The Nonlinear Regime . . . . .                                 | 114        |
| 4.5      | Summary and Discussion . . . . .                               | 130        |
| <b>5</b> | <b>Prandtl Number Effects on Vertically Stratified Disks</b>   | <b>135</b> |
| 5.1      | Introduction . . . . .   | 136        |
| 5.2      | Shearing Box Implementation . . . . .                          | 138        |
| 5.2.1    | Source Terms . . . . .   | 139        |
| 5.2.2    | Boundary Conditions . . . . .                                  | 139        |
| 5.2.3    | Orbital Advection . . . . .                                    | 141        |
| 5.2.4    | Physical Dissipation . . . . .                                 | 142        |
| 5.3      | Resolving Physical Dissipation in Unstratified Disks . . . . . | 144        |
| 5.4      | Vertically Stratified Simulations . . . . .                    | 153        |
| 5.4.1    | Baseline Simulations . . . . .                                 | 153        |
| 5.4.2    | Turbulent and Non-turbulent States . . . . .                   | 161        |
| 5.4.3    | The Prandtl Number Effect on Sustained Turbulence . . . . .    | 181        |
| 5.5      | Summary and Discussion . . . . .                               | 182        |
| <b>6</b> | <b>Conclusions and Outlook</b>                                 | <b>190</b> |

# List of Figures

|     |   |    |
|-----|---|----|
| 1.1 | A cartoon of two springs orbiting a point mass at different radii, connected by a spring with tension $T$ . The inner mass, $m_i$ , moves at a higher angular velocity than the outer mass, $m_o$ , thus stretching the spring. This stretching causes angular momentum to be transported from $m_i$ to $m_o$ , which separates the two masses even more. The result is a runaway. This picture serves to conceptualize the linear growth of the magnetorotational instability (Balbus & Hawley 1998, Fig. 16).   | 11 |
| 1.2 | The volume averaged magnetic and kinetic energy evolutions and Maxwell and Reynolds stress evolutions for a fiducial shearing box simulation in Hawley et al. (1995). The horizontal axis is time in units of orbits (defined at the center of the local domain). Note that in the coordinate system of the shearing box, $x$ corresponds to the radial direction, and $y$ corresponds to the azimuthal direction (see Hawley et al. (1995) or Chapter 2 below). The development of the MRI is clearly shown. The positive values for the Maxwell and Reynolds stresses indicate outward angular momentum transport (Hawley et al. 1995, Fig. 3).   | 17 |
| 3.1 | Volume-averaged energy densities and stresses normalized to the initial gas pressure versus time for the NZ128 simulation. In the upper two plots, the black line is the total energy density, the green line is the component of the energy density in the $x$ direction, the red line is the $y$ direction component, and the blue line is the $z$ direction component. The upper left plot shows the volume-averaged magnetic energy density, the upper right plot shows the perturbed kinetic energy density (i.e., with the shear subtracted off of $v_y$ ), and the lower left plot is the volume-averaged total stress (black), Maxwell stress (pink), and Reynolds stress (blue). The lower right plot is the total energy density, including gravitational energy (solid line), and the thermal energy density (dashed line). The $y$ axes have the same range for all plots except for the total/thermal energy density plot. | 41 |

- 3.2 Volume-averaged energy densities and stresses normalized to the initial gas pressure versus time for the SZ128 simulation. In the upper two plots, the black line is the total energy density, the green line is the component of the energy density in the  $x$  direction, the red line is the  $y$  direction component, and the blue line is the  $z$  direction component. The upper left plot shows the volume-averaged magnetic energy density, the upper right plot shows the perturbed kinetic energy density (i.e., with the shear subtracted off of  $v_y$ ), and the lower left plot is the volume-averaged total stress (black), Maxwell stress (pink), and Reynolds stress (blue). The lower right plot is the total energy density, including gravitational energy (solid line), and the thermal energy density (dashed line). The  $y$  axes have the same range for all plots except for the total/thermal energy density plot. . . . . 42
- 3.3 Time- and volume-averaged energy densities normalized to the initial pressure for various resolutions. The two upper plots correspond to the net flux simulations, and the two lower plots correspond to the zero net flux simulations. The left plots are the averaged magnetic energy densities, and the right plots are the averaged perturbed kinetic energy densities (i.e., with shear subtracted off of  $v_y$ ). In all plots, the black symbols are the total energy density, the green symbols are the  $x$  component of the energy density, the red symbols are the  $y$  component, and the blue symbols are the  $z$  component. The time averages are done from orbit 20 to 100, and the error bars indicate one standard deviation over this period. . . . . 43
- 3.4 The development and destruction of a channel flow during the NZ128 simulation. The upper left plot shows a fluctuation in the volume-averaged magnetic energy density from  $t = 80$  orbits to  $t = 85$  orbits. The remaining plots show the  $y$ -averaged perturbed  $y$  velocity (colors) and  $v_x$  and  $v_z$  (vectors). The upper right plot occurs at  $t = 82.5$  orbits, the lower left plot occurs at  $t = 83$  orbits, and the lower right plot occurs at  $t = 84$  orbits. These times are indicated on the upper left plot by the arrows. At  $t = 82.5$  orbits, one can see the development of a two-channel flow, in which one channel has  $v_x < 0$  and  $\delta v_y < 0$ , and the other channel has  $v_x > 0$  and  $\delta v_y > 0$ . At  $t = 83$  orbits, this channel flow is even more developed as the perturbations to the  $y$  velocity have become even stronger and  $v_x$  dominates over  $v_z$  everywhere. The development of this channel flow coincides with an increase in volume-averaged magnetic energy density. By  $t = 84$  orbits, the channel flow has been destroyed, coinciding with the decrease in magnetic energy density. . . . . 46

- 3.5 Spatial power spectra of various energy densities in the saturated state of the standard net flux (left panels) and zero net flux simulations (right panels). The spectra were obtained via an average over 161 frames in the saturated state and an average over shells of constant modulus  $|\mathbf{k}|$ . In each column, the first plot shows magnetic energy density, the second shows kinetic energy density, and the third shows perturbed kinetic energy density (as defined in the text). The effect of resolution is shown in each individual plot; the dotted line corresponds to the resolution with  $N_x = 16$ , the dot-dashed line corresponds to  $N_x = 32$ , the dashed line corresponds to  $N_x = 64$ , and the solid line corresponds to  $N_x = 128$ . All energy densities have been normalized to the initial gas pressure and are plotted against a dimensionless wave number ( $L$  is the length of the smallest dimension of the box). . . . . 51
- 3.6 Time derivative of various volume-averaged energy densities for a 20 orbit period in the NZ128 simulation. The time derivative of the energy densities have been multiplied by an orbital time over the initial gas pressure. The dark blue line is the energy injection rate,  $E_{\text{in}}$ , the black line is the thermal energy density derivative,  $\dot{T}$ , the green line is the kinetic energy density derivative,  $\dot{K}$ , and the red line is the magnetic energy density derivative,  $\dot{M}$ . The dotted line indicates zero. . . . . 57
- 3.7 Correlation coefficients calculated over orbits 20 to 100 in the NZ128 simulation. The plot on the left was calculated by correlating the energy injection rate,  $E_{\text{in}}$ , against the thermal energy time derivative,  $\dot{T}$ . The  $x$ -axis is the correlation length in time, and the  $y$ -axis is the coefficient multiplied by an orbital period over the initial gas pressure. The plot on the right was calculated by correlating the magnetic energy derivative,  $\dot{M}$ , (solid line) and kinetic energy derivative,  $\dot{K}$ , (dashed line) against the thermal energy derivative. The dotted line indicates  $C_{AB} = 0$ . Note that the two plots have different  $y$  scales. . . . . 58
- 3.8 Various terms in the volume-averaged magnetic, kinetic, and thermal energy density evolution equations over a two orbit period of NZ128. The energy terms are  $\dot{T}$  (black),  $E_{\text{in}}$  (blue),  $-Q_{\text{k}}$  (green),  $-Q_{\text{m}}$  (red), and the volume-averaged transfer rate from kinetic to magnetic energy (pink). All of these terms are defined in the text and have been multiplied by an orbital period over the initial gas pressure. . . . . 61

- 3.9 Correlation coefficient calculated over the saturated state of the SZ128 simulation. The coefficient was calculated by correlating the energy injection rate against the thermal energy density derivative. The  $x$ -axis is the correlation length in time, and the  $y$ -axis is the coefficient multiplied by an orbital period over the initial gas pressure. The narrow peaks in the curve correspond to residual effects from rebinning the energy derivatives (described in the text). The broader peak in the correlation function occurs at  $\Delta t \sim -0.2$  orbits. . . . . 62
- 3.10 Volume-averaged magnetic and kinetic energy densities in the first 1.5 orbits of NZD128 (top) and SZD128 (bottom). In both plots, the upper curves correspond to the kinetic energy density and the lower curves correspond to the magnetic energy density. In SZD128, high frequency oscillations appear in the kinetic energy evolution. To smooth away these oscillations, a moving window average was applied to the kinetic energy density. The unsmoothed kinetic energy is shown by the dotted line, while the smoothed kinetic energy is the solid line. The magnetic energy density in the SZD128 plot has also been smoothed for consistency. Both the kinetic and magnetic energy densities have been normalized to their respective (unsmoothed) values at  $t = 40$  orbits. 65
- 3.11 Magnetic Fourier transfer functions versus a dimensionless wave number ( $L$  is the length of the smallest dimension in the box) for SZ128. Each plot is displayed in two components; the left part shows the data for  $1 < kL/(2\pi) < 20$ , and the right part shows the data for  $20 < kL/(2\pi) < 64$  by changing the  $x$  and  $y$  axis scaling. In all plots, the solid line is the average value for the transfer function. This average was obtained over 161 frames in the saturated state and shells of constant  $|\mathbf{k}|$ . The upper (lower) dashed line that matches color with the solid line correspond to the transfer function plus (minus) one temporal standard deviation. From top to bottom, the plots show  $S$  (red) and  $A$  (black),  $T_{bb}$ ,  $T_{divv}$ , and  $T_{bv}$ . . . . . 72
- 3.12 Kinetic Fourier transfer functions versus a dimensionless wave number ( $L$  is the length of the smallest dimension in the box) for SZ128. Each plot is displayed in two components; the left part shows the data for  $1 < kL/(2\pi) < 20$ , and the right part shows the data for  $20 < kL/(2\pi) < 64$  by changing the  $x$  and  $y$  axis scaling. In all plots, the solid line is the average value for the transfer function. This average was obtained over 161 frames in the saturated state and shells of constant  $|\mathbf{k}|$ . The upper (lower) dashed line that matches color with the solid line correspond to the transfer function plus (minus) one temporal standard deviation. From top to bottom, the plots show  $T_{vv}$ ,  $T_{vb}$ ,  $T_{press}$  (red) and  $T_{comp}$  (black), and  $T_{\phi}$ . . . . . 73

- 3.13 Numerical dissipation quantities plotted against a dimensionless wave number ( $L$  is the length of the smallest dimension in the box). These plots correspond to data from SZ128. The upper left plot shows the dissipation rate of kinetic energy (green) and magnetic energy (red) in Fourier space. The upper right plot shows the ratio of these two dissipation rates. The lower left plot shows the effective numerical viscosity (green) and resistivity (red). The lower right plot shows the ratio of the viscosity to resistivity (i.e., the effective Prandtl number). In all plots, the solid line is the average value for the quantity of interest. For  $D_{\text{kin}}$  and  $D_{\text{mag}}$ , this average was obtained from averaging over shells of constant  $|\mathbf{k}|$  and over 161 frames in the saturated state. The averaged viscosity and resistivity values were calculated as described in the text. The upper and lower dashed lines correspond to the error propagated from one temporal standard deviation. . . . . 77
- 3.14 Averaged dissipation related quantities as a function of grid resolution. These plots correspond to data from the zero net flux simulations, SZ16, SZ32, SZ64, and SZ128. The upper left plot shows the effective viscosity versus  $x$  resolution. The dashed line shows  $\nu_{\text{eff}} \propto N_x^{-2}$ . The upper right plot shows the effective resistivity versus  $x$  resolution. Again, the dashed line shows  $\eta_{\text{eff}} \propto N_x^{-2}$ . The lower left plot shows the ratio of kinetic to magnetic dissipation versus  $x$  resolution. The lower right plot shows the effective Prandtl number versus  $x$  resolution. For each resolution, the data point was obtained from averaging the quantity as a function of  $k$  over values of  $k$  where the error in this quantity is not much larger than the mean value. The error bars represent the propagated errors from the temporal statistics. . . . . 78
- 3.15 Magnetic dissipation rate from the SZ128 simulation for three versions of the transfer function analysis. The upper left plot and the red lines in the lower left plot correspond to the analysis in which  $B_y = 0$  was assumed. The upper right plot and the red lines in the lower right plot correspond to the analysis in which both  $B_y = 0$  and  $k_y = 0$  were assumed. The black lines in the lower plots result from relaxing both of these assumptions. The solid lines in the upper plots correspond to  $D_{\text{mag}}$  whereas the dashed lines correspond to  $\eta T_\eta$  with  $\eta = 10^{-7}$  chosen to provide a reasonable match to  $D_{\text{mag}}$  at large  $k$ . The dashed lines in the lower plots correspond to one standard deviation above and below the quantity represented by the solid line of the same color. A horizontal line at zero is shown in all plots as the blue dotted line. Note the difference in  $y$ -axis scale between the upper and lower plots. 81

- 3.16 Magnetic Fourier transfer functions versus a dimensionless wave number ( $L$  is the length of the smallest dimension in the box) for NZ128. Each plot is displayed in two components; the left part shows the data for  $1 < kL/(2\pi) < 20$ , and the right part shows the data for  $20 < kL/(2\pi) < 64$  by changing the  $x$  and  $y$  axis scaling. In all plots, the solid line is the average value for the transfer function. This average was obtained over 161 frames in the saturated state and shells of constant  $|\mathbf{k}|$ . The upper (lower) dashed line that matches color with the solid line correspond to the transfer function plus (minus) one temporal standard deviation. From top to bottom, the plots show  $S$  (red) and  $A$  (black),  $T_{bb}$ ,  $T_{divv}$ , and  $T_{bv}$ . . . . . 84
- 3.17 Kinetic Fourier transfer functions versus a dimensionless wave number ( $L$  is the length of the smallest dimension in the box) for NZ128. Each plot is displayed in two components; the left part shows the data for  $1 < kL/(2\pi) < 20$ , and the right part shows the data for  $20 < kL/(2\pi) < 64$  by changing the  $x$  and  $y$  axis scaling. In all plots, the solid line is the average value for the transfer function. This average was obtained over 161 frames in the saturated state and shells of constant  $|\mathbf{k}|$ . The upper (lower) dashed line that matches color with the solid line correspond to the transfer function plus (minus) one temporal standard deviation. From top to bottom, the plots show  $T_{vv}$ ,  $T_{vb}$ ,  $T_{press}$  (red) and  $T_{comp}$  (black), and  $T_{\phi}$ . . . . . 85
- 3.18 Numerical dissipation quantities plotted against a dimensionless wave number ( $L$  is the length of the smallest dimension in the box). These plots correspond to data from NZ128. The upper left plot shows the dissipation rate of kinetic energy (green) and magnetic energy (red) in Fourier space. The upper right plot shows the ratio of these two dissipation rates. The lower left plot shows the effective numerical viscosity (green) and resistivity (red). The lower right plot shows the ratio of the viscosity to resistivity (i.e., the effective Prandtl number). In all plots, the solid line is the average value for the quantity of interest. For  $D_{kin}$  and  $D_{mag}$ , this average was obtained from averaging over shells of constant  $|\mathbf{k}|$  and over 161 frames in the saturated state. The averaged viscosity and resistivity values were calculated as described in the text. The upper and lower dashed lines correspond to the error propagated from one temporal standard deviation. . . . . 86

- 3.19 Averaged dissipation related quantities as a function of grid resolution. These plots correspond to data from the net flux simulations, NZ16, NZ32, NZ64, and NZ128. The upper left plot shows the effective viscosity versus  $x$  resolution. The dashed line shows  $\nu_{\text{eff}} \propto N_x^{-2}$ . The upper right plot shows the effective resistivity versus  $x$  resolution. Again, the dashed line shows  $\eta_{\text{eff}} \propto N_x^{-2}$ . The lower left plot shows the ratio of kinetic to magnetic dissipation versus  $x$  resolution. The lower right plot shows the effective Prandtl number versus  $x$  resolution. For each resolution, the data point was obtained from averaging the quantity as a function of  $k$  over values of  $k$  where the error in this quantity is not much larger than the mean value. The error bars represent the propagated errors from the temporal statistics. . . . . 89
- 4.1 Numerical error as a function of  $x$  resolution for the three-dimensional decaying linear wave problem. The boxes are the errors for a decaying Alfvén wave, and the asterisks are the errors for a decaying sound wave. The error is calculated from the square root of the sum of the squared errors in the density and momenta (for the sound wave) and the density, momenta, and magnetic field (for the Alfvén wave) obtained using the analytic solution. The dashed line shows the slope corresponding to second-order convergence. . . . . 102
- 4.2 Time- and volume-averaged stress parameter  $\alpha$  as a function of  $P_m$  in the SZ simulations;  $\alpha \equiv \langle \langle \rho v_x \delta v_y - B_x B_y \rangle \rangle / P_o$ , where the average is calculated over the entire simulation domain and from 20 orbits to the end of the simulation. Only simulations with sustained turbulence are plotted. The  $P_m = 4$  model has  $Rm = 12500$  whereas the other two have  $Rm = 12800$ . There is a nearly linear increase in  $\alpha$  with  $P_m$ . . . 107
- 4.3 Time evolution of volume-averaged magnetic energy density normalized by the gas pressure for the SZ runs with  $Re = 1600$  and varying  $P_m$ . The volume average is calculated over the entire simulation domain. The solid line corresponds to  $P_m = 8$ , the dashed line corresponds to  $P_m = 4$ , and the dotted line corresponds to  $P_m = 2$ . The turbulence decays for the lowest two  $P_m$  values, with the  $P_m = 4$  case taking roughly 60 orbits to decay. . . . . 108
- 4.4 Time evolution of volume-averaged magnetic energy density normalized by the gas pressure for the YN runs with  $Re = 25600$  (black curve) and  $Re = 1600$  (colored curves). The volume average is calculated over the entire simulation domain. The colors indicate  $P_m$ ; green corresponds to  $Rm = 800$  ( $P_m = 0.5$ ), light blue to  $Rm = 1600$  ( $P_m = 1$ ), red to  $Rm = 3200$  ( $P_m = 2$ ), and dark blue to  $Rm = 6400$  ( $P_m = 4$ ). Increasing  $Rm$  ( $P_m$ ) leads to enhanced turbulence. . . . . 117

- 4.5 Time- and volume-averaged stress parameter  $\alpha$  as a function of  $Rm$  in the YN simulations;  $\alpha \equiv \langle\langle \rho v_x \delta v_y - B_x B_y \rangle\rangle / P_o$ . The time average runs from 50 orbits onward, and the volume average is calculated over the entire simulation domain. The colors correspond to  $Re$  values, and the symbols correspond to  $P_m$  values. Red symbols are  $Re = 400$ , green  $Re = 800$ , dark blue  $Re = 1600$ , black  $Re = 3200$ , pink  $Re = 6400$ , and light blue are  $Re = 12800$ . Circles are  $P_m = 0.25$ , crosses  $P_m = 0.5$ , asterisks  $P_m = 1$ , diamonds  $P_m = 2$ , triangles  $P_m = 4$ , squares  $P_m = 8$ , and X's are  $P_m = 16$ . Note that some of the decayed turbulence ( $\alpha = 0$ ) simulations are not plotted for clarity. Increasing  $Rm$  results in larger  $\alpha$  values, and for  $Rm$  less than 800–1600, the turbulence decays. . . . . 121
- 4.6 Time- and volume-averaged stress parameter  $\alpha$  as a function of  $Re$  in the YN simulations;  $\alpha \equiv \langle\langle \rho v_x \delta v_y - B_x B_y \rangle\rangle / P_o$ . The time average runs from 50 orbits onward, and the volume average is calculated over the entire simulation domain. The colors correspond to  $Rm$  values, and the symbols correspond to  $P_m$  values. Light blue symbols are  $Rm = 800$ , green  $Rm = 1600$ , dark blue  $Rm = 3200$ , black  $Rm = 6400$ , and red are  $Rm = 12800$ . Circles are  $P_m = 0.25$ , crosses  $P_m = 0.5$ , asterisks  $P_m = 1$ , diamonds  $P_m = 2$ , triangles  $P_m = 4$ , squares  $P_m = 8$ , and X's are  $P_m = 16$ . Note that some of the decayed turbulence ( $\alpha = 0$ ) simulations are not plotted for clarity. Increasing  $Re$  leads to decreasing  $\alpha$  values. . . . . 122
- 4.7 Time- and volume-averaged stress parameter  $\alpha$  as a function of  $P_m$ ;  $\alpha \equiv \langle\langle \rho v_x \delta v_y - B_x B_y \rangle\rangle / P_o$ . The time average runs from 50 orbits onward, and the volume average is calculated over the entire simulation domain. The colors correspond to  $Rm$  values, and the symbols to  $Re$  values. Light blue symbols are  $Rm = 800$ , green  $Rm = 1600$ , dark blue  $Rm = 3200$ , black  $Rm = 6400$ , and red are  $Rm = 12800$ . Crosses are  $Re = 400$ , asterisks  $Re = 800$ , diamonds  $Re = 1600$ , triangles  $Re = 3200$ , squares  $Re = 6400$ , and circles are  $Re = 12800$ . Note that some of the decayed turbulence ( $\alpha = 0$ ) simulations are not plotted for clarity. The average stress increases with increasing  $P_m$ . . . . . 123

- 4.8 Ratio of kinetic to magnetic energy dissipation rate as a function of  $P_m$  (top panel) and  $\alpha$  (bottom panel) for select YN runs;  $\alpha \equiv \langle \langle \rho v_x \delta v_y - B_x B_y \rangle \rangle / P_o$ . The colors and symbols are the same as in Fig. 4.6. The kinetic and magnetic dissipation rates as well as  $\alpha$  have been averaged in volume and time. The volume average is calculated over the entire simulation domain and the time average is calculated from  $t = 70 - 90$  orbits for YNRe400Pm16 (black X) and YNRe12800Pm0.25 (blue circle),  $t = 110 - 130$  orbits for YNRe800Pm2 (green diamond) and YNRe800Pm8 (black square), and  $t = 110.6 - 130.6$  orbits for YNRe800Pm4 (blue triangle) and YNRe3200Pm4 (red triangle). The ratio of viscous to resistive heating generally increases as either  $\alpha$  or  $P_m$  increases, although not monotonically. . . . . 126
- 4.9 Ratio of Reynolds stress to Maxwell stress as a function of  $\alpha$  for select YN runs;  $\alpha \equiv \langle \langle \rho v_x \delta v_y - B_x B_y \rangle \rangle / P_o$ . The colors and symbols are the same as in Fig. 4.6. The Maxwell and Reynolds stresses as well as  $\alpha$  have been averaged in volume and time. The volume average is calculated over the entire simulation domain and the time average is calculated from  $t = 70 - 90$  orbits for YNRe400Pm16 (black X) and YNRe12800Pm0.25 (blue circle),  $t = 110 - 130$  orbits for YNRe800Pm2 (green diamond) and YNRe800Pm8 (black square), and  $t = 110.6 - 130.6$  orbits for YNRe800Pm4 (blue triangle) and YNRe3200Pm4 (red triangle). The ratio of Reynolds to Maxwell stress generally decreases with increasing  $\alpha$ . . . . . 127
- 4.10 Ratio of Reynolds stress to perturbed kinetic energy as a function of  $Re$  in the sustained turbulence YN simulations. Both the Reynolds stress and the perturbed kinetic energy are time and volume averaged, with the time average calculated from orbit 50 onward and the volume average calculated over the entire simulation domain. The colors correspond to  $Rm$  values, and the symbols correspond to  $P_m$  values. Green symbols are  $Rm = 1600$ , blue  $Rm = 3200$ , black  $Rm = 6400$ , and red are  $Rm = 12800$ . Circles are  $P_m = 0.25$ , crosses  $P_m = 0.5$ , asterisks  $P_m = 1$ , diamonds  $P_m = 2$ , triangles  $P_m = 4$ , squares  $P_m = 8$ , and X's are  $P_m = 16$ . The ratio of stress to energy increases with increasing viscosity but does not change with resistivity. . . . . 129
- 5.1 Time- and volume-averaged stress parameter  $\alpha$  as a function of grid zones per  $H$  in the SZ simulations;  $\alpha \equiv \langle \langle \rho v_x \delta v_y - B_x B_y \rangle \rangle / \langle P \rangle$ , where the average is calculated over the entire simulation domain and from 20 orbits to the end of the simulation. Only simulations with sustained turbulence are plotted. By 32 zones per  $H$ , the  $\alpha$  values appear to be relatively close to the higher resolution values. . . . . 149

- 5.2 Volume-averaged Reynolds and Maxwell stresses normalized by the the volume-averaged gas pressure as a function of time in orbits in the unstratified, net toroidal field simulations. The black line corresponds to  $Re = 800$  and  $P_m = 4$ , magenta is  $Re = 800$  and  $P_m = 8$ , green is  $Re = 1600$  and  $P_m = 0.5$ , light blue is  $Re = 1600$  and  $P_m = 2$ , dark blue is  $Re = 1600$  and  $P_m = 4$ , and red is  $Re = 6400$  and  $P_m = 0.5$ . There is a clear dependence on  $P_m$ , and for sufficiently low  $Rm$ , the turbulence decays. . . . . 150
- 5.3 Time- and volume-averaged stress parameter  $\alpha$  as a function of  $P_m$  in the lower resolution FT simulations (asterisks) and the higher resolution, net toroidal field simulations of Chapter 4 (diamonds). In the FT simulations,  $\alpha \equiv \langle \langle \rho v_x \delta v_y - B_x B_y \rangle \rangle / \langle P \rangle$ , whereas in the higher resolution simulations,  $\alpha \equiv \langle \langle \rho v_x \delta v_y - B_x B_y \rangle \rangle / P_o$ ; see Chapter 4. These definitions are roughly equivalent since  $\langle P \rangle \approx P_o$ . For the FT simulations, the average is calculated over the entire simulation domain and from 120 orbits to the end of the simulation. Only simulations with sustained turbulence are plotted. The dashed lines are linear fits to the data in log-log space. Both resolutions show a clear  $P_m$  dependence, but this dependence is steeper at the lower resolution. . . . . 152
- 5.4 Space-time diagram of the horizontally averaged  $B_y$  (top panel) and total stress normalized by the volume-averaged gas pressure (bottom panel). The volume-average is done for all  $x$  and  $y$  and for  $|z| \leq 2H$ . The white contours on the top panel denote where  $\beta$  goes from greater to less than unity, and the black contours mark the boundaries between buoyantly stable and unstable gas. The horizontally averaged  $B_y$  appears to rise vertically into the upper  $z$  layers, being replaced in the mid-plane region by  $B_y$  of the opposite sign. The rise speed of the field increases after  $|z| \sim 2H$  is reached. The sign flipping in  $B_y$  has a period of  $\sim 10$  orbits. . . . . 156
- 5.5 Left: Time evolution of volume-averaged  $B_y$  in 32Num. The volume average is done for all  $x$  and  $y$  and for  $|z| \leq 0.5H$ . The dashed line corresponds to  $\langle B_y \rangle = 0$ . Right: Temporal power spectrum of  $\langle B_y \rangle$  from the left plot, calculated from orbit 50 to 1050. The 10 orbit period oscillations in  $\langle B_y \rangle$  are immediately apparent in both plots, particularly as the peak in the power spectrum. The 10 orbit oscillations are modulated on longer timescales, ranging from tens to hundreds of orbits. . . . . 157

- 5.6 Time evolution of volume-averaged field components for part of 32Num. Red is  $\langle B_x \rangle$ , black is  $\langle B_y \rangle$ , and blue is  $\langle B_z \rangle$  as calculated from  $\langle B_x \rangle$  using a simple toy model discussed in the text. The volume average is done for all  $x$  and  $y$  and for  $|z| \leq 0.5H$ . The dashed line corresponds to  $\langle B_{x,y} \rangle = 0$ .  $\langle B_x \rangle$  has been multiplied by a factor of 5 relative to  $\langle B_y \rangle$  to make a more direct comparison possible. The variations in  $\langle B_x \rangle$  are accompanied by variations in  $\langle B_y \rangle$ , which are offset in time, and the toy model shows that the evolution of  $\langle B_y \rangle$  is controlled by shear of radial field and buoyant removal of toroidal field. . . . . 158
- 5.7 Time- and horizontally-averaged vertical distributions of various quantities in 32Num. Upper left: gas density; upper right: Maxwell (solid) and Reynolds (dashed) stresses; lower left: gas pressure (solid), magnetic energy (dashed), and kinetic energy (dotted); lower right: gas  $\beta$  defined as the time- and horizontally-averaged gas pressure divided by the time- and horizontally-averaged magnetic energy density. The time average is done from orbit 100 to the end of the simulation. The stress and magnetic energy is relatively flat for  $|z| \lesssim 2H$  but drops off substantially for larger  $|z|$ . Outside of  $|z| \sim 2H$ , the magnetic energy dominates over gas pressure. . . . . 162
- 5.8 Magnetic field structure at  $t = 100$  orbits in 32Num, produced via a stream line integration. The field strength (in code units) is displayed via color and not the density of the field lines. The magnetic field has a primarily toroidal structure but has a smaller, tangled structure in the  $x$  and  $z$  directions. . . . . 163
- 5.9 Volume-averaged Reynolds and Maxwell stresses normalized by the volume-averaged gas pressure as a function of time in orbits in the vertically stratified simulations at 64 (left) and 32 (right) grid zones per  $H$ . The volume-average is done for all  $x$  and  $y$  and for  $|z| \leq 2H$ . The black line corresponds to  $Re = 800$  and  $P_m = 4$ , green is  $Re = 1600$  and  $P_m = 0.5$ , light blue is  $Re = 1600$  and  $P_m = 2$ , dark blue is  $Re = 1600$  and  $P_m = 4$ , and red is  $Re = 6400$  and  $P_m = 0.5$ . Some of the simulations appear to undergo periods of decay followed by regeneration of the MRI. This can occur on very long timescales of  $\sim 100$  orbits in some cases. . . . . 164

- 5.10 Quantitative measurement of how well resolved the MRI is in the toroidal ( $Q_y$ ; left plot) and vertical ( $Q_z$ ; right plot) directions as a function of time. The solid line corresponds to run 32Re1600Pm4 and the dashed line is 64Re1600pm4. The dotted horizontal line corresponds to  $Q = 6$ , below which the MRI is considered to be under-resolved (Sano et al. 2004).  $Q_i$  is calculated using the volume average of the magnetic energy and gas density for all  $x$  and  $y$  and for  $|z| \leq 0.5H$  (see text). The toroidal field MRI at both resolutions as well as the vertical field MRI at the higher resolution appear to be reasonably well-resolved. However, at the lower resolution, the vertical field MRI is only marginally resolved. . . . . 166
- 5.11 Space-time diagram of the horizontally averaged  $B_x$  (top panel) and  $B_y$  (bottom panel) for the first 200 orbits of 32Re1600Pm0.5. The turbulence initially decays, leaving a net  $B_x$  within the mid-plane region, which shears into toroidal field. This appears to eventually reenergize the MRI, but the large resistivity quickly quenches the turbulence again. . . . . 168
- 5.12 Space-time diagram of the horizontally averaged  $B_x$  (top left) and  $B_y$  (bottom left) for a 300 orbit period in 32Re6400Pm0.5, and the average of  $B_x$  (top right) and  $B_y$  (bottom right) over all  $x$  and  $y$  and for  $|z| \leq 0.5H$  as a function of time in orbits for the same 300 orbit period. During the period of no MRI turbulence, a net radial field still exists within the mid-plane region. This field appears to flip signs occasionally, leading to corresponding flips in  $B_y$  due to shear. . . . 170
- 5.13 Volume-averaged Reynolds and Maxwell stresses normalized by the volume-averaged gas pressure as a function of time in orbits in 32Re1600Pm2 (solid line) and 32Re1600Pm2\_By+ (dashed line). The volume average is done over all  $x$  and  $y$  and for  $|z| \leq 2H$ . The run in which a net  $B_y$  is added into the mid-plane region (dashed line) has the MRI reactivated, followed by subsequent periods of decay and growth. . . . . 173
- 5.14 Space-time diagram of the horizontally averaged  $B_x$  (top panel) and  $B_y$  (bottom panel) for 32ShearBx. The uniform radial field that is present initially shears into toroidal field, which eventually becomes strong enough to launch the MRI. . . . . 174

5.15 Volume-averaged total stress normalized by the volume-averaged gas pressure as a function of time in orbits for a series of unstratified shearing box simulations. The volume-average is done over the entire simulation domain. In each plot, the black line is from a simulation with only numerical dissipation. The colored lines are simulations with physical dissipation, initiated from the numerical dissipation run at orbit 100. The red lines correspond to  $Re = 1600$ ,  $P_m = 2$  and the blue line is  $Re = 1600$ ,  $P_m = 1$ . The top panel is initiated with a background toroidal field characterized by  $\beta = 1000$ , and the bottom panel has  $\beta = 10000$ . The weaker toroidal field appears to be killed off at a lower resistivity compared to the stronger background field. . . . . 175

5.16 Magnetic field structure at  $t = 550$  orbits in 32Re1600Pm2\_By+, produced via a stream line integration. The field strength (in code units) is displayed via color and not the density of the field lines. The color scale is the same as that in Fig. 5.8 for comparison. This snapshot corresponds to a state in which the turbulence has decayed. The magnetic field is almost completely toroidal near the mid-plane but has a tangled structure in the upper  $|z|$  regions, more reminiscent of the active state. . . . . 180

5.17 Volume-averaged total stress normalized by the volume-averaged gas pressure as a function of time in orbits in the lower resolution, vertically stratified simulations where turbulence remains sustained. The volume-average is done for all  $x$  and  $y$  and for  $|z| \leq 2H$ . The left plot is the first 120 orbits of the evolution, whereas the right plot is 350 orbits of the evolution. The black line corresponds to  $Re = 800$  and  $P_m = 4$ , dark blue is  $Re = 1600$  and  $P_m = 4$ , magenta is  $Re = 800$  and  $P_m = 8$ , and brown is  $Re = 6250$  and  $P_m = 1$ . The vertical axis has been chosen to match that of Fig. 5.2 for comparison. . . . . 183

5.18 Time- and volume-averaged stress parameter  $\alpha$  as a function of  $P_m$  in the unstratified FT simulations (left plot) and the stratified simulations (right plot);  $\alpha \equiv \langle \langle \rho v_x \delta v_y - B_x B_y \rangle \rangle / \langle P \rangle$ . The average is calculated over the entire domain (all  $x$  and  $y$  and for  $|z| \leq 2H$ ) and from 120 (150) orbits to the end of the simulation for the unstratified (stratified) runs. The dashed lines are linear fits to the data in log-log space, and the error bars denote one standard deviation about the temporal average. Both cases show a clear  $P_m$  dependence. However, in the stratified runs, this dependence is less steep, and there is considerable temporal variability. . . . . 183

5.19 Time- and horizontally-averaged total stress as a function of  $z$  on a linear (left) and logarithmic (right) vertical scale. The stress is normalized by the time- and volume-averaged gas pressure, where the volume average is done for all  $x$  and  $y$  and for  $|z| \leq 2H$ . The time average is done from orbit 150 until the end of each simulation. The solid line corresponds to 32Re800Pm8, the dashed line is 32Re800Pm4, the dotted line is 32Re1600Pm4, and the dot-dashed line is 32Re6250Pm1. The stress appears to increase with  $P_m$  for nearly all  $z$ , and for all  $P_m$ , there is a sharp decrease in the stress for  $|z| \gtrsim 2H$ . . . . . 184

# List of Tables

|     |  |     |
|-----|--|-----|
| 3.1 | Unstratified Simulations with Numerical Dissipation . . . . .          | 37  |
| 3.2 | Saturation Characteristics in Unstratified MRI Turbulence . . . . .    | 55  |
| 4.1 | Zero Net Flux Simulations with Physical Dissipation . . . . .          | 105 |
| 4.2 | Toroidal Field Simulations Initialized from Linear Perturbations . . . | 111 |
| 4.3 | Toroidal Field Simulations Initialized from Nonlinear Turbulence . . . | 115 |
| 5.1 | Unstratified Simulations to Calibrate Physical Dissipation . . . . .   | 146 |
| 5.2 | Vertically Stratified Shearing Box Simulations . . . . .               | 154 |

# Chapter 1

## Introduction

Whether it be the beautiful rings around Saturn, the flattened, spiral structure of the Milky Way, or the primordial disk from which our very own solar system formed, the Universe has a strong affinity for the formation of disks. This common phenomenon is simply the direct result of angular momentum conservation; astrophysical systems undergoing gravitational collapse spin up and the resulting centrifugal acceleration leads to the flattening of material into a disk.

Perhaps most intriguing is a certain subclass of these structures, known as *accretion disks*, which get their name from their ability to move gas inward and onto the object at the center of the gravitational potential. This accretion is interesting because of the crucial role it plays in many astrophysical environments. In protostellar systems, for example, the mass of the protostar is largely controlled by the accretion of gas through the disk via dramatic increases in accretion rates and observed luminosity known as FU Ori outbursts (e.g., Hartmann 1998). Furthermore, the formation of planets is inextricably connected to accretion disks in young stellar systems; not only do planets directly form out of the disk material, but the accretion process itself may play a pivotal role in the coagulation of dust particles into planetesimals (e.g.,

Kretke & Lin 2007; Johansen 2009; Oishi & Low 2009; Yang et al. 2009; Dzyurkevich et al. 2010) and the migration of planetary bodies (e.g., Winters et al. 2003; Nelson & Papaloizou 2003, 2004; Papaloizou et al. 2004; Yang et al. 2009).

Accretion disks are also important in the final stages of stars' lives, particularly those in binary systems. The strong gravity of the “dead” compact star (i.e., a white dwarf, neutron star, or black hole) strips gas off of the surface of the companion star. This gas accretes onto the dead star via a disk, while heating up to considerable temperatures and emitting light (up to X-ray wavelengths in some systems). These binary systems are also quite variable, producing such observed phenomena as dwarf nova outbursts in white dwarf systems and spectral state transitions in compact X-ray binaries. This strong variability is thought to be directly related to the physics of accretion itself.

The luminous distant quasars as well as other forms of Active Galactic Nuclei (AGN) are believed to be powered by the accretion of gas onto a supermassive black hole through a disk. As in their smaller mass cousins, these disks release an enormous amount of gravitational energy as light, allowing us to see some of the most distant objects in the Universe. Furthermore, given the strong relationship between supermassive black hole mass and properties of the host galaxy (Ferrarese & Merritt 2000; Gebhardt et al. 2000), this disk accretion is likely to be causally linked to the formation of larger scale structures.

It should now be clear that disk accretion is a very ubiquitous phenomenon in the Universe, and that by understanding the physics of this process, we can begin to unlock many of the Universe's mysteries and answer some of the most profound questions formulated to-date. It is the aim of this thesis to further our understanding of accretion through a theoretical study of its physics.

## 1.1 The $\alpha$ Model for Accretion Disks

Perhaps the most pervasive and important question in accretion disk physics is: what removes angular momentum from the disk gas, allowing it to accrete inwards? One might naively guess that the microphysical viscosity of the gas serves as a torque between differentially rotating fluid elements and thus transports angular momentum outward. This viscosity, however, is orders of magnitude too small to account for the observed accretion rates. For example, consider fully ionized gas of temperature  $T \sim 10^4$  K and density  $n_{\text{H}} \sim 10^{14} \text{ cm}^{-3}$ , appropriate for an AGN disk around a  $10^8 M_{\odot}$  black hole (Balbus & Henri 2008). From Spitzer (1962), we estimate the viscosity to be  $\nu \sim 10^5 \text{ cm}^2 \text{ s}^{-1}$ . Assuming an accretion timescale on the order of the viscous diffusion time,

$$\tau \sim \frac{R^2}{\nu} \tag{1.1}$$

where  $R \sim 10^{15}$  cm is a typical length scale for these disks and corresponds to 30 Schwarzschild radii. This implies  $\tau \sim 10^{17}$  yr, which is much greater than the age of the Universe. Microphysical viscosity cannot provide the necessary angular momentum transport in accretion disks.

If the disk gas were somehow turbulent, then perhaps the interaction of turbulent eddies can lead to a net transfer of angular momentum outward. While this notion of enhanced *turbulent viscosity* has been around for some time, it was the seminal work of Shakura & Syunyaev (1973) that first put this idea within the context of accretion disks.

The disk-height-integrated radial angular momentum flux (e.g., Balbus & Hawley 1998) can be written as

$$\Sigma R \left[ v_K \langle v_R \rangle_z + \left\langle \delta v_\phi \delta v_R - \frac{\delta B_\phi \delta B_R}{4\pi\rho} \right\rangle_z \right], \quad (1.2)$$

where the coordinates are cylindrical  $(R, \phi, z)$ ,  $\Sigma$  is the height-integrated disk surface density,  $\rho$  is the gas volume density,  $v_K$  is the Keplerian velocity, and  $\delta$  denotes fluctuations from an average. Thus,  $\delta v_\phi$  is the departure from Keplerian velocity,  $\delta v_R$  is the radial velocity fluctuation from the average,  $\langle v_R \rangle_z$ , and  $\delta B_R$  and  $\delta B_\phi$  are the magnetic field fluctuations from the average  $R$  and  $\phi$  components respectively. The  $z$  subscripts on the angled brackets denote density-weighted height integrations.

If matter slowly spirals inward, then  $\langle v_R \rangle_z$  is negative; this term represents the inward flux of angular momentum carried by the accreting material. The second term on the right-hand-side is completely composed of fluctuations, and it represents the turbulent *outward* angular momentum flux. The turbulence can be magnetohydrodynamic in nature, hence the magnetic field fluctuations in the outward flux. The basic idea put forth by Shakura & Syunyaev (1973) is that correlations in the turbulent fluctuations dominate the angular momentum flux, leading to net outward angular momentum transport, while a small amount of angular momentum is dragged inward (since  $\langle v_R \rangle_z < 0$ ) with the majority of the gas. Thus, the so-called turbulent viscous stress tensor responsible for outward radial angular momentum transport is written as

$$W_{R\phi} \equiv \left\langle \delta v_\phi \delta v_R - \frac{\delta B_\phi \delta B_R}{4\pi\rho} \right\rangle_z. \quad (1.3)$$

While Shakura & Syunyaev hypothesized that turbulence is responsible for momentum transport, they did not know the origin of this turbulence. Therefore, they could not definitively state what sets the value of  $W_{R\phi}$  (i.e., what does  $W_{R\phi}$  functionally depend on?). They did, however, make the assumption that the amplitude of the

turbulent fluctuations is limited by the local sound speed, leading to the so-called  $\alpha$  prescription for the stress,

$$W_{R\phi} = \alpha c_s^2, \quad (1.4)$$

where  $c_s$  is the gas sound speed, and  $\alpha$  is a dimensionless parameter that quantifies the level of angular momentum transport. This assumption was based on the argument that any velocities in excess of the sound speed would form shocks and quickly dissipate to subsonic values. They also made the assumption that the gravitational energy released as matter accretes inward would be rapidly radiated away. In other words, the stress leading to angular momentum transport is locally correlated with the radiation of gravitational energy. While these assumptions seemed reasonable, there was still no obvious or robust origin for this turbulence; this mystery would remain unsolved for nearly two more decades.

## 1.2 The Magnetorotational Instability (MRI)

As discussed above, it had long been in the mind of astrophysicists that magnetic fields may play a role in the turbulence proposed by Shakura & Syunyaev (1973). However, it was not until the discovery of the magnetorotational instability (MRI) by Balbus & Hawley (1991) that the importance of this role was fully realized. Magnetic fields are not just another component of the stress tensor, acting to further enhance transport; they are in fact, the cause of the turbulence. In the presence of a negative angular velocity gradient, a weak magnetic field of any orientation will rapidly destabilize the flow, leading not only to enhanced turbulence but to a sustained, positive value for

$W_{R\phi}$ .<sup>1</sup> In what follows, we will describe the basic physics of the MRI, first focusing on the linear growth regime of the instability and then on the nonlinear, fully turbulent saturated state.

### 1.2.1 MHD Equations

Before launching into a detailed description of the MRI, it is useful to write down the equations of MHD, which are at the heart of disk dynamics and the MRI. A magnetized, compressible fluid is described by,

$$\frac{\partial \rho}{\partial t} + \nabla \cdot (\rho \mathbf{v}) = 0, \quad (1.5)$$

$$\rho \frac{\partial \mathbf{v}}{\partial t} + \rho \mathbf{v} \cdot \nabla \mathbf{v} = -\nabla \left( P + \frac{1}{2} B^2 \right) - \rho \nabla \Phi + \mathbf{B} \cdot \nabla \mathbf{B} + \nabla \cdot \mathbf{T}, \quad (1.6)$$

$$\frac{\partial \mathbf{B}}{\partial t} = \nabla \times (\mathbf{v} \times \mathbf{B} - \eta \nabla \times \mathbf{B}). \quad (1.7)$$

The first equation describes mass conservation, the second equation is the momentum equation, and the third equation is the magnetic induction equation. Our notation is standard;  $\rho$  is the density,  $\mathbf{v}$  is the velocity,  $P$  is the (isotropic) gas pressure, and  $\mathbf{B}$  is the the magnetic field. The gravitational potential (as of yet undefined) is written as  $\Phi$ . The only microphysical effects we consider here are Ohmic resistivity,  $\eta$ , and shear viscosity,  $\nu$ , included via a viscous stress tensor,

$$T_{ij} = \rho \nu \left( \frac{\partial v_i}{\partial x_j} + \frac{\partial v_j}{\partial x_i} - \frac{2}{3} \delta_{ij} \nabla \cdot \mathbf{v} \right). \quad (1.8)$$

This system of equations also contains an equation of state. For an isothermal fluid, this is

---

<sup>1</sup>Here, *weak magnetic field* simply means that there are Alfvén modes with phase speed less than the orbital speed. This will be quantified later.

$$P = \rho c_s^2 \quad (1.9)$$

where  $c_s$  is the isothermal sound speed. In the case of an adiabatic gas, which we will also consider in this work, an equation of total energy conservation is included,

$$\frac{\partial(E + \rho\Phi)}{\partial t} + \nabla \cdot \left[ \left( E + \rho\Phi + P + \frac{1}{2}B^2 \right) \mathbf{v} - \mathbf{B}(\mathbf{B} \cdot \mathbf{v}) - \mathbf{v} \cdot \mathbf{T} + \eta(\nabla \times \mathbf{B}) \times \mathbf{B} \right] = -\nabla \cdot \mathbf{F}_{\text{rad}}, \quad (1.10)$$

where the total energy is defined as

$$E = \epsilon + \frac{1}{2}\rho v^2 + \frac{1}{2}B^2, \quad (1.11)$$

and the thermal energy is

$$\epsilon = P/(\gamma - 1). \quad (1.12)$$

$\gamma$  is the adiabatic index, which in this work will always be  $\gamma = 5/3$ . Note that we could have just as well defined  $E$  to include the gravitational energy contribution,  $\rho\Phi$ . However, in our code (described in Chapter 2), the gravitational term is generally separated from the total energy. The energy equation shows that total energy (including gravity) is conserved except for losses represented by the radiative flux,  $\mathbf{F}_{\text{rad}}$ . Finally, note that from now on, we will use a system of units with magnetic permeability  $\mu = 1$ .

### 1.2.2 The Linear MRI

In this section, we closely follow the description presented in Section IV B of Balbus & Hawley (1998), which is a simple treatment of the linear MRI. A more detailed derivation can be found in Section IV C of that review. This simplified explanation gives a more intuitive description of the physical mechanism for the MRI, and is sufficient for this introduction, particularly since the work presented here has focused on the nonlinear regime.

We start at an arbitrary radius in a disk with some (as of yet unspecified) radial angular velocity profile. The disk gas is in circular orbits and is threaded with a vertical magnetic field. The system is completely axisymmetric, and for the purposes of this analysis, we assume that we are in a frame co-rotating with the fluid at the circular orbit radius. The gas is then perturbed from its circular orbit by a distance  $\xi$ . Let the spatial dependence of this perturbation vector be  $e^{ikz}$  and the amplitude of the perturbed magnetic field be  $\delta\mathbf{B}$ . We linearize the MHD equations of the previous section to keep only terms that are first order in the perturbation amplitude.

From equation (1.7), one then obtains the relationship between the perturbed field amplitude and the displacement vector,

$$\delta\mathbf{B} = ikB\xi. \quad (1.13)$$

Furthermore,  $\nabla \cdot \mathbf{B} = 0$  implies that  $\delta B_z = 0$  and  $\xi_z = 0$ , where the  $z$  subscript on  $B$  and  $\xi$  denotes the component in the  $z$  direction. From the momentum equation, the magnetic tension is  $\mathbf{B} \cdot \nabla \mathbf{B}$ . With the perturbation applied, this term becomes

$$\frac{ik}{\rho} B \delta\mathbf{B} = -(\mathbf{k} \cdot \mathbf{v}_A)^2 \xi, \quad (1.14)$$

where the right side of the equation follows from using equation (1.13), and  $v_A$  is the Alfvén speed ( $v_A \equiv B/\sqrt{\rho}$ ).

Applying equation (1.14) to the momentum equation and assuming that the gas is incompressible, the equations of motion become

$$\ddot{\xi}_R - 2\Omega\dot{\xi}_\phi = - \left[ \frac{d\Omega^2}{d\ln R} + (\mathbf{k} \cdot \mathbf{v}_A)^2 \right] \xi_R, \quad (1.15)$$

$$\ddot{\xi}_\phi + 2\Omega\dot{\xi}_R = - (\mathbf{k} \cdot \mathbf{v}_A)^2 \xi_\phi, \quad (1.16)$$

where  $\Omega$  is the angular velocity. The second term on the left hand sides of the equations accounts for the Coriolis force, and the first term on the right hand side of equation (1.15) is the tidal force; these terms result from boosting into the co-rotating frame. The final term on the right hand sides of the equations accounts for magnetic tension.

To reiterate, these equations describe the displacement of a fluid element from its circular orbit in the presence of a vertical magnetic field. There are a few interesting features to point out from these equations. First of all, as described by Balbus & Hawley (1998), these equations are mathematically equivalent to two orbiting masses connected via a massless spring with spring constant  $(\mathbf{k} \cdot \mathbf{v}_A)^2$ . In fact, if one removes the rotational motion (i.e.,  $\Omega = 0$ ,  $d\Omega^2/d\ln R = 0$ ), the exact equation for motion of mass on a spring (i.e., the harmonic oscillator) is recovered. The system stably exhibits oscillations unless the spring constant is negative, which is impossible because  $(\mathbf{k} \cdot \mathbf{v}_A)^2$  cannot be negative. However, adding the tidal potential term back in changes the picture. The effective spring constant in equation (1.15) then becomes negative when

$$\frac{d\Omega^2}{d\ln R} < 0, \quad (1.17)$$

and

$$\left| \frac{d\Omega^2}{d\ln R} \right| > (\mathbf{k} \cdot \mathbf{v}_A)^2; \quad (1.18)$$

i.e., the orbital velocity decreases outward (which is satisfied in a Keplerian disk) and the spring is weak compared to the orbital stretching. In this case, the negative effective spring constant causes continued growth of  $\xi_R$  through equation (1.15) and thus growth of  $\xi_\phi$  through equation (1.16). The system is unstable.

This basic mechanism is further illustrated in Fig. 1.1. The inner mass is moving at a larger angular velocity than the outer mass, stretching the spring. This stretching transports angular momentum from the inner mass to the outer mass. As the inner mass loses angular momentum, it falls to a smaller orbit and increases its angular velocity. The outer mass moves to a larger orbit and decreases its angular velocity. But now the spring is stretched even more as a result of the increased velocity and orbital separation. Thus, the two masses continually move apart with the spring continually being stretched, leading to a runaway. For magnetized disks, magnetic tension takes the place of spring tension, but the end result is the same; an instability.

Even from this simple description of the linear MRI, one can see that outward angular momentum transport is at the heart of the instability. Indeed, the “stretching” of the magnetic field due to the shear leads to a torque that outwardly transfers angular momentum. However, this linear approximation cannot remain in effect forever; as the instability sets in, the perturbations grow exponentially in amplitude. This is evident from again consulting equations (1.15) and (1.16). If the prefactor on the right hand side of equation (1.15) is positive, then oscillations are replaced by

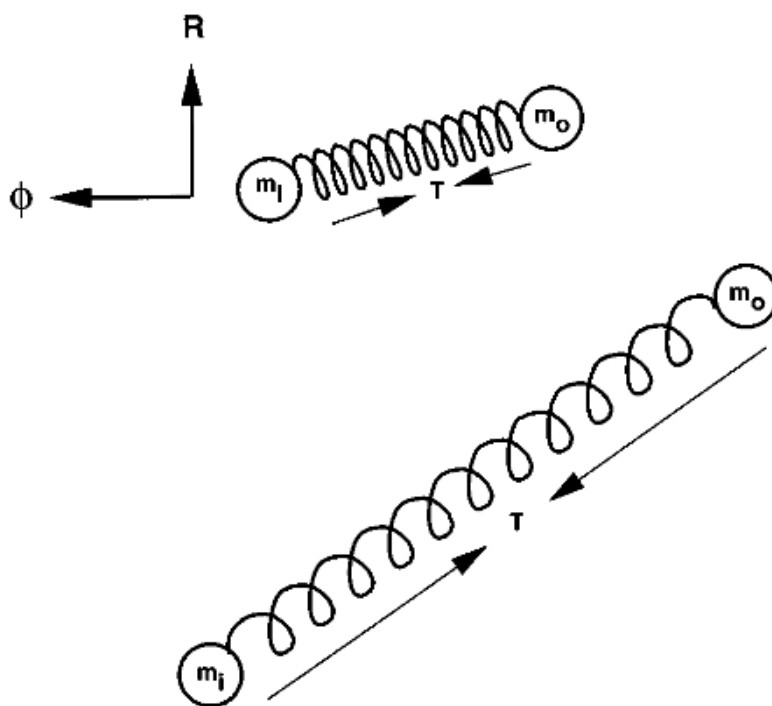


Fig. 1.1.— A cartoon of two springs orbiting a point mass at different radii, connected by a spring with tension  $T$ . The inner mass,  $m_i$ , moves at a higher angular velocity than the outer mass,  $m_o$ , thus stretching the spring. This stretching causes angular momentum to be transported from  $m_i$  to  $m_o$ , which separates the two masses even more. The result is a runaway. This picture serves to conceptualize the linear growth of the magnetorotational instability (Balbus & Hawley 1998, Fig. 16).

continual growth; increasing  $\xi_R$  leads to an increase in  $\ddot{\xi}_R$ , and the system runs away. By assuming a time dependence of  $e^{-i\omega t}$  for the perturbations, we can calculate (after a bit of math) the dispersion relation for the MRI,

$$\omega^4 - \omega^2 [\kappa^2 + 2(\mathbf{k} \cdot \mathbf{v}_A)^2] + \left[ (\mathbf{k} \cdot \mathbf{v}_A)^2 + \frac{d\Omega^2}{d\ln R} \right] = 0, \quad (1.19)$$

where  $\kappa$  is the epicyclic frequency defined via

$$\kappa^2 \equiv 4\Omega^2 + \frac{d\Omega^2}{d\ln R}, \quad (1.20)$$

which equals  $\Omega^2$  for Keplerian rotation.

The instability sets in for  $\omega^2 < 0$ , and from the dispersion relation, one can calculate the growth rate for the fastest growing mode. For Keplerian rotation, this maximum growth rate is

$$|\omega_{\max}| = \frac{3}{4}\Omega, \quad (1.21)$$

which occurs for

$$(\mathbf{k} \cdot \mathbf{v}_A)_{\max} = \frac{\sqrt{15}}{4}\Omega. \quad (1.22)$$

In other words, the fastest growing mode grows on an orbital (i.e., dynamical) timescale and has a characteristic scale of roughly the distance an Alfvén wave can travel in an orbital time.

It is clear that the MRI leads to rapid, exponential growth of small perturbations; again, these perturbations will not remain small forever, and eventually the linear approximation breaks down. What happens next requires knowledge of the nonlinear regime, which becomes much less accessible by analytic methods.

### 1.2.3 Hydrodynamic Transport?

Before moving onto a description of the nonlinear MRI, we want to reemphasize the importance that magnetic fields play in angular momentum transport by once again consulting equations (1.15)-(1.16), this time with the magnetic component removed (i.e,  $\mathbf{v}_A = 0$ ),

$$\ddot{\xi}_R - 2\Omega\dot{\xi}_\phi = -\frac{d\Omega^2}{d\ln R}\xi_R, \quad (1.23)$$

$$\ddot{\xi}_\phi + 2\Omega\dot{\xi}_R = 0. \quad (1.24)$$

From the second equation, one can time-integrate  $\ddot{\xi}_\phi$  to find a relationship between  $\dot{\xi}_\phi$  and  $\xi_R$ . Plugging this into the first equation and simplifying with the help of equation (1.20) yields,

$$\ddot{\xi}_R = -\kappa^2\xi_R. \quad (1.25)$$

For an outwardly decreasing angular velocity (such as is present in Keplerian disks),  $\kappa^2 > 0$ , and we are left with the equation of a harmonic oscillator. With the removal of the destabilizing term,  $(\mathbf{k} \cdot \mathbf{v}_A)^2$ , the tidal and Coriolis forces act to restore displacements from circular orbits. Instead of rapidly growing modes, we get simple epicyclic motion with frequency  $\kappa$ ; there is no avenue for linear instability present in purely hydrodynamic Keplerian disks!

While this simple exercise is illustrative in demonstrating how magnetic fields alter orbital flow in a fundamental way, it is somewhat limited in that it only applies to the linear regime. Can nonlinear amplitude disturbances lead to hydrodynamic transport? This question has been investigated many times through both numerical

and analytic work (e.g., Brandenburg et al. 1995; Balbus et al. 1996; Hawley et al. 1996; Balbus & Hawley 1998; Hawley et al. 1999; Lesur & Longaretti 2005; Shen et al. 2006). By writing the equations for averaged kinetic energy fluctuations in a purely hydrodynamic disk, Balbus & Hawley (1998) showed that if nonlinear instability were to create outward angular momentum flux via turbulent fluctuations, epicyclic motions actually serve as a dynamic sink for these fluctuations, and the turbulence would likely die away; epicyclic oscillations are a stabilizing force, even in the nonlinear regime! In agreement with this work, numerical simulations have shown *no* evidence for any sustained hydrodynamic turbulence resulting from nonlinear perturbations. Furthermore, arguments by Lesur & Longaretti (2005) suggest that even if hydrodynamic turbulence initiated from nonlinear perturbations does exist, the resulting angular momentum transport would be negligible.

Finally, we should note that other, purely hydrodynamic mechanisms for angular momentum transport have been investigated. One such example is that of transport induced via turbulent convection, though the effect of this turbulence on the actual transport of angular momentum is not entirely clear. Numerical simulations by Stone & Balbus (1996) have shown that such momentum transport is actually directed inward in the presence of convection. More recent work by Lesur & Ogilvie (2010) and Käpylä et al. (2010) have shown that in some cases, convection can lead to outward angular momentum transport. However, there are concerns about whether or not such convection is efficient enough at extracting energy from the shear flow to sustain itself. In other words, to sustain the convective turbulence, there would need to be a continual source of heating within the disk other than differential rotation (e.g., radioactive or chemical reaction heating) (Lesur & Ogilvie 2010).

Another possible transport mechanism is gravitational instability (e.g., Hartmann

1998, and references therein). When the disk is sufficiently massive or cool, the gas can become self-gravitating; self-gravity wins over the counteracting forces of thermal pressure and orbital shear. The resulting “clumping” of the gas leads to torques that outwardly transport angular momentum. However, because of the limited conditions under which this mechanism operates, it is not likely to be a viable source of transport in many disk systems (e.g., compact binary disks).

In summary, there are some possibilities for purely hydrodynamic angular momentum transport. This is perhaps good news since, in weakly ionized regions such as the dead zones of protoplanetary and protostellar disks (see Gammie 1996), the magnetic field may be insufficiently coupled to the gas to lead to MRI turbulence.<sup>2</sup> However, as briefly outlined above, these purely hydrodynamic mechanisms often require that quite restrictive conditions be satisfied in order for angular momentum to be transported outward. The MRI, on the other hand, is very robust; all one needs is a sufficiently magnetized gas and a weak magnetic field. This mechanism is thus the most viable option for momentum transport in most accretion disk environments.

### 1.2.4 The Nonlinear Regime

What happens beyond the exponential growth regime of the linear MRI? To answer this question, one must solve the full set of nonlinear MHD equations given in § 1.2.1. These equations are analytically solvable in very few cases, and the nonlinear regime of the MRI is *not* one of these cases. Thus, we must turn to another method in the theorist’s tool box: numerical simulations.

The first MRI simulations appeared in the early 1990’s, in the form of axisymmetric calculations of a small patch of disk (Hawley & Balbus 1991, 1992). While

---

<sup>2</sup>Though, consider Turner et al. (2007) who show that the MRI-active layers of protostellar disks can cause large scale magnetic fields to diffuse into the deadzone, leading to a nonzero stress there.

simplistic, this preliminary work showed that the linear growth of the MRI in simulations agreed with the analytic results and that once the nonlinear regime was reached, angular momentum was transported outward via enhanced turbulence.<sup>3</sup>

In Hawley et al. (1995) and Hawley et al. (1996), the sustained outward transport of angular momentum was confirmed for a variety of initial field geometries in full three-dimensional simulations of a local, co-rotating patch of accretion disk (referred to as the shearing box). For example, see Fig. 1.2, taken from Hawley et al. (1995), which shows that after the exponential growth out of the linear regime, the MRI saturates and continually transports angular momentum outward via enhanced Maxwell stress,  $-B_r B_\phi / 4\pi$ , and Reynolds stress,  $\rho \delta v_r \delta v_\phi$ , which are accompanied by increased magnetic and kinetic energies. That is, not only is the gas turbulent, but the turbulent fluctuations are correlated to produce outward momentum transport. This early work provided the baseline for future studies of the MRI via local simulations, and we describe these studies a bit more in detail both in § 1.3 and in the introductions to the chapters of this thesis.

Local simulations are quite useful for several reasons. First, they provide the fewest number of ingredients needed to produce MRI turbulence: orbital shear and magnetized gas. While such a simplistic approach is hardly enough to make direct connections between theory and observation, it provides a first principles understanding of the MRI from which one can advance towards more complicated simulations and analytic models. Second, local simulations are particularly useful for studying the microphysics of MRI turbulence. As recent results have shown (e.g., Fromang & Papaloizou 2007; Fromang et al. 2007; Lesur & Longaretti 2007), the smallest scales of the disk, where microphysical viscosity and Ohmic resistivity become important,

---

<sup>3</sup>Though, in the special case of a net vertical magnetic field, the nonlinear outcome of the MRI is the so-called channel mode, which breaks down in three-dimensional simulations (Hawley & Balbus 1992; Hawley et al. 1995).

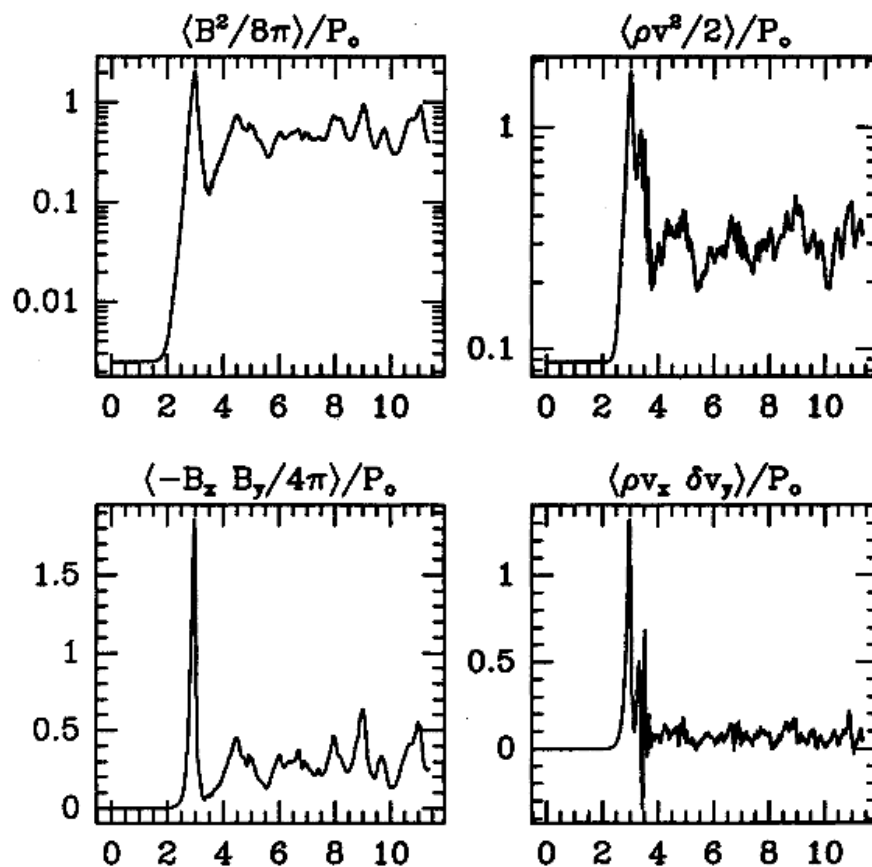


Fig. 1.2.— The volume averaged magnetic and kinetic energy evolutions and Maxwell and Reynolds stress evolutions for a fiducial shearing box simulation in Hawley et al. (1995). The horizontal axis is time in units of orbits (defined at the center of the local domain). Note that in the coordinate system of the shearing box,  $x$  corresponds to the radial direction, and  $y$  corresponds to the azimuthal direction (see Hawley et al. (1995) or Chapter 2 below). The development of the MRI is clearly shown. The positive values for the Maxwell and Reynolds stresses indicate outward angular momentum transport (Hawley et al. 1995, Fig. 3).

may have a substantial influence over the saturation level of the MRI. Furthermore, understanding the thermodynamic processes in MRI turbulence (e.g., turbulent energy flow, heating, and radiation), requires resolving the smallest disk scales possible, as these small scales are responsible for turbulent energy dissipation.

Local simulations are usually confined to a size on order the vertical scale height. Thus, these simulations are limited in the spatial scales that they can probe, and understanding the behavior of the MRI on larger scales requires the use of global simulations. With the advent of powerful supercomputers, global simulations with sufficient resolution to evolve the MRI have become feasible. As the focus of this thesis is on local simulations of the MRI, we will not describe in any detail the results from global simulations. However, from the earliest global MRI simulations, such as Hawley (2001), to more recent work (e.g., Beckwith et al. 2008a; Noble et al. 2010), these calculations have shown that the MRI does indeed operate on large scales, leading to significant mass accretion onto the central object as well as other interesting features, such as a strongly magnetized corona and the launching of jets, which is itself a function of disk magnetic field topology (e.g., Beckwith et al. 2008a).

### **1.3 Motivation: Connecting MRI Transport to Disk Phenomenology**

While global simulations may ultimately be the best method of connecting first principles accretion disk simulations to observations, the resolutions necessary to capture microphysical processes (e.g., viscosity and resistivity) in these simulations are currently far beyond computational capabilities. Furthermore, including complex radiation physics in such calculations is still quite a ways off. The current most promising

route to relating theory directly to observations is to create phenomenological models of accretion disks that include the effects of MRI turbulence in a sort of “sub-grid” manner.

Perhaps the best example of disk phenomenology is  $\alpha$  disk theory. As discussed above, it assumes that the stress is set by the gas and radiation pressure and that stress and energy dissipation/radiation are locally correlated. As we now know that the origin of the turbulence is the MRI, these assumptions should be reexamined. Is the stress set by the pressure? If not, what does set the saturation level of the stress? Furthermore, how well correlated are stress and the thermalization and subsequent radiation of turbulent energy? Again, answering such questions not only provides a better understanding of the angular momentum transport processes in disks but is also currently the best hope for developing phenomenological accretion disk models.

Numerous studies have investigated the pressure dependence of MRI turbulent stresses. In general, they have made it increasingly clear that the basic  $\alpha$  stress parameterization is not only too simplistic, it is actually misleading. Both the early shearing boxes of Hawley et al. (1995) as well as more recent work by Sano et al. (2004) have provided evidence that stress is *not* determined by pressure, at least in the usual manner of the  $\alpha$  disk. More specifically, the comprehensive parameter study by Sano et al. (2004) observed at best only a very weak gas pressure dependence. Instead, stress is (in some cases) proportional to the *magnetic* pressure (Hawley et al. 1995, 1996; Blackman et al. 2008), but the magnetic energy is not itself directly determined by the gas or radiation pressure. The implications of these results are significant. In particular, recent local simulations using vertically stratified shearing boxes and radiation transport (Hirose et al. 2009) have found no evidence of the thermal instability long believed to be present in radiation-pressure supported  $\alpha$  disks.

If stress is proportional to magnetic rather than gas or radiation pressure, what determines the magnetic pressure in a disk? Apart from the expectation that the field will remain subthermal, this remains uncertain. The simplest shearing box simulations using ideal MHD have a limited range of significant parameters; this is both a strength and a weakness of that model. The magnetic energy in the saturated state could depend upon such factors as box size, the amplitude and geometry of the imposed initial magnetic field, and the ratio of the gas pressure to magnetic pressure (the plasma  $\beta$  value). Hawley et al. (1995) and Hawley et al. (1996) studied the effect of initial magnetic field topology on the resulting stress and found that although the MRI leads to turbulence regardless of the initial field, simulations that have an imposed net vertical field produce higher turbulence levels than an imposed toroidal field or a simulation that began with zero net magnetic flux within the domain. Hawley et al. (1995) found that the total magnetic energy and the resulting stress in the saturated turbulent state was a function of the initial plasma  $\beta$  with a uniform vertical or toroidal field, namely that larger  $\beta$  (i.e., weaker fields) leads to smaller saturation levels.

A physical influence that has, until recently, received less attention is physical dissipation, namely shear viscosity  $\nu$  and Ohmic resistivity  $\eta$ . The linear dispersion relation for the vertical field MRI in the presence of  $\nu$  and  $\eta$  was derived by Balbus & Hawley (1998). Both terms can reduce the effectiveness of the MRI. In the linear regime, viscosity damps the MRI growth rates and changes the wavelength of the fastest growing mode, but does not alter the wavenumbers that are unstable. Resistivity introduces a cutoff on the unstable wavelengths where the resistive diffusion time becomes comparable to the MRI growth time (see, e.g., the discussion in Masada & Sano 2008). Nonaxisymmetric MRI modes with Ohmic resistivity were

examined by Papaloizou & Terquem (1997). They found that resistivity reduces the amplification of such modes, and if large enough, can stabilize the toroidal field MRI.

Simulations by Hawley et al. (1996), Sano et al. (1998), Fleming et al. (2000), Sano & Inutsuka (2001), Ziegler & Rüdiger (2001), and Sano & Stone (2002b) have investigated the influence of  $\eta$  on the saturated state. The main result of these studies is that increasing  $\eta$  leads to a decrease in turbulence, independent of the magnetic field configuration. In zero net field models, the effect of  $\eta$  on the turbulence is larger than one might expect from the linear MRI relation (Fleming et al. 2000), with the turbulence decaying to zero for relatively low values of resistivity.

Recently, the work of Fromang et al. (2007) and Lesur & Longaretti (2007) has sparked new interest in the effects of non-ideal MHD on the MRI. Fromang et al. (2007) showed that both  $\eta$  and  $\nu$  are important in determining the stress level in MRI turbulent flows with zero net magnetic field. Lesur & Longaretti (2007) came to the same conclusion for models with a net vertical field. The results were characterized in terms of the magnetic Prandtl number, defined as  $P_m = \nu/\eta$ , and it was found that the saturation level increases with increasing  $P_m$ . Fromang et al. (2007) also found that for the zero net field case, there exists a  $P_m$  below which the turbulence dies out, and that this critical  $P_m$  decreases with decreasing  $\nu$  (at least for the range in  $\nu$  and  $\eta$  examined in the paper).

One of the primary goals of this thesis work is a detailed investigation of this  $P_m$  effect on the MRI. Specifically, what is the  $P_m$  dependence of the saturated stress for different numerical algorithms, different magnetic field topologies, and other physical effects, such as vertical gravity? Answering these questions is an important step towards understanding the saturation of the MRI in real accretion disks.

Determining the stress levels in MRI turbulence is only one aspect of the problem;

another is exploring how that turbulence is dissipated into heat. Again, the  $\alpha$  model assumes that the accretion energy is deposited as heat locally and rapidly, and Balbus & Papaloizou (1999) showed that this property should hold for the energetics of MHD turbulence as well. In the simulations, we can determine the rate at which turbulent energy is thermalized and the path that energy takes as it moves from the free energy of the shear flow to turbulence and then to heat. Such issues were briefly touched on by Brandenburg et al. (1995) who found that the turbulent magnetic energy was  $\sim 6$  times greater than the perturbed kinetic energy, but dissipational heating resulted from roughly equal contributions of magnetic and kinetic energy dissipation. This result led them to suggest that there was a net transfer of magnetic energy to turbulent kinetic energy. Sano & Inutsuka (2001) studied energy flow in the context of MRI channel modes, which are strong radial streaming motions that result from the linear growth of the vertical field MRI (Hawley & Balbus 1992; Balbus & Hawley 1998). Their work included resistivity (but not viscosity) and showed that resistive heating dominated the thermalization of energy stored in these channel modes. Dissipational heating also plays an important role in radiative effects and determining disk structure, both of which may be observable properties of disks (e.g., Beckwith et al. 2008b).

Thus, given the importance of understanding disk heating, another goal of this thesis work is a detailed investigation of the “locality” of MRI-driven turbulence, specifically focusing on the second assumption of the  $\alpha$  model. How well correlated are the stresses that drive angular momentum transport and thermalization of the turbulent energy?

## 1.4 Thesis Structure

The structure of this thesis is as follows. In Chapter 2, we provide a description of the general Athena algorithm and the modifications made for the shearing box simulations. In Chapter 3, we present a series of MRI simulations without physical dissipation or vertical gravity. These simulations are utilized for comparison with previous ZEUS-based results in the literature, for an analysis of the locality of turbulent disk heating, and to quantify the numerical dissipation of Athena in preparation for including physical dissipation. Chapter 4 explores the effect of  $P_m$  on MRI-driven turbulence in the presence of a net toroidal field, and in Chapter 5, we examine the effect of  $P_m$  on MRI turbulence in the presence of vertical gravity. Finally, we wrap up with our main conclusions and some general thoughts in Chapter 6.

## Chapter 2

# Numerical Methods

All of the simulations discussed here are performed with the Athena code. In this chapter, we first describe the details of the Athena algorithm and then its application to the shearing box problem.

### 2.1 Athena

The Athena code is a second-order accurate Godunov scheme for solving the equations of MHD in conservative form using the dimensionally unsplit corner transport upwind (CTU) method of Colella (1990) coupled with the third-order in space piecewise parabolic method (PPM) of Colella & Woodward (1984) and a constrained transport (CT; Evans & Hawley 1988) algorithm for preserving the  $\nabla \cdot \mathbf{B} = 0$  constraint.

Considerable effort has been put into testing Athena and documenting the results; a very detailed description of the algorithm and tests can be found in Stone et al. (2008), Gardiner & Stone (2005b) and Gardiner & Stone (2008). As these sources are comprehensive, we will not repeat all the details here but will instead provide a summary of the general methodology.

Athena solves the MHD equations of § 1.2.1 in conservative form,

$$\frac{\partial \rho}{\partial t} + \nabla \cdot (\rho \mathbf{v}) = 0, \quad (2.1)$$

$$\frac{\partial \rho \mathbf{v}}{\partial t} + \nabla \cdot (\rho \mathbf{v} \mathbf{v} - \mathbf{B} \mathbf{B}) + \nabla \left( P + \frac{1}{2} B^2 \right) = 0, \quad (2.2)$$

$$\frac{\partial \mathbf{B}}{\partial t} - \nabla \times (\mathbf{v} \times \mathbf{B}) = 0. \quad (2.3)$$

$$\frac{\partial E}{\partial t} + \nabla \cdot \left[ \left( E + P + \frac{1}{2} B^2 \right) \mathbf{v} - \mathbf{B} (\mathbf{B} \cdot \mathbf{v}) \right] = 0. \quad (2.4)$$

The notation is the same as in § 1.2.1, and we have neglected the viscous, resistive, and gravitational terms for the time being. We write the equations in this form to demonstrate that each equation can be written as the time derivative of some conserved quantity plus the divergence of the flux of that quantity.<sup>1</sup> The conserved quantities for these equations are mass, momentum, magnetic flux, and total energy.

The discretization of the above equations is done in such a manner as to ensure the global conservation of these quantities. Specifically, a Riemann solver is fed “left” and “right” state values for the gas variables at every interface between grid cells. These left/right state values have been spatially interpolated from the grid cell center to the interface. The flux for each conserved quantity is then calculated at the interfaces via the Riemann solver. Since the fluxes at every interface are calculated simultaneously, integrating the conservation equations forward in time through finite-differencing ensures the global conservation of the conserved quantities. The specific Riemann solver used for the simulations in this thesis is described in each chapter’s

---

<sup>1</sup>The pressure gradient term in equation (2.2) is not written as the divergence of a flux but when writing out the components of the gradient, the  $i$ th component of the gradient becomes the derivative of a flux term for the  $i$ th component of the momentum. Furthermore, equation (2.3) is written in terms of the curl of an electromotive force (EMF), not the divergence of a flux. One can recast this as the divergence of a flux, but the CT method evolves the magnetic field components based on the above formulation (Stone et al. 2008). Thus, we display it in this fashion.

“method” section.

The induction equation is solved via the CT method (Evans & Hawley 1988), which is similar to the flux-conserving method, but uses the electromotive force (EMF) at the corners between grid cells to conserve magnetic flux through the grid cell interfaces. There are many details involved in combining this CT method with the Riemann solver approach used for the other conserved quantities. Again, we refer the reader to Stone et al. (2008), Gardiner & Stone (2005b), and Gardiner & Stone (2008) for more information.

The viscous, resistive, and gravitational terms can be added to the above equations in a conservative manner. For example, the viscosity can be added as the divergence of the viscous stress tensor given by equation (1.8). Similarly, resistivity can be added to the induction equation as a resistive EMF, thus ensuring that  $\nabla \cdot \mathbf{B} = 0$  is maintained. The details of implementation for these additional terms varies depending on the specific simulations run, and we describe them in the later chapters as appropriate.

As mentioned above, Athena enforces strict conservation of total energy via equation (2.4). Thus, the internal energy equation is not solved, unlike most versions of ZEUS (see Stone & Norman (1992a,b) for more information about ZEUS). Instead, when the internal energy is needed, it is calculated by subtracting the magnetic and kinetic energies from the total energy,

$$\epsilon = E - \frac{1}{2}\rho v^2 - \frac{1}{2}B^2. \quad (2.5)$$

This approach ensures that dissipated kinetic and magnetic energy (either via numerical or physical dissipation) ultimately ends up as heat and cannot leave the grid via truncation error. This property makes Athena particularly advantageous for studies of energy flow and dissipation, such as the work presented in Chapter 3.

## 2.2 The Local Shearing Box Approximation

We use the local shearing box approximation in all of the simulations presented here. The shearing box is a model for a local disk region whose size is small compared to the radial location of the region, allowing us to expand the MHD equations in Cartesian form (see Hawley et al. (1995) for more details). The box co-rotates with an angular velocity  $\Omega$  corresponding to the value at the center of the box. Boosting into this co-rotating frame requires adding source terms to the momentum and total energy equations to account for the gravitational, centrifugal, and Coriolis forces. The modified momentum equation for ideal MHD is

$$\frac{\partial \rho \mathbf{v}}{\partial t} + \nabla \cdot (\rho \mathbf{v} \mathbf{v} - \mathbf{B} \mathbf{B}) + \nabla \left( P + \frac{1}{2} B^2 \right) = 2q\rho\Omega^2 \mathbf{x} - \rho\Omega^2 \mathbf{z} - 2\boldsymbol{\Omega} \times \rho \mathbf{v}, \quad (2.6)$$

and the modified total energy equation is

$$\frac{\partial E}{\partial t} + \nabla \cdot \left[ \left( E + P + \frac{1}{2} B^2 \right) \mathbf{v} - \mathbf{B} (\mathbf{B} \cdot \mathbf{v}) \right] = 2q\Omega^2 \rho \mathbf{v} \cdot \mathbf{x} - \Omega^2 \rho \mathbf{v} \cdot \mathbf{z}, \quad (2.7)$$

where  $q$  is the shear parameter, defined as  $q = -d\ln\Omega/d\ln R$ . We use  $q = 3/2$ , appropriate for a Keplerian disk. In this Cartesian expansion,  $x$  corresponds to the radial displacement from the center of the box,  $y$  is the azimuthal coordinate, and  $z$  is the vertical coordinate. The first source term on the right-hand side of equations (2.6) and (2.7) corresponds to radial tidal forces (gravity and centrifugal) in the corotating frame, and the second term in these equations corresponds to the vertical component of gravity from the central object. The third term in equation (2.6) is the Coriolis force. In some of the simulations, we have omitted the vertical gravity terms, making

them “unstratified” shearing box simulations. Finally, note that unlike in § 1.2.1, the gravitational terms are added as source terms to the energy equation; this was done to reflect the method of handling gravity separately from the core Athena algorithm, which we now describe.

The general procedure for the addition of source terms into Athena is as follows (we again refer the reader to Stone et al. (2008) for details on the CTU-CT based Athena algorithm).

1. After the spatial reconstruction step along the  $x$  direction, the  $x$  and  $y$  accelerations (i.e., gravity plus Coriolis) are added to the interface values for  $v_x$  and  $v_y$ , respectively.
2. After the spatial reconstruction step along  $z$ , the vertical gravity acceleration is added to the interface values for  $v_z$ .
3. When the  $x$ -direction, transverse flux correction is added to the  $y$  and  $z$  interface  $\rho v_x$  and  $\rho v_y$  values, add the  $x$  and  $y$  forces, respectively. Similarly, add the appropriate source terms to the  $y$  and  $z$  interface values for  $E$  if the total energy equation is evolved.
4. When the  $z$ -direction, transverse flux correction is added to the  $x$  and  $y$  interface  $\rho v_z$  values, add the vertical gravity force. Similarly, add the vertical gravity source term to the  $x$  and  $y$  interface values for  $E$  if the total energy equation is evolved.
5. After the cell-centered momentum components are updated to the half-time-step, add the appropriate source terms to these components. These updated half-time-step values are used in the calculation of the half-time-step corner values of the EMFs.

6. After the cell-centered momentum components and total energy are updated to the full time step, add the appropriate source terms again.

There are some simulations in which this procedure varies slightly, and we note these cases in the appropriate chapters below.

Another important component of shearing box simulations is the shearing periodic boundary conditions at the  $x$  boundaries, which are implemented as described in Hawley et al. (1995) with a few modifications for Athena. First, to summarize Hawley et al. (1995), fluid quantities within the  $x$  boundary ghost zones are mapped according to their shear displacement from the opposite  $x$  boundary. Mathematically, this can be written as

$$f(x, y, z) = f(x + L_x, y - q\Omega L_x t, z), \quad (2.8)$$

for the inner  $x$  boundary, where  $L_x$  is the size of the domain in the  $x$  direction. The function  $f$  represents any of the conserved fluid variables, except for the  $y$  momentum and the total energy. The  $y$  momentum is adjusted to account for the shear across the  $x$  boundaries as fluid moves out one boundary and enters at the other. Thus, at the inner boundary the  $y$  momentum,  $m_y$ , is

$$m_y(x, y, z) = m_y(x + L_x, y - q\Omega L_x t, z) + q\Omega L_x. \quad (2.9)$$

The total energy is then adjusted to account for this difference in  $y$  momentum. Similar expressions exist for the outer  $x$  boundary, but with the opposite sign on the  $q\Omega$  terms.

In the case that the difference in  $y$  positions between the two boundaries is a non-integer number of grid cells, the  $y$ -shifted quantities must be reconstructed in

the ghost zones to account for the remaining fraction of a grid cell. Furthermore, the precise conservation of a quantity depends on how this reconstruction is performed, and in general, the fluxes of a particular conserved quantity must be reconstructed to globally conserve the quantity to roundoff level. For example, consider the conservation of magnetic flux through the computational domain. For the magnetic flux through the box to be conserved to machine precision, the line integral of the electromotive force (EMF),  $\mathcal{E} = -\mathbf{v} \times \mathbf{B}$ , along the boundaries must remain zero. The  $y$  and  $z$  boundary conditions are periodic, and therefore, the line integrated EMFs along these boundaries cancel. This is not the case with the shearing periodic boundaries, however. In particular, the net  $B_z$  flux through the grid will be conserved if  $\mathcal{E}_y = v_z B_x - v_x B_z$  is zero when integrated along both  $x$  boundaries. Computing the EMF using ghost zone variables  $v_z, B_x, v_x$ , and  $B_z$  after reconstruction introduces a truncation error, and the  $B_z$  flux is not conserved. This is avoided if we instead perform the shearing-periodic reconstruction step on  $\mathcal{E}_y$  itself. A similar argument applies to conservation of mass and  $B_y$  flux; one needs to reconstruct the density flux and  $\mathcal{E}_z$  in the shearing boundaries to ensure conservation of these quantities.<sup>2</sup> We have found that the non-conservation of  $B_y$  flux is generally not a problem in our simulations, as we describe in the appropriate chapters. However, we have noticed that if the density flux is not reconstructed, mass is continually lost from the grid, which can be a problem for long evolution times. Whether or not this reconstruction is performed depends on the particular simulation, and we note it appropriately in each chapter.

---

<sup>2</sup>In principle, the same argument applies to momentum and energy conservation, but these equations are not always conserved to machine precision due to the existence of source terms.

## Chapter 3

# Local Simulations with Numerical Dissipation

We apply a new, second-order Godunov code, Athena, to studies of the MRI using unstratified shearing box simulations with a uniform net vertical field and a sinusoidally varying zero net vertical field. The Athena results agree well with similar studies that used different numerical algorithms, including the observation that the turbulent energy decreases with increasing resolution in the zero net field model. We conduct analyses to study the flow of energy from differential rotation to turbulent fluctuations to thermalization. A study of the time-correlation between the rates of change of different volume-averaged energy components shows that energy injected into turbulent fluctuations dissipates on a timescale of  $\Omega^{-1}$ , where  $\Omega$  is the orbital frequency of the local domain. Magnetic dissipation dominates over kinetic dissipation, although not by as great a factor as the ratio of magnetic to kinetic energy. We Fourier-transform the magnetic and kinetic energy evolution equations and, using the assumption that the time-averaged energies are constant, determine the level of numerical dissipation as a function of length scale and resolution. By modeling

numerical dissipation as if it were physical in origin, we characterize numerical resistivity and viscosity in terms of effective Reynolds and Prandtl numbers. The resulting effective magnetic Prandtl number is  $\sim 2$ , independent of resolution or initial field geometry. MRI simulations with effective Reynolds and Prandtl numbers determined by numerical dissipation are not equivalent to those where these numbers are set by physical resistivity and viscosity. These results serve, then, as a baseline for future shearing box studies where dissipation is controlled by the inclusion of explicit viscosity and resistivity.<sup>1</sup>

### 3.1 Introduction

A large number of previous MRI studies have utilized the unstratified shearing box in the absence of physical dissipation terms (relying instead on grid-scale effects to act as dissipation), beginning with the earliest work of Hawley et al. (1995). Such studies have been useful in understanding dependencies of the MRI stresses on properties such as field topology (Hawley et al. 1995, 1996) and gas pressure (e.g., Sano et al. 2004) without the complicating physics of radiation, vertical gravity, or physical dissipation.

However, in any study that depends on simulations, there remain factors which cannot be overlooked: the effects due to numerics and finite resolution. The majority of the results to-date were obtained with numerical codes based on the finite-difference ZEUS algorithm (Stone & Norman 1992a,b), carried out at relatively low resolution. ZEUS is effectively first-order in asymptotic convergence, and in its most widely used form, evolves the internal rather than the total energy equation. There have been improvements in both the available computational power, which makes higher

---

<sup>1</sup>This work was published in *The Astrophysical Journal*, Vol. 690, p.974, 2009; see Simon et al. (2009)

resolutions and longer evolution times possible, and in the algorithms for compressible MHD. In this work, we will reexamine the properties of MHD turbulence in the shearing box using a higher-order, Godunov code, Athena.

Athena represents an improvement over ZEUS in several ways including true second-order convergence, increased effective resolution (see Stone & Gardiner 2005), accurate shock capturing, and conservation of total energy. The version of Athena we use here does not include explicit resistivity or viscosity and instead relies on numerical dissipation to thermalize the turbulent energy. Nevertheless, this work will serve as a starting point for studies of non-ideal effects, including the influence of  $P_m$  on the turbulence (Fromang et al. 2007; Lesur & Longaretti 2007). As an important part of establishing a baseline of simulations, we will characterize the numerical resistivity and viscosity of Athena for the shearing box problem. To do so, we will follow the work of Fromang & Papaloizou (2007) who studied the numerical effects of ZEUS on the saturated state of MRI shearing box simulations that begin with zero net field. They found that the amplitude of the turbulence decreases with increasing resolution and developed several useful diagnostics with which to quantify the effective numerical resistivity and viscosity in the problem.

Finally, we utilize the energy-conserving properties of Athena in order to investigate the question of turbulent locality. Specifically, we examine temporal correlations of energy fluctuations in the saturated state of the MRI for an adiabatic equation of state and measure how rapidly energy is extracted from the shear flow, pumped into turbulent fluctuations, and then dissipated into thermal energy.

The structure of this chapter is as follows. In § 3.2, we describe the set of simulations performed in this work. In § 3.3, we reexamine some of the results from previous MRI studies and provide a comparison with these studies. In § 3.4, we present the

energy fluctuation analysis used to study the locality of the turbulence. We then characterize the numerical dissipation of Athena using Fourier transfer functions in § 3.5. Finally, we discuss the results and summarize our conclusions in § 3.6.

## 3.2 Numerical Simulations

While we gave a general description of the Athena shearing box in Chapter 2, many of the simulation details vary between the different chapters of this thesis, and we now describe the Athena implementation used here.

First, the  $x$  boundary conditions are the standard shearing periodic boundaries, as described in Chapter 2 with the flux reconstruction approach only applied to the  $y$  EMFs at the  $x$  boundaries; this conserves the net vertical magnetic flux through the domain to machine precision. These simulations do not include a mass flux reconstruction step, and as a result, mass is continually lost from the domain during the evolution. To quantify the level of this mass loss, the total percentage of mass lost over 100 orbits of evolution is  $\sim 2\%$  for our highest resolution simulations (see below for a description of our simulations) and  $\sim 10\%$  for our lowest resolution simulations; we observe convergence of mass conservation with resolution.

Second, as all of the simulations in this chapter are adiabatic, more information about the energy evolution is needed. Although Athena conserves total energy, the shearing boundaries do work on the fluid and represent a significant energy source. As was shown in Hawley et al. (1995), one can integrate the total energy plus gravitational potential energy,  $E + \rho\Phi$ , where  $\Phi = q\Omega^2(\frac{L_x^2}{12} - x^2)$ , over the domain to obtain

$$\frac{\partial\langle E + \rho\Phi \rangle}{\partial t} = \frac{q\Omega}{L_y L_z} \int_X (\rho v_x \delta v_y - B_x B_y) dy dz, \quad (3.1)$$

where  $L_x$ ,  $L_y$ , and  $L_z$  are the domain sizes in the  $x$ ,  $y$ , and  $z$  directions respectively,

$$\delta v_y \equiv v_y + q\Omega x, \quad (3.2)$$

and the integral is calculated over one of the  $x$  boundaries. In our simulations, equation (3.1) is satisfied to truncation level with the error coming from the tidal potential source term in equation (2.7). It is possible to rewrite this source term to guarantee that equation (3.1) is satisfied to roundoff level (see Gardiner & Stone 2005a), but we have found that this makes very little difference to how the total energy evolves.

Gardiner & Stone (2005a) and Stone & Gardiner (2010) point out that the source terms in the momentum equation cannot be written in a purely conservative form and that the  $x$  and  $y$  momenta are tightly coupled through these terms. In the hydrodynamic limit, the source terms account for epicyclic oscillations, and if the epicyclic kinetic energy (see their equation 8) is not conserved to machine precision, coupling between long wavelength modes and epicyclic oscillation modes can result from truncation error. Over time this coupling can artificially increase the kinetic energy. To ensure the conservation of epicyclic energy, Gardiner & Stone (2005a) and Stone & Gardiner (2010) evolved the angular momentum fluctuations directly rather than the  $y$  momentum, casting the equations into a form consistent with uniform epicyclic motion. They then employed a Crank-Nicholson scheme to evolve the source terms that govern the evolution of the momentum fluctuations. In MHD, however, oscillatory epicyclic motion is replaced by unstable, growing MRI modes. Epicyclic kinetic energy is not conserved and these special techniques are not required. Therefore, we use the standard Athena algorithm (see Stone et al. 2008, and Chapter 2) to evolve the momentum equations.

Finally, we note that the Riemann solver used in all of these simulations is the linearized Roe solver of Roe (1981), which has been extended to MHD (see Cargo & Gallice 1997).

As was done in the original shearing box simulations (Hawley et al. 1995) our standard shearing box has a radial size  $L_x = 1$ , an azimuthal size  $L_y = 2\pi$ , and a vertical size  $L_z = 1$ . We initialize a velocity flow with  $\mathbf{v} = -q\Omega x \hat{\mathbf{y}}$ , with  $q = 3/2$ ,  $\Omega = 0.001$ , and  $-L_x/2 \leq x \leq L_x/2$ . In an isothermal disk, the sound speed is  $c_s \sim \Omega H$  where  $H$  is the scale height. With  $L_z = H$ ,  $c_s = L_z \Omega$ , and the initial pressure is defined as  $P = \rho \Omega^2 L_z^2$ . With  $\rho = 1$ , we have  $P = 10^{-6}$ . In this chapter, we consider two initial magnetic field geometries that are commonly used in shearing box studies. Models labeled NZ (for Net Z-field) have an initial uniform vertical magnetic field,  $B_z$ , and models labeled SZ (for Sine Z-field) begin with a sinusoidal distribution of  $B_z$  and have zero net flux through the box. Specifically, we initialize the NZ runs with  $\mathbf{B} = \sqrt{2P/\beta} \hat{\mathbf{z}}$ , and the SZ runs with  $\mathbf{B} = \sqrt{2P/\beta} \sin[(2\pi/L_x)x] \hat{\mathbf{z}}$ . In both cases,  $\beta = 1600$ . This determines the ratio of the vertical box size to the fastest growing linear MRI wavelength as  $L_z/\lambda_c \sim 4$ , where  $\lambda_c = 2\pi\sqrt{16/15}|v_A|/\Omega$ , and  $v_A$  is the Alfvén speed. To seed the MRI, we introduce random adiabatic perturbations to  $P$  and  $\rho$  with amplitude  $\delta P/P = 0.01$ .

For both of these initial field configurations, we have run a full range of grid resolutions, from  $N_x = 16$ ,  $N_y = 32$ ,  $N_z = 16$  to the highest resolution used in this study,  $N_x = 128$ ,  $N_y = 256$ ,  $N_z = 128$ , proceeding by factors of two. All of the simulations were run for a total of 100 orbits.

In addition to the standard shearing box simulations, we have run some additional experiments designed to further investigate magnetic and kinetic energy dissipation. First, we perform a set of simulations in which we remove the velocity shear and the

Table 3.1. Unstratified Simulations with Numerical Dissipation

| Label  | Initial Field Geometry | Resolution ( $N_x \times N_y \times N_z$ ) | Domain ( $L_x \times L_y \times L_z$ ) | Description                  |
|--------|------------------------|--|--|------------------------------|
| NZ16   | net flux               | $16 \times 32 \times 16$                   | $1 \times 2\pi \times 1$               | –                            |
| NZ32   | net flux               | $32 \times 64 \times 32$                   | $1 \times 2\pi \times 1$               | –                            |
| NZ64   | net flux               | $64 \times 128 \times 64$                  | $1 \times 2\pi \times 1$               | –                            |
| NZ128  | net flux               | $128 \times 256 \times 128$                | $1 \times 2\pi \times 1$               | fiducial run - net flux      |
| NZD128 | net flux               | $128 \times 256 \times 128$                | $1 \times 2\pi \times 1$               | decaying turbulence          |
| SZ16   | zero net flux          | $16 \times 32 \times 16$                   | $1 \times 2\pi \times 1$               | –                            |
| SZ32   | zero net flux          | $32 \times 64 \times 32$                   | $1 \times 2\pi \times 1$               | –                            |
| SZ64   | zero net flux          | $64 \times 128 \times 64$                  | $1 \times 2\pi \times 1$               | –                            |
| SZ128  | zero net flux          | $128 \times 256 \times 128$                | $1 \times 2\pi \times 1$               | fiducial run - zero net flux |
| SZD128 | zero net flux          | $128 \times 256 \times 128$                | $1 \times 2\pi \times 1$               | decaying turbulence          |
| NZAR1  | net flux               | $16 \times 64 \times 32$                   | $\frac{1}{2} \times 2\pi \times 1$     | varied aspect ratio          |
| NZAR2  | net flux               | $64 \times 64 \times 32$                   | $2 \times 2\pi \times 1$               | varied aspect ratio          |
| NZAR3  | net flux               | $32 \times 32 \times 32$                   | $1 \times \pi \times 1$                | varied aspect ratio          |
| NZAR4  | net flux               | $16 \times 32 \times 32$                   | $\frac{1}{2} \times \pi \times 1$      | varied aspect ratio          |
| NZAR5  | net flux               | $64 \times 32 \times 32$                   | $2 \times \pi \times 1$                | varied aspect ratio          |
| NZAR6  | net flux               | $128 \times 32 \times 32$                  | $4 \times \pi \times 1$                | varied aspect ratio          |

tidal and Coriolis force terms, thus removing the energy source that maintains the turbulence. The purpose of these simulations is to investigate energy flow and dissipation in the absence of the shear, which is the driving force for the turbulence. We perform these simulations by restarting each of the standard shearing box runs at a time when the shearing periodic boundaries are strictly periodic. These “periodic points” are given by  $t_n = n L_y / q \Omega L_x$ , with  $n = 0, 1, 2, \dots$ , (see Hawley et al. 1995). We choose the restart time to be 40 orbits. We then evolve the system to follow the decay of the kinetic and magnetic energies.

Finally, we run a set of low resolution simulations with varying aspect ratio to examine the effect of secondary parasitic modes on the channel solution (see § 3.3.2). These simulations have the same initial conditions as the net flux simulation with  $N_x = 32$ ,  $N_y = 64$ , and  $N_z = 32$  but with varying domain size in the  $x$  and  $y$  dimensions. The grid cell size (e.g.,  $L_x/N_x$  in the  $x$  direction) in each dimension is kept constant. All simulations are summarized in Table 3.1.

### 3.3 General Properties of MRI Turbulence

This work represents the first detailed study of the MRI with Athena, which has an algorithm significantly different from that used in ZEUS. To begin, we will reexamine many of the shearing box models and the results already documented in the literature. Any significant differences between Athena results and those previously published could indicate where numerical effects (algorithm, resolution) have an influence. Since Athena is an energy-conserving, shock-capturing algorithm it has at least the potential to produce somewhat different results. Conversely, agreement between Athena and other codes would support the robustness of the shearing box results to date.

In this section, we describe some of the general properties of MRI turbulence as

simulated with Athena and compare our results with those in the literature. These properties will also serve as a starting point for further analysis presented in the following sections. In what follows, the highest resolution runs NZ128 and SZ128 will serve as our fiducial simulations for each initial field geometry. We study resolution effects for each field geometry using the lower resolution simulations.

### 3.3.1 Characteristics of Saturation

Figures 3.1 and 3.2 show the development of the MRI and the subsequent evolution of the resulting MHD turbulence for the fiducial NZ128 and SZ128 runs respectively. The MRI saturates before orbit 5 and the MHD turbulent state lasts for the remainder of the 100 orbit simulation. Along with these figures, we list several time- and volume-averaged quantities from the fiducial runs in Table 3.2. The time average is done from orbits 20 to 100, and the errors are given by one standard deviation over this period. Volume-averaged values are indicated by the single-angled bracket notation (e.g.,  $\langle B^2 \rangle$ ), and time- and volume- averaged values are denoted by double-angled brackets (e.g.,  $\langle\langle B^2 \rangle\rangle$ ). In both fiducial runs, the toroidal field magnetic energy dominates with  $\langle B_y^2/2 \rangle > \langle B_x^2/2 \rangle > \langle B_z^2/2 \rangle$ . Examining the components of the kinetic energy and perturbed kinetic energy, which is  $(\rho/2)(v_x^2 + \delta v_y^2 + v_z^2)$  with  $\delta v_y$  given by equation (3.2), we find they are closer to each other in value than are the components of the magnetic energy. The relative ordering is similar except that the  $x$  kinetic energy is larger than the perturbed  $y$  kinetic energy,  $\rho\delta v_y^2/2$ , in SZ128. Another feature of note is the greater saturation level and fluctuation amplitude of the NZ128 run compared to that of SZ128. As in past studies, the Maxwell stress dominates over the Reynolds; the ratio of the Maxwell to Reynolds stress oscillates between 1 and 10. Similarly, past studies have shown a tight correlation between Maxwell (and total) stress and

the magnetic energy density (see, e.g., Blackman et al. 2008). Here the ratio of the Maxwell stress to the magnetic energy density is roughly 1/2. These values and the overall observations are generally consistent with the results of Hawley et al. (1995), Hawley et al. (1996), and Sano et al. (2004).

One major difference from past ZEUS simulations is the evolution of the total ( $E + \rho\Phi$ ) and thermal ( $\epsilon$ ) energy densities, shown in the lower right plot of Figs. 3.1 and 3.2 for the NZ128 and SZ128 runs respectively. Since we evolve an adiabatic equation of state and there is no cooling term in the energy equation, the total energy increases with time at a rate given by equation (3.1). The total energy increases because the free energy of the shearing fluid is being thermalized by the turbulence, but the shearing box boundary conditions continuously reinforce that shear. The stresses at the radial boundaries therefore constitute a source term. Equation (3.1) also explains why the total energy reaches a higher value at the end of the simulation in NZ128 compared to SZ128. Since the volume-averaged stress (which is roughly equal to the stress at the radial boundaries) is higher in NZ128, the energy injection rate will be larger. These plots also show that the thermal energy follows the total energy very closely. That is, the injected energy ends up as thermal energy a short time later (Gardiner & Stone 2005a). We will further study the thermalization of injected energy in § 3.4 and § 3.5.

Does the significant increase in thermal energy affect the turbulence in any way? This question was examined by Sano et al. (2004) in an extensive series of simulations. They found evidence of a very weak dependence of the time-averaged Maxwell stress on the gas pressure. Such an increase is not apparent from a first look at Figs. 3.1 and 3.2, but short timescale fluctuations are a dominant feature of these volume-averaged quantities. We examined the long term behavior of the Maxwell stress using

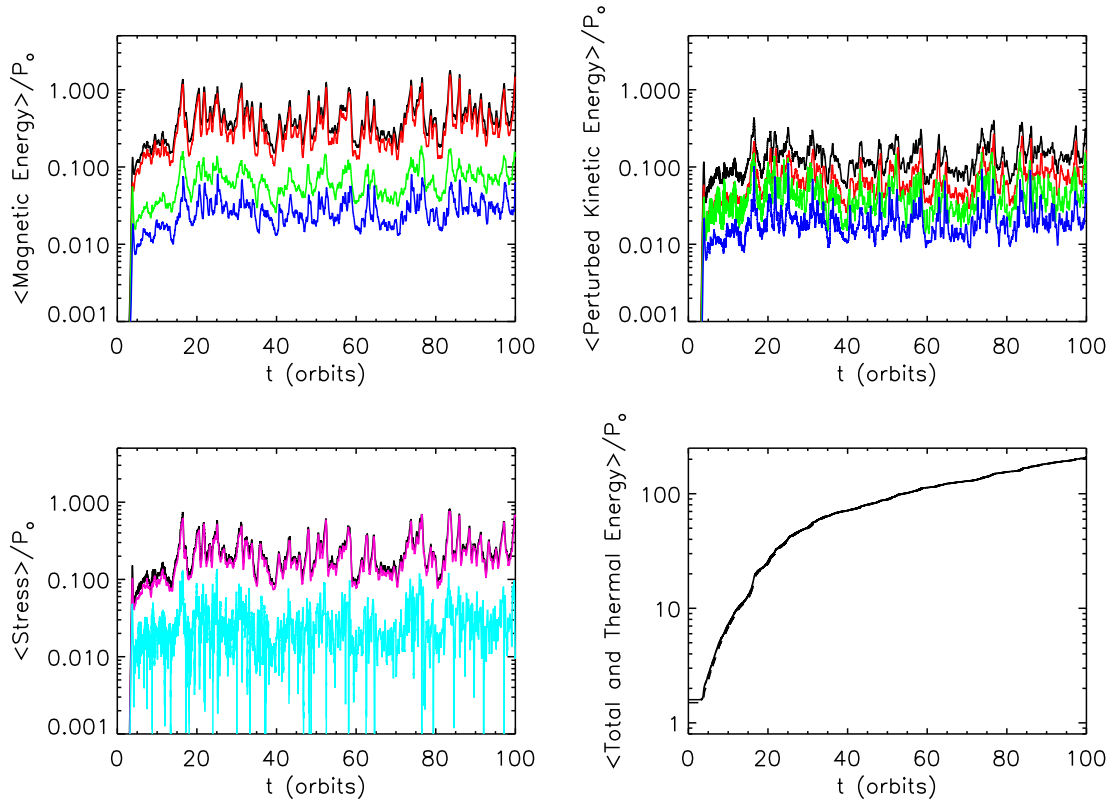


Fig. 3.1.— Volume-averaged energy densities and stresses normalized to the initial gas pressure versus time for the NZ128 simulation. In the upper two plots, the black line is the total energy density, the green line is the component of the energy density in the  $x$  direction, the red line is the  $y$  direction component, and the blue line is the  $z$  direction component. The upper left plot shows the volume-averaged magnetic energy density, the upper right plot shows the perturbed kinetic energy density (i.e., with the shear subtracted off of  $v_y$ ), and the lower left plot is the volume-averaged total stress (black), Maxwell stress (pink), and Reynolds stress (blue). The lower right plot is the total energy density, including gravitational energy (solid line), and the thermal energy density (dashed line). The  $y$  axes have the same range for all plots except for the total/thermal energy density plot.

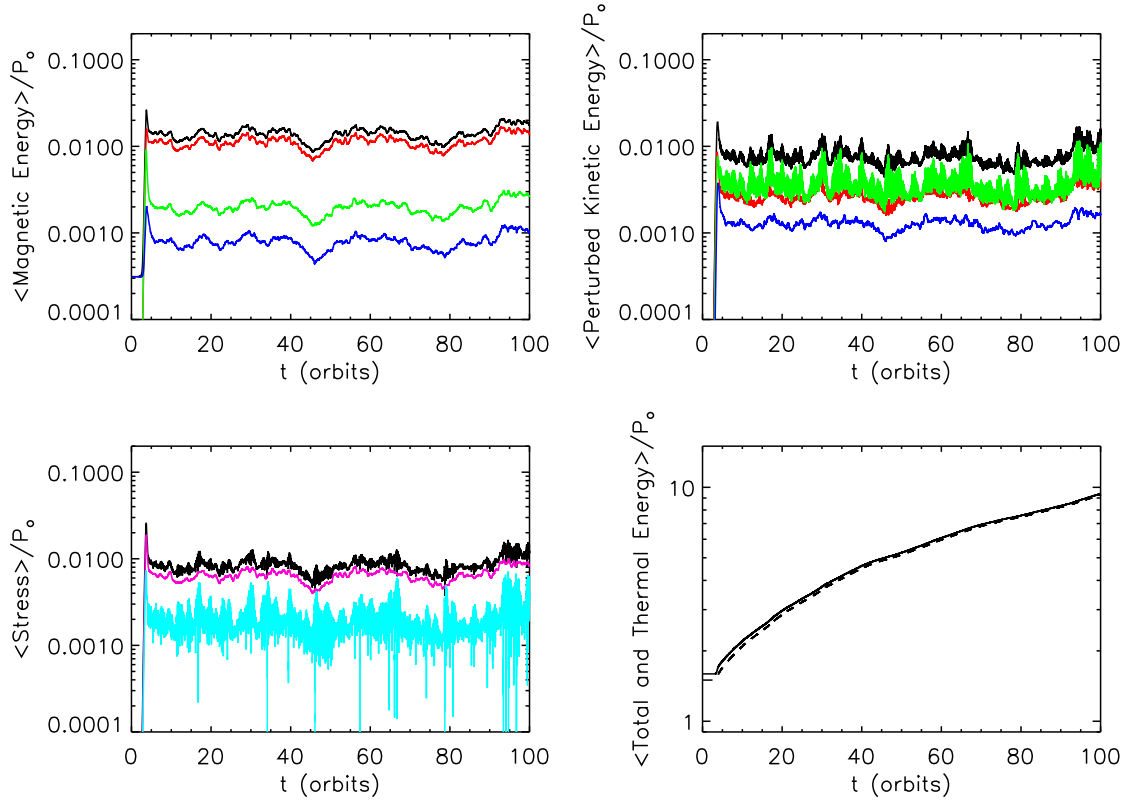


Fig. 3.2.— Volume-averaged energy densities and stresses normalized to the initial gas pressure versus time for the SZ128 simulation. In the upper two plots, the black line is the total energy density, the green line is the component of the energy density in the  $x$  direction, the red line is the  $y$  direction component, and the blue line is the  $z$  direction component. The upper left plot shows the volume-averaged magnetic energy density, the upper right plot shows the perturbed kinetic energy density (i.e., with the shear subtracted off of  $v_y$ ), and the lower left plot is the volume-averaged total stress (black), Maxwell stress (pink), and Reynolds stress (blue). The lower right plot is the total energy density, including gravitational energy (solid line), and the thermal energy density (dashed line). The  $y$  axes have the same range for all plots except for the total/thermal energy density plot.

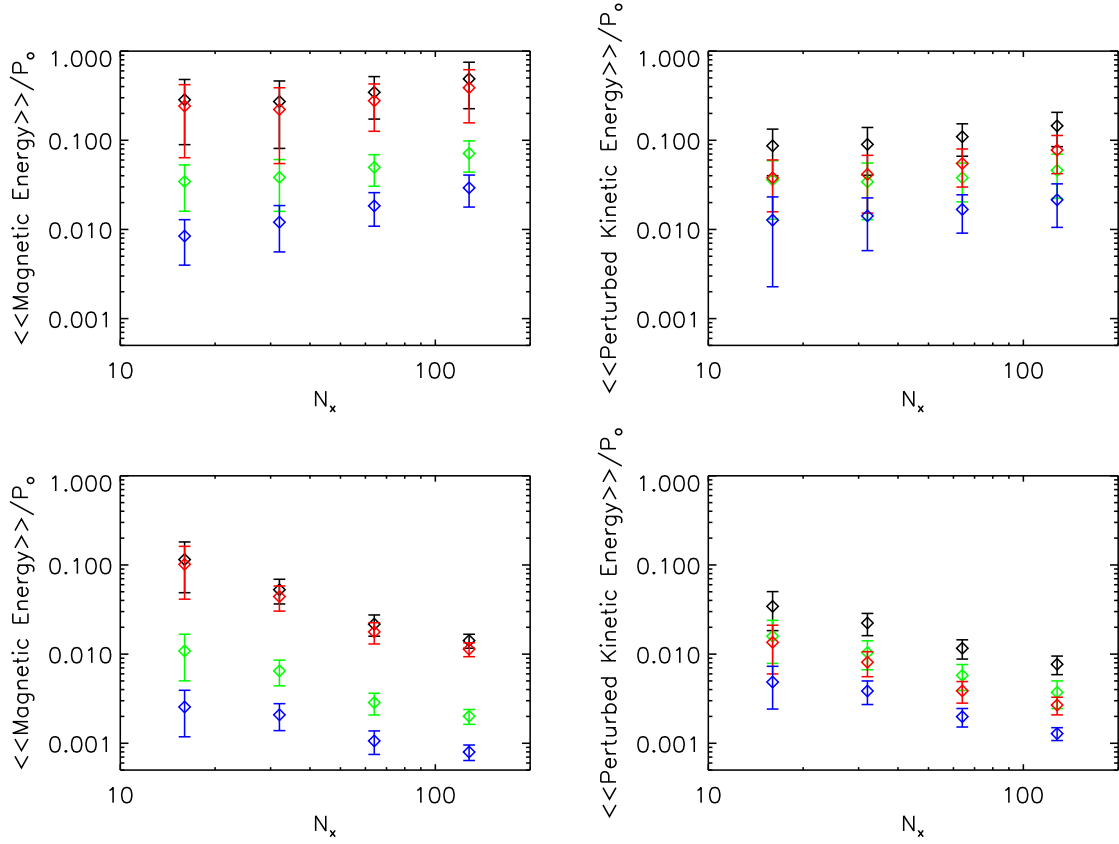


Fig. 3.3.— Time- and volume-averaged energy densities normalized to the initial pressure for various resolutions. The two upper plots correspond to the net flux simulations, and the two lower plots correspond to the zero net flux simulations. The left plots are the averaged magnetic energy densities, and the right plots are the averaged perturbed kinetic energy densities (i.e., with shear subtracted off of  $v_y$ ). In all plots, the black symbols are the total energy density, the green symbols are the  $x$  component of the energy density, the red symbols are the  $y$  component, and the blue symbols are the  $z$  component. The time averages are done from orbit 20 to 100, and the error bars indicate one standard deviation over this period.

time-averaging procedures to smooth away the fluctuations (which do not appear to change over long timescales). We found marginal evidence for a weak dependence of the Maxwell stress on the gas pressure in some, but not all, of the data. While it is possible that longer evolution times and a wider exploration of parameter space could be useful to address this question further, it is clear the stress has barely changed despite an increase in thermal pressure by a factor of order 100 in run NZ128. Thus if there is any dependence of the stress on the pressure, it is very weak and does not significantly affect the characteristics of local MRI turbulence.

We study the effect of resolution through a series of lower resolution simulations (see Table 3.1). Figure 3.3 shows the time- and volume-averaged magnetic and perturbed kinetic energies as a function of grid resolution for both the net flux and zero net flux initial conditions. The time average is calculated from orbits 20 to 100; the error bars indicate one standard deviation. For the net flux simulation, there appears to be a slight trend of increasing energy with resolution, as observed in Hawley et al. (1995). Resolution has a more obvious effect on the zero net flux initial condition. The turbulent energies *decrease* with increasing resolution. This resolution effect was previously reported for zero net field initial conditions in other simulations (Fromang & Papaloizou 2007; Pessah et al. 2007) using different numerical algorithms. With Athena, the time- and volume-averaged total magnetic energy density decreases by roughly a factor of two for each factor of two resolution increase. The amplitude of the fluctuations in the total magnetic energy density decreases by roughly a factor of two to four for each resolution increment. At all resolutions, the  $y$  magnetic energy density continues to be the largest, followed by the  $x$  energy, and then the  $z$  energy. As was the case for NZ128,  $\rho\delta v_y^2/2$  dominates for all net flux simulations, followed by  $\rho v_x^2/2$ , and then  $\rho v_z^2/2$ . In the zero net flux simulations, the  $x$  kinetic energy density

is greater than the perturbed  $y$  kinetic energy density. These components of the perturbed kinetic energy density are close in value, and it is often the case that the  $x$  and  $y$  components are within one standard deviation of each other. The ratio of time- and volume-averaged Maxwell stress to time- and volume-averaged magnetic energy density is constant with resolution. The ratio of time- and volume-averaged Maxwell stress to time- and volume-averaged Reynolds stress has a slight increase with resolution in the net flux simulations and a slight decrease with resolution in the zero net flux simulations. However, we point out that the observed trends in the ratio of stresses are subject to considerable uncertainty given the large error bars calculated for the various quantities.

### 3.3.2 Channel Solution

One of the interesting aspects of the vertical field MRI in a shearing box is that the fastest growing mode leads to axisymmetric radial streaming motions, dubbed “channel solutions” (Hawley & Balbus 1992). Goodman & Xu (1994) pointed out that for the vertical field in an unstratified box, the linear MRI eigenmode is also a nonlinear solution in the incompressible limit. They further show that the nonlinear channel solution is itself unstable to “parasitic modes.” These modes require radial and azimuthal wavelengths larger than the vertical wavelength of the channel solution and will disrupt the channel flow if the box is large enough (Balbus & Hawley 1998).

In the present simulations, the initial vertical field is sufficiently weak that the fastest growing vertical wavelength is less than the radial and azimuthal dimensions of the box, and any initial tendency toward the channel solution at the end of the linear growth phase is quickly disrupted. However, we find that the large fluctuations

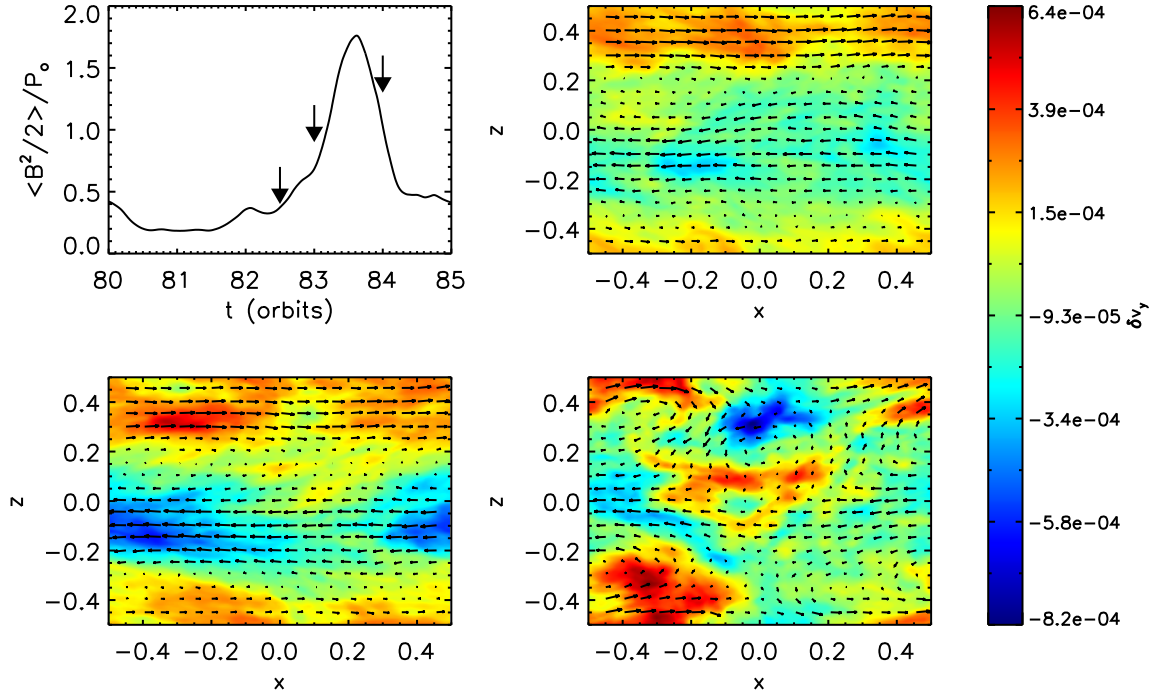


Fig. 3.4.— The development and destruction of a channel flow during the NZ128 simulation. The upper left plot shows a fluctuation in the volume-averaged magnetic energy density from  $t = 80$  orbits to  $t = 85$  orbits. The remaining plots show the  $y$ -averaged perturbed  $y$  velocity (colors) and  $v_x$  and  $v_z$  (vectors). The upper right plot occurs at  $t = 82.5$  orbits, the lower left plot occurs at  $t = 83$  orbits, and the lower right plot occurs at  $t = 84$  orbits. These times are indicated on the upper left plot by the arrows. At  $t = 82.5$  orbits, one can see the development of a two-channel flow, in which one channel has  $v_x < 0$  and  $\delta v_y < 0$ , and the other channel has  $v_x > 0$  and  $\delta v_y > 0$ . At  $t = 83$  orbits, this channel flow is even more developed as the perturbations to the  $y$  velocity have become even stronger and  $v_x$  dominates over  $v_z$  everywhere. The development of this channel flow coincides with an increase in volume-averaged magnetic energy density. By  $t = 84$  orbits, the channel flow has been destroyed, coinciding with the decrease in magnetic energy density.

in the magnetic energy density for NZ128 are a result of recurring channel solutions.<sup>2</sup> Figure 3.4 shows the azimuthally-averaged velocities at several times during the amplification and subsequent decay of one such fluctuation. The flow organizes itself into a two-channel solution, which becomes more well-defined as the magnetic energy increases. The channel solution is eventually destroyed via secondary, parasitic instabilities (see Goodman & Xu 1994), which coincides with a decrease in magnetic energy. The same channel solution appears during other instances of large magnetic energy fluctuation in NZ128 and does not appear in SZ128. Furthermore, the recurring channel flows appear in the lower resolution net magnetic flux simulations. As observed previously, the channel solution and large magnetic energy fluctuations are a property of simulations with a uniform  $B_z$  field (Sano & Inutsuka 2001).

Since the channel solution is subject to parasitic modes that depend on the available wavelengths that can fit in the box, we expect that this behavior is influenced by the domain aspect ratio employed. To verify this, we have run several low resolution simulations (labelled NZAR1 – NZAR6, see § 3.2) using different aspect ratios. We found that for large enough  $L_x$ , the intermittent channel modes no longer occur; this behavior was also observed by Bodo et al. (2008). The prominence of intermittent channel flows is a consequence of the restrictions introduced by the domain size. However, we use this property in § 3.4, where the large fluctuations in turbulent energy created by the channel solutions provide a clear marker of energy injection by the boundaries. We can then track the subsequent thermalization of that energy.

---

<sup>2</sup>The recurrence of the channel solution presumably results from the fact that the net vertical magnetic field can never be destroyed or removed from the domain, given the periodic boundary conditions and the strict conservation of  $z$  magnetic flux.

### 3.3.3 Energy Power Spectra

The nature of MRI-driven MHD turbulence can be characterized in part by the power spectrum of kinetic and magnetic energies. To obtain such power spectra, we do a full 3D Fourier transform on the simulation data employing the procedures outlined in Hawley et al. (1995) to account for the shearing-periodic boundaries. Briefly, the shearing periodic boundary conditions in the  $x$  direction allow the domain to be strictly periodic in the  $x$  direction only at certain times, called periodic points  $t_n$  (described in § 3.2). To perform a standard fast Fourier transform (FFT) at some time  $t$  that is not equal to  $t_n$ , we transform the data into a frame where the  $x$  boundaries are strictly periodic. We then calculate the FFT in this frame and remap to the original frame.

The turbulent magnetic, kinetic, and perturbed kinetic energy densities in Fourier space are defined as

$$\frac{1}{2}|\widetilde{\mathbf{B}}(\mathbf{k})|^2 \equiv \frac{1}{2} \left[ |\widetilde{B}_x(\mathbf{k})|^2 + |\widetilde{B}_y(\mathbf{k})|^2 + |\widetilde{B}_z(\mathbf{k})|^2 \right], \quad (3.3)$$

$$\frac{1}{2}|\widetilde{\sqrt{\rho}\mathbf{v}}(\mathbf{k})|^2 \equiv \frac{1}{2} \left[ |\widetilde{\sqrt{\rho}v_x}(\mathbf{k})|^2 + |\widetilde{\sqrt{\rho}v_y}(\mathbf{k})|^2 + |\widetilde{\sqrt{\rho}v_z}(\mathbf{k})|^2 \right], \quad (3.4)$$

$$\frac{1}{2}|\widetilde{\sqrt{\rho}\delta\mathbf{v}}(\mathbf{k})|^2 \equiv \frac{1}{2} \left[ |\widetilde{\sqrt{\rho}v_x}(\mathbf{k})|^2 + |\widetilde{\sqrt{\rho}\delta v_y}(\mathbf{k})|^2 + |\widetilde{\sqrt{\rho}v_z}(\mathbf{k})|^2 \right], \quad (3.5)$$

where  $\widetilde{f}$  means the Fourier transform of  $f$  defined by

$$\widetilde{f}(\mathbf{k}) = \int \int \int f(\mathbf{x}) e^{-i\mathbf{k}\cdot\mathbf{x}} d^3\mathbf{x}. \quad (3.6)$$

Note that for the kinetic energies, we include the density along with the velocity

when calculating the Fourier transform, resulting in the appearance of  $\sqrt{\rho}$  in the above equations. To obtain these quantities as a function of length scale and to improve statistics, we average our data over shells of constant  $k = |\mathbf{k}|$ . For further improvement of statistics, we average each of these terms over 161 frames (i.e., from orbit 20 to 100 in increments of 0.5 orbits).

Figure 3.5 shows the power spectra of these energy densities for the net flux and zero net flux runs. The figure shows resolution effects as different lines in each plot. In all cases, the largest scales account for most of the energy. The general shape of the energy power spectra agrees with previous studies (e.g., Hawley et al. 1995; Fromang & Papaloizou 2007). For the net flux simulations, the magnetic energy dominates over the kinetic and perturbed kinetic energies at all scales, independent of resolution. As the resolution is increased, the power spectra extend to higher  $k$ , but the general shape remains constant. At some values for  $k$ , the uncertainty in energy (not plotted), represented by one temporal standard deviation around the mean, is large enough to overlap with other energy components, making it difficult to conclusively say which energy dominates at these particular scales.

We calculated a power law index in Fourier space for each energy density and at each resolution. This slope was determined by a linear fit to the energy densities in log space from  $kL/(2\pi) = 1$  to the maximum scale for the given resolution. There is some uncertainty in this measurement because the power spectra are not strictly linear in log space (see Fig. 3.5). In NZ128, the energy density is proportional to  $[kL/(2\pi)]^n$  with  $n \approx -4$  for every energy density. This index is approximately constant with resolution, but there is evidence that  $n$  becomes more negative at higher resolutions. In determining an error in the value of  $n$ , we found that this error is often dominant. Thus, such a resolution dependence is somewhat tentative.

There is a noticeable resolution dependence in the zero net flux simulations. First, as resolution is increased, the magnetic energy density decreases at all scales. This effect was discussed in § 3.3.1; the power spectra are consistent with the power spectrum analysis of Fromang & Papaloizou (2007). The same resolution dependence is observed for the perturbed kinetic energy density. The magnetic energy density at small  $k$  decreases faster with resolution than does the perturbed kinetic energy density. The total kinetic energy density (i.e., including shear) remains constant with resolution, which simply results from the fact that the shear velocity, which dominates the kinetic energy, is constant with resolution. The uncertainty in each energy component appears to be smaller than in the net flux simulations. However, there are still some values of  $k$  at which the calculated errors overlap.

We calculated a power law index in Fourier space for each energy density and resolution for the zero net flux simulations. The procedure we used was the same as for the net flux simulations. For the kinetic and perturbed kinetic energy densities, we found that  $n$  lies between -3.5 and -4, whereas for the magnetic energy density,  $n$  lies between -3 and -3.5. There does not appear to be any resolution dependence in  $n$  for the magnetic energy density, but there is a tentative decrease in  $n$  (similar to the net flux case) with increasing resolution for the kinetic and perturbed kinetic energy densities.

### 3.4 Locality of Turbulence

Athena evolves the equation for total energy, the volume-average of which will change only due to the Maxwell and Reynold stresses at the radial boundaries (equation 3.1). As was discussed in § 3.3, the individual volume-averaged magnetic and kinetic energies are highly variable throughout the evolution as energy is continuously transferred

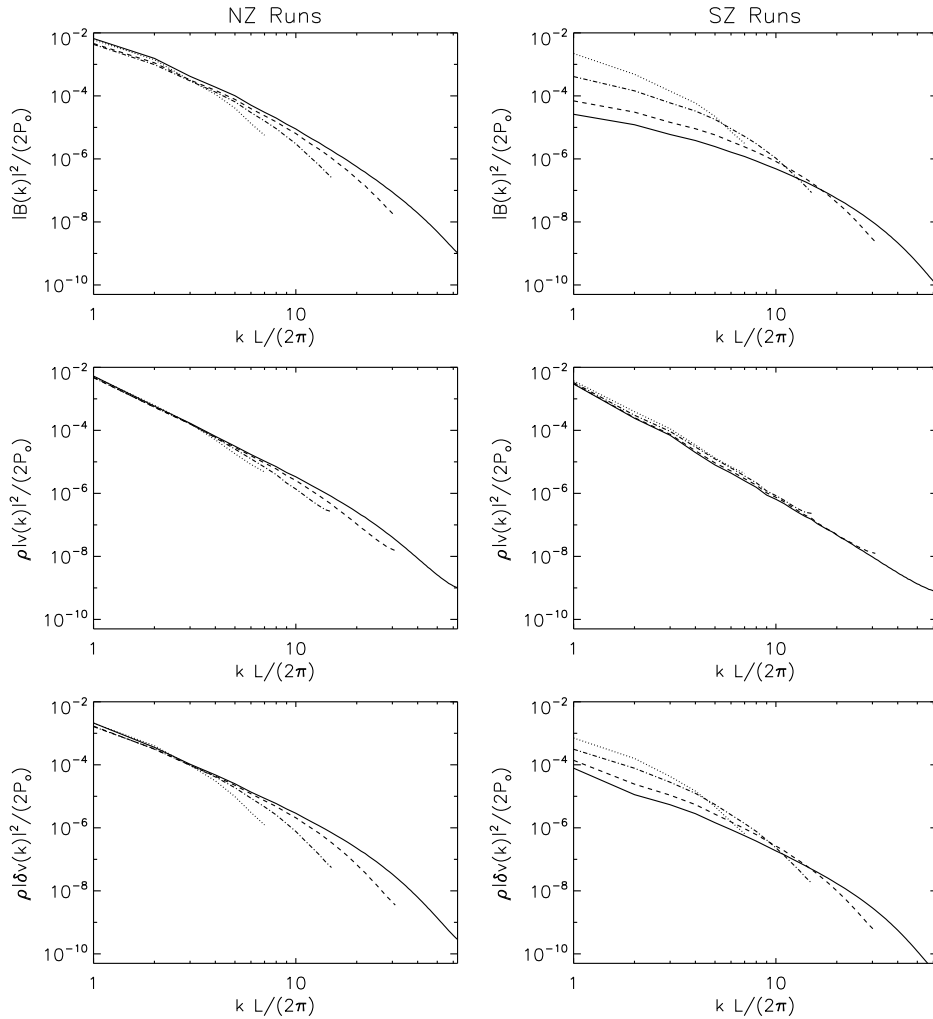


Fig. 3.5.— Spatial power spectra of various energy densities in the saturated state of the standard net flux (left panels) and zero net flux simulations (right panels). The spectra were obtained via an average over 161 frames in the saturated state and an average over shells of constant modulus  $|\mathbf{k}|$ . In each column, the first plot shows magnetic energy density, the second shows kinetic energy density, and the third shows perturbed kinetic energy density (as defined in the text). The effect of resolution is shown in each individual plot; the dotted line corresponds to the resolution with  $N_x = 16$ , the dot-dashed line corresponds to  $N_x = 32$ , the dashed line corresponds to  $N_x = 64$ , and the solid line corresponds to  $N_x = 128$ . All energy densities have been normalized to the initial gas pressure and are plotted against a dimensionless wave number ( $L$  is the length of the smallest dimension of the box).

between magnetic, kinetic and thermal components. We can study these energy flow processes by tracking the energy injected at the boundaries as it is subsequently thermalized in the turbulence. For this purpose, the existence of the recurring channel solution in the net magnetic field simulation is very useful; the sudden increase in stress provides a clear injection of energy that can be traced using several diagnostics. Having developed these diagnostics we can then apply them to the zero net magnetic flux simulations. Finally, to gain additional insight into dissipation in the turbulence, we conduct an experiment in which the shear flow and gravity terms have been removed.

### 3.4.1 Sustained Turbulence

The total energy density, including the gravitational potential energy density, is defined as

$$E_{\text{tot}} = E + \rho\Phi = \epsilon + \frac{1}{2}\rho v^2 + \frac{1}{2}B^2 + \rho\Phi \quad (3.7)$$

where  $\Phi$  is given in § 3.2. Averaging equation (3.7) over the entire domain, taking the time derivative, and rearranging the terms, we obtain,

$$\dot{T} = E_{\text{in}} - \dot{K} - \dot{M} - \dot{G}. \quad (3.8)$$

where  $E_{\text{in}} \equiv \partial\langle E_{\text{tot}}\rangle/\partial t$  is the energy injection rate due to stress at the boundaries (see equation (3.1)),  $\dot{T} \equiv \partial\langle\epsilon\rangle/\partial t$  is the rate of change of thermal energy density,  $\dot{K} \equiv \partial\langle\frac{1}{2}\rho v^2\rangle/\partial t$  is the rate of change of the kinetic energy density,  $\dot{M} \equiv \partial\langle\frac{1}{2}B^2\rangle/\partial t$  is the rate of change of the magnetic energy density, and  $\dot{G} \equiv \partial\langle\rho\Phi\rangle/\partial t$  is the time derivative of the tidal potential energy density. The brackets indicate a volume-average over the

simulation domain.  $\dot{G}$  is the change in a fluid element's gravitational energy as it moves within the domain. We expect the contribution of the tidal potential term to be insignificant, an expectation borne out by direct computation. We will ignore this term in most of the subsequent discussion. The stress terms at the radial boundaries are generally positive, which means energy is being injected into the box via the work done by this stress ( $E_{\text{in}} > 0$ ). The remaining terms in equation (3.8) can be either positive or negative.

The lower right plot in Fig. 3.1 shows that the thermal energy density closely follows the total energy density, but with a short time delay. This can be better seen in Fig. 3.6, which shows the individual terms from equation (3.8) for a 20 orbit period in the NZ128 simulation. There is a clear time delay of less than one orbit between significant changes in the energy injection rate and the thermal energy derivative, suggesting a comparable delay before the injected energy is thermalized, a property noted in Sano & Inutsuka (2001) as well as in Gardiner & Stone (2005a). These features in the energy derivatives result from the creation and destruction of channel flows. During this time interval, the magnetic and kinetic energies are also changing. By examining the maxima in the thermal energy derivative and the corresponding features in the kinetic and magnetic energy derivatives, it appears that the magnetic energy dissipation dominates the thermalization process.

It is useful to define a temporal correlation function for the various energy components by writing

$$C_{AB} \equiv \begin{cases} \frac{\frac{1}{N-|L|} \sum_{i=0}^{N-|L|-1} A_{i+|L|} B_i}{\frac{1}{N} \sum_{i=0}^{N-1} A_i} & \text{if } L < 0 \\ \frac{\frac{1}{N-|L|} \sum_{i=0}^{N-|L|-1} A_i B_{i+L}}{\frac{1}{N} \sum_{i=0}^{N-1} A_i} & \text{if } L \geq 0 \end{cases} \quad (3.9)$$

where  $A$  and  $B$  are two time-series datasets  $N$  elements in length. The quantity  $L$  is the number of elements over which to shift  $A$  and  $B$  with respect to each other to calculate the correlation coefficient. We apply equation (3.9) to the energy rates by setting  $A = \dot{T}$ , and  $B = \dot{K}$ ,  $\dot{M}$ , or  $E_{\text{in}}$ . This allows us to correlate the energy injection rate and the change in kinetic and magnetic energies against the change in thermal energy over certain timescales. Since  $\dot{T} > 0$ , if the correlation between  $\dot{T}$  and  $\dot{K}$  (or  $\dot{M}$ ) is negative, then kinetic energy (or magnetic energy) must be decreasing, and a strong negative correlation would suggest that kinetic energy (or magnetic energy) is being thermalized.

Figure 3.7 is the correlation function for  $B = E_{\text{in}}$ ,  $\dot{K}$ , and  $\dot{M}$  calculated over orbits 20 to 100. The  $x$ -axis is the correlation timescale in units of orbits. We only look at correlation times of  $\lesssim 1$  orbit as the degree to which the thermal energy evolution follows that of the total energy (see Figs. 3.1 and 3.2) indicate that thermalization happens over that timescale. To examine the correlation function on longer timescales would be misleading since peaks in the function would suggest a correlation between two events that are not causally related (e.g., the injection of energy for one channel event being correlated with the thermalization of energy for another channel event).

Table 3.2. Saturation Characteristics in Unstratified MRI Turbulence

| Quantity   | NZ128             | SZ128                            |
|--|-------------------|----------------------------------|
| $\langle\langle -B_x B_y \rangle\rangle / P_o$   | $0.216 \pm 0.116$ | $(6.55 \pm 1.15) \times 10^{-3}$ |
| $\langle\langle \rho v_x \delta v_y \rangle\rangle / P_o$                                    | $0.028 \pm 0.019$ | $(1.91 \pm 0.76) \times 10^{-3}$ |
| $\langle\langle B^2/2 \rangle\rangle / P_o$  | $0.488 \pm 0.262$ | $0.014 \pm 0.003$                |
| $\langle\langle B_x^2/2 \rangle\rangle / P_o$  | $0.071 \pm 0.027$ | $(2.01 \pm 0.38) \times 10^{-3}$ |
| $\langle\langle B_y^2/2 \rangle\rangle / P_o$  | $0.388 \pm 0.231$ | $0.011 \pm 0.002$                |
| $\langle\langle B_z^2/2 \rangle\rangle / P_o$  | $0.029 \pm 0.011$ | $(7.98 \pm 1.57) \times 10^{-4}$ |
| $\langle\langle \rho \delta v^2/2 \rangle\rangle / P_o$                                      | $0.145 \pm 0.060$ | $(7.69 \pm 1.81) \times 10^{-3}$ |
| $\langle\langle \rho v_x^2/2 \rangle\rangle / P_o$   | $0.046 \pm 0.024$ | $(3.73 \pm 1.27) \times 10^{-3}$ |
| $\langle\langle \rho \delta v_y^2/2 \rangle\rangle / P_o$                                    | $0.078 \pm 0.035$ | $(2.68 \pm 0.60) \times 10^{-3}$ |
| $\langle\langle \rho v_z^2/2 \rangle\rangle / P_o$   | $0.021 \pm 0.011$ | $(1.28 \pm 0.21) \times 10^{-3}$ |
| $\langle\langle -B_x B_y \rangle\rangle / \langle\langle \rho v_x \delta v_y \rangle\rangle$ | $7.60 \pm 6.47$   | $3.43 \pm 1.49$                  |
| $\langle\langle -B_x B_y \rangle\rangle / \langle\langle B^2/2 \rangle\rangle$               | $0.443 \pm 0.336$ | $0.462 \pm 0.116$                |

The left plot of the figure shows that  $E_{\text{in}}$  is strongly correlated with  $\dot{T}$  on a timescale of  $\Delta t \sim -0.2$  orbits. This correlation is exactly what we observed in Fig. 3.6. The energy injected by the stress at the boundaries ends up as heat less than one orbit later. The negative sign on this value of  $\Delta t$  simply means that the injection happens before the thermalization. In the right plot, both  $\dot{K}$  and  $\dot{M}$  are negatively correlated with  $\dot{T}$  suggesting that magnetic and kinetic energy are being thermalized. The stronger magnetic correlation further suggests that magnetic dissipation contributes more to thermalization than kinetic dissipation. The positive correlation between  $\dot{K}$  and  $\dot{M}$  against  $\dot{T}$  at negative  $\Delta t$  values is a result of the magnetic and kinetic energies increasing along with the energy injection into the box. That is, the stress at the boundaries increases the magnetic and kinetic energies which are dissipated a short time later.

An interesting feature is evident in Fig. 3.7: the negative peak in the magnetic and kinetic correlation functions occur for  $\Delta t$  slightly greater than zero. Similarly, in Fig. 3.6 one can see that peaks in the magnetic and kinetic energy derivatives are offset with respect to the energy injection and thermalization peaks. For example, the maximum rate for magnetic energy loss occurs after the maximum rate for thermal energy gain. Of course, these are plots of the time derivative of the energy, so a peak simply indicates where the second derivative is zero. The magnetic energy is both losing energy to dissipation while gaining energy from the shear at the boundaries. When the energy injection rate peaks decline, the thermalization rate is still growing and the magnetic energy rate also peaks and begins to decline. Similarly, the slope of the magnetic energy loss rate will change sign after the thermalization rate has peaked and when the energy injection rate is no longer itself in decline.

As a test, we performed this correlation analysis on the lower resolution net-flux

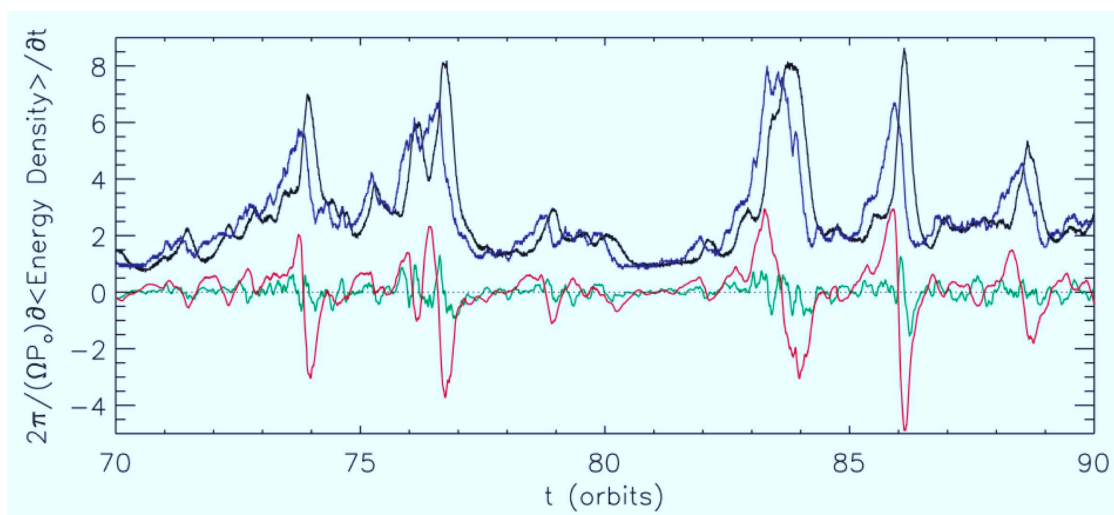


Fig. 3.6.— Time derivative of various volume-averaged energy densities for a 20 orbit period in the NZ128 simulation. The time derivative of the energy densities have been multiplied by an orbital time over the initial gas pressure. The dark blue line is the energy injection rate,  $E_{\text{in}}$ , the black line is the thermal energy density derivative,  $\dot{T}$ , the green line is the kinetic energy density derivative,  $\dot{K}$ , and the red line is the magnetic energy density derivative,  $\dot{M}$ . The dotted line indicates zero.

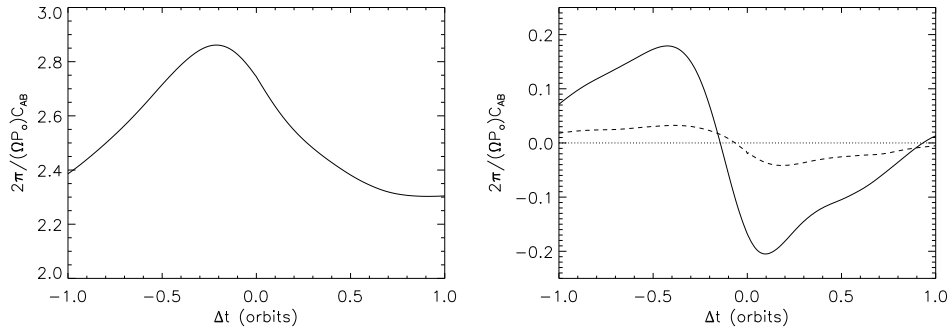


Fig. 3.7.— Correlation coefficients calculated over orbits 20 to 100 in the NZ128 simulation. The plot on the left was calculated by correlating the energy injection rate,  $E_{\text{in}}$ , against the thermal energy time derivative,  $\dot{T}$ . The  $x$ -axis is the correlation length in time, and the  $y$ -axis is the coefficient multiplied by an orbital period over the initial gas pressure. The plot on the right was calculated by correlating the magnetic energy derivative,  $\dot{M}$ , (solid line) and kinetic energy derivative,  $\dot{K}$ , (dashed line) against the thermal energy derivative. The dotted line indicates  $C_{AB} = 0$ . Note that the two plots have different  $y$  scales.

simulations and find that energy injection precedes thermalization by  $\sim 0.2$  orbits, independent of resolution. Furthermore, magnetic dissipation dominates over kinetic dissipation for all net flux simulations.

The analysis so far has only examined the rate of change in the energy terms, not specifically how they change. For example, does a “dip” in  $\dot{M}$  correspond to direct thermalization of magnetic energy, or is there a transfer of energy from magnetic to kinetic? To examine the energy flow in more detail, we focus on orbits 50 to 52 in NZ128, for which we ran the NZ128 simulation at high temporal resolution. This high time resolution allows us to resolve short timescale features, but also generates many large data files. Therefore, we restrict this part of the analysis to the two orbit period mentioned above. Consider the evolution equation for the volume-averaged kinetic energy given by

$$\begin{aligned} \dot{K} = & - \left\langle \nabla \cdot \left[ \mathbf{v} \left( \frac{1}{2} \rho v^2 + \frac{1}{2} B^2 + P + \rho \Phi \right) - \mathbf{B}(\mathbf{v} \cdot \mathbf{B}) \right] \right\rangle \\ & + \left\langle \left( P + \frac{1}{2} B^2 \right) \nabla \cdot \mathbf{v} \right\rangle - \langle \mathbf{B} \cdot (\mathbf{B} \cdot \nabla \mathbf{v}) \rangle - \dot{G} - Q_k, \end{aligned} \quad (3.10)$$

where  $Q_k$  is the volume-averaged (numerical) kinetic energy dissipation rate. The evolution equation for the volume-averaged magnetic energy is given by

$$\dot{M} = - \left\langle \nabla \cdot \left( \frac{1}{2} B^2 \mathbf{v} \right) \right\rangle - \left\langle \frac{1}{2} B^2 \nabla \cdot \mathbf{v} \right\rangle + \langle \mathbf{B} \cdot (\mathbf{B} \cdot \nabla \mathbf{v}) \rangle - Q_m \quad (3.11)$$

where  $Q_m$  is the volume-averaged (numerical) magnetic energy dissipation rate. We have calculated each term in these equations over the two orbit period and find that the dominant terms are  $-\langle \nabla \cdot (\frac{1}{2} \rho v^2) \mathbf{v} \rangle$ ,  $\langle \nabla \cdot [\mathbf{B}(\mathbf{v} \cdot \mathbf{B})] \rangle$ ,  $\langle \mathbf{B} \cdot (\mathbf{B} \cdot \nabla \mathbf{v}) \rangle$ ,  $Q_k$ , and  $Q_m$ .  $Q_k$  and  $Q_m$  are what remain after calculating all other terms in the energy equations at a particular instant in time. Calculating the volume-averages of the first two terms yields the radial boundary Reynolds and Maxwell stresses in Equation (3.1) (Hawley et al. 1995), namely the energy injection rate by the shearing periodic boundaries. The third of the dominant terms is the transfer rate of kinetic to magnetic energy via field line stretching. Figure 3.8 plots the time-history of this term (pink line) along with  $\dot{T}$  (black line), the energy injection rate  $E_{\text{in}}$  (blue line), and  $-Q_k$  and  $-Q_m$  (green and red lines, respectively). As energy is injected into the grid, a significant fraction of this energy is transferred to the magnetic field via field line stretching, presumably through the shear flow. Thermalization follows 0.2 orbits later and is marked by increases in the absolute value of  $Q_k$  and  $Q_m$ , with  $|Q_m| > |Q_k|$ . The ratio of kinetic to magnetic dissipation is approximately constant in time over this period,

with  $Q_k/Q_m \approx 0.6$ . This suggests that the details of the thermalization do not vary with intermittent increases in  $E_{\text{in}}$  that occur when the fluid experiences a channel flow.

As discussed, the recurring channel modes in the net flux simulations create distinguishable points of energy injection that make it straightforward to follow the subsequent thermalization. Such modes do not exist in the zero net flux simulations, which makes the identification of specific correlations slightly more difficult. The situation is further complicated by the overall reduced levels of the turbulence which causes the time derivative of the thermal energy to be dominated by very high frequency oscillations due to propagating spiral density waves (Gardiner & Stone 2005a). We have determined that these waves are created by compressibility and have very little effect on the dissipational heating within the box. To remove their dominance in the energy derivatives, we rebin the time data using a “neighborhood” averaging procedure in which the rebinned data points are calculated from averages of a specified number of original data points. We then apply equation (3.9) between  $E_{\text{in}}$  and  $\dot{T}$ ; the result is shown in Fig. 3.9. The correlation curve has several narrow peaks, which result from residual effects of the rebinning process. The curve has a broader peak near  $\Delta t \sim -0.2$  orbits, which agrees with the same curves for NZ128 (Fig. 3.7). The correlation function for SZ128 is not as sharply peaked as that for NZ128, which is most likely a result of the lower amplitude variability in the rebinned SZ128 data. Applying this analysis to the lower resolution zero net flux simulations, we find that the correlation function always has a broad peak at  $\Delta t \sim -0.2$  orbits. Thus, as was the case in the net flux simulations, the energy injection/thermalization timescale is independent of resolution.

Finally, we note that the saturated state of SZ128 is too complex to obtain correla-

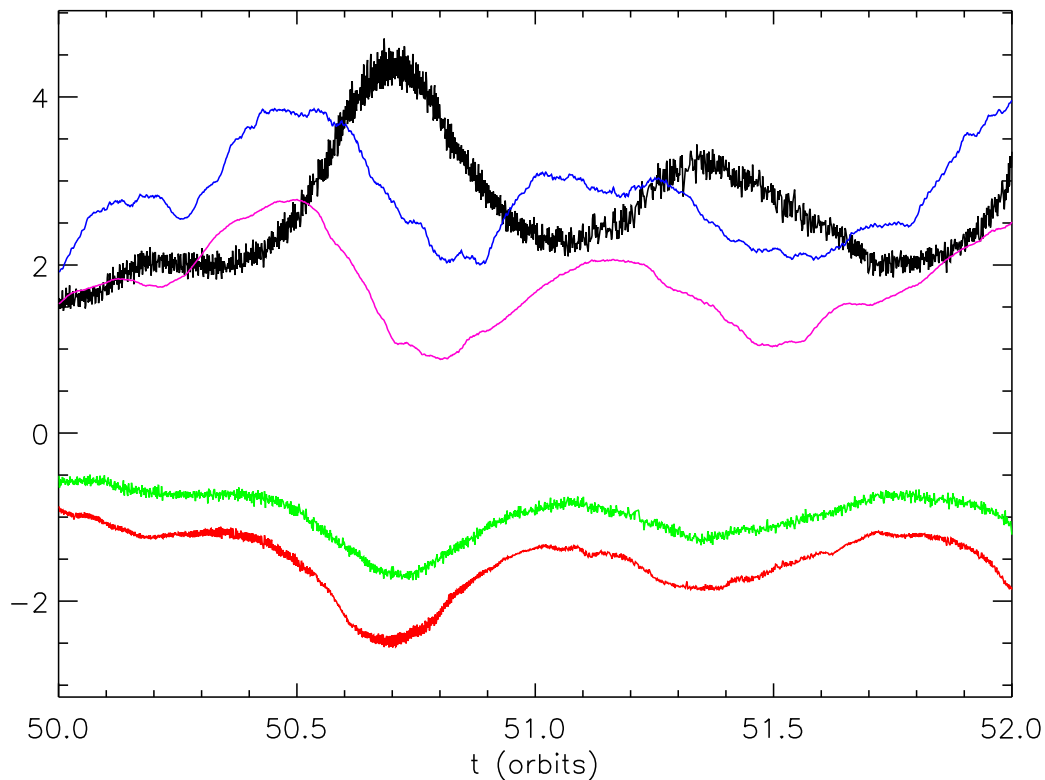


Fig. 3.8.— Various terms in the volume-averaged magnetic, kinetic, and thermal energy density evolution equations over a two orbit period of NZ128. The energy terms are  $\dot{T}$  (black),  $E_{\text{in}}$  (blue),  $-Q_{\text{k}}$  (green),  $-Q_{\text{m}}$  (red), and the volume-averaged transfer rate from kinetic to magnetic energy (pink). All of these terms are defined in the text and have been multiplied by an orbital period over the initial gas pressure.

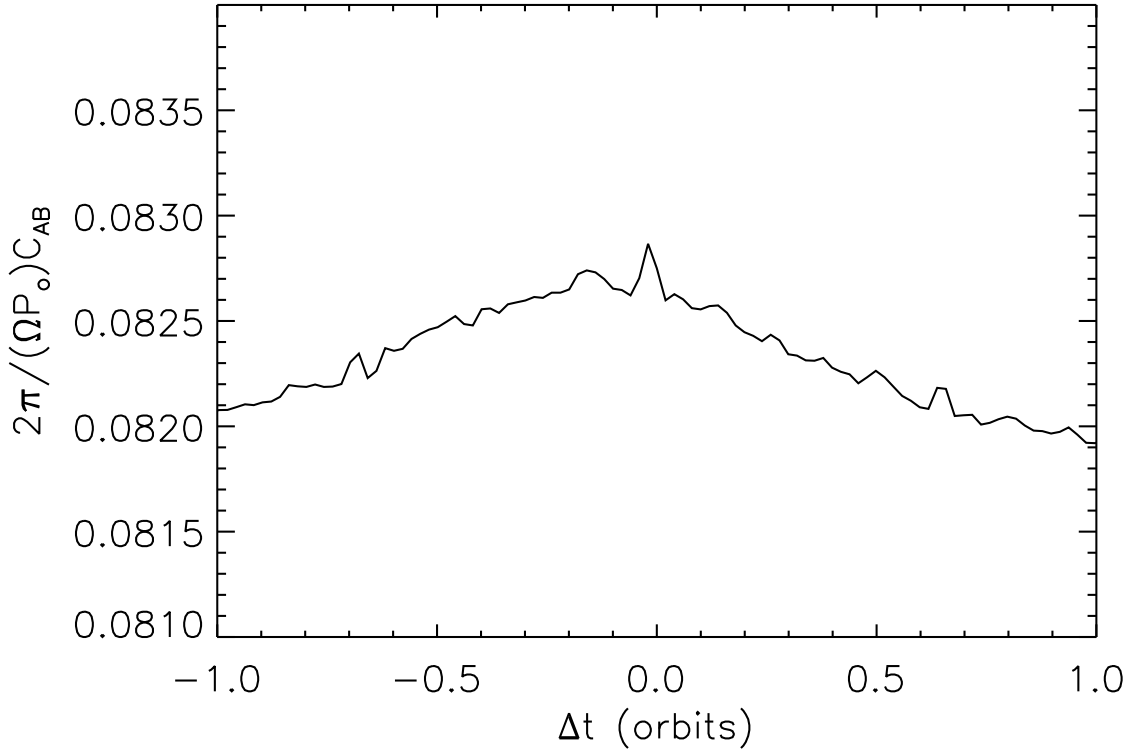


Fig. 3.9.— Correlation coefficient calculated over the saturated state of the SZ128 simulation. The coefficient was calculated by correlating the energy injection rate against the thermal energy density derivative. The  $x$ -axis is the correlation length in time, and the  $y$ -axis is the coefficient multiplied by an orbital period over the initial gas pressure. The narrow peaks in the curve correspond to residual effects from rebinning the energy derivatives (described in the text). The broader peak in the correlation function occurs at  $\Delta t \sim -0.2$  orbits.

tions between  $\dot{M}$ ,  $\dot{K}$ , and  $\dot{T}$ , such as was done for NZ128. In the net flux simulations, the recurring channel modes lead to the build up and thermalization of magnetic energy. The creation and thermalization of magnetic energy are events that are well-separated in time, making it easy to study the flow of energy between various components. In the zero net flux simulations, however, the average properties of the turbulence remain more constant in time. We will further investigate the dissipation of magnetic and kinetic energy for the zero net flux geometry in § 3.4.2 and § 3.5.1.

### 3.4.2 Decaying Turbulence

As noted by Hawley et al. (1995), the MHD turbulence decays without differential rotation to sustain the MRI. We make use of this to observe how rapidly thermalization occurs when there is no further input of energy. This analysis should provide some additional insight into the thermalization process for each field geometry. We remove the net shear flow and the Coriolis and tidal forces from a state taken from the sustained MRI turbulence in the fiducial models. These runs are labeled “NZD” and “SZD” in Table 3.1 and are described in more detail in § 3.2. Figure 3.10 shows the subsequent magnetic and kinetic energy decay for both runs. In the figure, the kinetic and magnetic energies have been normalized to their values at the starting time of  $t = 40$  orbits.

In NZD128, the ratio of total magnetic to kinetic energy at  $t = 40$  orbits is 3.4. The figure shows that the magnetic energy decays more rapidly than the kinetic energy at early times, losing almost half its initial value within 0.2 orbits. In SZD128, the ratio of total magnetic to kinetic energy at  $t = 40$  orbits is 1.4. The kinetic energy shows high frequency oscillations about an average value that decays in time. These oscillations are due to the same compressive, spiral waves that exist in the sustained

turbulence simulations. The magnetic energy is unaffected by these waves. The average decay of kinetic energy, calculated from smoothing away the oscillations, is also shown in the figure. Both the kinetic and magnetic energies decay quickly over time. Again, almost half the magnetic energy is lost within 0.2 orbits. The high frequency oscillations also decay in amplitude over time. As was the case in NZD128, the magnetic dissipation rate is initially faster than that for the kinetic energy. After about one orbit, the decay rates become comparable.

Finally, we checked the contributions from the various terms in equations (3.10) and (3.11). In both NZD128 and SZD128, there is some transfer from magnetic to kinetic energy during the decay. However, the transfer rate is small compared to the decay rate of the magnetic energy and is such that the numerical dissipation of magnetic energy dominates over that of kinetic energy.

### 3.5 Measuring Numerical Dissipation

In their investigation of convergence of zero net flux shearing box simulations, Fromang & Papaloizou (2007) carried out an analysis based on the evolution of magnetic energy in Fourier space. This analysis shows how magnetic energy is created, transferred from one scale to another, and finally lost due to numerical dissipation. Their study used the ZEUS code and assumed an isothermal equation of state. Here we repeat and expand upon their analysis to understand dissipation as a function of length scale in Athena.

We note several differences between our work and that of Fromang & Papaloizou (2007). First, they focus on magnetic energy evolution and did not provide a comparable calculation for the kinetic energy. Second, recognizing that the  $y$  direction is dominated by the largest scales, they restricted their analysis to axisymmetric modes,

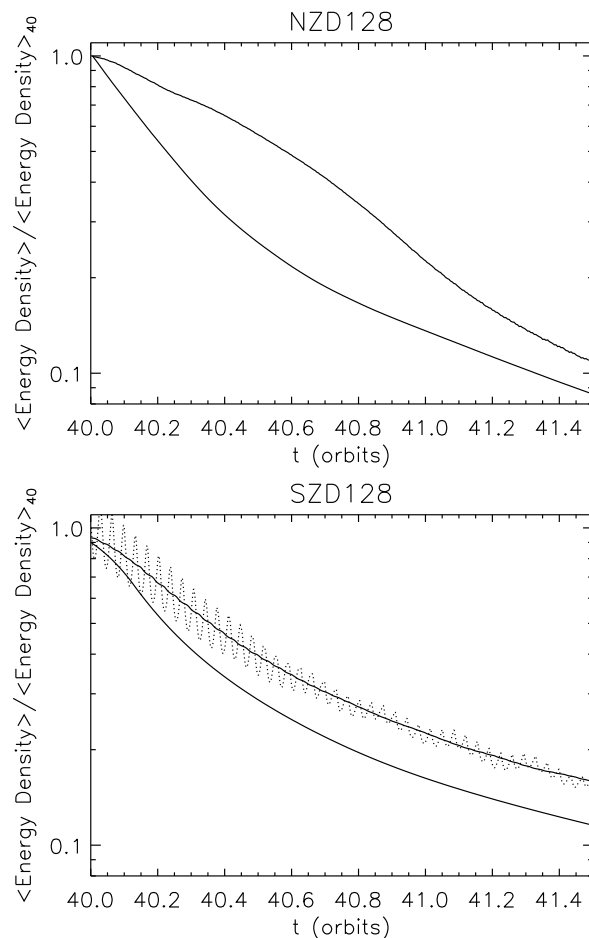


Fig. 3.10.— Volume-averaged magnetic and kinetic energy densities in the first 1.5 orbits of NZD128 (top) and SZD128 (bottom). In both plots, the upper curves correspond to the kinetic energy density and the lower curves correspond to the magnetic energy density. In SZD128, high frequency oscillations appear in the kinetic energy evolution. To smooth away these oscillations, a moving window average was applied to the kinetic energy density. The unsmoothed kinetic energy is shown by the dotted line, while the smoothed kinetic energy is the solid line. The magnetic energy density in the SZD128 plot has also been smoothed for consistency. Both the kinetic and magnetic energy densities have been normalized to their respective (unsmoothed) values at  $t = 40$  orbits.

namely  $k_y = 0$ . Finally, as they were primarily interested in how poloidal field could be regenerated as part of a dynamo process, a portion of their analysis concentrated on the poloidal components rather than the full magnetic field. We have chosen to extend the Fromang & Papaloizou (2007) analysis more generally to include a kinetic energy density evolution, nonaxisymmetric effects, and the effects of a nonzero toroidal field.

Following Fromang & Papaloizou (2007), we decompose the velocity field of the flow into the mean flow,  $\mathbf{V}_{\text{sh}}$ , and the turbulent velocity,  $\mathbf{v}_t$ , via

$$\mathbf{v} = \mathbf{V}_{\text{sh}} + \mathbf{v}_t. \quad (3.12)$$

The mean flow is defined as

$$\mathbf{V}_{\text{sh}} = V_{\text{sh}} \hat{\mathbf{y}} = \frac{\hat{\mathbf{y}}}{L_y L_z} \int \int v_y(x, y, z) dy dz. \quad (3.13)$$

Turning next to the induction equation, we substitute equation (3.12) for the velocity, take the Fourier transform, and dot the result with the complex conjugate of  $\tilde{\mathbf{B}}(\mathbf{k})$ , which is defined by equation (3.6) with  $f = \mathbf{B}$ . All Fourier transforms are done via equation (3.6) using a standard FFT and replacing  $f$  with the appropriate quantity. The data is mapped into a frame in which the  $x$  boundaries are periodic and then remapped into the original frame after performing the FFT.

The result of this calculation is an equation describing the magnetic energy density evolution in Fourier space,

$$\frac{1}{2} \frac{\partial |\tilde{\mathbf{B}}(\mathbf{k})|^2}{\partial t} = A + S + T_{bb} + T_{\text{div}v} + T_{bv} + D_{\text{mag}}, \quad (3.14)$$

where

$$A = -Re \left[ \tilde{\mathbf{B}}^*(\mathbf{k}) \cdot \int \int \int V_{\text{sh}} \frac{\partial \mathbf{B}}{\partial y} e^{-i\mathbf{k} \cdot \mathbf{x}} d^3 \mathbf{x} \right], \quad (3.15)$$

$$S = +Re \left[ \tilde{B}_y^*(\mathbf{k}) \cdot \int \int \int B_x \frac{\partial V_{\text{sh}}}{\partial x} e^{-i\mathbf{k} \cdot \mathbf{x}} d^3 \mathbf{x} \right], \quad (3.16)$$

$$T_{bb} = -Re \left[ \tilde{\mathbf{B}}^*(\mathbf{k}) \cdot \int \int \int (\mathbf{v}_t \cdot \nabla) \mathbf{B} e^{-i\mathbf{k} \cdot \mathbf{x}} d^3 \mathbf{x} \right], \quad (3.17)$$

$$T_{\text{div}v} = -Re \left[ \tilde{\mathbf{B}}^*(\mathbf{k}) \cdot \int \int \int (\nabla \cdot \mathbf{v}_t) \mathbf{B} e^{-i\mathbf{k} \cdot \mathbf{x}} d^3 \mathbf{x} \right], \quad (3.18)$$

$$T_{bv} = +Re \left[ \tilde{\mathbf{B}}^*(\mathbf{k}) \cdot \int \int \int (\mathbf{B} \cdot \nabla) \mathbf{v}_t e^{-i\mathbf{k} \cdot \mathbf{x}} d^3 \mathbf{x} \right]. \quad (3.19)$$

The  $D_{\text{mag}}$  term has no analytic expression; it is simply what is left over and accounts for numerical losses of magnetic energy (Fromang & Papaloizou 2007). In the present simulations, there is no physical resistivity. The other terms have the following meanings:  $A$  is the transfer of magnetic energy between scales by the shear flow,  $S$  is the creation of magnetic energy from this shear flow,  $T_{bb}$  is the advection of magnetic energy between scales by the turbulent velocity field,  $T_{\text{div}v}$  results from the turbulent compressibility, and  $T_{bv}$  describes the creation of magnetic field by the turbulent velocity fluctuations. In each case,  $Re$  signifies the real part of the transform.

One can follow a similar procedure using the momentum equation to determine the evolution of the kinetic energy density in Fourier space. As described previously, we include the density in our Fourier transforms. Consider the time derivative of  $\sqrt{\rho} \mathbf{v}$  given by

$$\frac{\partial \sqrt{\rho} \mathbf{v}}{\partial t} = \sqrt{\rho} \frac{\partial \mathbf{v}}{\partial t} + \frac{\mathbf{v}}{2\sqrt{\rho}} \frac{\partial \rho}{\partial t}. \quad (3.20)$$

Note that here, for simplicity, we do not decompose the velocity into mean and turbulent components. Using a combination of the continuity and momentum equations, this equation can be written as

$$\begin{aligned} \frac{\partial \sqrt{\rho} \mathbf{v}}{\partial t} = & \sqrt{\rho} \left[ -\mathbf{v} \cdot \nabla \mathbf{v} - \frac{1}{\rho} \nabla (P + \frac{1}{2} B^2) + \frac{1}{\rho} (\mathbf{B} \cdot \nabla \mathbf{B}) - 2\boldsymbol{\Omega} \times \mathbf{v} + 2q\Omega^2 x \hat{\mathbf{x}} \right] \\ & + \frac{\mathbf{v}}{2\sqrt{\rho}} [-\rho(\nabla \cdot \mathbf{v}) - \mathbf{v} \cdot \nabla \rho], \end{aligned} \quad (3.21)$$

If we take the Fourier transform of this equation and dot the result with the complex conjugate of

$$\widetilde{\sqrt{\rho} \mathbf{v}}(\mathbf{k}) = \int \int \int \sqrt{\rho}(\mathbf{x}) \mathbf{v}(\mathbf{x}) e^{-i\mathbf{k} \cdot \mathbf{x}} d^3 \mathbf{x}, \quad (3.22)$$

we arrive at

$$\frac{1}{2} \frac{\partial |\widetilde{\sqrt{\rho} \mathbf{v}}(\mathbf{k})|^2}{\partial t} = T_{vv} + T_{\text{comp}} + T_{vb} + T_{\text{press}} + T_{\text{cor}} + T_{\phi} + D_{\text{kin}}, \quad (3.23)$$

where

$$\frac{1}{2} |\widetilde{\sqrt{\rho} \mathbf{v}}(\mathbf{k})|^2 \equiv \frac{1}{2} \left[ |\widetilde{\sqrt{\rho} v_x}(\mathbf{k})|^2 + |\widetilde{\sqrt{\rho} v_y}(\mathbf{k})|^2 + |\widetilde{\sqrt{\rho} v_z}(\mathbf{k})|^2 \right], \quad (3.24)$$

$$T_{vv} = -\text{Re} \left[ \widetilde{\sqrt{\rho} \mathbf{v}}^*(\mathbf{k}) \cdot \int \int \int [\sqrt{\rho}(\mathbf{v} \cdot \nabla) \mathbf{v} + \frac{\mathbf{v}}{2\sqrt{\rho}} (\mathbf{v} \cdot \nabla) \rho] e^{-i\mathbf{k} \cdot \mathbf{x}} d^3 \mathbf{x} \right], \quad (3.25)$$

$$T_{\text{comp}} = -Re \left[ \widetilde{\sqrt{\rho}\mathbf{v}^*}(\mathbf{k}) \cdot \int \int \int \frac{\sqrt{\rho}\mathbf{v}}{2} (\nabla \cdot \mathbf{v}) e^{-i\mathbf{k}\cdot\mathbf{x}} d^3\mathbf{x} \right], \quad (3.26)$$

$$T_{vb} = +Re \left[ \widetilde{\sqrt{\rho}\mathbf{v}^*}(\mathbf{k}) \cdot \int \int \int \frac{1}{\sqrt{\rho}} (\mathbf{B} \cdot \nabla) \mathbf{B} e^{-i\mathbf{k}\cdot\mathbf{x}} d^3\mathbf{x} \right], \quad (3.27)$$

$$T_{\text{press}} = -Re \left[ \widetilde{\sqrt{\rho}\mathbf{v}^*}(\mathbf{k}) \cdot \int \int \int \frac{1}{\sqrt{\rho}} \nabla (P + \frac{1}{2}B^2) e^{-i\mathbf{k}\cdot\mathbf{x}} d^3\mathbf{x} \right], \quad (3.28)$$

$$T_{\text{cor}} = -Re \left[ \widetilde{\sqrt{\rho}\mathbf{v}^*}(\mathbf{k}) \cdot \int \int \int (2\boldsymbol{\Omega} \times \sqrt{\rho}\mathbf{v}) e^{-i\mathbf{k}\cdot\mathbf{x}} d^3\mathbf{x} \right], \quad (3.29)$$

$$T_{\phi} = +Re \left[ \widetilde{\sqrt{\rho}v_x^*}(\mathbf{k}) \cdot \int \int \int 2\sqrt{\rho}q\Omega^2 x e^{-i\mathbf{k}\cdot\mathbf{x}} d^3\mathbf{x} \right], \quad (3.30)$$

and  $D_{\text{kin}}$  accounts for the dissipation of kinetic energy. Again, this dissipation is numerical as we have not included an explicit viscosity term in our equations. Equation (3.23) describes the evolution of the kinetic energy density in Fourier space.  $T_{vv}$  is a term that describes the transfer of kinetic energy between scales by the velocity field (both the mean and turbulent velocity),  $T_{\text{comp}}$  results from turbulent compressibility,  $T_{vb}$  describes how kinetic energy changes from magnetic tension,  $T_{\text{press}}$  represents the effect of both gas and magnetic pressure on the kinetic energy, and  $T_{\phi}$  is the effect of the tidal potential on the kinetic energy. Note that  $T_{\text{cor}}$  is analytically equal to zero, and it is not included in any of the following analysis or discussion.

In the saturated state of the MRI, the magnetic and kinetic energy densities should be in a steady state on average (although they do show strong fluctuations over short periods of time). If we consider the time-averages of equations (3.14) and (3.23), then we can set the left hand sides to zero. We then rewrite these equations as

$$T_{vv} + T_{\text{comp}} + T_{vb} + T_{\text{press}} + T_{\phi} + D_{\text{kin}} = 0, \quad (3.31)$$

$$A + S + T_{bb} + T_{\text{div}v} + T_{bv} + D_{\text{mag}} = 0, \quad (3.32)$$

where each of these terms is now a time-average. Here we average over 161 snapshots from orbit 20 to 100 in increments of 0.5 orbits. Each of these terms is a function of  $k_x$ ,  $k_y$ , and  $k_z$ , and in what follows we average the terms on shells of constant  $k = |\mathbf{k}|$  as was done in Fromang & Papaloizou (2007).<sup>3</sup> Note that unlike the averaging described in that paper, we include  $k_y$  in the calculation of  $k$ .

### 3.5.1 Zero Net Magnetic Flux

#### Fiducial Run

In this section, we focus on the Fourier transfer functions for the fiducial zero net magnetic flux simulation. Figure 3.11 plots the magnetic transfer functions defined in equations (3.15)-(3.19) as a function of length scale for SZ128, and Fig. 3.12 plots the kinetic transfer functions defined in equations (3.25)-(3.30). The dashed lines correspond to plus or minus one standard deviation around the mean value of the time average. Most of the transfer functions show large variation at small  $k$  values which may be due to poor statistics at small  $k$  and relatively large time variability. Because the transfer functions approach zero rapidly, we plot the ranges  $1 < kL/(2\pi) < 20$  and  $20 < kL/(2\pi) < 64$  in the same figure, but with different  $y$  scalings.

The shear term  $S$  is positive at all scales, as observed in Fromang & Papaloizou (2007), meaning that  $B_y$  is created by the shear flow at all scales.  $A$  is small at all

---

<sup>3</sup>In our analysis, the average over shells of constant  $k$  was done before the temporal average.

scales, supporting the assumption made in Fromang & Papaloizou (2007) that  $A \approx 0$ .  $T_{bv}$  is primarily negative at the largest scales, although there are large fluctuations, and becomes positive for  $kL/(2\pi) \gtrsim 35$ . The turbulent velocity fluctuations seem to be creating magnetic energy at the smallest scales, but at larger scales, the magnetic field appears to lose energy via this interaction with the turbulence.  $T_{bb}$  is negative for  $k$  smaller than  $kL/(2\pi) \sim 20$ , meaning that the turbulence is transferring magnetic energy away from these scales. Although this analysis doesn't determine the direction of this cascade, at the largest scale (i.e., the box size) the energy can only cascade to smaller scales. In terms of absolute value,  $S$  and  $T_{bb}$  are dominant on the largest scales, while on small scales,  $T_{bb} > T_{bv} > S > 0$ .

It is difficult to say anything conclusive about the kinetic transfer functions on the largest scales as they are subject to considerable uncertainty, although  $T_{vb} < 0$  appears reasonably well constrained at these scales. At smaller scales, the two dominant terms are  $T_{vv}$  and  $T_{vb}$ , with  $T_{vb} > T_{vv} > 0$ ; kinetic energy is being transferred to these scales by the turbulence, and being created by magnetic field.

Equations (3.31) and (3.32) have been set to zero from the assumption that the magnetic and kinetic energies are in a time-averaged steady state. The dissipation terms  $D_{\text{mag}}$  and  $D_{\text{kin}}$  are simply what is left over after the other transfer functions have been computed. The top plots in Fig. 3.13 are the kinetic and magnetic dissipation and the ratio  $D_{\text{kin}}/D_{\text{mag}}$  as a function of  $k$  for  $20 < kL/(2\pi) < 64$ ; the scatter at small  $k$  is large and there is considerable uncertainty in the dissipation values. At small scales, magnetic dissipation dominates kinetic dissipation by a factor of roughly three. The kinetic and magnetic dissipation rate increases in magnitude towards larger scales.

Following Fromang & Papaloizou (2007), we can determine an effective resistivity

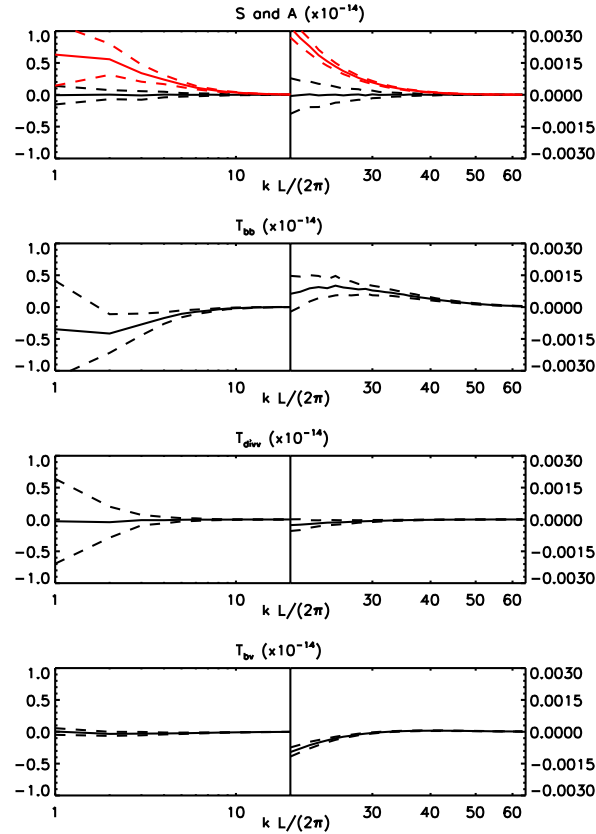


Fig. 3.11.— Magnetic Fourier transfer functions versus a dimensionless wave number ( $L$  is the length of the smallest dimension in the box) for SZ128. Each plot is displayed in two components; the left part shows the data for  $1 < kL/(2\pi) < 20$ , and the right part shows the data for  $20 < kL/(2\pi) < 64$  by changing the  $x$  and  $y$  axis scaling. In all plots, the solid line is the average value for the transfer function. This average was obtained over 161 frames in the saturated state and shells of constant  $|\mathbf{k}|$ . The upper (lower) dashed line that matches color with the solid line correspond to the transfer function plus (minus) one temporal standard deviation. From top to bottom, the plots show  $S$  (red) and  $A$  (black),  $T_{bb}$ ,  $T_{divv}$ , and  $T_{bv}$ .

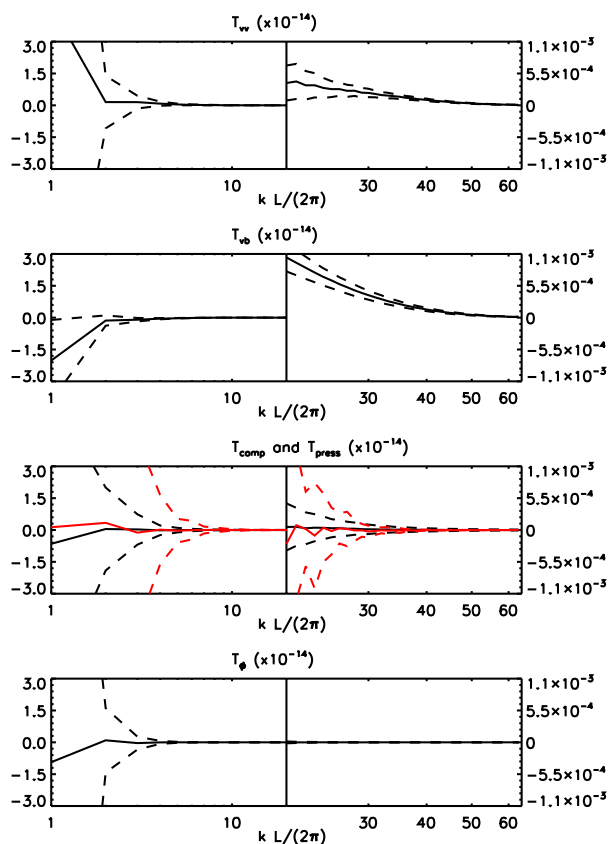


Fig. 3.12.— Kinetic Fourier transfer functions versus a dimensionless wave number ( $L$  is the length of the smallest dimension in the box) for SZ128. Each plot is displayed in two components; the left part shows the data for  $1 < kL/(2\pi) < 20$ , and the right part shows the data for  $20 < kL/(2\pi) < 64$  by changing the  $x$  and  $y$  axis scaling. In all plots, the solid line is the average value for the transfer function. This average was obtained over 161 frames in the saturated state and shells of constant  $|\mathbf{k}|$ . The upper (lower) dashed line that matches color with the solid line correspond to the transfer function plus (minus) one temporal standard deviation. From top to bottom, the plots show  $T_{vv}$ ,  $T_{vb}$ ,  $T_{\text{press}}$  (red) and  $T_{\text{comp}}$  (black), and  $T_{\phi}$ .

and viscosity as a function of length scale by assuming that the numerical effects behave as if they were physical resistivity and viscosity. For example, with a constant Ohmic resistivity, the induction equation would have an additional term proportional to  $\nabla^2 B$ , with the constant of proportionality being the resistivity. If we take the Fourier transform of this term and dot it with the complex conjugate of  $\tilde{\mathbf{B}}(\mathbf{k})$ , the real part is

$$T_\eta = +Re \left[ \tilde{\mathbf{B}}^*(\mathbf{k}) \cdot \int \int \int \nabla^2 \mathbf{B} e^{-i\mathbf{k}\cdot\mathbf{x}} d^3\mathbf{x} \right] = -k^2 |\tilde{\mathbf{B}}(\mathbf{k})|^2. \quad (3.33)$$

We can then define an effective resistivity as a function of  $k$  by

$$\eta_{\text{eff}}(k) \equiv \frac{D_{\text{mag}}(k)}{T_\eta(k)}. \quad (3.34)$$

Similarly, a constant kinematic shear viscosity would add a term proportional to  $\sqrt{\rho}[\nabla^2 \mathbf{v} + \frac{1}{3}\nabla(\nabla \cdot \mathbf{v})]$  to equation (3.21), with the constant of proportionality being the viscosity. Note that we only consider shear viscosity here for simplicity. We take the Fourier transform of the viscous term, dot it with the complex conjugate of equation (3.22), and take the real part. The result is

$$T_\nu = +Re \left[ \widetilde{\sqrt{\rho}\mathbf{v}^*}(\mathbf{k}) \cdot \int \int \int \sqrt{\rho}[\nabla^2 \mathbf{v} + \frac{1}{3}\nabla(\nabla \cdot \mathbf{v})] e^{-i\mathbf{k}\cdot\mathbf{x}} d^3\mathbf{x} \right]. \quad (3.35)$$

This equation can be made simpler by realizing that the second term of the integrand, related to the divergence of  $\mathbf{v}$ , is negligible. We can also assume that the density is relatively constant, and arrive at

$$T_\nu = -k^2 |\widetilde{\sqrt{\rho}\delta\mathbf{v}}(\mathbf{k})|^2. \quad (3.36)$$

We have substituted the perturbed velocity here because it is the only velocity that can lead to *numerical* dissipation of kinetic energy. That is, a pure shear flow will not encounter any numerical viscosity, and we can subtract off this flow. We define an effective viscosity by

$$\nu_{\text{eff}}(k) \equiv \frac{D_{\text{kin}}(k)}{T_\nu(k)}. \quad (3.37)$$

We can also characterize the effective resistivity and viscosity in terms of a Reynolds number,

$$Re_{\text{eff}}(k) \equiv \frac{c_o H}{\nu_{\text{eff}}(k)}, \quad (3.38)$$

and magnetic Reynolds number,

$$Rm_{\text{eff}}(k) \equiv \frac{c_o H}{\eta_{\text{eff}}(k)}, \quad (3.39)$$

where we have used the initial isothermal sound speed,  $c_o = 0.001$ , as a characteristic velocity, and  $H = L_z$  is a characteristic length. These numbers quantify the numerical dissipation coefficients in a dimensionless manner.

Finally, we define an effective Prandtl number by

$$P_{m,\text{eff}}(k) \equiv \frac{\nu_{\text{eff}}(k)}{\eta_{\text{eff}}(k)} \quad (3.40)$$

The effective viscosity and resistivity as well as the effective Prandtl number are shown in the bottom plots of Fig. 3.13. The viscosity and resistivity are fairly constant at large  $k$ . The effective Reynolds numbers are on the order of  $Re_{\text{eff}} \sim 12000$ , and  $Rm_{\text{eff}} \sim 20000$  at large  $k$ . The Prandtl number is also relatively flat at these scales, and  $P_{m,\text{eff}} \sim 1.6$ . This result agrees with Fromang & Papaloizou (2007), where

$P_{m,\text{eff}} > 1$  for ZEUS. While the numerical dissipation of Athena is not physical, the “flatness” of  $\nu_{\text{eff}}$  and  $\eta_{\text{eff}}$  suggests a resemblance to physical dissipation at small scales.

Finally, note that although the Prandtl number is greater than unity, the magnetic dissipation dominates over kinetic dissipation. Evidently,  $T_\eta$  is larger than  $T_\nu$  because there is more magnetic energy than kinetic energy at a given scale. In particular,

$$\frac{T_\eta}{T_\nu} = \frac{|\tilde{\mathbf{B}}(\mathbf{k})|^2}{|\sqrt{\rho}\delta\mathbf{v}(\mathbf{k})|^2}. \quad (3.41)$$

Since there is more magnetic energy than perturbed kinetic energy at a given scale, magnetic dissipation dominates.

### Resolution Effects

To gauge the effect of resolution on these various quantities, we perform the same analysis on the lower resolution runs, SZ16, SZ32, and SZ64. We focus, in particular, on the small scales (i.e., large  $k$ ) where our quantities are statistically more well-determined. Figure 3.14 shows  $\nu_{\text{eff}}$ ,  $\eta_{\text{eff}}$ ,  $P_{m,\text{eff}}$ , and the ratio of  $D_{\text{kin}}$  to  $D_{\text{mag}}$  as a function of  $x$  resolution,  $N_x$ . The data points are calculated by averaging the quantity of interest over  $k$  in the regions of  $k$ -space where the error on the quantity is less than its mean value.<sup>4</sup> The displayed error bars are the propagation of the errors from the temporal statistics. At these large values of  $k$ ,  $\nu_{\text{eff}}$ ,  $\eta_{\text{eff}}$ ,  $P_{m,\text{eff}}$ , and  $D_{\text{kin}}/D_{\text{mag}}$  are relatively flat, varying by a factor of at most 2. Consequently, these averages should be representative at small scales.

The numerical viscosity and resistivity decrease as a function of resolution. The dashed lines in the two upper panels of the figure show the line  $\nu_{\text{eff}}, \eta_{\text{eff}} \propto N_x^{-2}$ . The viscosity and resistivity decrease slower than this with increasing  $N_x$ ; we measured

---

<sup>4</sup>There are some quantities for which the error is never less than the mean. In these cases, we average over regions where the mean is greater than 80% of the error.

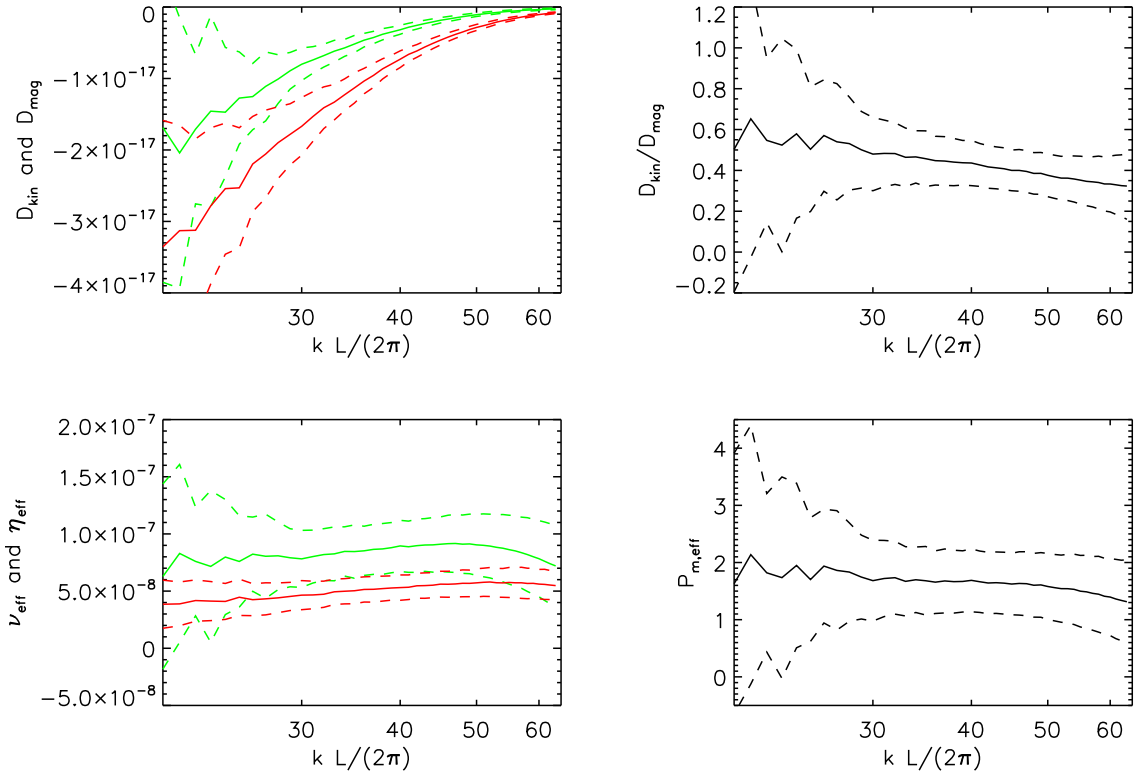


Fig. 3.13.— Numerical dissipation quantities plotted against a dimensionless wave number ( $L$  is the length of the smallest dimension in the box). These plots correspond to data from SZ128. The upper left plot shows the dissipation rate of kinetic energy (green) and magnetic energy (red) in Fourier space. The upper right plot shows the ratio of these two dissipation rates. The lower left plot shows the effective numerical viscosity (green) and resistivity (red). The lower right plot shows the ratio of the viscosity to resistivity (i.e., the effective Prandtl number). In all plots, the solid line is the average value for the quantity of interest. For  $D_{\text{kin}}$  and  $D_{\text{mag}}$ , this average was obtained from averaging over shells of constant  $|\mathbf{k}|$  and over 161 frames in the saturated state. The averaged viscosity and resistivity values were calculated as described in the text. The upper and lower dashed lines correspond to the error propagated from one temporal standard deviation.

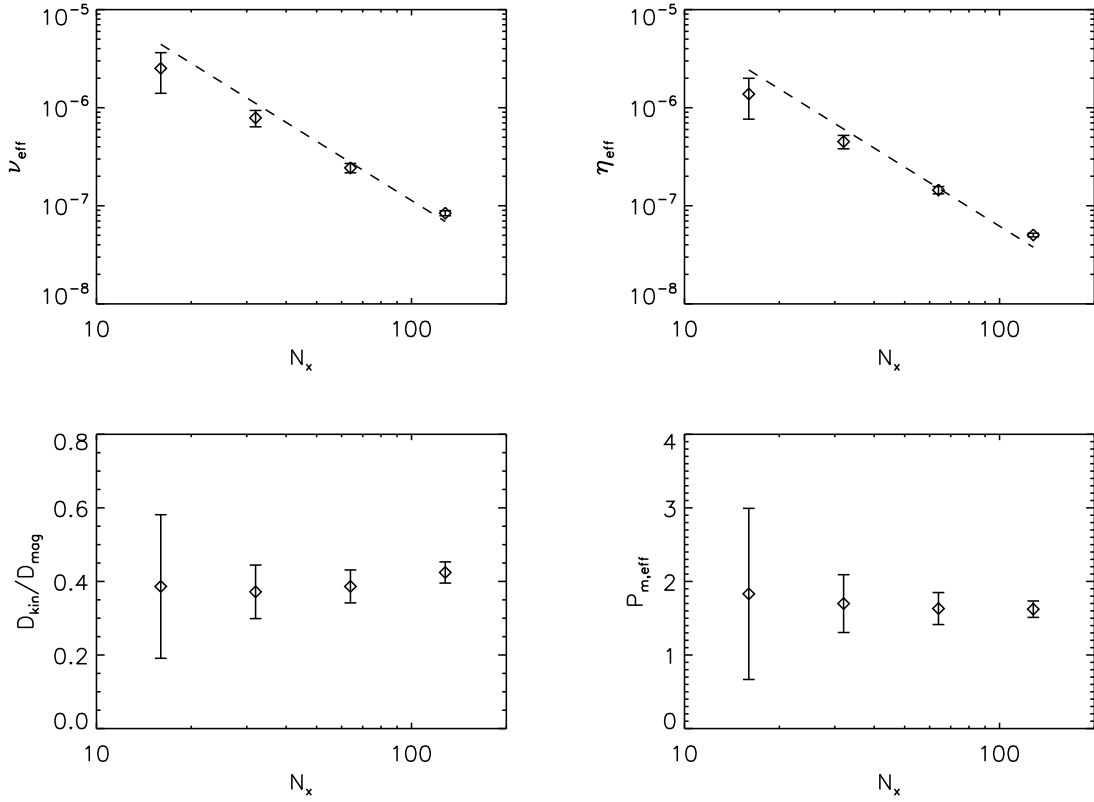


Fig. 3.14.— Averaged dissipation related quantities as a function of grid resolution. These plots correspond to data from the zero net flux simulations, SZ16, SZ32, SZ64, and SZ128. The upper left plot shows the effective viscosity versus  $x$  resolution. The dashed line shows  $\nu_{\text{eff}} \propto N_x^{-2}$ . The upper right plot shows the effective resistivity versus  $x$  resolution. Again, the dashed line shows  $\eta_{\text{eff}} \propto N_x^{-2}$ . The lower left plot shows the ratio of kinetic to magnetic dissipation versus  $x$  resolution. The lower right plot shows the effective Prandtl number versus  $x$  resolution. For each resolution, the data point was obtained from averaging the quantity as a function of  $k$  over values of  $k$  where the error in this quantity is not much larger than the mean value. The error bars represent the propagated errors from the temporal statistics.

$\nu_{\text{eff}}, \eta_{\text{eff}} \propto N_x^{-1.6}$ . The figure also shows that both the effective Prandtl number and the ratio of kinetic to magnetic dissipation are constant with resolution to within the error bars.

### Comparison with Previous Results

Fromang & Papaloizou (2007) were interested in the transfer function for the poloidal field, as the regeneration of this field is key to a self-sustaining dynamo. They found that the magnetic dissipation of ZEUS for the poloidal magnetic field departs from the physical dissipation model at small  $k$  and could even be a nonphysical “positive” dissipation. We repeat the same analysis as performed in that paper, but with SZ128, for comparison. First, we examine the magnetic dissipation for the full 3D Fourier analysis described above. Second, we do the same procedure but setting  $B_y = 0$  to focus on the effect of only including poloidal field. Finally, we perform the procedure with  $B_y = 0$  and in the plane  $k_y = 0$  (i.e., axisymmetry). These simplifications allow us to reproduce the poloidal field analysis of Fromang & Papaloizou (2007).

The results are shown in Fig. 3.15. The left two plots correspond to the Fourier analysis in which only  $B_y = 0$  is assumed. The right plots assume  $B_y = 0$  and  $k_y = 0$ . The black lines in the bottom two plots correspond to the magnetic dissipation for the full 3D Fourier analysis with  $B_y \neq 0$  and  $k_y \neq 0$ . It is apparent that when  $B_y = 0$  is assumed in the calculations, the magnetic dissipation becomes positive at large scales. However, when  $B_y$  is included, the magnetic dissipation remains negative. Whether or not  $k_y = 0$  is assumed seems to make very little difference, supporting the notion that small  $k_y$  dominates. Since Athena and ZEUS both find positive  $D_{\text{mag}}$  at small  $k$ , it is unlikely that this effect can be attributed to algorithmic limitations specific to ZEUS. Since  $D_{\text{mag}}$  is not a derived quantity but simply what remains after all the

transfer functions are calculated, it seems likely that the positive  $D_{\text{mag}}$  values for the poloidal field analysis are due to incomplete statistics at large scales, or other inadequacies of the analysis when applied solely to the poloidal field. At small  $k$ , the standard deviations of the quantities (dashed lines) are considerable. The standard deviation on  $D_{\text{mag}}$  when  $B_y \neq 0$  is significantly larger than when one sets  $B_y = 0$ . This reflects the large variability of  $\langle B_y^2/2 \rangle$  compared to the other components of magnetic energy (see e.g., Fig. 3.2). At any given time,  $D_{\text{mag}}$  can be positive; the assumption of time-stationarity does not hold at any point in time. But when the data are time-averaged,  $D_{\text{mag}} < 0$ .

Finally, we compare the numerical magnetic Reynolds number calculated with equation (3.39) but with the  $B_y = 0$  and  $k_y = 0$  assumptions. For SZ128, we find that  $Rm_{\text{eff}} \sim 11000$ , and for SZ64,  $Rm_{\text{eff}} \sim 3500$ . Fromang & Papaloizou (2007) find  $Rm_{\text{eff}} \sim 30000$  for their  $N_x = 128$  run, and  $Rm_{\text{eff}} \sim 10000$  for their  $N_x = 64$  run; both of their calculated effective Reynolds numbers are larger than those calculated for Athena. This result seems to suggest that ZEUS is actually less dissipative than Athena. However, there are several points to consider. First, numerical dissipation is a nonlinear function of resolution, sharply increasing as the number of zones per wavelength decreases (high wavenumbers). The effective Reynolds number is obtained by measuring dissipation at the high  $k$  end of the spectrum. As reported by Shen et al. (2006) Athena appears to have higher dissipation than ZEUS for poorly resolved waves, as evidenced by the ability of Athena to avoid the aliasing errors seen with ZEUS for hydrodynamic shearing box waves. They further point out that for wavelengths larger than 16 grid points Athena is less dissipative. Further, 2D simulations of decaying turbulence have demonstrated that when saturation amplitude is reached, the decay time is longer in Athena than in ZEUS, consistent with Athena

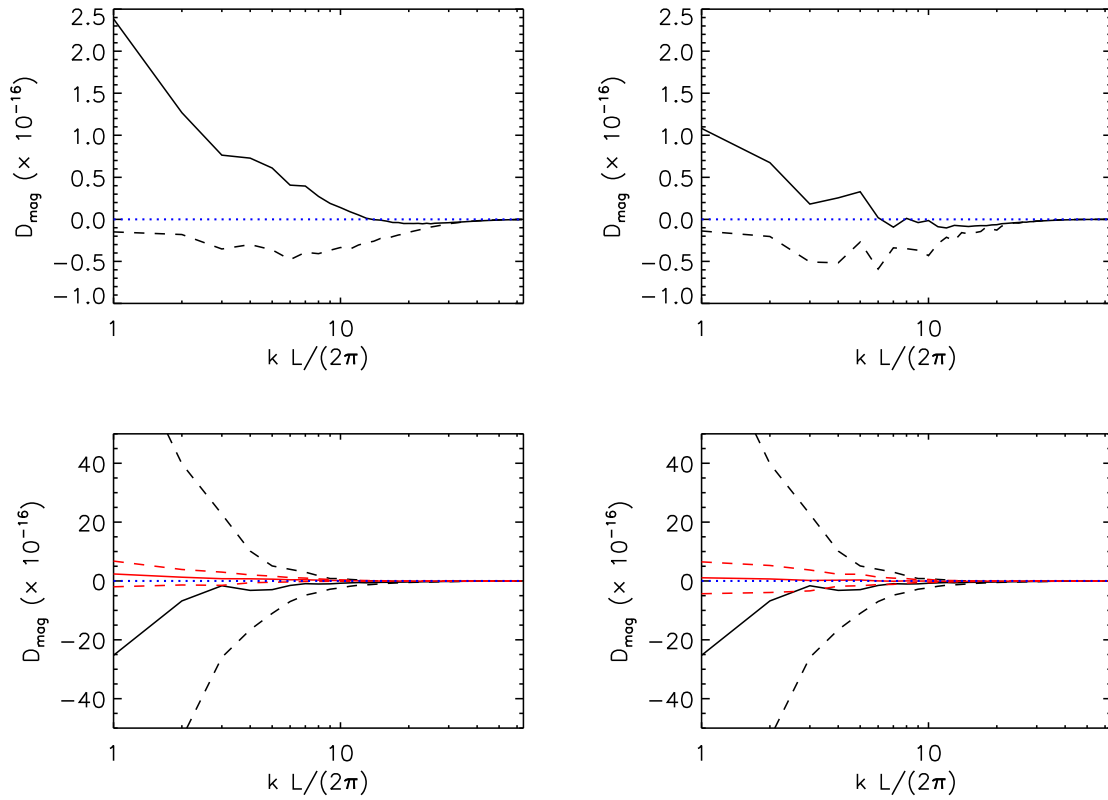


Fig. 3.15.— Magnetic dissipation rate from the SZ128 simulation for three versions of the transfer function analysis. The upper left plot and the red lines in the lower left plot correspond to the analysis in which  $B_y = 0$  was assumed. The upper right plot and the red lines in the lower right plot correspond to the analysis in which both  $B_y = 0$  and  $k_y = 0$  were assumed. The black lines in the lower plots result from relaxing both of these assumptions. The solid lines in the upper plots correspond to  $D_{\text{mag}}$  whereas the dashed lines correspond to  $\eta T_\eta$  with  $\eta = 10^{-7}$  chosen to provide a reasonable match to  $D_{\text{mag}}$  at large  $k$ . The dashed lines in the lower plots correspond to one standard deviation above and below the quantity represented by the solid line of the same color. A horizontal line at zero is shown in all plots as the blue dotted line. Note the difference in  $y$ -axis scale between the upper and lower plots.

having a higher effective resolution (Stone & Gardiner 2005). In the present context, we find that the time- and volume-averaged total stresses in our simulations are larger than those calculated in the simulations of Fromang & Papaloizou (2007). Stronger turbulence leads to larger kinetic and magnetic turbulent fluctuations, which in turn enhances dissipation via grid-scale effects. Finally, we reemphasize that assuming  $B_y = 0$  may have a significant impact on the measurement of effective magnetic dissipation via this analysis.

### 3.5.2 Net Vertical Magnetic Flux

#### Fiducial Run

We perform the same transfer function analysis on the fiducial net magnetic flux run, NZ128. The various transfer function terms as a function of  $k$  are shown in Figs. 3.16–3.17. As was the case in the zero net flux simulation,  $S$  is positive at all scales and dominates at small  $k$ ;  $A$  is relatively small throughout.  $T_{bv}$  and  $T_{bb}$  are negative at large scales and positive at small scales, with  $T_{bb} > 0$  for  $kL/(2\pi) \gtrsim 5$ , and  $T_{bv} > 0$  for  $kL/(2\pi) \gtrsim 20$ . At small scales,  $T_{bb} > T_{bv} > S > 0$ . Of the kinetic terms,  $T_{vv}$  and  $T_{vb}$  dominate with  $T_{vb} > T_{vv} > 0$ . These results are in general agreement with SZ128, except that the magnitude of the various terms is larger for NZ128 than for SZ128, and  $T_{bb}$  and  $T_{bv}$  become positive at smaller  $k$  values compared to SZ128.

As before, we calculate the kinetic and magnetic dissipation as well as effective values for the viscosity and resistivity. Figure 3.18 shows these quantities for NZ128 at the smallest scales. As was the case for SZ128, the mean magnetic dissipation dominates over kinetic dissipation by a factor of roughly three at these scales. Note, however, the large error bars associated with these plots, which encompass values of  $D_{\text{kin}}/D_{\text{mag}} > 1$ . Again, the error bars are the temporal standard deviation of the

transfer functions. Since NZ128 has a larger temporal variability, larger error bars are expected. The mean value for  $D_{\text{kin}}/D_{\text{mag}}$  is on the order of 0.6-0.7, which is consistent with the analysis in § 3.4.1 in which we found  $Q_k/Q_m \sim 0.6$ .

The effective viscosity and resistivity show the same basic result as in the SZ128 case.  $\nu_{\text{eff}}$ ,  $\eta_{\text{eff}}$ , and  $P_{m,\text{eff}}$  change by a factor of order unity at large  $k$ . The effective Reynolds numbers are on the order of  $Re_{\text{eff}} \sim 4000$ , and  $Rm_{\text{eff}} \sim 8000$  at large  $k$ .  $P_{m,\text{eff}}$  has a mean value of  $\sim 1.9$ . Again, there is considerable uncertainty in these values due to the large amplitude fluctuations in the turbulence. The error bars encompass values of  $P_{m,\text{eff}}$  less than unity. As a result, it is more difficult to conclusively say that the dissipation behaves the same way in NZ128 as in SZ128. However, in an average sense, the two simulations agree well qualitatively.

### Resolution Effects

We can again look at the effect of resolution on these various dissipation quantities. Figure 3.19 shows this effect for the net flux simulations (NZ16, NZ32, NZ64, and NZ128). The procedure by which to average over  $k$  is the same as described in § 3.5.1. The displayed error bars are the propagation of the errors from the temporal statistics. At these large values of  $k$ ,  $\nu_{\text{eff}}$ ,  $\eta_{\text{eff}}$ ,  $P_{m,\text{eff}}$ , and  $D_{\text{kin}}/D_{\text{mag}}$  are relatively flat, varying by a factor of at most 2.

The numerical viscosity and resistivity decrease as a function of resolution. The dashed lines in the two upper panels of the figure show the line  $\nu_{\text{eff}}, \eta_{\text{eff}} \propto N_x^{-2}$ . The viscosity and resistivity decrease slower than this with increasing  $N_x$ ; we measured  $\nu_{\text{eff}}, \eta_{\text{eff}} \propto N_x^{-1.3}$ . The figure shows that the effective Prandtl number is constant with resolution to within the error bars. There appears to be a slight increase in  $D_{\text{kin}}/D_{\text{mag}}$  with resolution, but this trend is not definitive given the large uncertainties on the

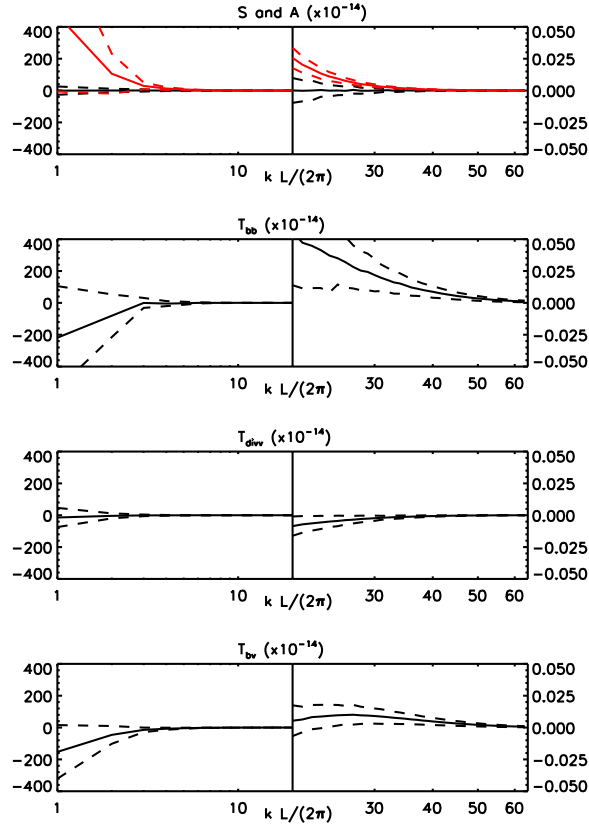


Fig. 3.16.— Magnetic Fourier transfer functions versus a dimensionless wave number ( $L$  is the length of the smallest dimension in the box) for NZ128. Each plot is displayed in two components; the left part shows the data for  $1 < kL/(2\pi) < 20$ , and the right part shows the data for  $20 < kL/(2\pi) < 64$  by changing the  $x$  and  $y$  axis scaling. In all plots, the solid line is the average value for the transfer function. This average was obtained over 161 frames in the saturated state and shells of constant  $|\mathbf{k}|$ . The upper (lower) dashed line that matches color with the solid line correspond to the transfer function plus (minus) one temporal standard deviation. From top to bottom, the plots show  $S$  (red) and  $A$  (black),  $T_{bb}$ ,  $T_{divv}$ , and  $T_{bv}$ .

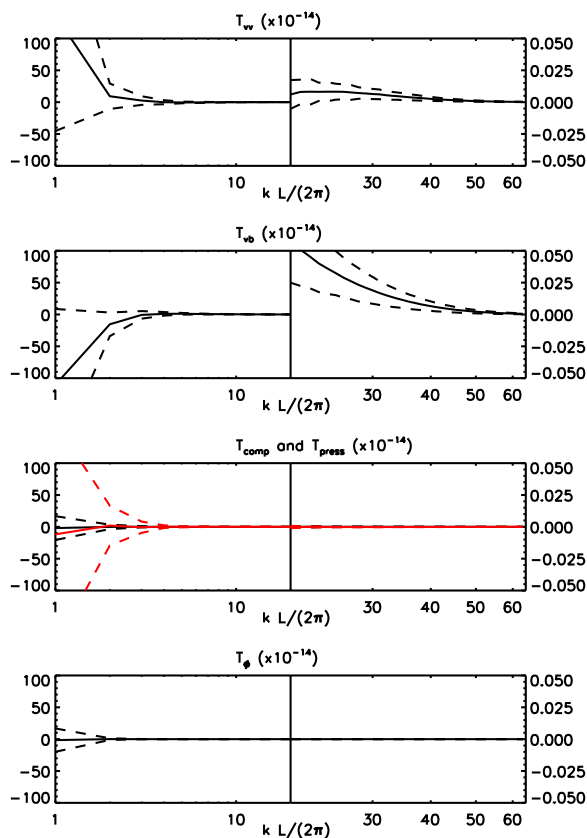


Fig. 3.17.— Kinetic Fourier transfer functions versus a dimensionless wave number ( $L$  is the length of the smallest dimension in the box) for NZ128. Each plot is displayed in two components; the left part shows the data for  $1 < kL/(2\pi) < 20$ , and the right part shows the data for  $20 < kL/(2\pi) < 64$  by changing the  $x$  and  $y$  axis scaling. In all plots, the solid line is the average value for the transfer function. This average was obtained over 161 frames in the saturated state and shells of constant  $|\mathbf{k}|$ . The upper (lower) dashed line that matches color with the solid line correspond to the transfer function plus (minus) one temporal standard deviation. From top to bottom, the plots show  $T_{vv}$ ,  $T_{vb}$ ,  $T_{\text{press}}$  (red) and  $T_{\text{comp}}$  (black), and  $T_{\phi}$ .

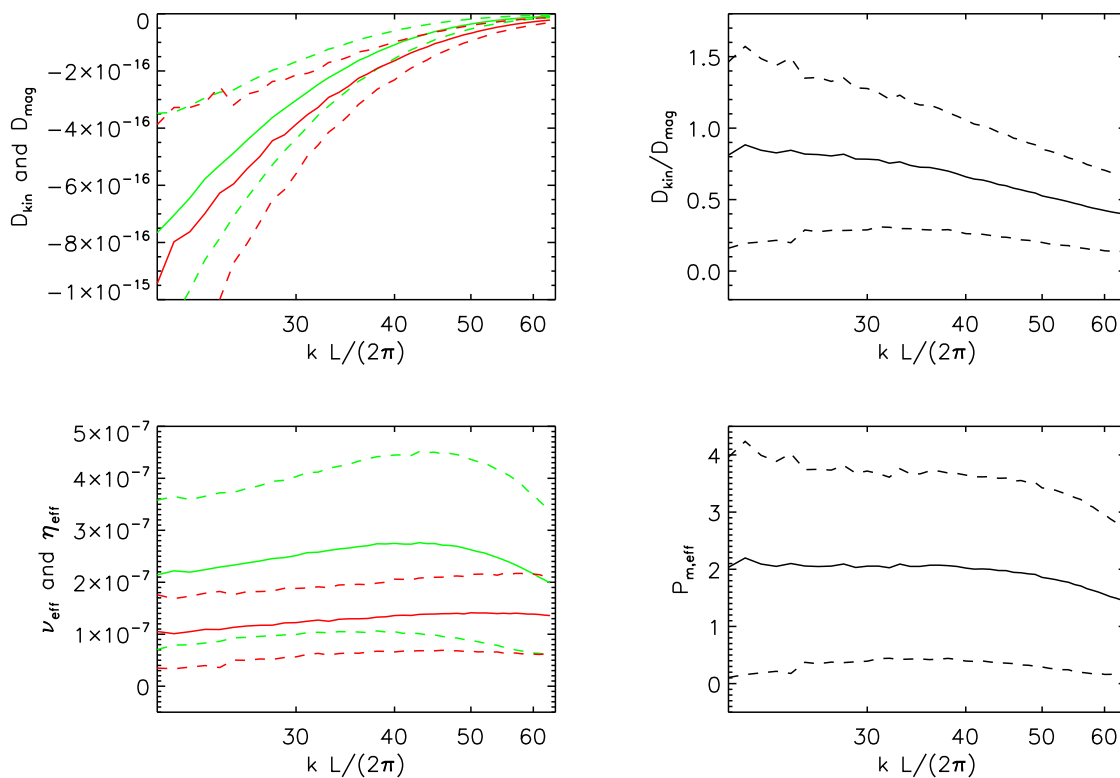


Fig. 3.18.— Numerical dissipation quantities plotted against a dimensionless wave number ( $L$  is the length of the smallest dimension in the box). These plots correspond to data from NZ128. The upper left plot shows the dissipation rate of kinetic energy (green) and magnetic energy (red) in Fourier space. The upper right plot shows the ratio of these two dissipation rates. The lower left plot shows the effective numerical viscosity (green) and resistivity (red). The lower right plot shows the ratio of the viscosity to resistivity (i.e., the effective Prandtl number). In all plots, the solid line is the average value for the quantity of interest. For  $D_{\text{kin}}$  and  $D_{\text{mag}}$ , this average was obtained from averaging over shells of constant  $|\mathbf{k}|$  and over 161 frames in the saturated state. The averaged viscosity and resistivity values were calculated as described in the text. The upper and lower dashed lines correspond to the error propagated from one temporal standard deviation.

data.

One might expect  $\nu_{\text{eff}}$  and  $\eta_{\text{eff}}$  to decrease with increasing resolution since these terms arise from truncation error. Linear wave advection test problems with Athena have shown that the truncation error converges at second order (e.g., Stone et al. 2008). On this basis, one would expect  $\nu_{\text{eff}}, \eta_{\text{eff}} \propto N_x^{-2}$ . We find a shallower decrease with  $N_x$ , but MRI turbulence is a fully nonlinear system and one in which the saturation level appears to be controlled (at least partially) by the dissipation scale. Thus, one should not necessarily expect the same convergence behavior as in a linear system with an analytic solution that is independent of the dissipation scale.

### 3.6 Summary and Discussion

We have carried out a series of local, unstratified shearing box simulations with the Athena code to study the characteristics of MRI driven turbulence. Athena uses a second-order, conservative, compressive MHD algorithm, which is significantly different from the algorithms employed in many of the previous MRI studies. In our work, we have run several standard models for comparison with previous work, and characterized the numerical dissipation of the Athena code for the shearing box problem. Furthermore, we have exploited the energy conservation property of Athena to carry out a study of energy flow within MRI-driven turbulence.

To compare with previous numerical results, we have investigated the effects of different initial field geometries (uniform or sinusoidal  $B_z$ ), varying domain aspect ratio, and numerical resolution. In all of our simulations, the MRI is initiated and sustained over many orbits. The time- and volume-averaged properties of the resulting turbulent flow, such as stress levels and magnetic and kinetic energies, are consistent with previous results. As in previous work, we find that boxes containing net vertical

field saturate at higher amplitudes compared to those without net fields. The total stress is proportional to the magnetic pressure with a constant of proportionality  $\sim 0.5$ , but is independent of the gas pressure. In the net field simulation, the gas pressure increases by a factor of 100, due to thermalization of the turbulence, without affecting the stress. The consistency of these results with past work indicate that these properties do not result from details of the employed algorithm.

Fourier analysis of the turbulence shows that the largest scales in the box dominate the energetics. In the presence of a net field, the amplitude of the spatial power spectra is largely independent of resolution on the largest scales. This is not true for the zero net flux simulations however. For those simulations, the amplitude decreases as resolution increases, which is consistent with the overall resolution behavior. For net field simulations, the averaged turbulent magnetic and kinetic energies increase slightly with resolution, whereas for the zero net field simulations, the energies decrease with increasing resolution roughly in proportion to the grid zone size. This apparent lack of convergence for the zero net field shearing box simulations was previously demonstrated by Fromang & Papaloizou (2007) using the ZEUS code.

The net field simulation shows intermittent channel flows which cause temporary increases in stress through amplification of large-scale MRI modes. The parasitic modes described by Goodman & Xu (1994) destroy the channel flow within about one orbit of time, but the rapid increase in stress produces a subsequent increase in thermal energy. The presence of these discrete channel flow events is a consequence of the box size—larger boxes do not experience them—but we use their presence to study the subsequent energy flow following a rapid increase in stress.

Because Athena evolves the total energy equation, magnetic and kinetic energy losses due to numerical grid-scale effects are added to the internal energy. This makes

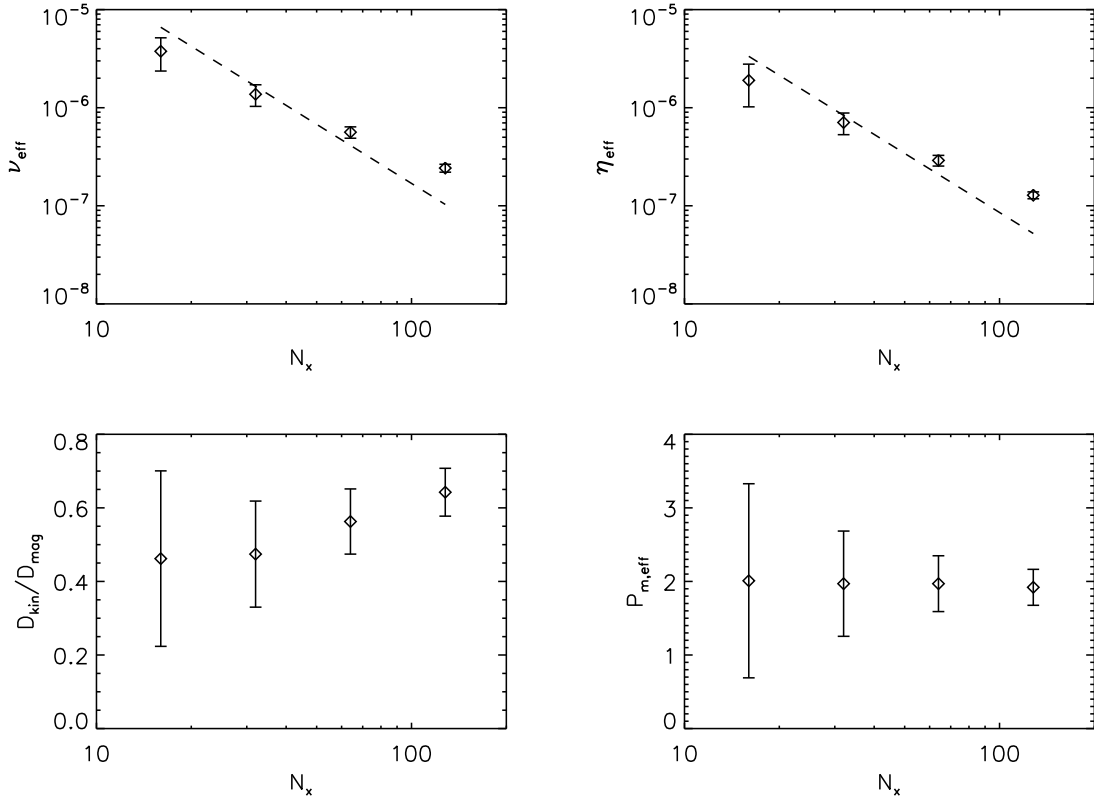


Fig. 3.19.— Averaged dissipation related quantities as a function of grid resolution. These plots correspond to data from the net flux simulations, NZ16, NZ32, NZ64, and NZ128. The upper left plot shows the effective viscosity versus  $x$  resolution. The dashed line shows  $\nu_{\text{eff}} \propto N_x^{-2}$ . The upper right plot shows the effective resistivity versus  $x$  resolution. Again, the dashed line shows  $\eta_{\text{eff}} \propto N_x^{-2}$ . The lower left plot shows the ratio of kinetic to magnetic dissipation versus  $x$  resolution. The lower right plot shows the effective Prandtl number versus  $x$  resolution. For each resolution, the data point was obtained from averaging the quantity as a function of  $k$  over values of  $k$  where the error in this quantity is not much larger than the mean value. The error bars represent the propagated errors from the temporal statistics.

Athena well suited to examining the turbulent energy flow and subsequent dissipation. The recurring channel flows in the net flux model provide a sudden injection of energy into the box by increasing the stress operating on the shearing boundaries of the box. The injected energy appears as heat after  $\sim 0.2$  orbits. This corresponds to a timescale  $\Omega^{-1}$ , which equals  $L_z/c_s$  where  $c_s$  is the initial soundspeed. This timescale determines the amplitude of the Alfvén speed,  $v_A$ , and its fundamental MRI wavelength,  $\lambda_{\text{MRI}}$ ;  $L_z/c_s \sim \lambda_{\text{MRI}}/v_A$ . The timescale is thus on the order of the eddy turnover time, indicating that dissipational heating is a local process and that energy is not carried over large distances before it is thermalized.

In the fiducial zero net magnetic flux simulation, SZ128, there are no recurring channel modes, making it more difficult to trace the flow of injected energy. The analysis is further complicated by the presence of compressive waves that dominate the time derivative of the thermal energy,  $\dot{T}$ . These waves are also present in the net field simulations, but their amplitude is smaller relative to the larger turbulent kinetic energy found with a net field. A detailed examination of the components of the internal energy equation indicate that the compressive waves do not appear to contribute significantly to irreversible heating. By averaging  $\dot{T}$  for the zero net flux simulation, we find a correlation of  $\dot{T}$  with  $E_{\text{in}}$  on the same timescale of  $\sim 0.2$  orbits.

In the net field simulation, the dissipation of magnetic energy is larger than that for the kinetic energy, not unexpected as the ratio of the average magnetic to perturbed kinetic energy is  $\sim 3.4$ . But the ratio of the magnetic to kinetic dissipation rate is roughly constant at  $\sim 1.7$ . The fact that the ratio of dissipation rates does not equal the ratio of energies may result from a couple of possibilities. First, there could be a net transfer of magnetic to *perturbed* kinetic energy as was suggested in Brandenburg et al. (1995).<sup>5</sup> Second, the difference in the ratios could arise from

---

<sup>5</sup>§ 3.4.1 shows that there is in fact a net transfer of kinetic to magnetic energy. However, this

the effective Prandtl number being larger than one. In particular, if  $Q_k \propto \nu_{\text{eff}} \delta v^2 / 2$  and  $Q_m \propto \eta_{\text{eff}} B^2 / 2$ , then  $(B^2 / \delta v^2)(Q_k / Q_m) \sim P_{m,\text{eff}}$ . With the above values for the energy and dissipation ratios, we find  $(B^2 / \delta v^2)(Q_k / Q_m) \sim 2$ , which is consistent with the determination of  $P_{m,\text{eff}}$  from the Fourier analysis (see discussion below). The agreement between the two separate calculations of  $P_{m,\text{eff}}$  may be coincidental, but it is suggestive of  $Q_k \propto \nu_{\text{eff}} \delta v^2 / 2$  and  $Q_m \propto \eta_{\text{eff}} B^2 / 2$ .

The turbulence is sustained by the continued action of the MRI in extracting energy from the differential rotation. This can be removed from the simulations allowing us to study the decay of the turbulence in detail (simulations NZD128 and SZD128). Figure 3.10 shows that magnetic losses dominate over kinetic losses during this decay. In both simulations nearly 50% of the magnetic energy and 20% of the kinetic energy has been dissipated after 0.2 orbits. By one orbit into the decay, most of the magnetic and kinetic energy has been lost. Although these decay timescales arise in a turbulent flow that lacks power input from the MRI, the results are consistent with the conclusion that turbulent energy dissipation occurs on a rapid timescale of order  $\Omega^{-1}$ .

Fromang & Papaloizou (2007) used a detailed Fourier analysis (§ 3.5) to study magnetic energy flow and thermalization as a function of length scale in the shearing box. In this analysis, the individual terms in the evolution equation for the magnetic energy are examined in Fourier space. Averaging over time and assuming that the magnetic energy is in a statistical steady state, one sets the sum of these terms equal to a remainder, which is credited to numerical effects. These numerical losses can then be modeled as an effective resistivity (and viscosity for the kinetic energy), allowing one to characterize the numerical dissipation in the simulation.

---

kinetic energy includes the shear flow, and thus, this result tells us nothing of the energy transfer between magnetic and *perturbed* kinetic energy.

We repeated their analysis with Athena and extended it to the kinetic energy. The dominant effect at large scales is the generation of magnetic field by the background shear. This energy is transferred to other scales by the turbulence. Net positive field creation by the turbulent flow and energy gains by the transfer between scales only happens at small wavelengths. This point of transition from loss to gain happens at smaller scales for the zero net field simulation compared to the net field model. Magnetic dissipation dominates over kinetic dissipation at small scales (i.e.,  $kL/(2\pi) \gtrsim 20$ ). Modeling these as an effective resistivity  $\eta$  and viscosity  $\nu$  shows that  $\eta$  and  $\nu$  drop with increasing resolution with a power that lies between first- and second-order in grid resolution. The effective Prandtl number, on the other hand, is nearly constant as a function of resolution with a value between  $\sim 1.5$  and  $2$ .

Fromang & Papaloizou (2007) observed what they described as “negative” resistivity in an analysis restricted to the poloidal field alone. In repeating their exact analysis with Athena, we also observed such an “anti-dissipation” at large scales. This indicates that this effect is not associated with a numerical algorithm limitation associated with ZEUS. More likely, it arises from the statistical uncertainty at large scales and from the failure of the assumptions that go into the definition of the dissipation term. We note that the inclusion of the toroidal field  $B_y$  in the analysis shows net dissipation at all scales, although again the statistical variation is large at large scales.

In conclusion, what do these results imply for shearing box simulations and the MRI? First, as observed by Fromang & Papaloizou (2007), the scales over which turbulent energy generation occurs are not well-separated from those where there is significant dissipation; the MRI operates over a wide range of scales. The MRI grows at a rate  $\sim kv_A$  for all  $k$  less than  $\Omega/v_A$ . At large scales, a weak field will grow more

slowly than the timescale over which energy is transferred between scales, between magnetic and kinetic forms, and ultimately thermalized. If a field is chopped up by reconnection, it may be reduced to small scales where the MRI no longer operates. In the presence of a net field, there will always be a significant driving term at the scales set by that imposed field. In the absence of such a field, however, the outcome will be determined by the complex interplay of loss due to dissipation and amplification by the MRI. In the numerical simulations with zero net field, increasing the resolution causes an overall decrease in the saturation energies. Fromang & Papaloizou (2007) attribute this to higher resolution enabling the MRI to operate at intermediate scales which facilitates the transfer of energy to small scales and promotes reconnection and dissipation. What is perhaps surprising is that resolving the MRI at these scales leads to greater field dissipation than would otherwise be accomplished by the numerical losses that would occur if those scales were underresolved. Because the same effect is observed with both Athena and ZEUS, it seems likely that this ability of the MRI to transfer energy away from the largest scales in the shearing box and to increase the total dissipation is a physical rather than numerical effect.

In related work, Fromang et al. (2007) and Lesur & Longaretti (2007) studied the effect of varying the physical (not numerical) magnetic Prandtl number,  $P_m$ , on the turbulence. They found that the saturation amplitudes were increased with increased  $P_m$ . Fromang et al. (2007) found evidence that there exists a critical  $P_m > 1$  below which zero net field simulations would die out rather than achieve a steady turbulent state. Our results in this investigation show that this Prandtl number dependence is a distinct effect from the observed dependence of the turbulence on resolution. We find the numerical  $P_m$  to be largely independent of resolution in Athena. Taken together, however, the dependence on physical  $P_m$  and the dependence on resolution point to

the importance of small and intermediate scale magnetic dissipation and reconnection to establishing saturation amplitudes in MRI-driven turbulence.

As discussed by Fromang & Papaloizou (2007), numerical dissipation can deviate significantly from physical dissipation. In § 3.5.1, we showed that  $\eta_{\text{eff}}$  and  $\nu_{\text{eff}}$  are relatively flat at small scales, suggesting a resemblance to physical dissipation. However, consider the numerical Reynolds number as calculated from equation (3.38) for our zero net flux simulations. For  $N_x = 128$ , we found  $Re_{\text{eff}} \sim 12000$ , and  $P_{m,\text{eff}} \sim 1.6$  for all of zero net flux simulations. From the parameter space studies of Fromang et al. (2007), these values for the Reynolds and Prandtl numbers correspond to marginal MRI turbulence; that is, they lie very close to the critical line between sustained and decaying turbulence. For  $N_x = 64$ ,  $Re_{\text{eff}} \sim 4100$ , and the Reynolds number is even smaller for the lower resolutions. These values are well within the decaying turbulence regime, but we find active MRI turbulence in all of our simulations. These results show that the effective Reynolds and Prandtl numbers of Athena as measured at large wavenumbers does not apply at smaller  $k$  values where there are many grid zones per wavelength. Thus, the Reynolds numbers and Prandtl numbers that we calculate should be taken as a measure of the effective numerical dissipation of the code and not equated to a flow with the same Reynolds and Prandtl number as determined by a simple physical resistivity and viscosity.

This result highlights an uncertainty associated with any MRI simulation that depends only on numerical rather than physical dissipation. It is apparent that the numerical Prandtl number can play an important role in determining the ratio of magnetic to kinetic dissipation. More speculatively, the Prandtl number may also play a role in the timescale over which thermalization occurs. In the present study, we found that both the thermalization timescale and the effective numerical Prandtl

number were largely independent of resolution. However, the turbulent energy thermalization timescales and properties we measure may be subject to change when explicit dissipation is included. It will be a very important next step in this work to include physical dissipation and verify these results.

This work is only the first step in applying Athena to the problem of the energetics of MRI turbulence. The present study provides a calibration of the numerical dissipation, which will be important in future studies that include explicit resistivity and viscosity. Furthermore, the unstratified shearing box has the virtue of simplicity and allows a detailed study of MRI turbulence without too many confounding factors, but it also may prove too limited for predictive application to accretion flows. The inclusion of vertical stratification and radiative cooling are both straightforward extensions to the present study. The detailed diagnostics developed and applied in this study should prove valuable in this planned work.

## Chapter 4

# Prandtl Number Effects on Unstratified Disks

Resistivity and viscosity play a significant role in establishing the energy levels in turbulence driven by the MRI in local astrophysical disk models. This study uses the Athena code to characterize the effects of a constant shear viscosity  $\nu$  and Ohmic resistivity  $\eta$  in unstratified shearing box simulations with a net toroidal magnetic flux. A previous study of shearing boxes with zero net magnetic field performed with the ZEUS code found that turbulence dies out for values of the magnetic Prandtl number,  $P_m = \nu/\eta$ , below  $P_m \sim 1$ ; for  $P_m \gtrsim 1$ , time- and volume-averaged stress levels increase with  $P_m$ . We repeat these experiments with Athena and obtain consistent results. Next, the influence of viscosity and resistivity on the toroidal field MRI is investigated both for linear growth and for fully-developed turbulence. In the linear regime, a sufficiently large  $\nu$  or  $\eta$  can prevent MRI growth;  $P_m$  itself has little direct influence on growth from linear perturbations. By applying a range of values for  $\nu$  and  $\eta$  to an initial state consisting of fully developed turbulence in the presence of a background toroidal field, we investigate their effects in the fully nonlinear system.

Here, increased viscosity enhances the turbulence, and the turbulence decays only if the resistivity is above a critical value; turbulence can be sustained even when  $P_m < 1$ , in contrast to the zero net field model. While we find preliminary evidence that the stress converges to a small range of values when  $\nu$  and  $\eta$  become small enough, the influence of dissipation terms on MRI-driven turbulence for relatively large  $\eta$  and  $\nu$  is significant, independent of field geometry.<sup>1</sup>

## 4.1 Introduction

Recently, the work of Fromang et al. (2007) and Lesur & Longaretti (2007) has sparked new interest in the effects of non-ideal MHD on the MRI. Fromang et al. (2007) showed that both resistivity and viscosity are important in determining the stress level in MRI turbulent flows with zero net magnetic field. Lesur & Longaretti (2007) came to the same conclusion for models with a net vertical field. The results were characterized in terms of the magnetic Prandtl number, defined as  $P_m = \nu/\eta$ . In these simulations, the saturation level increases with increasing  $P_m$ . Fromang et al. (2007) also find that for the zero net field case, there exists a  $P_m$  below which the turbulence dies out, and that this critical  $P_m$  decreases with decreasing viscosity (at least for the range in viscosity and resistivity examined in the paper).

One magnetic field geometry that has not yet been explored with both physical resistivity and viscosity is that of a net toroidal field. Such fields could be the most relevant to astrophysical disks. Following the arguments of Guan et al. (2009) and references therein, both global and local disk simulations as well as observations of disk galaxies show a dominance of toroidal field over other field components. Indeed,

---

<sup>1</sup>This work was published in *The Astrophysical Journal*, Vol. 707, p. 833, 2009; see Simon & Hawley (2009)

the background shear flow naturally creates toroidal field from radial field. It seems likely that any given region of an accretion disk will contain some net azimuthal field.

In this chapter, we perform the first investigation of the toroidal field MRI in the presence of *both* viscosity and resistivity and compare the results with those obtained for zero net and net vertical field simulations. The structure of the chapter is as follows. In § 4.2, we describe our algorithm, parameters, and tests of our viscosity and resistivity implementation. For comparison purposes, we reexamine the simulations of Fromang et al. (2007) with our code in § 4.3. Our main results, focusing on the toroidal field simulations, are presented in § 4.4. We wrap up with our discussion and conclusions in § 4.5.

## 4.2 Numerical Simulations

In the simulations presented here, the  $x$  boundary conditions are the standard shearing periodic boundaries, as described in Chapter 2 with the flux reconstruction approach applied to the  $y$  EMFs at the  $x$  boundaries (to conserve net vertical magnetic flux) and the density flux at the  $x$  boundaries (to conserve mass). This flux reconstruction step is not applied to the EMFs responsible for the evolution of the net toroidal field. Consequently, in the simulations initialized with a net toroidal field, the resulting truncation error produces a loss of net  $B_y$  flux from the domain;  $\sim 5$ - $10$  % of the initial toroidal field is lost per 100 orbits for the high resolution, sustained turbulence simulations. This corresponds to a background  $\beta$  value of  $\sim 110$ - $120$  at 100 orbits. While this truncation error does not appear to have any significant affect on the turbulent energy levels in our simulations, it may become important to conserve  $B_y$  to roundoff level for longer evolution times.

The shearing box source terms are included in the algorithm in a directionally

unsplit manner, consistent with the CTU algorithm. We do not use the Crank-Nicholson method of Gardiner & Stone (2005a) that ensures precise conservation of epicyclic energy. As in Chapter 3, we have found this added complexity to be unnecessary for simulations dominated by the MRI.

The Riemann solver used in all of these simulations is the linearized Roe solver of Roe (1981), which has been extended to MHD (see Cargo & Gallice 1997).

Both the viscosity and resistivity are added via operator splitting; the fluid variables updated from the CTU integrator are used to calculate the viscous and resistive terms. In these simulations, the viscosity term is calculated in a slightly different (and simpler) form than in equations (1.6) and (1.8). The modified momentum equation for these calculations is

$$\frac{\partial \rho \mathbf{v}}{\partial t} + \nabla \cdot (\rho \mathbf{v} \mathbf{v} - \mathbf{B} \mathbf{B}) + \nabla \left( P + \frac{1}{2} B^2 \right) = 2q\rho\Omega^2 \mathbf{x} - 2\mathbf{\Omega} \times \rho \mathbf{v} + \nabla \cdot (\rho \nu \nabla \mathbf{v}) + \nabla \left( \frac{1}{3} \rho \nu \nabla \cdot \mathbf{v} \right), \quad (4.1)$$

These two different methods are equivalent when  $\rho\nu$  is spatially constant, which is generally a good assumption. In particular, we have performed a few shearing box experiments with both implementations, and find no significant differences in turbulent stress evolution. Specifically, we restarted a few simulations using the form in equation (1.8), and we found that the volume-averaged magnetic energies are initially indistinguishable between the two approaches. Due to the chaotic nature of the MRI, the two curves eventually diverge, but nevertheless maintain the same time average.

The viscous and resistive terms are discretized in a flux-conservative manner consistent with the Athena algorithm. In particular, the third and fourth terms on the right-hand side of equation (4.1) are written so that  $\rho\nu\nabla\mathbf{v}$  and  $(1/3)\rho\nu\nabla\cdot\mathbf{v}$  are defined

as fluxes at the cell faces. Taking the divergence of the third term and the gradient of the fourth term via finite-differencing ensures that momentum conservation is not violated by the viscous terms. The resistive contribution to the induction equation is added in a manner consistent with the EMFs; the term  $\eta \nabla \times \mathbf{B}$  is computed at cell corners to ensure that when differenced via the curl operator,  $\nabla \cdot \mathbf{B} = 0$  is maintained. Note that this resistive contribution to the EMF must also be reconstructed at the shearing-periodic boundaries in order to preserve  $B_z$  precisely.

The addition of viscosity and resistivity places an additional constraint on the time step,

$$\Delta t = C_o \text{MIN} \left( \Delta t_{\text{CTU}}, 0.75 \frac{\Delta^2}{8/3\nu}, 0.75 \frac{\Delta^2}{2\eta} \right), \quad (4.2)$$

where  $C_o$  is the CFL number ( $C_o = 0.4$  here),  $\Delta t_{\text{CTU}}$  is the time step limit from the main integration algorithm (see Stone et al. 2008), and  $\Delta$  is the minimum grid spacing,  $\Delta = \text{MIN}(\Delta x, \Delta y, \Delta z)$ . Several three-dimensional tests of viscosity and resistivity revealed that if the viscous or resistive time step is close to  $\Delta t_{\text{CTU}}$ , the evolution becomes numerically unstable. This problem was remedied by multiplying the viscous and resistive time steps by 0.75. The additional 4/3 factor in the denominator of the viscous time step results from the last term on the right-hand side of equation (4.1). This can be most easily understood by considering a one-dimensional problem, in which case the effective  $\nu$  value increases by a factor of 4/3 due to the compressibility term. Therefore, the effective  $\nu$  that goes into the time step calculation is taken as  $(4/3)\nu$ . Note that most of our simulations will have  $\nu$  and  $\eta$  sufficiently small that the viscous and resistive time steps are large compared to  $\Delta t_{\text{CTU}}$ . In fact, only the simulations with the largest values of  $\eta$  and  $\nu$  reach the diffusion limit on  $\Delta t$ .

### 4.2.1 Tests of Physical Dissipation

We performed a number of problems to test the implementation of viscosity and resistivity within Athena. Resistivity was tested by solving the diffusion of a current sheet along one dimension; a uniform magnetic field is initialized with a change in sign across one grid zone. This problem has a simple analytic solution (see e.g., Komissarov 2007). The agreement between the numerical and analytic solution was excellent. By replacing the magnetic field with a uniform velocity flow, the identical test can be performed for the viscosity. Again, the numerical solution agreed with the analytic solution.

Next, we initialized a uniform vertical magnetic field in a shearing box with nonzero viscosity and resistivity and measured the growth of various MRI modes in the linear regime. We compared the measured values with those from analytic linear theory (see e.g., Masada & Sano 2008; Pessah & kwan Chan 2008) and found excellent agreement for a wide range in viscosity and resistivity.

Finally, we examined the propagation of small amplitude, isothermal sound and Alfvén waves in the presence of viscosity and resistivity. Again, the numerical solution can be compared directly to an analytic solution. These tests were done in one, two, and three dimensions; in the multidimensional tests, the propagation direction of the wave was chosen to be along the grid diagonal. The resistivity was tested via the decay of the Alfvén waves, and the viscosity was tested via the decay of the sound waves. The error as a function of  $x$  resolution for two of these tests is given in Fig. 4.1. The error is calculated from the square root of the sum of the squared errors in the density and momenta (for the sound wave) and the density, momenta, and magnetic field (for the Alfvén wave). The solution to each wave converges at a rate very close to second order, shown by the dashed line.

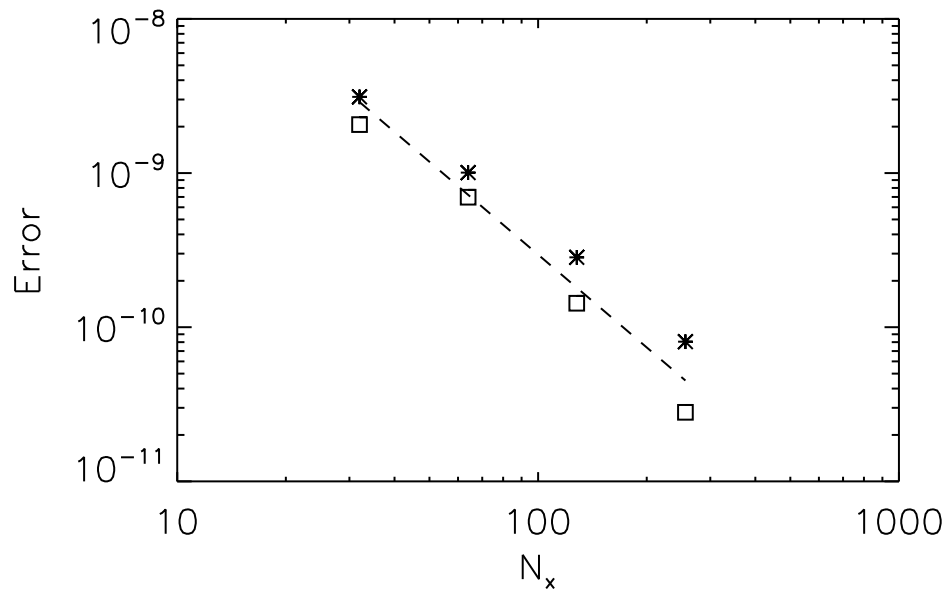


Fig. 4.1.— Numerical error as a function of  $x$  resolution for the three-dimensional decaying linear wave problem. The boxes are the errors for a decaying Alfvén wave, and the asterisks are the errors for a decaying sound wave. The error is calculated from the square root of the sum of the squared errors in the density and momenta (for the sound wave) and the density, momenta, and magnetic field (for the Alfvén wave) obtained using the analytic solution. The dashed line shows the slope corresponding to second-order convergence.

### 4.2.2 Shearing Box Parameters

The shearing box used in this study has radial size  $L_x = 1$ , azimuthal size  $L_y = 4$ , and vertical size  $L_z = 1$ . Most of the simulations presented here use  $128 \times 200 \times 128$  equally spaced grid zones; some simulations use half the number of zones in each direction. The initial velocity is  $\mathbf{v} = -q\Omega x \hat{\mathbf{y}}$ , with  $q = 3/2$ ,  $\Omega = 0.001$ , and  $-L_x/2 \leq x \leq L_x/2$ . The isothermal sound speed is  $c_s = \Omega H$  where  $H$  is the scale height. With  $L_z = H$ , we have  $c_s = L_z \Omega$ , and with  $\rho = 1$ , the initial pressure is  $P = \rho \Omega^2 L_z^2 = 10^{-6}$ .

The dissipation terms  $\nu$  and  $\eta$  are parameterized in terms of the Reynolds number,

$$Re \equiv \frac{c_s H}{\nu}, \quad (4.3)$$

the magnetic Reynolds number,

$$Rm \equiv \frac{c_s H}{\eta}, \quad (4.4)$$

and the magnetic Prandtl number,

$$P_m \equiv \frac{\nu}{\eta} = \frac{Rm}{Re}. \quad (4.5)$$

Since the properties of the MRI are more directly determined by the Alfvén speed rather than the sound speed, another useful dimensionless quantity is the Elsasser number,

$$\Lambda \equiv \frac{v_A^2}{\eta \Omega}, \quad (4.6)$$

where  $v_A$  is the Alfvén speed. With  $c_s = \Omega H$  and  $\beta = 2c_s^2/v_A^2$ , we can relate  $Rm$  to  $\Lambda$ ,

$$\Lambda = \frac{2}{\beta} Rm. \quad (4.7)$$

In addition to the explicit dissipation terms, there will also be some effective diffusion due to numerical effects. Generally speaking, numerical diffusion will not behave in the same manner as physical diffusion (e.g., it is not a simple function of a gradient in field or velocity); numerical diffusion generally has a much stronger effect at small scales than at large scales. Also the effects of numerical diffusion may be different from one type of simulation to another. By calculating numerical losses at high wavenumbers in Fourier space and modeling those as if they were physical viscosity and resistivity, we quantified the numerical dissipation of Athena in Chapter 3. We found that the effective  $Rm$  for the zero net field and net  $z$  field simulations at  $N_x = 128$  were 20000 and 8000 respectively, and 7000 and 5000 for  $N_x = 64$ . The effective  $P_m$  is  $\sim 2$  for these simulations. Since numerical dissipation is problem-dependent, these numbers should be regarded as estimates, and their values will likely be somewhat different in different applications. However, they serve as a guideline for including physical dissipation. In the present study, numerical and physical dissipation may be comparable at large wavenumbers for  $Re, Rm \gtrsim 10000$ . The physical dissipation in some of our simulations may fall into this marginally resolved regime. Nevertheless, we can explore a large enough range in  $Re$  and  $Rm$  values to observe clear effects due to viscosity and resistivity.

### 4.3 Zero Net Flux Simulations

Fromang & Papaloizou (2007) and Pessah et al. (2007) presented the surprising result that for zero net field shearing box simulations without any explicit dissipation

Table 4.1. Zero Net Flux Simulations with Physical Dissipation

| Label       | $Re$ | $P_m$ | $Rm$  | Turbulence? | $\alpha$ |
|-------------|------|-------|-------|-------------|----------|
| SZRe800Pm4  | 800  | 4     | 3200  | No          | -        |
| SZRe800Pm8  | 800  | 8     | 6400  | Yes         | 0.031    |
| SZRe800Pm16 | 800  | 16    | 12800 | Yes         | 0.046    |
| SZRe1600Pm2 | 1600 | 2     | 3200  | No          | -        |
| SZRe1600Pm4 | 1600 | 4     | 6400  | No          | -        |
| SZRe1600Pm8 | 1600 | 8     | 12800 | Yes         | 0.026    |
| SZRe3125Pm1 | 3125 | 1     | 3125  | No          | -        |
| SZRe3125Pm2 | 3125 | 2     | 6250  | No          | -        |
| SZRe3125Pm4 | 3125 | 4     | 12500 | Yes         | 0.013    |

terms, the steady-state turbulent energy decreases with increasing grid resolution. In Chapter 3, we obtained the same result for zero net field simulations without explicit dissipation using the Athena code. These results pointed to the importance of including explicit dissipation terms in such simulations.

Fromang et al. (2007) showed that turbulent activity is strongly influenced by these dissipation terms; the saturated stress increases with increasing  $P_m$ . Here we return to the zero net field problem and include the dissipative terms to compare with the results of Fromang et al. (2007). The simulations are initialized with  $\mathbf{B} = \sqrt{2P/\beta} \sin[(2\pi/L_x)x] \hat{\mathbf{z}}$  where  $\beta = 400$ . These runs are labeled SZ for sinusoidal z-field and have resolution  $N_x = 128$ ,  $N_y = 200$ ,  $N_z = 128$ . The viscosity and resistivity in these simulations are chosen to reproduce the calculations of Fromang et al. (2007). The initial state is perturbed in each grid zone with random fluctuations in  $\rho$  at amplitude  $\delta\rho/\rho = 0.01$ . The SZ simulations are listed in Table 4.1. The column labeled “Turbulence?” states whether or not the turbulence was sustained in a given simulation. The column labeled “ $\alpha$ ” gives the resulting turbulent stress in terms of the dimensionless value  $\alpha \equiv \langle\langle \rho v_x \delta v_y - B_x B_y \rangle\rangle / P_o$ , with  $\delta v_y \equiv v_y + q\Omega x$ .  $P_o$  is the initial gas pressure and the double bracket denotes a time and volume average. The time average is calculated from orbit 20 until the end of the simulation, and as is the case throughout this paper, volume average refers to an average over the entire simulation domain.

The results of these simulations are consistent with those of Fromang et al. (2007). For example, Fromang et al. (2007) lists  $\alpha$  values for a  $Re = 3125$  and  $Rm = 12500$  model run with four different codes, including ZEUS. These values range from  $\alpha = 0.0091$  to  $0.011$ ; we obtain  $0.013$ . The increase in turbulent energy levels with  $P_m$  is demonstrated by a series of simulations with the same  $Rm$  and increasing viscosity.

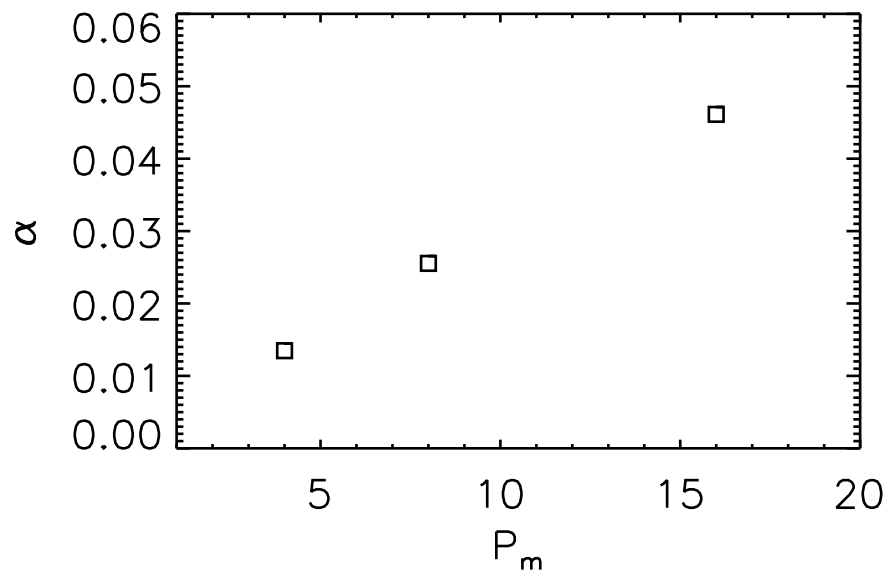


Fig. 4.2.— Time- and volume-averaged stress parameter  $\alpha$  as a function of  $P_m$  in the SZ simulations;  $\alpha \equiv \langle\langle \rho v_x \delta v_y - B_x B_y \rangle\rangle / P_o$ , where the average is calculated over the entire simulation domain and from 20 orbits to the end of the simulation. Only simulations with sustained turbulence are plotted. The  $P_m = 4$  model has  $Rm = 12500$  whereas the other two have  $Rm = 12800$ . There is a nearly linear increase in  $\alpha$  with  $P_m$ .

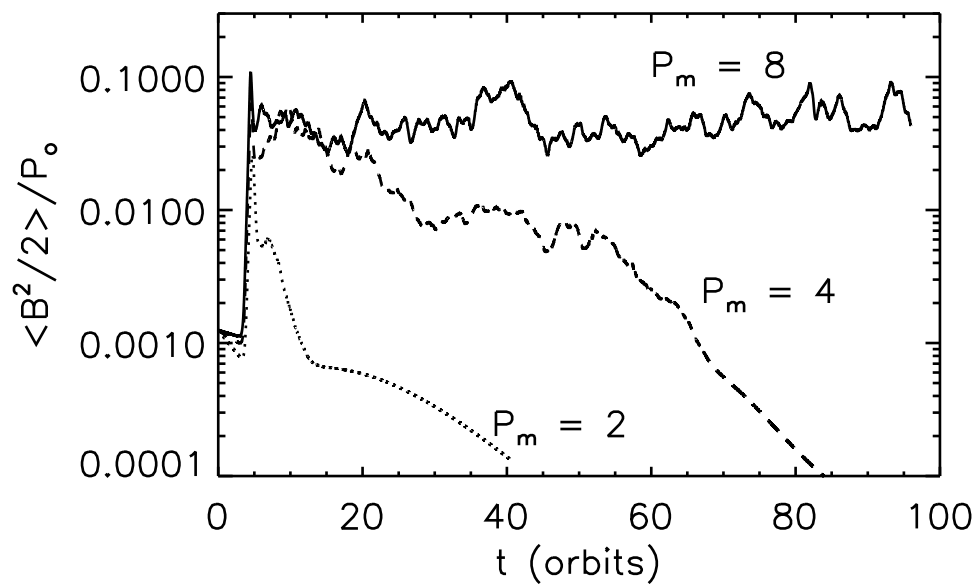


Fig. 4.3.— Time evolution of volume-averaged magnetic energy density normalized by the gas pressure for the SZ runs with  $Re = 1600$  and varying  $P_m$ . The volume average is calculated over the entire simulation domain. The solid line corresponds to  $P_m = 8$ , the dashed line corresponds to  $P_m = 4$ , and the dotted line corresponds to  $P_m = 2$ . The turbulence decays for the lowest two  $P_m$  values, with the  $P_m = 4$  case taking roughly 60 orbits to decay.

For example, for a constant  $Rm \approx 12800$  (some of the simulations had  $Rm = 12800$  while others had  $Rm = 12500$ ; see Fromang et al. (2007)),  $P_m$  values were varied by factors of 2 from 1 to 16. Sustained turbulence was seen for  $P_m \geq 4$  with  $\alpha$  values increasing from 0.0091 for  $P_m = 4$  to 0.019 and 0.044 for  $P_m = 8$  and 16 respectively. The Athena runs have  $\alpha$  values of 0.013, 0.026, and 0.046. These data are plotted in Fig. 4.2, which shows that the increase in  $\alpha$  with  $P_m$  is nearly linear.

The largest differences between the Athena simulations and the ZEUS simulations of Fromang et al. (2007) lie in the marginally turbulent cases. For example, we find decaying turbulence for  $Re = 1600$ ,  $P_m = 4$ , whereas ZEUS produces sustained turbulence for these parameters. Figure 4.3 shows the volume-averaged magnetic energy density normalized by the gas pressure versus time for the three  $P_m$  values at  $Re = 1600$ . The lowest  $P_m$  simulation decays quite rapidly, whereas the  $P_m = 4$  case takes roughly 60 orbits to decay. Differences in the numerical properties of Athena and ZEUS might account for these results, given the sensitivity to numerical factors as shown by zero net field simulations. We also note that we use a slightly larger domain size in  $y$  than in Fromang et al. (2007). The boundary in parameter space between sustained turbulence and decay is unlikely to be hard and fast, and detailed numerical surveys that attempt to define that boundary are probably not warranted. Some such studies may, however, provide additional insights into the sensitivity of the MRI turbulence to specific numerical factors.

## 4.4 Toroidal Field Simulations

To examine the effect of viscosity and resistivity on the MRI with a net toroidal field, we have run a series of simulations initialized with  $\mathbf{B} = \sqrt{2P/\beta}\hat{\mathbf{y}}$ , where  $\beta = 100$ , and with varied  $Re$  and  $Rm$  values.  $Re$  ranges from 100 to 25600, and  $P_m$  ranges

from 0.25 to 16 (though, in some simulations, we set either  $\eta$  or  $\nu$  equal to zero). We will consider the influence of the physical dissipation terms on two types of problems: the linear MRI growth regime, and fully nonlinear turbulence.

#### 4.4.1 The Linear Regime

The linear nonaxisymmetric MRI was first examined by Balbus & Hawley (1992). For nonaxisymmetric modes, the MRI tends to be most robust in the presence of a poloidal field. However, even the purely toroidal field case is unstable, although, as emphasized by Balbus & Hawley (1992), that case is somewhat singular. As always with the ideal MRI, the most unstable mode has  $\mathbf{k} \cdot \mathbf{v}_A \simeq \Omega$ . The linear analysis is complicated by the background shear which causes radial wavenumbers to evolve with time. Amplification of a given mode occurs when the wavenumber ratio  $k/k_z$  goes through a minimum as the radial wavenumber swings from leading to trailing. In general, the purely toroidal MRI favors high  $k_z$  wavenumbers and small values of  $k_y/k_z$ , in contrast to the vertical field MRI where the wavenumber  $k_z$  of the most unstable mode is determined by the Alfvén speed.

Papaloizou & Terquem (1997) examined the toroidal field MRI with the addition of resistivity. They point out that because  $k_x$  grows arbitrarily large, all linear modes will eventually damp out in the presence of resistivity. For small enough resistivities, however, there can be a period of growth when  $k_x \sim 0$ . For the MRI to become self-sustaining, this growth has to continue long enough for the perturbations to reach nonlinear amplitudes. Resistivity is also particularly important for the pure toroidal field MRI because large  $k_z$  is favored for mode growth. Equation (32) of Papaloizou & Terquem (1997) provides an approximate condition for transient amplification of the MRI in the presence of resistivity. For Keplerian shear and for modes where

Table 4.2. Toroidal Field Simulations Initialized from Linear Perturbations

| Label          | $Re$  | $P_m$ | $Rm$   | $\Lambda$ | $N_x = 64$ | $N_x = 128$ |
|----------------|-------|-------|--------|-----------|------------|-------------|
| YLRe800Pm0.5   | 800   | 0.5   | 400    | 8         | No         | -           |
| YLRe800Pm1     | 800   | 1     | 800    | 16        | No         | -           |
| YLRe800Pm2     | 800   | 2     | 1600   | 32        | No         | -           |
| YLRe800Pm4     | 800   | 4     | 3200   | 64        | No         | -           |
| YLRe800Pm8     | 800   | 8     | 6400   | 128       | No         | -           |
| YLRe1600Pm0.5  | 1600  | 0.5   | 800    | 16        | No         | -           |
| YLRe1600Pm1    | 1600  | 1     | 1600   | 32        | No         | -           |
| YLRe1600Pm2    | 1600  | 2     | 3200   | 64        | No         | -           |
| YLRe1600Pm4    | 1600  | 4     | 6400   | 128       | No         | -           |
| YLRe1600Pm8    | 1600  | 8     | 12800  | 256       | No         | -           |
| YLRe3200Pm0.5  | 3200  | 0.5   | 1600   | 32        | No         | No          |
| YLRe3200Pm1    | 3200  | 1     | 3200   | 64        | No         | No          |
| YLRe3200Pm2    | 3200  | 2     | 6400   | 128       | Yes        | No          |
| YLRe3200Pm4    | 3200  | 4     | 12800  | 256       | -          | Yes         |
| YLRe6400Pm0.5  | 6400  | 0.5   | 3200   | 64        | Yes        | No          |
| YLRe6400Pm1    | 6400  | 1     | 6400   | 128       | Yes        | Yes         |
| YLRe6400Pm2    | 6400  | 2     | 12800  | 256       | Yes        | Yes         |
| YLRe6400Pm4    | 6400  | 4     | 25600  | 512       | Yes        | Yes         |
| YLRe12800Pm0.5 | 12800 | 0.5   | 6400   | 128       | Yes        | Yes         |
| YLRe12800Pm1   | 12800 | 1     | 12800  | 256       | Yes        | Yes         |
| YLRe12800Pm2   | 12800 | 2     | 25600  | 512       | Yes        | Yes         |
| YLRe12800Pm4   | 12800 | 4     | 51200  | 1024      | Yes        | Yes         |
| YLRe25600Pm0.5 | 25600 | 0.5   | 12800  | 256       | Yes        | Yes         |
| YLRe25600Pm1   | 25600 | 1     | 25600  | 512       | Yes        | Yes         |
| YLRe25600Pm2   | 25600 | 2     | 51200  | 1024      | Yes        | Yes         |
| YLRe25600Pm4   | 25600 | 4     | 102400 | 2048      | Yes        | Yes         |

$\mathbf{k} \cdot \mathbf{v}_A \sim \Omega$ , this reduces to the condition

$$k_z^2 \eta \sim \Omega. \quad (4.8)$$

In other words, there is no amplification of modes for which the diffusion time is comparable to the orbital frequency. Although viscosity was not included in the analysis, one might expect it to be similarly influential.

Simulations of the linear growth of the MRI in the presence of resistivity for a purely toroidal  $\beta = 100$  initial field were first carried out by Fleming et al. (2000) using a ZEUS code with an adiabatic equation of state. For this field strength, the critical MRI wavelength in the azimuthal direction is  $2\pi v_A/\Omega \approx H$ . They found field decay for a  $Rm = 2000$  simulation, but field growth to turbulent saturation for  $Rm = 5000$  and above.

In this section, we follow the growth of the MRI in a shearing box with a purely toroidal field while including both resistivity and viscosity. The system is seeded within each grid zone with random perturbations in  $\rho$  at amplitude  $\delta\rho/\rho = 0.01$ . The simulations were run at two resolutions,  $N_x = 64$ ,  $N_y = 100$ ,  $N_z = 64$  and  $N_x = 128$ ,  $N_y = 200$ ,  $N_z = 128$  and are labelled YL for y-field, linear regime. In this standard set of simulations, the range of  $Re$  examined runs from 800 to 25600, and the range of  $Rm$  is from 400 to 102400. Table 4.2 lists these simulations. The last two columns state whether or not MRI growth is observed for the  $N_x = 64$  and  $N_x = 128$  resolutions, respectively. A dash in either of these columns means that the simulation was not run at that particular resolution. MRI growth is defined by the evolution of the volume-averaged magnetic and kinetic energy components. A simulation is considered to have zero growth if after 20–40 orbits, the various energy components are either decaying or constant in time without any indication of exponential increase.

Growth to saturation is observed in cases when  $Re$  and  $Rm$  are at 6400 and above.

Clearly, a sufficiently large viscosity or resistivity can inhibit growth. But what about the very high or very low  $P_m$  limits? To approach that question, we carried out simulations where only  $\nu$  or  $\eta$  was nonzero. These experiments were done at the  $N_x = 64$  resolution. In our first experiments, we set  $\eta$  to zero and  $Re$  to 100 and 800. The  $Re = 800$  run showed growth to saturation, but the  $Re = 100$  case had no growth. Next we set  $\nu$  to zero and  $Rm$  to 800 and 1600. The lower resistivity ( $Rm = 1600$ ) grew to saturation, whereas the higher resistivity ( $Rm = 800$ ) did not. Although the existence of a critical  $Rm$  value is consistent with the results of Fleming et al. (2000), the value of  $Rm$  at which growth is prevented is smaller here than what they found. We note that there remains unavoidable numerical dissipation associated with grid scale effects, which will make the value of a critical  $Rm$  obtained through simulations somewhat dependent on algorithm and resolution.

The effect of numerical resolution is not necessarily obvious. Consider model YLRe3200Pm2, which has  $Re = 3200$  and  $Rm = 6400$ , and model YLRe6400Pm0.5, which has these values reversed. In both cases, the  $N_x = 64$  simulations show growth but the  $N_x = 128$  models do not. One difference between the two resolutions is in the initial perturbations. While the density perturbations have the same amplitude in both resolutions, the higher resolution initial density is given power at smaller scales because the perturbations are applied to each grid zone. This leads to a smaller amplitude for each Fourier mode. Does this account for the difference seen in these two resolutions? To investigate this, we ran both  $N_x = 64$  versions of YLRe3200Pm2 and YLRe6400Pm0.5 with initial perturbations of amplitude  $\delta\rho/\rho = 0.005$  and  $\delta\rho/\rho = 0.001$ . Note that these amplitudes lead to comparable ( $\delta\rho/\rho = 0.005$ ) or smaller ( $\delta\rho/\rho = 0.001$ ) amplitude modes in Fourier space com-

pared to the  $\delta\rho/\rho = 0.01$  initialized modes at the higher resolution. Neither of the smaller amplitude YLRe3200Pm2 simulations showed any growth (as of 20-30 orbits), but both YLRe6400Pm0.5 simulations showed growth to saturation.

From these experiments it seems that the effects of viscosity and resistivity are comparable and that the transition region between decay and growth to turbulence lies between Reynolds numbers of 3200 and 6400 for  $P_m$  near unity. This corresponds to a critical vertical wavelength, defined in terms of equation (4.8), of  $\lambda_c/H \sim 2\pi/Rm^{1/2} = 0.111$  and  $0.079$ , respectively. As viscosity (resistivity) is increased, MRI growth can be achieved by decreasing the resistivity (viscosity). This trend only works up to certain limits; if either the viscosity or resistivity is large enough, MRI growth is completely quenched, independent of the value of the other dissipation term.

#### 4.4.2 The Nonlinear Regime

Of potentially greater interest than the linear MRI regime is the effect of viscosity and resistivity on fully developed MRI-driven turbulence. To study this nonlinear regime, we begin with model YLRe25600Pm4, a simulation with  $Re = 25600$  and  $P_m = 4$  at  $N_x = 128$ ,  $N_y = 200$ ,  $N_z = 128$  (Table 4.2) that was run to 59 orbits in time. The MRI grows and the flow becomes fully turbulent. Averaging from  $t = 15$  to 59 orbits gives a stress value of  $\alpha = 0.05$ . We use this simulation at  $t = 36$  orbits to initialize a series of simulations with different values of  $Re$  and  $Rm$ . These runs are labelled YN for y-field, nonlinear regime, and they are all run to 200 orbits, except for simulation YNRe12800Pm0.25, which was run to 100 orbits. All the YN simulations are listed in Table 4.3.

When evolving onward from orbit 36 with modified dissipation terms, a simulation shows a rapid readjustment followed by either sustained turbulence at a new

Table 4.3. Toroidal Field Simulations Initialized from Nonlinear Turbulence

| Label           | $Re$  | $P_m$ | $Rm$  | Turbulence? | $\alpha$ | $\langle\langle\Lambda\rangle\rangle$ | $\langle\langle\Lambda_z\rangle\rangle$ |
|-----------------|-------|-------|-------|-------------|----------|---------------------------------------|---|
| YNRe400Pm0.5    | 400   | 0.5   | 200   | No          | -        | 4                                     | -                                       |
| YNRe400Pm1      | 400   | 1     | 400   | No          | -        | 8                                     | -                                       |
| YNRe400Pm2      | 400   | 2     | 800   | No          | -        | 15                                    | -                                       |
| YNRe400Pm4      | 400   | 4     | 1600  | No          | -        | 30                                    | -                                       |
| YNRe400Pm8      | 400   | 8     | 3200  | Yes         | 0.043    | 614                                   | 16.8                                    |
| YNRe400Pm16     | 400   | 16    | 6400  | Yes         | 0.068    | 1983                                  | 58.2                                    |
| YNRe800Pm0.25   | 800   | 0.25  | 200   | No          | -        | 4                                     | -                                       |
| YNRe800Pm0.5    | 800   | 0.5   | 400   | No          | -        | 8                                     | -                                       |
| YNRe800Pm1      | 800   | 1     | 800   | No          | -        | 15                                    | -                                       |
| YNRe800Pm2      | 800   | 2     | 1600  | Yes         | 0.019    | 137                                   | 3.87                                    |
| YNRe800Pm4      | 800   | 4     | 3200  | Yes         | 0.038    | 495                                   | 18.0                                    |
| YNRe800Pm8      | 800   | 8     | 6400  | Yes         | 0.054    | 1413                                  | 56.2                                    |
| YNRe1600Pm0.5   | 1600  | 0.5   | 800   | No          | -        | 15                                    | -                                       |
| YNRe1600Pm1     | 1600  | 1     | 1600  | Yes         | 0.018    | 120                                   | 4.45                                    |
| YNRe1600Pm2     | 1600  | 2     | 3200  | Yes         | 0.033    | 403                                   | 18.6                                    |
| YNRe1600Pm4     | 1600  | 4     | 6400  | Yes         | 0.044    | 1120                                  | 52.6                                    |
| YNRe3200Pm0.5   | 3200  | 0.5   | 1600  | Yes         | 0.016    | 106                                   | 4.53                                    |
| YNRe3200Pm1     | 3200  | 1     | 3200  | Yes         | 0.025    | 314                                   | 16.4                                    |
| YNRe3200Pm2     | 3200  | 2     | 6400  | Yes         | 0.035    | 860                                   | 47.4                                    |
| YNRe3200Pm4     | 3200  | 4     | 12800 | Yes         | 0.043    | 2170                                  | 127                                     |
| YNRe6400Pm0.5   | 6400  | 0.5   | 3200  | Yes         | 0.021    | 263                                   | 14.9                                    |
| YNRe6400Pm1     | 6400  | 1     | 6400  | Yes         | 0.031    | 748                                   | 45.2                                    |
| YNRe6400Pm2     | 6400  | 2     | 12800 | Yes         | 0.038    | 1880                                  | 118                                     |
| YNRe12800Pm0.25 | 12800 | 0.25  | 3200  | Yes         | 0.021    | 262                                   | 15.8                                    |

amplitude or decay to smooth flow, depending on the new values of  $Re$  and  $Rm$ . The column labeled “Turbulence?” in Table 4.3 states whether or not the given simulation has sustained turbulence. Note that for  $Rm \gtrsim 1600$ , the turbulence is sustained except for the relatively viscous  $Re = 400$  model. This critical  $Rm$  value is below the critical value obtained above for sustained growth in the linear regime when the resistivity and viscosity are comparable but near the critical  $Rm$  value in the linear regime in the absence of explicit viscosity. For simulations where turbulence is sustained, the column labeled “ $\alpha$ ” gives the time- and volume-averaged dimensionless stress, where the time average is calculated onward from orbit 50.

The column labeled “ $\langle\langle\Lambda\rangle\rangle$ ” gives a time- and volume-averaged  $\Lambda$  value in the final state of each simulation. Unlike  $Rm$ ,  $\Lambda$  will change with the evolving magnetic field strength. Beginning with equation (4.7), we write

$$\beta = \frac{2c_s^2\langle\rho\rangle}{\langle B^2\rangle} \quad (4.9)$$

to give

$$\langle\Lambda\rangle = \frac{Rm}{c_s^2} \frac{\langle B^2\rangle}{\langle\rho\rangle}, \quad (4.10)$$

where the angled brackets denote a volume average. One could also volume-average the square of the Alfvén speed in the calculation of  $\beta$  instead of averaging  $B^2$  and  $\rho$  separately (e.g.,  $\beta = 2c_s^2/\langle v_A^2\rangle$ ). We have calculated  $\langle\Lambda\rangle$  using both types of averages for several frames in the saturated state of a few simulations. We have found at most a factor of 2 difference between the different calculations. Since  $\langle B^2\rangle$  varies by a similar factor in the saturated state (see Fig. 4.4), this factor of 2 difference is within the uncertainty of  $\Lambda$  at any given time. The time-average of the volume-averaged Elsasser number,  $\langle\langle\Lambda\rangle\rangle$ , as given in the table, is calculated from orbit 50 until the end of the simulation. For the decayed turbulence simulations in which the turbulence has

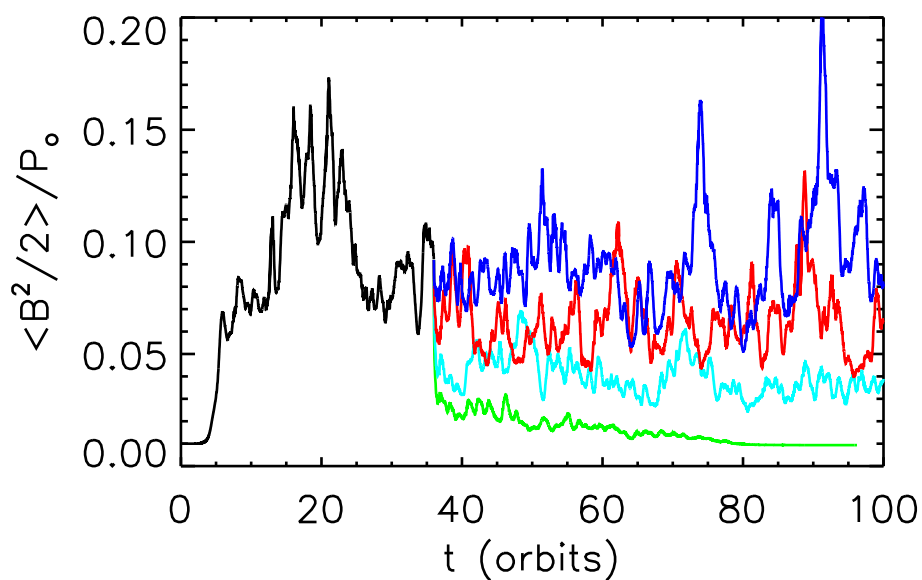


Fig. 4.4.— Time evolution of volume-averaged magnetic energy density normalized by the gas pressure for the YN runs with  $Re = 25600$  (black curve) and  $Re = 1600$  (colored curves). The volume average is calculated over the entire simulation domain. The colors indicate  $P_m$ ; green corresponds to  $Rm = 800$  ( $P_m = 0.5$ ), light blue to  $Rm = 1600$  ( $P_m = 1$ ), red to  $Rm = 3200$  ( $P_m = 2$ ), and dark blue to  $Rm = 6400$  ( $P_m = 4$ ). Increasing  $Rm$  ( $P_m$ ) leads to enhanced turbulence.

not fully decayed by orbit 50, the time average is calculated onward from a point at which the volume-averaged magnetic energy is constant in time. Note that for these decayed turbulence simulations,  $\langle\langle\Lambda\rangle\rangle$  should equal the  $\beta = 100$  value associated with the net toroidal field, as given in Table 4.2. However, because of the evolution of the net  $B_y$  (see § 4.2), the value of  $\langle\langle\Lambda\rangle\rangle$  after the turbulence has decayed will be slightly different than the  $\beta = 100$  value.

Since the magnetic field varies within the domain, the local value of  $\Lambda$  can also vary from the overall average. Histograms showing the number of grid zones with  $v_A^2$  of a certain value reveal that the percentage of grid zones that have  $\Lambda < 1$  is at most  $\sim 0.01\%$ . For the sustained turbulence models,  $\langle\langle\Lambda\rangle\rangle$  is typically on the order of 100-1000; the smallest value for a run with sustained turbulence is 106, and the largest value associated with a run that decays is 30.

The behavior of the MRI is often characterized by the vertical component of the Alfvén speed, and as such, we have also calculated the Elsasser number using only the vertical component of the magnetic field,

$$\langle\Lambda_z\rangle = \frac{Rm}{c_s^2} \frac{\langle B_z^2 \rangle}{\langle \rho \rangle}, \quad (4.11)$$

where the angled brackets denote a volume average. We have calculated the time average of this number,  $\langle\langle\Lambda_z\rangle\rangle$ , onward from orbit 50 for all the sustained turbulence YN simulations. This number is displayed in the last column of Table 4.3. The decayed turbulence simulations have  $B_z$  approaching zero, and we do not calculate a vertical Elsasser number for these. Again, we calculated the vertical Elsasser number both by averaging  $B_z^2$  and  $\rho$  separately as well as by averaging the ratio  $B_z^2/\rho$ . We compared the two calculations for several frames and found at most a factor of 1.3 difference between them.

The  $\langle\langle\Lambda_z\rangle\rangle$  values for the runs that have  $Rm$  closest to the critical value are on the order unity, with the smallest value being 3.87. As touched upon by Fleming et al. (2000), growth of the vertical field MRI is largely suppressed for  $v_{\Lambda_z}^2/(\eta\Omega) \lesssim 1$  (i.e., for vertical Elsasser numbers less than unity). That we find  $\langle\langle\Lambda_z\rangle\rangle \sim 1$  close to the “decayed turbulence” regime may suggest that the vertical field MRI plays an important role in the sustained nonlinear turbulence of these toroidal field simulations. One trend to note from these data is that the ratio of  $\langle\langle\Lambda_z\rangle\rangle$  to  $\langle\langle\Lambda\rangle\rangle$  increases with both decreasing  $\nu$  and decreasing  $\eta$ ; the vertical magnetic energy becomes a larger fraction of the total magnetic energy as either dissipation term is reduced.

The evolution of the magnetic energy in a typical set of simulations is shown in Fig. 4.4. For these runs,  $Re = 1600$  and  $Rm$  varies by factors of two from  $Rm = 800$  to 6400. The black line shows the initial evolution of YLRe25600Pm4, whose state at 36 orbits serves as the initial condition. It is clear that decreasing the resistivity (increasing the  $P_m$  number) enhances the saturation level, and for a large enough resistivity, the turbulence decays.

To quantify the dependence of the saturation amplitude on the dissipation coefficients, we plot the  $\alpha$  values for the ensemble of simulations as a function of  $Re$ ,  $Rm$  and  $P_m$ . Figure 4.5 shows  $\alpha$  versus  $Rm$ ; the color indicates  $Re$  value, and the symbols correspond to the  $P_m$  value. The simulations with  $\alpha = 0$  are those where the turbulence decayed away, which include all simulations with  $Rm \leq 800$  and the  $Re = 400$ ,  $Rm = 1600$  simulation. Overall there is a general trend of increasing  $\alpha$  value with decreasing resistivity.

The dependence of  $\alpha$  on  $Re$  is shown in Fig. 4.6. Here the color indicates the  $Rm$  value, whereas  $P_m$  is again represented by a symbol. Evidently, if the resistivity is low enough, increasing the viscosity will increase the  $\alpha$  values. However, consider the

YN simulations with  $Rm = 1600$ . These simulations suggest that if the resistivity is close to some critical value, increasing the viscosity will cause the turbulence to decay. Another feature of note is that as  $Re$  increases, the range of  $\alpha$  for different  $Rm$  values becomes smaller, and  $\alpha$  appears to converge to  $\sim 0.02 - 0.04$  for all  $Rm$ . This could indicate that as  $\nu$  and  $\eta$  decrease, their influence on the turbulence level might decrease. However, for large values of  $Re$  or  $Rm$ , the dissipation lengthscales are under-resolved, and higher resolution is needed to test this possibility.

We plot the dependence of  $\alpha$  on  $P_m$  in Fig. 4.7. In this figure, the colors represent varying  $Rm$  while the symbols denote different  $Re$  values. The clearest trend is that if  $Rm$  is large enough to sustain turbulence, increasing  $P_m$  leads to larger  $\alpha$  values. Note that turbulence can be sustained even for  $P_m$  less than unity, if  $Rm$  is large enough. At constant  $Rm$ , we find that  $\alpha \propto Re^{\delta_1}$  with  $\delta_1$  ranging from -0.1 to -0.3 (calculated by a linear fit to the data in log space for non-decayed turbulence simulations only). At constant  $Re$  value, we find  $\alpha \propto Rm^{\delta_2}$  with  $\delta_2$  in the range 0.4-0.8 and  $\delta_2$  generally decreasing with increasing  $Re$ .

These results naturally lead to the question of why increasing  $\nu$  or decreasing  $\eta$  causes an increase in turbulence. Magnetic reconnection and dissipation of field lines, either due to an explicit resistivity or to grid-scale effects, presumably play the primary role in limiting the amplitude of the MHD turbulence. Balbus & Hawley (1998) hypothesized that increased viscosity would inhibit reconnection by preventing velocity motions that would bring field together on small scales. When  $P_m > 1$ , the viscous length is greater than the resistive one, and magnetic field dissipation becomes less efficient, leading to an increase in turbulent stress (e.g., Balbus & Henri 2008). If this hypothesis is correct, there may also be a change in the dissipation of kinetic and magnetic energy into heat. To investigate this possibility, we carry out an analysis of

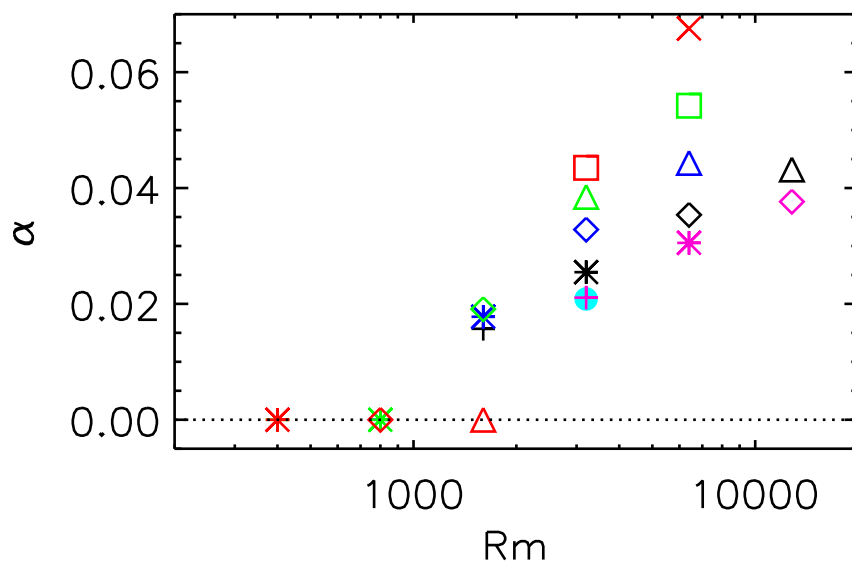


Fig. 4.5.— Time- and volume-averaged stress parameter  $\alpha$  as a function of  $Rm$  in the YN simulations;  $\alpha \equiv \langle \langle \rho v_x \delta v_y - B_x B_y \rangle \rangle / P_o$ . The time average runs from 50 orbits onward, and the volume average is calculated over the entire simulation domain. The colors correspond to  $Re$  values, and the symbols correspond to  $P_m$  values. Red symbols are  $Re = 400$ , green  $Re = 800$ , dark blue  $Re = 1600$ , black  $Re = 3200$ , pink  $Re = 6400$ , and light blue are  $Re = 12800$ . Circles are  $P_m = 0.25$ , crosses  $P_m = 0.5$ , asterisks  $P_m = 1$ , diamonds  $P_m = 2$ , triangles  $P_m = 4$ , squares  $P_m = 8$ , and X's are  $P_m = 16$ . Note that some of the decayed turbulence ( $\alpha = 0$ ) simulations are not plotted for clarity. Increasing  $Rm$  results in larger  $\alpha$  values, and for  $Rm$  less than 800–1600, the turbulence decays.

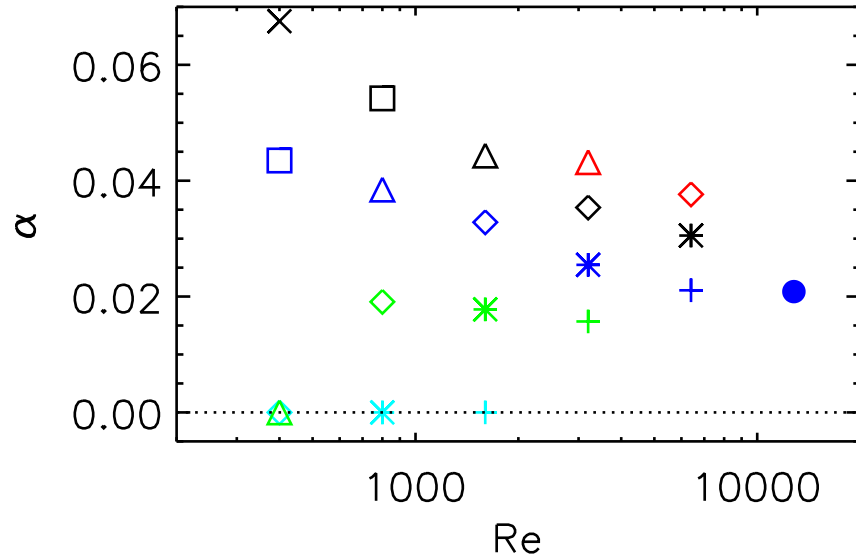


Fig. 4.6.— Time- and volume-averaged stress parameter  $\alpha$  as a function of  $Re$  in the YN simulations;  $\alpha \equiv \langle \langle \rho v_x \delta v_y - B_x B_y \rangle \rangle / P_o$ . The time average runs from 50 orbits onward, and the volume average is calculated over the entire simulation domain. The colors correspond to  $Rm$  values, and the symbols correspond to  $P_m$  values. Light blue symbols are  $Rm = 800$ , green  $Rm = 1600$ , dark blue  $Rm = 3200$ , black  $Rm = 6400$ , and red are  $Rm = 12800$ . Circles are  $P_m = 0.25$ , crosses  $P_m = 0.5$ , asterisks  $P_m = 1$ , diamonds  $P_m = 2$ , triangles  $P_m = 4$ , squares  $P_m = 8$ , and X's are  $P_m = 16$ . Note that some of the decayed turbulence ( $\alpha = 0$ ) simulations are not plotted for clarity. Increasing  $Re$  leads to decreasing  $\alpha$  values.

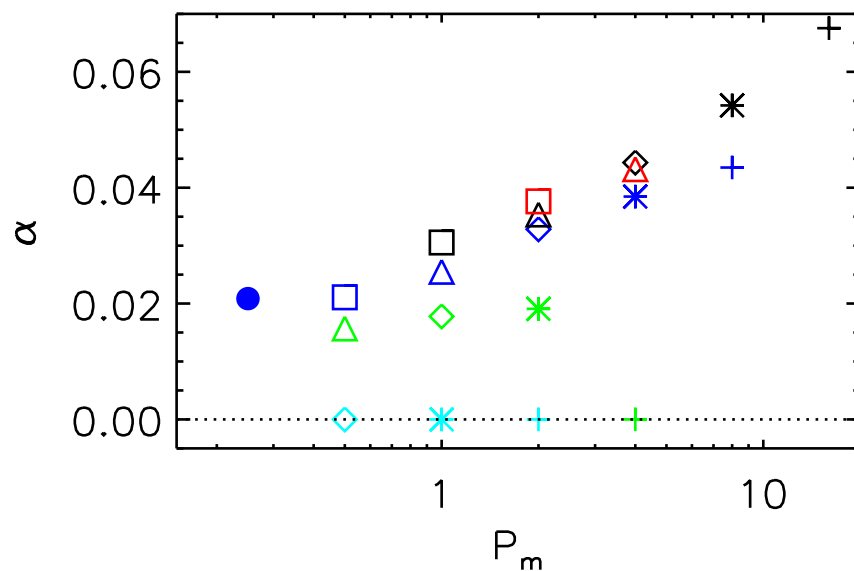


Fig. 4.7.— Time- and volume-averaged stress parameter  $\alpha$  as a function of  $P_m$ ;  $\alpha \equiv \langle \langle \rho v_x \delta v_y - B_x B_y \rangle \rangle / P_o$ . The time average runs from 50 orbits onward, and the volume average is calculated over the entire simulation domain. The colors correspond to  $Rm$  values, and the symbols to  $Re$  values. Light blue symbols are  $Rm = 800$ , green  $Rm = 1600$ , dark blue  $Rm = 3200$ , black  $Rm = 6400$ , and red are  $Rm = 12800$ . Crosses are  $Re = 400$ , asterisks  $Re = 800$ , diamonds  $Re = 1600$ , triangles  $Re = 3200$ , squares  $Re = 6400$ , and circles are  $Re = 12800$ . Note that some of the decayed turbulence ( $\alpha = 0$ ) simulations are not plotted for clarity. The average stress increases with increasing  $P_m$ .

viscous and resistive heating for several of the simulations.

Consider the volume-averaged kinetic and magnetic energy evolution equations,

$$\begin{aligned} \dot{K} = & - \left\langle \nabla \cdot \left[ \mathbf{v} \left( \frac{1}{2} \rho v^2 + \frac{1}{2} B^2 + P + \rho \Phi \right) - \mathbf{B}(\mathbf{v} \cdot \mathbf{B}) \right] \right\rangle \\ & + \left\langle \left( P + \frac{1}{2} B^2 \right) \nabla \cdot \mathbf{v} \right\rangle - \langle \mathbf{B} \cdot (\mathbf{B} \cdot \nabla \mathbf{v}) \rangle - \dot{G} - Q_k, \end{aligned} \quad (4.12)$$

and

$$\dot{M} = - \left\langle \nabla \cdot \left( \frac{1}{2} B^2 \mathbf{v} \right) \right\rangle - \left\langle \frac{1}{2} B^2 \nabla \cdot \mathbf{v} \right\rangle + \langle \mathbf{B} \cdot (\mathbf{B} \cdot \nabla \mathbf{v}) \rangle - Q_m. \quad (4.13)$$

Here,  $\dot{K}$  and  $\dot{M}$  are the time derivatives of the volume-averaged kinetic and magnetic energies, respectively. The time derivative of the volume-averaged gravitational potential energy is given by  $\dot{G}$ , and  $Q_k$  and  $Q_m$  are the volume-averaged kinetic and magnetic energy dissipation rates, respectively. The gravitational potential is  $\Phi = q\Omega^2(\frac{L_x^2}{12} - x^2)$ .

We determine  $Q_k$  and  $Q_m$  for select YN models by computing the time average of each of the source terms in the energy evolution equations using 200 data files equally spaced in time over 20 orbits. We assume  $\dot{G}$  is zero in the time-average; the analysis in Chapter 3 found  $\dot{G}$  is always negligibly small. The time-derivatives,  $\dot{K}$  and  $\dot{M}$ , are calculated by differentiating the volume-averaged kinetic and magnetic energy history data with respect to time and then sampling these data to the times associated with the data files. The dissipation terms  $Q_k$  and  $Q_m$ , which include both physical and numerical effects, are the remainder after all the other terms are calculated.

Figure 4.8 shows the ratio of the time-average  $\langle Q_k \rangle$  to  $\langle Q_m \rangle$  as a function of

$P_m$  and  $\alpha$  for select YN runs. The colors and symbols are the same as in Fig. 4.6. The time average is calculated from  $t = 70 - 90$  orbits for YNRe400Pm16 (black X) and YNRe12800Pm0.25 (blue circle),  $t = 110 - 130$  orbits for YNRe800Pm2 (green diamond) and YNRe800Pm8 (black square), and  $t = 110.6 - 130.6$  orbits for YNRe800Pm4 (blue triangle) and YNRe3200Pm4 (red triangle). The ratio of viscous to resistive heating generally increases as either  $\alpha$  or  $P_m$  increases, although not monotonically. The relative heating ratio is not simply proportional to  $P_m$  as one might naively expect.

The data suggest a general relationship between saturated stress and  $\langle Q_k \rangle / \langle Q_m \rangle$ . We know that the stress level sets the *total* dissipation rate,  $Q_k + Q_m$  (see Chapter 3); stronger stresses extract more energy from the background shear flow, and that turbulence is rapidly dissipated into heat. However, does stronger turbulence by itself change the heating ratio, or is the change in the heating ratio mainly determined by changes in  $P_m$ , which also increase the turbulence levels? This question of causality cannot be definitively answered from these data.

Further insight may come from examining the ratio of averaged Reynolds stress,  $\langle \langle \rho v_x \delta v_y \rangle \rangle$ , to averaged Maxwell stress,  $\langle \langle -B_x B_y \rangle \rangle$ , as a function of  $\alpha$ ; this is shown in Fig. 4.9. The colors and symbols are the same as in Fig. 4.8. The double brackets for the stresses denote time and volume averages, where the time average is calculated over the same 20 orbit period as in Fig. 4.8. There is a decrease in the ratio of the Reynolds to Maxwell stress as the total stress increases. These stresses are proportional to the perturbed magnetic and kinetic energies at the largest scales, and if this continued down to the dissipation scale, we might expect that the ratio  $\langle Q_k \rangle / \langle Q_m \rangle$  would behave similarly with  $\alpha$ . In fact, the heating ratio shows the opposite trend with  $\alpha$ , indicating that a transfer of energy from magnetic to kinetic fluctuations

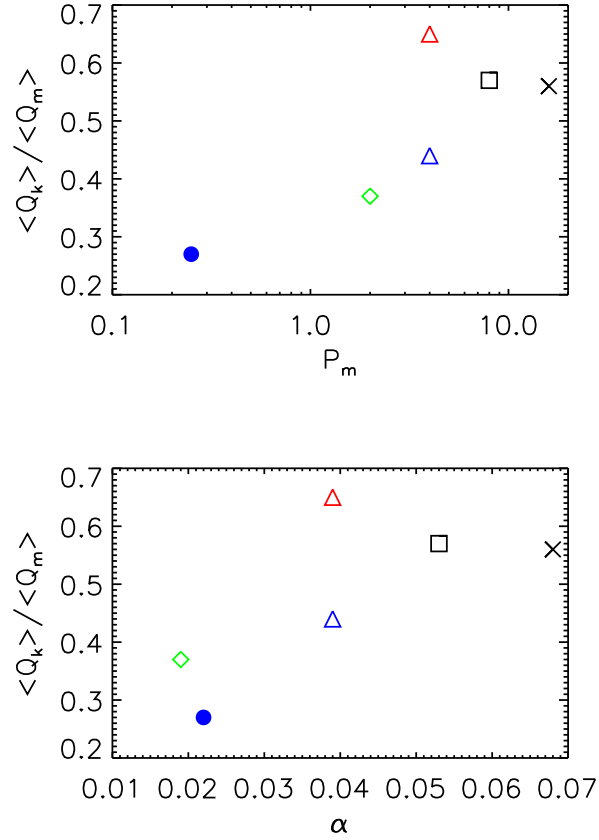


Fig. 4.8.— Ratio of kinetic to magnetic energy dissipation rate as a function of  $P_m$  (top panel) and  $\alpha$  (bottom panel) for select YN runs;  $\alpha \equiv \langle \langle \rho v_x \delta v_y - B_x B_y \rangle \rangle / P_o$ . The colors and symbols are the same as in Fig. 4.6. The kinetic and magnetic dissipation rates as well as  $\alpha$  have been averaged in volume and time. The volume average is calculated over the entire simulation domain and the time average is calculated from  $t = 70 - 90$  orbits for YNRe400Pm16 (black X) and YNRe12800Pm0.25 (blue circle),  $t = 110 - 130$  orbits for YNRe800Pm2 (green diamond) and YNRe800Pm8 (black square), and  $t = 110.6 - 130.6$  orbits for YNRe800Pm4 (blue triangle) and YNRe3200Pm4 (red triangle). The ratio of viscous to resistive heating generally increases as either  $\alpha$  or  $P_m$  increases, although not monotonically.

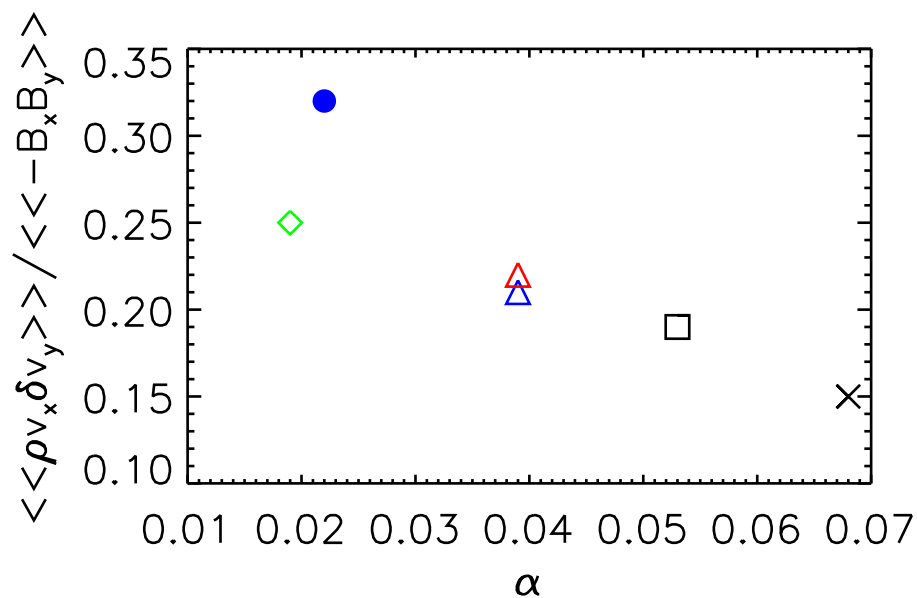


Fig. 4.9.— Ratio of Reynolds stress to Maxwell stress as a function of  $\alpha$  for select YN runs;  $\alpha \equiv \langle\langle\rho v_x \delta v_y - B_x B_y\rangle\rangle / P_o$ . The colors and symbols are the same as in Fig. 4.6. The Maxwell and Reynolds stresses as well as  $\alpha$  have been averaged in volume and time. The volume average is calculated over the entire simulation domain and the time average is calculated from  $t = 70 - 90$  orbits for YNRe400Pm16 (black X) and YNRe12800Pm0.25 (blue circle),  $t = 110 - 130$  orbits for YNRe800Pm2 (green diamond) and YNRe800Pm8 (black square), and  $t = 110.6 - 130.6$  orbits for YNRe800Pm4 (blue triangle) and YNRe3200Pm4 (red triangle). The ratio of Reynolds to Maxwell stress generally decreases with increasing  $\alpha$ .

must occur in the turbulent cascade.

Past net toroidal field simulations without explicit dissipation terms also find a trend for a decrease in the ratio of the Reynolds to Maxwell stress with increasing  $\alpha$  (e.g., Hawley et al. 1995). So this may be a general result independent of  $P_m$ . The quantity  $\langle Q_k \rangle / \langle Q_m \rangle$  has not been extensively studied in past shearing box simulations, but in Chapter 3, we found a ratio of  $\sim 0.6$  for a net vertical field model without explicit dissipation terms.

In summary, these observations are consistent with the hypothesis that decreasing  $P_m$  increases the efficiency of magnetic reconnection and hence reduces the overall stress level. However, a more in-depth study would be required to better understand the full causal relationship between the ratio of dissipation terms and the saturation levels.

Finally, we note that the ratio of Reynolds stress to perturbed kinetic energy increases with increasing  $\nu$ , as shown in Fig. 4.10. There is no observed trend with  $\eta$ . As  $\nu$  is increased, the fluid motions that are not being directly driven by the MRI become increasingly damped. The fluid motions that are driven by the magnetic field in the form of Reynolds stress follow the behavior of the Maxwell stress with  $\nu$ . This is also consistent with the hypothesis that increased  $\nu$  leads to less efficient magnetic reconnection; the kinetic fluctuations become damped relative to the driving via the MRI, making it difficult to bring field lines close together for reconnection.

Overall, resistivity seems to play a more fundamental role than viscosity in these net toroidal field simulations. There is a critical  $Rm$  below which turbulence decays or fails to grow from linear perturbations. For a given resistivity near this critical value, a relatively low viscosity leads to MRI growth (linear regime) or sustained turbulence (nonlinear regime). A high viscosity can prevent growth (linear regime)

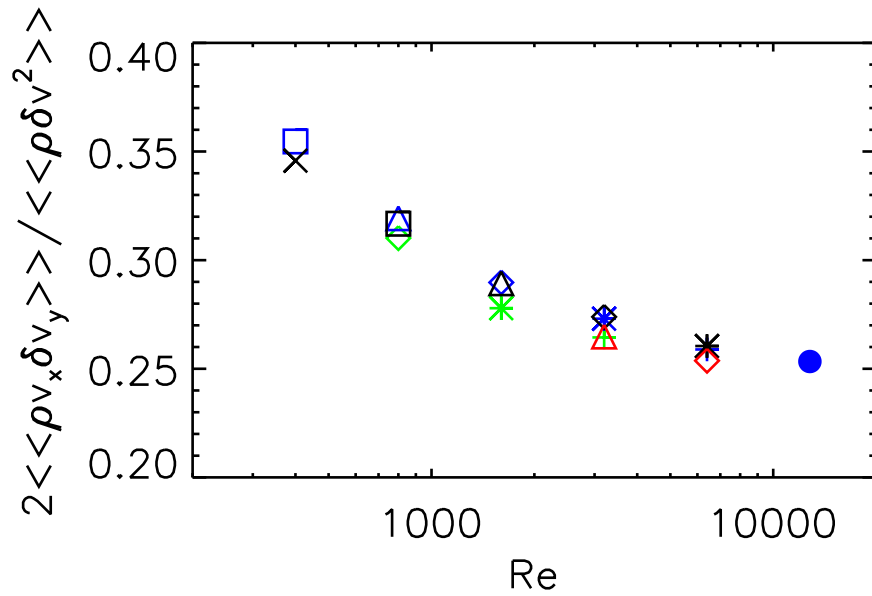


Fig. 4.10.— Ratio of Reynolds stress to perturbed kinetic energy as a function of  $Re$  in the sustained turbulence YN simulations. Both the Reynolds stress and the perturbed kinetic energy are time and volume averaged, with the time average calculated from orbit 50 onward and the volume average calculated over the entire simulation domain. The colors correspond to  $Rm$  values, and the symbols correspond to  $P_m$  values. Green symbols are  $Rm = 1600$ , blue  $Rm = 3200$ , black  $Rm = 6400$ , and red are  $Rm = 12800$ . Circles are  $P_m = 0.25$ , crosses  $P_m = 0.5$ , asterisks  $P_m = 1$ , diamonds  $P_m = 2$ , triangles  $P_m = 4$ , squares  $P_m = 8$ , and X's are  $P_m = 16$ . The ratio of stress to energy increases with increasing viscosity but does not change with resistivity.

or cause decay (nonlinear regime). Once the resistivity is sufficiently low to ensure MRI growth to saturation and continued turbulence, the effect of viscosity changes and higher viscosity gives larger  $\alpha$  values.

## 4.5 Summary and Discussion

In this study, we carried out a series of local, unstratified shearing box simulations of the MRI with Athena including the effects of constant shear viscosity and Ohmic resistivity. The first simulations were initialized with a zero net magnetic flux in the domain for comparison with the results of Fromang et al. (2007). The second set of simulations are the first investigation of the impact of both viscosity and resistivity on models with a net toroidal field.

For the values of viscosity and resistivity they studied, Fromang et al. (2007) found that turbulence was sustained only above a critical  $P_m$  value, specifically when  $P_m \gtrsim 1$ . There was evidence that this critical  $P_m$  value decreases as  $Re$  increases (viscosity is reduced). We repeated these experiments and found that the saturation level of the MRI depends strongly on both viscosity and resistivity, and for every  $Re$ , there exists a critical  $P_m$  value below which the turbulence dies out. For those simulations where turbulence was sustained, we found good agreement between the Athena  $\alpha$  values and those of Fromang et al. (2007).

Zero net field simulations are fundamentally different from net field models because an imposed background field cannot be removed as a result of the simulation evolution. The net field remains unstable and can drive fluid motion even during the fully nonlinear turbulence phase, assuming that that field was unstable to begin with. Lesur & Longaretti (2007) examined the effects of diffusion on models with a net  $\beta = 100$  vertical field in a  $1 \times 4 \times 1$  shearing box using a pseudo-spectral incompressible

code. They found a relation  $\alpha \propto P_m^\delta$  with  $\delta = 0.25\text{--}0.5$  for values of  $P_m$  ranging from 0.12 to 8, but they found no case where the turbulence died out completely for the range of viscosities and resistivities studied.

Among net field models, the purely vertical field case is significantly different from the purely toroidal field model, hence the need for the study we have presented here. For a vertical field, the linear MRI favors wavenumbers  $k_z \sim \Omega/v_A$  and  $k_x = k_y = 0$ . The purely toroidal case favors  $k_y \sim \Omega/v_A$  with  $k/k_z$  minimized. Since  $k_x$  is time dependent due to the background shear, a given mode undergoes a finite period of amplification as  $k_x$  swings from leading to trailing. These properties suggest that purely toroidal field models might be more sensitive to dissipation than the vertical field case.

In our numerical study of the linear growth regime of the toroidal MRI, we have found that increasing either the viscosity or the resistivity can prevent the growth of MRI modes. As the viscosity (resistivity) increases, the MRI needs a smaller resistivity (viscosity) in order to grow. However, for large enough values of either the viscosity or the resistivity, MRI growth is suppressed, even in the absence of the other dissipation term. Because of the importance of small wavelength (large wavenumber) modes, the critical  $Rm$  values, below which growth is inhibited, tends to be larger than what one would expect from an axisymmetric vertical field analysis, even in the absence of viscosity. Here, for comparable values of viscosity and resistivity, the critical  $Rm$  value was around 3200–6400.

Because the linear toroidal field MRI is time dependent, turbulence can only be sustained if nonlinear amplitudes are reached during the growth phase. Thus, the outcome of the linear MRI phase can be sensitive to the initial amplitude of the perturbations in a simulation where the viscous or resistive values are near the critical

value.

In the nonlinear regime, we found that viscosity generally acts in an opposite sense to that in the linear regime; increased viscosity *enhances* angular momentum transport. Furthermore, increasing the resistivity appears to decrease the saturation level, in agreement with previous studies, and the critical  $Rm$ , below which the turbulence dies is  $\sim 800$ – $1600$ . Near the critical  $Rm$ , however, increasing the viscosity causes the turbulence to decay, a behavior more in line with the linear regime.

In our simulations, as well as those of Lesur & Longaretti (2007),  $P_m < 1$  did not necessarily quench the nonlinear turbulence or prevent growth from linear perturbations. Resistivity or viscosity above a certain level can stabilize the system against these perturbations, but if both are sufficiently small, their ratio has no influence on MRI growth. The *presence* of turbulence, however, is distinct from the saturation level of that turbulence, and here  $P_m$  can have a significant effect. For both net toroidal and net vertical field simulations,  $\alpha$  increases with increasing  $P_m$  for the range of values studied.

What do these results imply for the effect of resistivity and viscosity on the MRI and on astrophysical systems? In principle, they could be quite significant. In protostellar disks, the resistivity is thought to be quite high near the midplane, leading to the existence of the dead zone (Gammie 1996). The  $Rm$  values studied here could be applicable to such systems. However, the implications for accretion disks with small values of viscosity and resistivity (e.g., X-ray binary disks) are less clear. Because the range of  $\alpha$  values we obtained decreases with increasing  $Re$  (Fig. 4.6), it is possible that  $\alpha$  may converge to a single value independent of  $P_m$  as  $Re$  and  $Rm$  are increased. If true, this would suggest that the dissipation scales might have very little influence on the saturation level of the MRI in astrophysical disks. This idea

will need to be tested with higher resolution simulations to ensure that the (small) viscous and resistive scales are adequately resolved. If, on the other hand,  $P_m$  still has an influence on the turbulence even for very small values of viscosity and resistivity, our results (taken together with those in the literature) could be applicable to such disks. The resistivity, viscosity, and  $P_m$  can vary quite substantially in these systems, not only between different astrophysical objects, but also within a given disk (e.g., Brandenburg & Subramanian 2005). Balbus & Henri (2008) analyze a possible  $P_m$  dependence on radius in X-ray binaries to suggest that such a dependence could be at the core of spectral state transitions in these systems.

The work to date is suggestive, but there remain several limitations associated with these shearing box simulations. First, the simulations are unstratified; vertical gravity may also play a role in establishing the overall turbulent state. For example, Davis et al. (2010) carried out a series of zero net field shearing box simulations with vertical gravity and explicit dissipation and found that the turbulence does not decay as readily as in the unstratified case. Secondly, all of the simulations to date have explored a relatively restricted range of parameters. Here, for example, we have examined only one value for the toroidal field strength and one domain size. Finally, as touched upon above, the range of values for  $Re$  and  $Rm$  that have been studied are somewhat restricted and certainly much smaller than would be appropriate for many astrophysical disk systems. While this limitation is partially computational and can be improved upon with higher resolutions, the question remains for astrophysical systems whether viscous and resistive processes that take place on relatively small lengthscales can have a significant influence on macroscopic stress terms whose scales are on order the pressure scale height in the disk. But regardless of the importance of resistivity and viscosity for astrophysical systems, the values of  $Re$  and  $Rm$  are

very important for setting  $\alpha$  in numerical simulations, much more so than many other shearing box parameters (e.g., pressure) studied to date. Without a more thorough understanding of the role that dissipation terms play, quantitative predictions of  $\alpha$  values from simulations will not be possible.

In summary, our experiments have explored the effect of changing viscosity and resistivity on MRI simulations with a net toroidal field. This work serves to expand upon previous investigations of the impact of small-scale dissipation. While the direct applicability of studies such as this to specific stress values within astrophysical systems remains uncertain, it is likely that for the conceivable future, numerical simulations will be our primary, if not only way to explore the nature of MRI-driven turbulence. A thorough understanding of MRI turbulence can only be obtained with a complete understanding of the effects of diffusion, both numerical and physical.

## Chapter 5

# Prandtl Number Effects on Vertically Stratified Disks

We have run a series of local, isothermal shearing box simulations with the Athena code to study the effect of vertical gravity, shear viscosity,  $\nu$ , and Ohmic resistivity,  $\eta$  on MRI-driven turbulence. Our first set of simulations are unstratified and serve to calibrate the effects of physical dissipation at low resolutions. We find that the effect of the magnetic Prandtl number,  $P_m = \nu/\eta$ , on the turbulence is well-converged by  $\sim 32$  grid zones per disk scale height,  $H$ . Our main simulations focus on the effect of vertical gravity on the MRI. In agreement with previous results, we find that enhanced, subthermal magnetic field is generated via the MRI for  $|z| \lesssim 2H$ . This predominantly toroidal field is produced via the shear of radial field and buoyantly rises out of the disk, leading to a magnetic pressure dominated region for  $|z| \gtrsim 2H$ . Radial and toroidal fields of opposite polarity are then generated near the mid-plane, leading to oscillations of the mean horizontal field within the mid-plane. These oscillations have a period of 10 orbits modulated by a longer timescale that ranges from tens to hundreds of orbits. As in unstratified simulations, increasing  $P_m$  leads to an increase in

volume-averaged stresses, but with a less steep dependence on  $P_m$  and considerably more temporal variability. Furthermore, if  $\eta \gtrsim c_s H/3200$ , where  $c_s$  is the sound speed, the turbulence undergoes periods of decay followed by regrowth of the MRI, on timescales ranging from 10 to 100 orbits. The regrowth of the MRI is caused by weak radial field shearing into toroidal field sufficiently strong to activate the toroidal field MRI.

## 5.1 Introduction

Vertical stratification alters the behavior of MRI-driven turbulence and the resulting disk structure significantly. Radial and toroidal fields are generated near the mid-plane via shear and MRI turbulence, buoyantly rise upwards, and are replaced with fields of the opposite sign in the mid-plane region. This behavior happens on a  $\sim 10$  orbit timescale and appears to be integrally connected with an MHD dynamo in these systems (e.g., Brandenburg et al. 1995; Stone et al. 1996; Hirose et al. 2006; Guan 2009; Shi et al. 2010; Gressel 2010; Davis et al. 2010). Furthermore, the vertical structure of the disk consists of MRI-turbulent gas that is marginally stable to buoyancy within  $|z| \sim 2H$ . Outside of this region, the gas is magnetically dominated, significantly less turbulent, and buoyantly unstable (e.g., Guan 2009; Shi et al. 2010). Since most of these results have come from ZEUS-based calculations, one of our goals is to further examine the spatial and temporal properties of vertically stratified MRI-driven turbulence with the higher-order Godunov code, Athena. How does the vertical structure of the turbulence as seen with Athena compare to previous ZEUS-based results? What more can we learn about the temporal variability in the averaged mid-plane fields and how it relates to the MHD dynamo?

Beyond these questions remains the issue of how physical dissipation affects the

MRI in the presence of vertical gravity. While the effect of Ohmic resistivity on the vertically stratified MRI in has been studied in some detail (e.g., Miller & Stone 2000), most of these calculations employ a very large resistivity in order to completely quench the MRI and create the dead zone thought to be present in protostellar disk systems (e.g., Gammie 1996; Fleming & Stone 2003; Fromang & Papaloizou 2006; Oishi et al. 2007; Turner & Sano 2008; Ilgner & Nelson 2008; Oishi & Low 2009; Turner et al. 2010). Furthermore, the effect of both viscosity,  $\nu$ , and resistivity,  $\eta$ , on vertically stratified turbulence has barely been examined. To our knowledge, the only such investigation was carried out by Davis et al. (2010); their simulations contained zero net magnetic flux and employed vertically periodic boundary conditions to maintain this zero net flux. They were specifically interested in understanding how vertical gravity would affect the unstratified zero net flux models of Fromang & Papaloizou (2007) and Fromang et al. (2007). They found that without physical dissipation, the volume-averaged stress level reaches a constant value as numerical resolution is increased; this is in stark contrast to unstratified simulations in which the stress level is proportional to the grid scale (Fromang & Papaloizou 2007). Furthermore, they examined three  $\nu$  and  $\eta$  values that lead to decay in unstratified boxes. With vertical gravity, these  $\nu$  and  $\eta$  values do not necessarily cause decay but lead to large amplitude, long timescale fluctuations in the volume averaged stress level; the turbulence is active for  $\sim 100$  orbits, then decays for another  $\sim 100$  orbits, and then becomes active again.

The primary goal of this work is to understand exactly how  $\nu$  and  $\eta$  affect MRI turbulence in vertically stratified shearing boxes. In particular, what is the origin of the fluctuations seen in Davis et al. (2010), and is it relevant to real accretion disks? How does increasing the magnetic Prandtl number,  $P_m = \nu/\eta$ , affect the

structure and amplitude of MRI-driven turbulence when vertical gravity is included? These simulations will also serve as an essential starting point for future studies that include more realistic, temperature- and density-dependent  $\nu$  and  $\eta$ .

The structure of this chapter is as follows. In § 5.2, we describe our numerical code, Athena, and the implementation of the vertically stratified shearing box methodology. We first present a series of unstratified shearing box simulations in § 5.3 to calibrate the effects of physical dissipation and serve as controls for the vertically stratified shearing boxes with constant  $\nu$  and  $\eta$ . In § 5.4, we discuss our vertically stratified simulations, which are the primary focus of this chapter. The first set of these simulations contain no physical dissipation, and we carry out several analyses to improve our understanding of vertically stratified MRI turbulence. The second set of simulations then includes physical dissipation to study the  $P_m$  effect. We wrap up with a discussion and our general conclusions in § 5.5.

## 5.2 Shearing Box Implementation

The implementation of the shearing box for the simulations presented in this chapter differs in several ways from that of the previous chapters. Specifically, while the basic description of the shearing box presented in Chapter 2 still applies, there are several distinct differences in the source terms, boundary conditions, and integration algorithm. These differences result from a separate development of the Athena shearing box by Thomas Gardiner and James Stone, and we closely follow the description of Stone & Gardiner (2010) in this section. Also, note that the Riemann solver used in all of these simulations is the HLLD solver (Miyoshi & Kusano 2005; Mignone 2007).

### 5.2.1 Source Terms

The shearing box source terms for these simulations consist of the Coriolis force and the radial and vertical gravitational forces in equation (2.6). All of the simulations in this chapter are isothermal, so we do not consider the energy equation source terms. The radial and vertical gravitational forces can be written as the negative gradient of a potential,  $-\rho\nabla\Phi_g$ , where

$$\Phi_g = -q\Omega^2 x^2 + \frac{1}{2}\Omega^2 z^2. \quad (5.1)$$

This potential is discretized on the grid such that differencing the potential returns the appropriate acceleration/force. This calculation of the force is done in a manner consistent with the CTU algorithm, as described in § 2.2, except for during the final flux update (i.e., after the fluxes are recomputed and everything is calculated to the half-time-step value; see Stone et al. (2008)). During this step, Crank-Nicholson time differencing is employed; the fluid quantities used to calculate the source terms are averaged to the half-time step value ( $n + 1/2$ ), as opposed to using the quantities at the previous time step ( $n$ ) as is done in the forward time differencing of the standard algorithm. This implementation precisely conserves the epicyclic kinetic energy (Gardiner & Stone 2005a; Stone & Gardiner 2010).

### 5.2.2 Boundary Conditions

The boundary conditions used in these simulations are slightly different than those of previous chapters. First of all, the  $y$  direction boundaries are periodic as usual. The  $x$  direction boundaries are the usual shearing-periodic boundary conditions, as described in Chapter 2. One difference, however, between the implementation here

and that in the other chapters is that the reconstruction of the fluid variables within the shifted grid zones is done on the fluid fluxes and not on the variables themselves. The ghost zone fluid variables are then updated via these reconstructed fluxes. The order of this reconstruction matches the spatial reconstruction in the physical grid, e.g., 3rd order reconstruction of the ghost zone fluxes is done when the PPM spatial reconstruction is employed. Note that this is in addition to the EMF/flux remapping described in Chapter 2.

Finally, the vertical boundary conditions are modified outflow conditions, which are summarized as follows.  $\rho$  is extrapolated into the ghost zones based upon an isothermal, hydrostatic equilibrium. The reference value is the last physical zone, denoted by  $ke$ . Therefore, for the upper vertical boundary, the  $\rho$  value in grid cell  $k$  is

$$\rho(k) = \rho(ke) \exp\left(-\frac{z(k)^2 - z(ke)^2}{H^2}\right), \quad (5.2)$$

where  $H$  is the vertical scale height (defined below). A similar expression holds for the lower vertical boundary. This extrapolation provides hydrostatic support against the opposing gravitational forces, which are also applied in the ghost zones. All velocity components,  $B_x$ , and  $B_y$  are copied into the ghost zones from the last physical zone assuming a zero slope extrapolation. If the sign of  $v_z$  in the last physical zone is such that an inward flow into the grid is present,  $v_z$  is set to zero in the ghost zones. Finally,  $B_z$  is set in the ghost zones to ensure that  $\nabla \cdot \mathbf{B} = 0$  and is thus calculated from the ghost zone values of  $B_x$  and  $B_y$ .

### 5.2.3 Orbital Advection

For our simulations in which the radial size of the shearing box is  $H$ , the velocity is initialized with

$$v_y = -q\Omega x. \quad (5.3)$$

However, for sufficiently large domains where  $|x| \gtrsim H/q$ ,  $v_y$  can become supersonic, resulting in a decrease in the Courant limited time step. Furthermore, the presence of this background shear flow can lead to a systematic change in truncation error with radial position in the box, which in turn causes features in the radial density and stress profiles (Johnson et al. 2008). For our larger radial domain simulations then, we implement an orbital advection scheme, which subtracts off the background shear flow and evolves it separately from the fluctuations in the fluid quantities (Masset 2000; Johnson et al. 2008; Davis et al. 2010; Stone & Gardiner 2010).

In the Athena implementation of orbital advection, the fluid is decomposed into shear flow components and fluctuations from this shear flow. In particular, the velocity fluctuations are defined as

$$\delta v_x = v_x, \quad (5.4)$$

$$\delta v_y = v_y + q\Omega x, \quad (5.5)$$

$$\delta v_z = v_z, \quad (5.6)$$

where  $q = 3/2$ . All other variables that are related to the velocity have a corresponding fluctuation variable that is defined in terms of the  $\delta v$  velocities. These fluctuation variables are then evolved with the usual Athena algorithm. The time step constraint (not including the viscosity/resistivity contributions; see below) is then

$$\Delta t_{\text{CTU}} = C_o \text{MIN} \left( \frac{\Delta x}{(|\delta v_x| + C_{fx})}, \frac{\Delta y}{(|\delta v_y| + C_{fy})}, \frac{\Delta z}{(|\delta v_z| + C_{fz})} \right) \quad (5.7)$$

where  $C_o$  is the CFL number ( $C_o = 0.4$  here),  $C_{fi}$  is the fast magnetosonic wavespeed in the  $i$ -th direction, and the MIN is taken over all grid zones. The shear flow components to the fluid variables are evolved via a remap corresponding to linear advection by the background flow. This remapping is done on the fluxes and on the EMFs so that conservation and  $\nabla \cdot \mathbf{B} = 0$  are maintained.

### 5.2.4 Physical Dissipation

Both the viscosity,  $\nu$ , and resistivity,  $\eta$ , are added via operator splitting; the fluid variables updated from the CTU integrator are used to calculate the viscous and resistive terms. The viscosity term is calculated via the divergence of the viscous stress tensor, equation (1.8), and the resistive term is included as an additional EMF within the induction equation, as in equation (1.7). As in Chapter 4, this formulation allows us to discretize the viscous and resistive terms in a flux-conservative and constrained-transport manner, consistent with the Athena algorithm. Specifically, the viscous stress tensor components are defined as fluxes at the cell faces, and the resistive EMF term is computed at cell corners. Note that this resistive contribution to the EMF must also be reconstructed at the shearing-periodic boundaries in order to preserve  $B_z$  precisely.

The addition of viscosity and resistivity places an additional constraint on the

time step,

$$\Delta t = \text{MIN} \left( \Delta t_{\text{CTU}}, C_o \frac{\Delta^2}{4\nu}, C_o \frac{\Delta^2}{4\eta} \right), \quad (5.8)$$

where  $\Delta t_{\text{CTU}}$  is the time step limit from the main integration algorithm (see Stone et al. (2008) or the definition above), and  $\Delta$  is the minimum grid spacing,  $\Delta = \text{MIN}(\Delta x, \Delta y, \Delta z)$ . Note that most of our simulations will have  $\nu$  and  $\eta$  sufficiently small that the viscous and resistive time steps are large compared to  $\Delta t_{\text{CTU}}$ .

In all of our simulations,  $\nu$  and  $\eta$  are parameterized in terms of the Reynolds number,

$$Re \equiv \frac{c_s H}{\nu}, \quad (5.9)$$

the magnetic Reynolds number,

$$Rm \equiv \frac{c_s H}{\eta}, \quad (5.10)$$

and the magnetic Prandtl number,

$$P_m \equiv \frac{\nu}{\eta} = \frac{Rm}{Re}. \quad (5.11)$$

The  $Re$ ,  $Rm$ , and  $P_m$  values are constant both in space and time,  $c_s$  is the isothermal sound speed, and  $H$  is the disk scale height as defined below.

### 5.3 Resolving Physical Dissipation in Unstratified Disks

The highest resolution runs of Davis et al. (2010) with physical dissipation have 64 grid zones per  $H$  (Davis, private communication). We have performed shearing boxes at this resolution, but simulations with sufficiently long evolution times to capture the observed long timescale variability are very computationally expensive. Since one of the goals of this work is a larger exploration of  $\nu$  and  $\eta$  parameter space, we have run most of our production simulations at 32 zones per  $H$ . To address the issue of resolving physical dissipation at this lower resolution, we begin with a resolution study of isothermal, unstratified shearing box simulations including physical dissipation.

The first set of unstratified simulations are the zero net magnetic flux shearing boxes investigated in Fromang et al. (2007) and Chapter 4; see Table 5.1. Specifically, they are initialized with  $\mathbf{B} = \sqrt{2P_o/\beta}\sin[(2\pi/L_x)x]\hat{\mathbf{z}}$  where  $\beta = 400$ . These runs are labelled with “SZ” for “Sine Z” (see Table 5.1). The isothermal sound speed is  $c_s = 0.001$ , corresponding to an initial gas pressure  $P_o = 10^{-6}$  with initial density  $\rho_o = 1$ . The orbital velocity of the local domain is  $\Omega = 0.001$ . Note that in these simulations, we define the scale height to be  $H \equiv c_s/\Omega = 1$ , which is a slightly different definition than for the vertically stratified simulations below (by a factor of  $\sqrt{2}$ ). In what follows, the SZ runs will have this definition of  $H$ , and the second set of unstratified simulations will have the definition of  $H$  given by equation (5.13).

All of these runs are initialized with physical dissipation, and we study four different cases of  $Re$ ,  $P_m$  values;  $Re = 800$ ,  $P_m = 16$ ;  $Re = 3125$ ,  $P_m = 4$ ;  $Re = 6250$ ,  $P_m = 1$ ; and  $Re = 12800$ ,  $P_m = 2$ . In each case, several resolutions are run in order to study convergence: 16, 32, and 64 grid zones per  $H$ . The labeling scheme of the

runs refers to resolution, field geometry, and dissipation values; e.g., 16SZRe800Pm16 corresponds to 16 zones per  $H$ , the ‘‘Sine Z’’ geometry, and  $Re = 800$ ,  $P_m = 16$ .

The MRI is seeded with random perturbations to the density and the velocity components introduced at the grid scale. The amplitude of the density perturbations is  $\delta\rho = 0.01$  and the amplitude of the velocity perturbations is  $(1/5)\delta\rho c_s$  for each component (though, a different randomization is applied for each component). We do not employ orbital advection in these simulations. All simulations are run to 400 orbits, except for the runs in which the turbulence decays and also 32SZRe800Pm16 and 32SZRe3125Pm4, which were run to 289 orbits and 246 orbits, respectively. We also include some higher resolution simulations from Chapter 4 in this work for additional information.

Figure 5.1 shows the resolution dependence of the time- and volume-averaged stress normalized by the gas pressure, the so-called  $\alpha$  parameter,

$$\alpha \equiv \left\langle \frac{\langle \rho v_x \delta v_y - B_x B_y \rangle}{\langle P \rangle} \right\rangle, \quad (5.12)$$

where the interior brackets denote a volume average, and the exterior brackets denote a time average. The volume average is calculated over the entire simulation domain, and the time average is calculated from orbit 20 to the end of the run. Since the gas is isothermal,  $\langle P \rangle = \langle \rho \rangle c_s^2$ . Note that the  $N_x = 128$  data points were taken from Chapter 4.  $N_y/N_x = 4$  in the simulations presented here, which differs from the Chapter 4 runs where  $N_y = 200$  and  $N_y/N_x = 1.56$ . Furthermore, the calculations done in Chapter 4 were performed with the Roe method for the Riemann solver, in contrast to the HLLD solver used here. We do not believe that these differences will lead to substantial deviations in the calculated  $\alpha$  values. To test this hypothesis, we have run both 64SZRe800Pm16 and 64SZRe3125Pm4 with the same version of

Table 5.1. Unstratified Simulations to Calibrate Physical Dissipation

| Label                       | $Re$  | $Rm$  | $P_m$ | Resolution<br>(zones per $H$ ) | $\alpha$           | Description                                  |
|-----------------------------|-------|-------|-------|--------------------------------|--------------------|--|
| 16SZRe800Pm16               | 800   | 12800 | 16    | 16                             | 0.011              | zero net flux                                |
| 32SZRe800Pm16               | 800   | 12800 | 16    | 32                             | 0.033              | zero net flux                                |
| 64SZRe800Pm16               | 800   | 12800 | 16    | 64                             | 0.042              | zero net flux                                |
| 128SZRe800Pm16 <sup>a</sup> | 800   | 12800 | 16    | 128                            | 0.046              | zero net flux                                |
| 16SZRe3125Pm4               | 3125  | 12500 | 4     | 16                             | 0.0043             | zero net flux                                |
| 32SZRe3125Pm4               | 3125  | 12500 | 4     | 32                             | 0.013              | zero net flux                                |
| 64SZRe3125Pm4               | 3125  | 12500 | 4     | 64                             | 0.015              | zero net flux                                |
| 128SZRe3125Pm4 <sup>a</sup> | 3125  | 12500 | 4     | 128                            | 0.013              | zero net flux                                |
| 16SZRe6250Pm1               | 6250  | 6250  | 1     | 16                             | decay              | zero net flux                                |
| 32SZRe6250Pm1               | 6250  | 6250  | 1     | 32                             | decay              | zero net flux                                |
| 64SZRe6250Pm1               | 6250  | 6250  | 1     | 64                             | decay              | zero net flux                                |
| 16SZRe12800Pm2              | 12800 | 25600 | 2     | 16                             | 0.0078             | zero net flux                                |
| 32SZRe12800Pm2              | 12800 | 25600 | 2     | 32                             | 0.010              | zero net flux                                |
| 64SZRe12800Pm2              | 12800 | 25600 | 2     | 64                             | 0.0078             | zero net flux                                |
| 32FTNum                     | -     | -     | -     | 32                             | 0.021              | flux tube, num. dissipation                  |
| 32FTNum $\beta$ 1000        | -     | -     | -     | 32                             | 0.020 <sup>b</sup> | flux tube, num. dissipation, $\beta = 1000$  |
| 32FTNum $\beta$ 10000       | -     | -     | -     | 32                             | 0.018 <sup>b</sup> | flux tube, num. dissipation, $\beta = 10000$ |
| 32FTRe800Pm4                | 800   | 3200  | 4     | 32                             | 0.028              | restarted from 32FTNum                       |
| 32FTRe800Pm8                | 800   | 6400  | 8     | 32                             | 0.041              | restarted from 32FTNum                       |
| 32FTRe1600Pm0.5             | 1600  | 800   | 0.5   | 32                             | decay              | restarted from 32FTNum                       |
| 32FTRe1600Pm1 $\beta$ 1000  | 1600  | 1600  | 1     | 32                             | decay              | restarted from 32FTNum $\beta$ 1000          |
| 32FTRe1600Pm2               | 1600  | 3200  | 2     | 32                             | 0.018              | restarted from 32FTNum                       |
| 32FTRe1600Pm2 $\beta$ 1000  | 1600  | 3200  | 2     | 32                             | 0.015 <sup>c</sup> | restarted from 32FTNum $\beta$ 1000          |
| 32FTRe1600Pm2 $\beta$ 10000 | 1600  | 3200  | 2     | 32                             | decay              | restarted from 32FTNum $\beta$ 10000         |
| 32FTRe1600Pm4               | 1600  | 6400  | 4     | 32                             | 0.029              | restarted from 32FTNum                       |
| 32FTRe6400Pm0.5             | 6400  | 3200  | 0.5   | 32                             | 0.0094             | restarted from 32FTNum                       |

<sup>a</sup>These runs were taken from Chapter 4<sup>b</sup>Time average done from orbit 20 to 110<sup>c</sup>Time average done from orbit 120 to 400

Athena and setup used in Chapter 4. Averaging from 20 to 100 orbits in each case, we find  $\alpha = 0.036$  and  $\alpha = 0.014$  for the  $Re = 800$ ,  $P_m = 16$  and  $Re = 3125$ ,  $P_m = 4$ , respectively; the differences in  $\alpha$  are not large compared to the change in going from 16 to 32 zones per  $H$ .

For the sustained turbulence simulations,  $\alpha$  appears to be converging with resolution. More specifically, by 32 grid zones per  $H$ ,  $\alpha$  appears to be within a factor of  $\sim 1.4$  of the corresponding value at 128 zones per  $H$ . There is also a considerable change in  $\alpha$  as one decreases the resolution to 16 zones per  $H$ , at least for 32SZRe800Pm16 and 32SZRe3125Pm4. All resolutions with  $Re = 6250$  and  $P_m = 1$  have decayed turbulence in agreement with the higher resolution simulations of Fromang et al. (2007).

The second set of unstratified simulations contain a net toroidal field. The runs with physical dissipation are initiated from the turbulent state (at  $t = 100$  orbits) of a run with only numerical dissipation. While these are not vertically stratified simulations, we define  $H$  to be that of a stratified, isothermal disk,

$$H = \frac{\sqrt{2}c_s}{\Omega}. \quad (5.13)$$

The isothermal sound speed,  $c_s = 7.07 \times 10^{-4}$ , corresponding to an initial value (and mid-plane value in stratified simulations) for the gas pressure of  $P_o = 5 \times 10^{-7}$ . With  $\Omega = 0.001$ , the value for the scale height is  $H = 1$ .

In the numerical dissipation run, the initial  $B_x$  and  $B_z$  are calculated from the  $y$  component of the vector potential,

$$A_y = \begin{cases} -\sqrt{\frac{2P_o}{\beta_p}} \frac{H}{2\pi} [1 + \cos(\frac{2\pi r}{H})] & \text{if } r < \frac{H}{2} \\ 0 & \text{if } r \geq \frac{H}{2} \end{cases} \quad (5.14)$$

where  $r = \sqrt{x^2 + z^2}$  and  $\beta_p = 1600$  is the poloidal field  $\beta$  value. The initial  $B_y$  is given by

$$B_y = \begin{cases} \sqrt{\frac{2P_\alpha}{\beta_y} - (B_x^2 + B_z^2)} & \text{if } B_x^2 + B_z^2 \neq 0 \\ 0 & \text{if } B_x^2 + B_z^2 = 0 \end{cases} \quad (5.15)$$

where  $\beta_y = 100$  is the toroidal field  $\beta$  value. This field configuration is the twisted azimuthal flux tube of Hirose et al. (2006), with minor modifications to the dimensions and  $\beta$  values. We seed the MRI with the same perturbations as the SZ runs described above.

These parameters and initial conditions were chosen to match those used in the vertically stratified simulations of § 5.4. These runs are labelled using the same scheme as the SZ simulations, but with “FT” for “Flux Tube” (see Table 5.1). Also, for simulations with no physical dissipation, we replace the “RePm” with “Num” for “Numerical dissipation”. The domain size is  $L_x = 2H$ ,  $L_y = 4H$ , and  $L_z = 1H$ , and the resolution is 32 zones per  $H$ . Orbital advection is employed in these calculations.

The calculation with only numerical dissipation was run to 150 orbits and has an  $\alpha$  value of 0.021, where the time average is done from orbit 20 to orbit 150. The simulations with physical dissipation were all run out to 220 orbits and the time history of the volume-averaged stress is displayed in Fig. 5.2. There is a clear dependence on the dissipation parameters and on  $P_m$  in particular (note that 32FTRe800Pm4 and 32FTRe1600Pm4 have the same  $P_m$  and nearly the same saturation level). For large enough resistivity (i.e., low  $Rm$ ), the turbulence decays; the critical  $Rm$  value is  $\sim 1000$ , in agreement with the higher resolution simulations of Chapter 4.

Averaging from orbit 120 to the end of the simulation, we calculate  $\alpha$ , and in Fig. 5.3, we plot  $\alpha$  versus  $P_m$  for these low resolution runs along with the higher

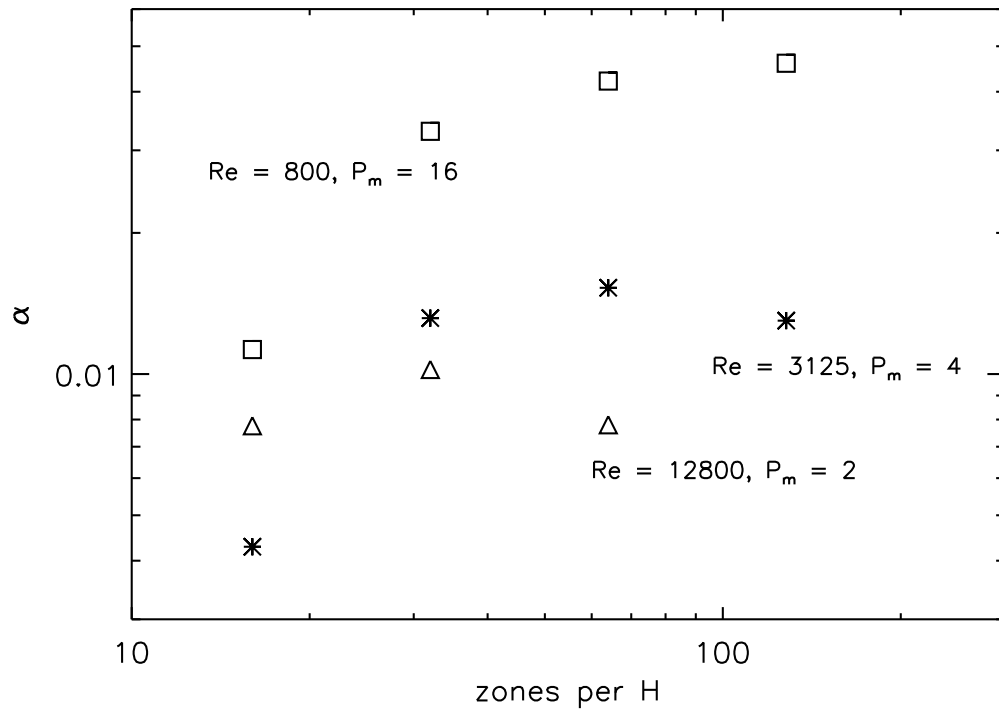


Fig. 5.1.— Time- and volume-averaged stress parameter  $\alpha$  as a function of grid zones per  $H$  in the SZ simulations;  $\alpha \equiv \langle \langle \rho v_x \delta v_y - B_x B_y \rangle \rangle / \langle P \rangle$ , where the average is calculated over the entire simulation domain and from 20 orbits to the end of the simulation. Only simulations with sustained turbulence are plotted. By 32 zones per  $H$ , the  $\alpha$  values appear to be relatively close to the higher resolution values.

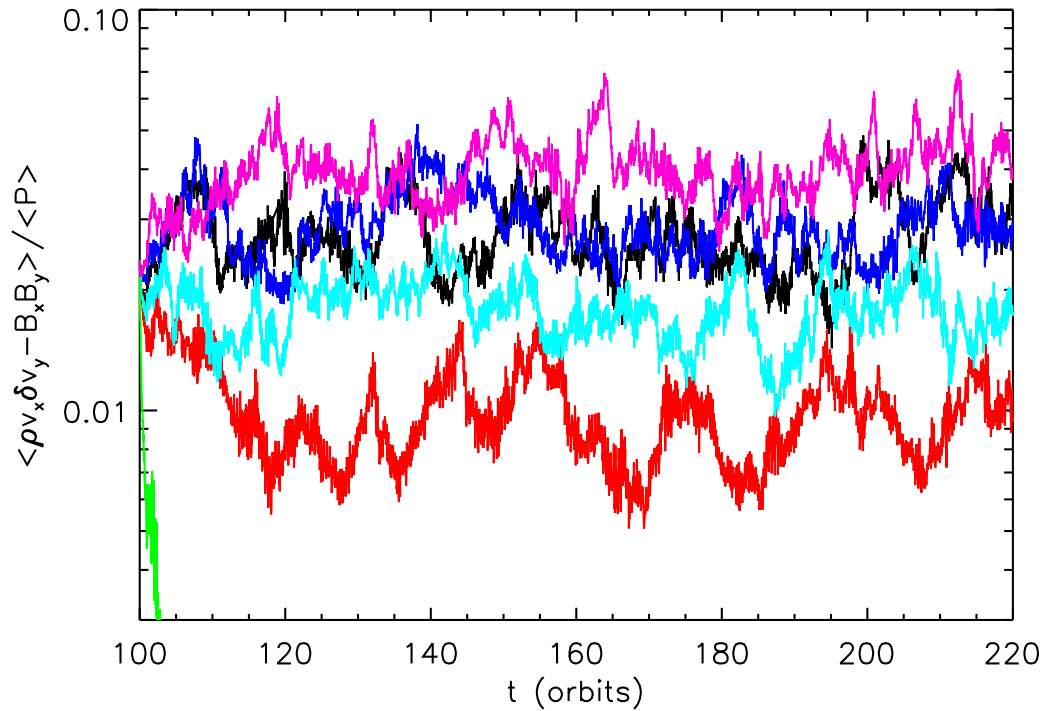


Fig. 5.2.— Volume-averaged Reynolds and Maxwell stresses normalized by the the volume-averaged gas pressure as a function of time in orbits in the unstratified, net toroidal field simulations. The black line corresponds to  $Re = 800$  and  $P_m = 4$ , magenta is  $Re = 800$  and  $P_m = 8$ , green is  $Re = 1600$  and  $P_m = 0.5$ , light blue is  $Re = 1600$  and  $P_m = 2$ , dark blue is  $Re = 1600$  and  $P_m = 4$ , and red is  $Re = 6400$  and  $P_m = 0.5$ . There is a clear dependence on  $P_m$ , and for sufficiently low  $Rm$ , the turbulence decays.

resolution counterparts of Chapter 4 (see Table 4.3). The dashed lines are a linear fit to the data in log-log space. From this linear fit, we calculate the parameter  $\delta$  in  $\alpha \propto P_m^\delta$ . For 32 grid zones per  $H$ ,  $\delta = 0.54$ , and for 128 grid zones per  $H$ ,  $\delta = 0.33$ ; there is a steeper  $P_m$  dependence at lower resolution. Furthermore, all  $\alpha$  values for the higher resolution simulations are larger than those in the lower resolution simulations. Again, the comparison between these two resolutions carries some uncertainty due to a difference in the details of the various simulations.

There are several points to make from these results. First, for zero net field calculations, the MRI saturation level does *not* continually decrease with increasing resolution in the presence of physical dissipation in contrast to simulations with only numerical dissipation (Fromang & Papaloizou 2007, Chapter 3). This is in agreement with the recent results of Fromang (2010), which show that even the presence of small  $\nu$  and  $\eta$  is sufficient to provide convergence in the zero net flux shearing box.

Furthermore, both the zero net flux and net toroidal flux results suggest that only moderate resolutions (i.e., 32 grid zones per  $H$ ) may be necessary to capture the general effects of changing  $\nu$  and  $\eta$ , at least for the range of  $Re$ ,  $Rm$ , and  $P_m$  values considered here. This contrasts with the assumption usually made that one must choose a sufficiently high resolution to ensure that the effective numerical dissipation scale is below the viscous and resistive dissipation scales (see e.g., Fromang et al. 2007, and Chapters 3 & 4). This is not to say that everything is sufficiently converged at 32 grid zones per  $H$ . Indeed, Fig. 5.3 shows a significant resolution effect. However, the general dependence of  $\alpha$  on dissipation parameters appears to be captured, even at these resolutions. This is an important point for our main calculations, in which we are limited to 32 grid zones per  $H$  for a comprehensive study of physical dissipation effects.

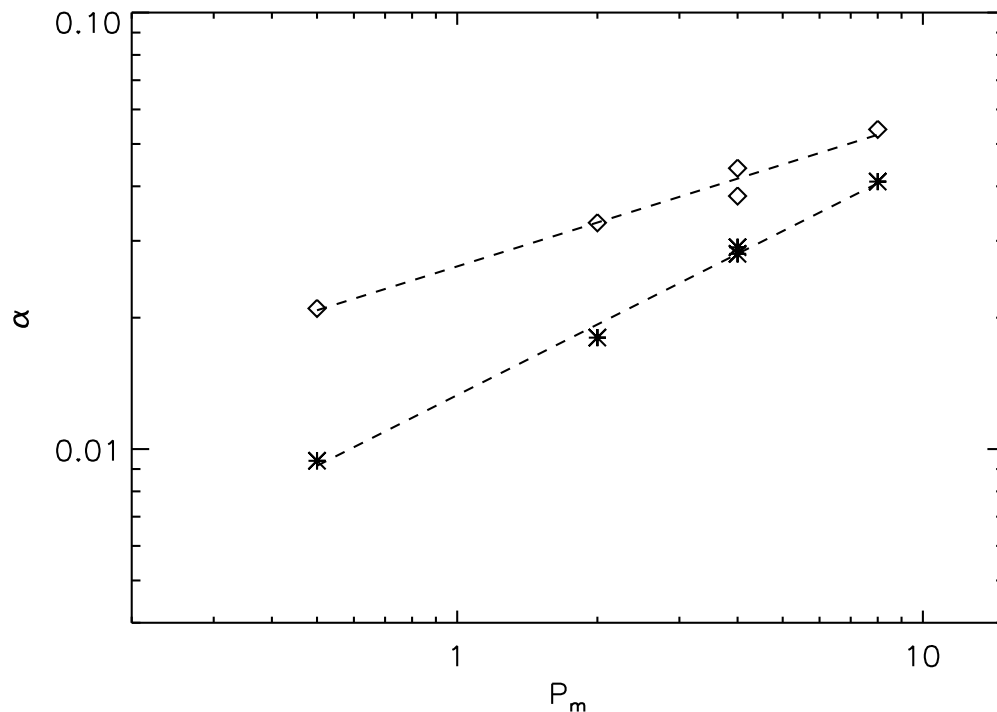


Fig. 5.3.— Time- and volume-averaged stress parameter  $\alpha$  as a function of  $P_m$  in the lower resolution FT simulations (asterisks) and the higher resolution, net toroidal field simulations of Chapter 4 (diamonds). In the FT simulations,  $\alpha \equiv \langle \langle \rho v_x \delta v_y - B_x B_y \rangle \rangle / \langle P \rangle$ , whereas in the higher resolution simulations,  $\alpha \equiv \langle \langle \rho v_x \delta v_y - B_x B_y \rangle \rangle / P_o$ ; see Chapter 4. These definitions are roughly equivalent since  $\langle P \rangle \approx P_o$ . For the FT simulations, the average is calculated over the entire simulation domain and from 120 orbits to the end of the simulation. Only simulations with sustained turbulence are plotted. The dashed lines are linear fits to the data in log-log space. Both resolutions show a clear  $P_m$  dependence, but this dependence is steeper at the lower resolution.

## 5.4 Vertically Stratified Simulations

In this section, we describe a series of vertically stratified, isothermal shearing box simulations that investigate the interplay between physical dissipation and vertical gravity. As such, we have run various  $Re$ ,  $Rm$ ,  $P_m$  combinations, summarized in Table 5.2. All physical dissipation calculations are initialized from the turbulent state of a baseline run with only numerical dissipation. The restart time from this baseline simulation is 100 orbits. All  $\alpha$  values are calculated via equation (5.12) with the volume average obtained over all  $x$  and  $y$  and for  $|z| \leq 2H$ .

### 5.4.1 Baseline Simulations

Before investigating the effect of dissipation coefficients, we describe our baseline runs without physical dissipation. The initial conditions for these runs are as follows. The density stratification corresponds to the hydrostatic equilibrium solution for a constant temperature throughout the domain,

$$\rho(x, y, z) = \rho_o \exp\left(-\frac{z^2}{H^2}\right), \quad (5.16)$$

where  $\rho_o = 1$  is the mid-plane density, and  $H$  is the scale height in the disk, as defined in § 5.3. A density floor of  $10^{-4}$  is applied to the physical domain at all times to ensure that the density does not get too small in the upper layers of the disk. A very small density leads to a large Alfvén speed and a very small time step. Furthermore, we have found that very small densities can lead to numerical effects that ultimately crash the code. All other parameters and initial conditions are identical to the corresponding FT runs of § 5.3.

The baseline calculation is done at 32 and 64 grid zones per  $H$ ; these runs are

Table 5.2. Vertically Stratified Shearing Box Simulations

| Label           | $Re$ | $Rm$ | $P_m$ | Resolution<br>(zones per $H$ ) | Integration time<br>$t_{\text{stop}} - t_{\text{start}}$ (orbits) | Description   |
|-----------------|------|------|-------|--------------------------------|---|---|
| 32Num           | –    | –    | –     | 32                             | 1058  | num. dissipation                                      |
| 32Re800Pm4      | 800  | 3200 | 4     | 32                             | 487   | –   |
| 32Re800Pm8      | 800  | 6400 | 8     | 32                             | 325   | –   |
| 32Re1600Pm0.5   | 1600 | 800  | 0.5   | 32                             | 263   | –   |
| 32Re1600Pm2     | 1600 | 3200 | 2     | 32                             | 1082  | –   |
| 32Re1600Pm4     | 1600 | 6400 | 4     | 32                             | 488   | –   |
| 32Re6400Pm0.5   | 6400 | 3200 | 0.5   | 32                             | 863   | –   |
| 32Re6250Pm1     | 6250 | 6250 | 1     | 32                             | 337   | –   |
| 32Re1600Pm2_By+ | 1600 | 3200 | 2     | 32                             | 584   | $B_y$ added at 50 orbits<br>net $B_x$ within midplane |
| 32ShearBx       | –    | –    | –     | 32                             | 45  | num. dissipation                                      |
| 64Num           | –    | –    | –     | 64                             | 159   | –   |
| 64Re800Pm4      | 800  | 3200 | 4     | 64                             | 84  | –   |
| 64Re1600Pm0.5   | 1600 | 800  | 0.5   | 64                             | 108   | –   |
| 64Re1600Pm2     | 1600 | 3200 | 2     | 64                             | 80  | –   |
| 64Re1600Pm4     | 1600 | 6400 | 4     | 64                             | 80  | –   |
| 64Re6400Pm0.5   | 6400 | 3200 | 0.5   | 64                             | 83  | –   |

32Num and 64Num in Table 5.2, respectively. 32Num is run to a total integration time of 1058 orbits; it has sustained turbulence at a level of  $\alpha = 0.028$ , where the time average is done from orbit 20 until the end of the calculation. 64Num is run to 159 orbits, and the turbulence is sustained with  $\alpha = 0.022$ , where the time average is done from orbit 20 until the end of the simulation.

One particularly useful diagnostic in these vertically stratified simulations is the space-time diagram of horizontally averaged quantities. Space-time plots of horizontally averaged  $B_y$  and total stress normalized by the volume-averaged gas pressure (within  $|z| \leq 2H$ ) for a 100 orbit period in the 64Num simulation are shown in Fig. 5.4. One can see from the top panel that  $B_y$  undergoes sign flipping accompanied by rising into the upper disk regions. This behavior has been noted in previous vertically stratified shearing boxes (e.g., Brandenburg et al. 1995; Stone et al. 1996; Hirose et al. 2006; Guan 2009; Shi et al. 2010; Gressel 2010; Davis et al. 2010), and the fact that our simulations reproduce it supports the robustness of this behavior. The period of this sign flipping is  $\sim 10$  orbits at both resolutions.

Two additional quantities are shown in the top panel. The white contours denote where the gas  $\beta$  value switches from greater than to less than unity. For  $|z| \gtrsim 2-2.5H$ ,  $\beta < 1$ , except for some regions very near the vertical boundaries where  $\beta > 1$  as a result of there being no magnetic field there. The black contours denote where the fluid becomes buoyantly unstable. Specifically, we follow the criterion of Newcomb (1961) as outlined in Guan (2009): The gas is buoyantly stable if

$$\left| \frac{d\rho}{dz} \right| > \left| \frac{\rho^2 g}{\gamma P} \right| \quad (5.17)$$

where  $\gamma = 1$  here because the gas is isothermal. The figure shows that for  $|z| \gtrsim 2H$ , the fluid is unstable to buoyancy and the slope of the  $B_y$  structures changes in the

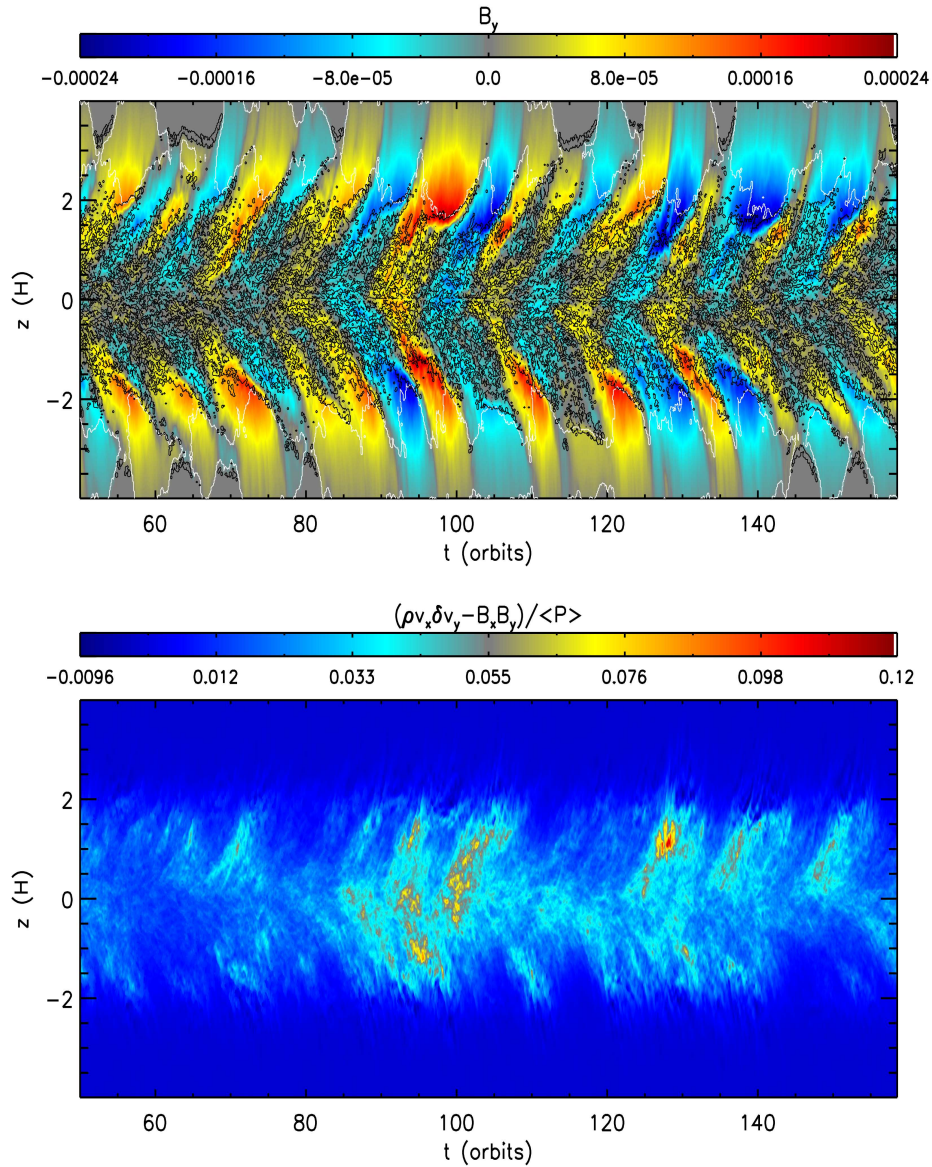


Fig. 5.4.— Space-time diagram of the horizontally averaged  $B_y$  (top panel) and total stress normalized by the volume-averaged gas pressure (bottom panel). The volume-average is done for all  $x$  and  $y$  and for  $|z| \leq 2H$ . The white contours on the top panel denote where  $\beta$  goes from greater to less than unity, and the black contours mark the boundaries between buoyantly stable and unstable gas. The horizontally averaged  $B_y$  appears to rise vertically into the upper  $z$  layers, being replaced in the mid-plane region by  $B_y$  of the opposite sign. The rise speed of the field increases after  $|z| \sim 2H$  is reached. The sign flipping in  $B_y$  has a period of  $\sim 10$  orbits.

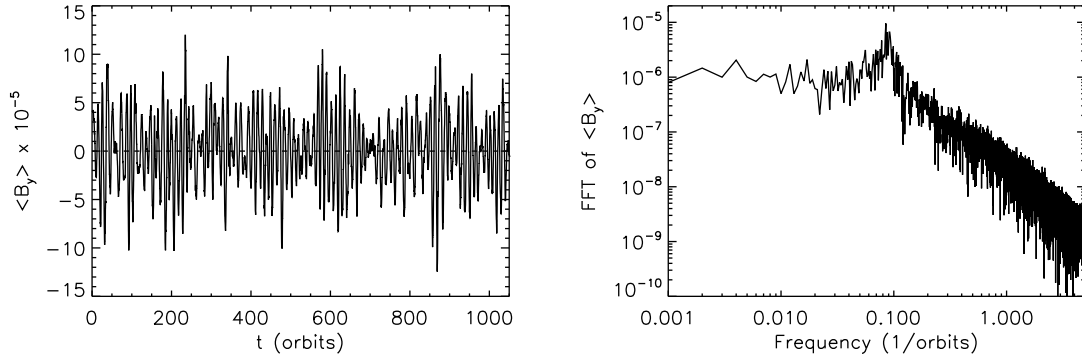


Fig. 5.5.— Left: Time evolution of volume-averaged  $B_y$  in 32Num. The volume average is done for all  $x$  and  $y$  and for  $|z| \leq 0.5H$ . The dashed line corresponds to  $\langle B_y \rangle = 0$ . Right: Temporal power spectrum of  $\langle B_y \rangle$  from the left plot, calculated from orbit 50 to 1050. The 10 orbit period oscillations in  $\langle B_y \rangle$  are immediately apparent in both plots, particularly as the peak in the power spectrum. The 10 orbit oscillations are modulated on longer timescales, ranging from tens to hundreds of orbits.

space-time diagram; the field rises faster for  $|z| \gtrsim 2H$ . For  $|z| \lesssim 2H$ , there are regions of buoyant instability and stability, and it is within this region that the MRI appears to be active as suggested by the bottom panel of the figure. Indeed, the total stress appears to drop off rapidly near  $|z| \sim 2H$ . It may be that the marginal buoyancy stability coupled with the turbulence induced via the MRI leads to a slower rise of field structures up until  $|z| \sim 2H$ , where the gas then becomes buoyantly unstable. These results are consistent with the recent ZEUS calculations of Guan (2009) with large radial extent as well as with Shi et al. (2010) using a version of ZEUS that includes radiation physics and total energy conservation. In particular, the top panel of Fig. 5.4 looks very similar to Figure 6 in Shi et al. (2010).

The oscillation of the volume-averaged toroidal field (within  $|z| \leq 0.5H$ ) is depicted more clearly in Fig. 5.5, which shows the evolution of this field and its temporal power spectrum. The figure shows that the 10 orbit period oscillation is dominant, and the oscillation amplitude appears to be modulated on longer timescales, ranging

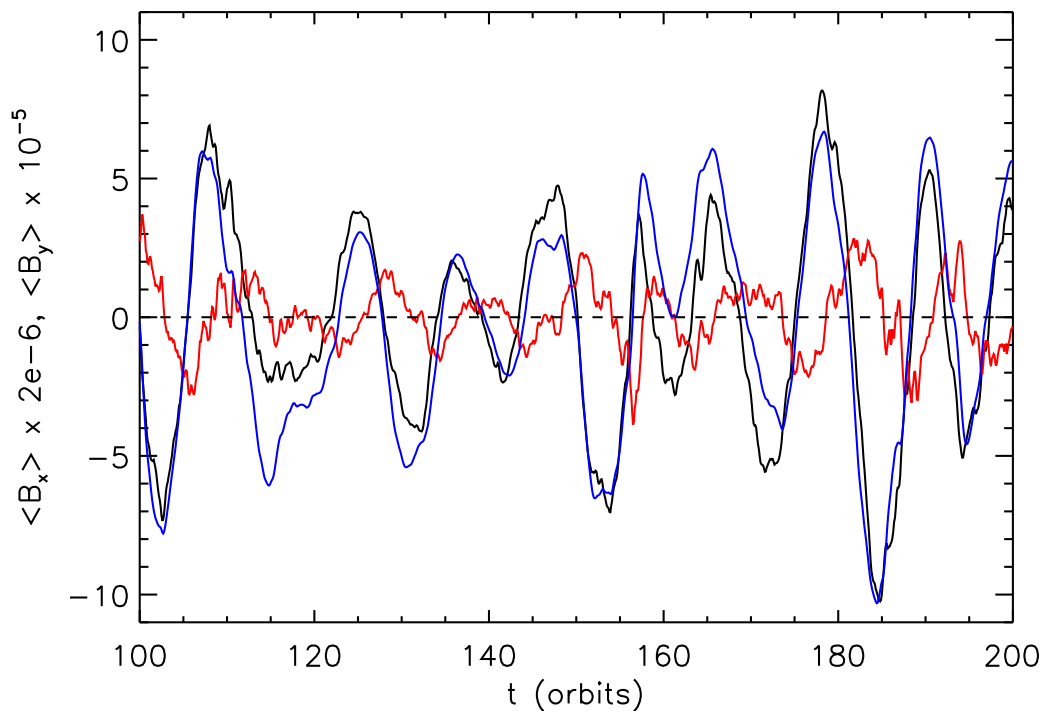


Fig. 5.6.— Time evolution of volume-averaged field components for part of 32Num. Red is  $\langle B_x \rangle$ , black is  $\langle B_y \rangle$ , and blue is  $\langle B_y \rangle$  as calculated from  $\langle B_x \rangle$  using a simple toy model discussed in the text. The volume average is done for all  $x$  and  $y$  and for  $|z| \leq 0.5H$ . The dashed line corresponds to  $\langle B_{x,y} \rangle = 0$ .  $\langle B_x \rangle$  has been multiplied by a factor of 5 relative to  $\langle B_y \rangle$  to make a more direct comparison possible. The variations in  $\langle B_x \rangle$  are accompanied by variations in  $\langle B_y \rangle$ , which are offset in time, and the toy model shows that the evolution of  $\langle B_y \rangle$  is controlled by shear of radial field and buoyant removal of toroidal field.

from tens to hundreds of orbits.

Furthermore, the averaged radial field appears to exhibit the same 10 orbit cyclic behavior as the toroidal field, but with a slight temporal lag, as shown in Fig. 5.6. This plot resembles very closely the behavior of the  $\alpha$ -dynamo model derived in Guan (2009). Specifically, the authors write simplified evolution equations for volume-averaged horizontal field components assuming an  $\alpha$  dynamo;

$$\frac{d\langle B_y \rangle}{dt} = -q\Omega\langle B_x \rangle - \frac{|v_A|}{2H}\langle B_y \rangle + \frac{\alpha_1}{2H}\langle B_x \rangle, \quad (5.18)$$

$$\frac{d\langle B_x \rangle}{dt} = -\frac{|v_A|}{2H}\langle B_x \rangle - \frac{\alpha_2}{2H}\langle B_y \rangle \quad (5.19)$$

The first term on the right hand side of equation (5.18) is simply the shear of radial field into toroidal. The second term is the buoyant rise of toroidal field, which is estimated to have a characteristic buoyant velocity equal to the Alfvén speed, and the Alfvén speed is approximated as the toroidal field Alfvén speed. The third term is the  $\alpha$ -dynamo term coupling  $B_x$  to the evolution of  $B_y$ . Equation (5.19) is nearly identical, except there is no shear term and the toroidal and radial field components have been flipped with respect to equation (5.18). Also, note that in general  $\alpha_1 \neq \alpha_2$ .

Guan (2009) numerically integrated this set of equations assuming  $\alpha_1 = \alpha_2 = -0.01$  and found a solution that looks strikingly similar to the red and black curves in Fig. 5.6. As a related experiment, we have numerically integrated the  $\langle B_y \rangle$  evolution equation using our simulation data for  $\langle B_x \rangle$  (the red curve) and the initial condition for  $\langle B_y \rangle$  taken from  $\langle B_y \rangle$  at  $t = 0$ . We have set  $\alpha_1 = 0$  but have kept the shear and buoyancy terms. The result is shown in the same figure as the blue curve. The agreement between the actual evolution of  $\langle B_y \rangle$  and the “modeled” evolution suggests that the evolution of the toroidal field within the mid-plane region is almost

completely controlled by the shearing of radial field and the buoyant removal of the generated toroidal field.

The remaining question, then, is what creates the radial field? If we set  $\alpha_2 = 0$  and numerically integrate the above equations assuming some initial conditions, both field components decay away. Along with those of Guan (2009), these results support the idea of an  $\alpha$ -dynamo, but what mechanism is responsible for  $\alpha_2 \neq 0$ ? The most likely candidate is MRI turbulence; turbulent fluctuations create EMFs that generate poloidal field (e.g., Brandenburg et al. 1995; Davis et al. 2010; Gressel 2010), but the physics of how this is accomplished is still not well understood.

In Fig. 5.7, we plot the time- and horizontally-averaged vertical distributions of various quantities. The data correspond to 32Num, and the time average is done from orbit 100 to the end of the calculation. The figure shows that the stress drops off rapidly near  $|z| \sim 2H$ . The shape of the distribution is generally the same for both Maxwell and Reynolds stresses, with the Maxwell stress always greater than the Reynolds stress by a factor that varies from 2.3 to 5.6 depending on  $z$ ; this factor is  $\sim 4$  when averaged over all  $z$ , in agreement with unstratified simulations (e.g., Hawley et al. 1995). Furthermore, as shown in the bottom two panels, the magnetic pressure is relatively flat and less than the gas pressure for  $|z| \lesssim 2H$ , whereas the upper layers of the disk are dominated by the magnetic energy which decreases with height. These results are consistent with previous studies of isothermal disks (Stone et al. 1996; Miller & Stone 2000; Guan 2009). What is perhaps even more interesting, however, is that the vertical structure of the turbulence is also consistent with simulations containing more complex physics, such as radiation pressure (Hirose et al. 2006; Krolik et al. 2007; Hirose et al. 2009). There are some differences between our results and other works, however. For example, we do not observe the double

peak profile in the stress as seen in the radiation-pressure-dominated simulations of Hirose et al. (2009).

Finally, we examine the three-dimensional structure of the magnetic field in the fully turbulent gas. A streamline integration of 32Num at  $t = 100$  orbits is shown in Fig. 5.8. The field strength is denoted by color rather than field line density. Within  $|z| \lesssim 2H$ , the field is primarily toroidal but has a smaller scale, tangled structure in the  $x$  and  $z$  directions. Very near the vertical boundaries, however, the field appears to develop larger excursions from being purely toroidal. We have checked several snapshots throughout the evolution of 32Num and find that this structure is typical of the saturated state, except for at  $t = 550$  orbits, in which the field near the boundaries is primarily vertical. It is not clear whether or not the different field structure at large  $|z|$  is a physical effect or simply due to the boundary conditions. Consider the shearing box in Hirose et al. (2006), which uses a vertical domain twice as large as 32Num. Comparing to their Fig. 16, the field structure of 32Num at  $|z| \sim 4H$  appears to be less toroidal. In fact, the field structure at this  $|z|$  in 32Num resembles more closely the field structure at  $|z| \sim 8H$  in their simulation. This may indicate the role of the vertical outflow boundary conditions on influencing the field structure very near the boundaries. Away from the vertical boundaries, the magnetic field in 32Num appears to have a very similar structure to that in Hirose et al. (2006).

#### 5.4.2 Turbulent and Non-turbulent States

Having established the baseline simulations without physical dissipation, we now turn to examining the effect of changing  $\nu$  and  $\eta$ . The relevant runs are listed in Table 5.2, with the labeling scheme of number of grid zones per  $H$ ,  $Re$ ,  $P_m$ ; thus, 32Re800Pm8 is a simulation at 32 zones per  $H$ ,  $Re = 800$ , and  $P_m = 8$ . The total stress time

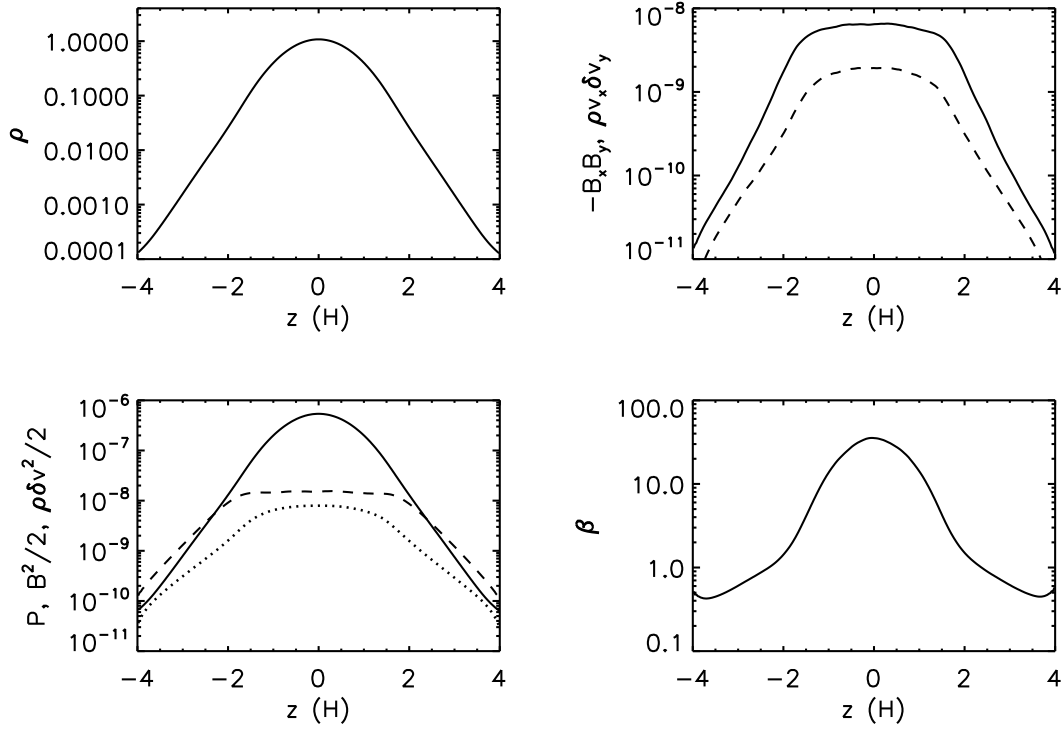


Fig. 5.7.— Time- and horizontally-averaged vertical distributions of various quantities in 32Num. Upper left: gas density; upper right: Maxwell (solid) and Reynolds (dashed) stresses; lower left: gas pressure (solid), magnetic energy (dashed), and kinetic energy (dotted); lower right: gas  $\beta$  defined as the time- and horizontally-averaged gas pressure divided by the time- and horizontally-averaged magnetic energy density. The time average is done from orbit 100 to the end of the simulation. The stress and magnetic energy is relatively flat for  $|z| \lesssim 2H$  but drops off substantially for larger  $|z|$ . Outside of  $|z| \sim 2H$ , the magnetic energy dominates over gas pressure.

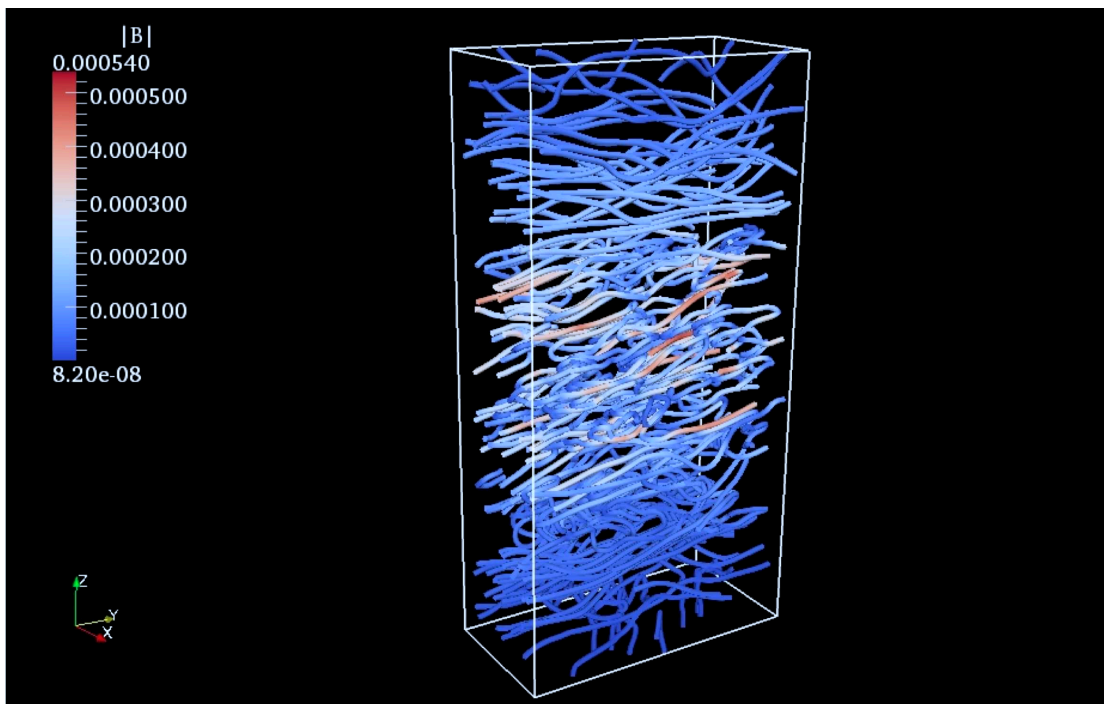


Fig. 5.8.— Magnetic field structure at  $t = 100$  orbits in 32Num, produced via a stream line integration. The field strength (in code units) is displayed via color and not the density of the field lines. The magnetic field has a primarily toroidal structure but has a smaller, tangled structure in the  $x$  and  $z$  directions.

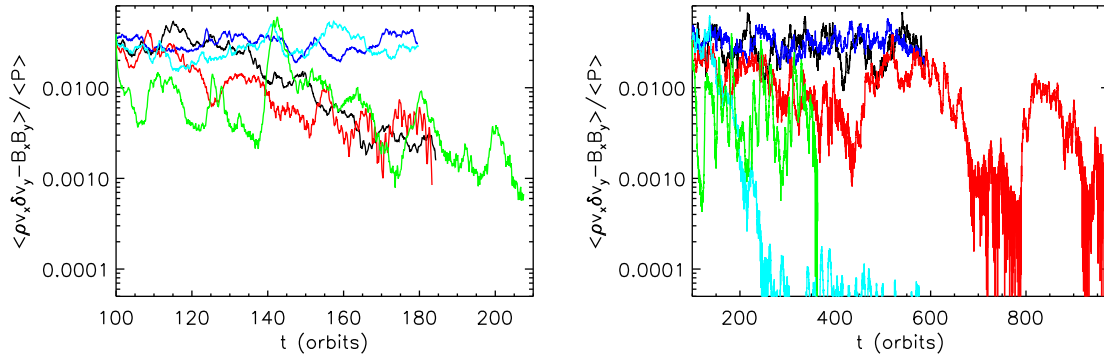


Fig. 5.9.— Volume-averaged Reynolds and Maxwell stresses normalized by the volume-averaged gas pressure as a function of time in orbits in the vertically stratified simulations at 64 (left) and 32 (right) grid zones per  $H$ . The volume-average is done for all  $x$  and  $y$  and for  $|z| \leq 2H$ . The black line corresponds to  $Re = 800$  and  $P_m = 4$ , green is  $Re = 1600$  and  $P_m = 0.5$ , light blue is  $Re = 1600$  and  $P_m = 2$ , dark blue is  $Re = 1600$  and  $P_m = 4$ , and red is  $Re = 6400$  and  $P_m = 0.5$ . Some of the simulations appear to undergo periods of decay followed by regeneration of the MRI. This can occur on very long timescales of  $\sim 100$  orbits in some cases.

evolution for a subset of these simulations performed with 64 zones per  $H$  is shown in the left panel of Fig. 5.9. From the figure, it would appear that 64Re6400Pm0.5, 64Re1600Pm0.5, and 64Re800Pm4 have decaying turbulence, while turbulence is sustained in the remaining simulations. Furthermore, 64Re1600Pm0.5 undergoes periods of enhanced stress followed by decay, though the overall trend is a decreasing average stress level with time.

The right panel of Fig. 5.9 is the stress evolution for the equivalent simulations with 32 zones per  $H$ . There is considerable variability on long timescales; 32Re6400Pm0.5 in particular exhibits periods of very low stress followed by significant increases in stress on timescales of  $\sim 100 - 200$  orbits. The more viscous and resistive run, 32Re1600Pm0.5, shows similar variability but on a much shorter timescale of  $\gtrsim 10$  orbits. From this figure, it would appear that the turbulence in 32Re1600Pm2 has decayed without any indication of regrowth. Furthermore, 32Re1600Pm4 and

32Re800Pm4 remain at their maximal stress levels, which are very similar between the two runs (likely a result of both runs having the same  $P_m$ ).

Is the decay and regrowth of turbulence an artifact of using a relatively low resolution in these calculations? Several pieces of evidence suggest this is not the case. First of all, both resolutions for  $Re = 1600$ ,  $P_m = 0.5$  show the same variable stress behavior on  $\gtrsim 10$  orbit timescales. Secondly, even at 32 zones per  $H$ , dissipation coefficients play a significant role in determining the stress level, as shown above. The fact that the low resolution, unstratified simulations show sustained turbulence for sufficiently small  $\eta$  whereas vertically stratified simulations exhibit this variability for the same parameters suggests that the variability is a direct result of adding in vertical gravity. Thirdly, this variability was (first) seen in the simulations of Davis et al. (2010), which were run at a higher resolution of 64 zones per  $H$  (Davis, private communication). We note, however, that while Davis et al. (2010) used the same numerical algorithm as in this work, they used a different initial magnetic field configuration and vertical boundary conditions. We will return to this point shortly.

Finally, we consider the  $Q$  criterion for resolution of the MRI given in Noble et al. (2010),

$$Q_i \equiv \frac{\lambda_{\text{MRI},i}}{\Delta x_i} = \frac{2\pi v_{\text{Ai}}}{\Omega \Delta x_i} \quad (5.20)$$

where the subscript  $i = (x, y, z)$  depending on the direction of interest (thus,  $\Delta x_i$  is the grid spacing in direction  $i$ ), and  $\lambda_{\text{MRI}}$  is the fastest growing MRI wavelength. For  $Q_i \lesssim 6$ , the growth of the underlying MRI can be suppressed (Sano et al. 2004) and we consider the MRI to be under-resolved, though this number has some uncertainty and should be taken only as an estimate. Figure 5.10 shows  $Q_y$  and  $Q_z$  as a function of time for 32Re1600Pm4 and 64Re1600pm4. The Alfvén speed for these runs is

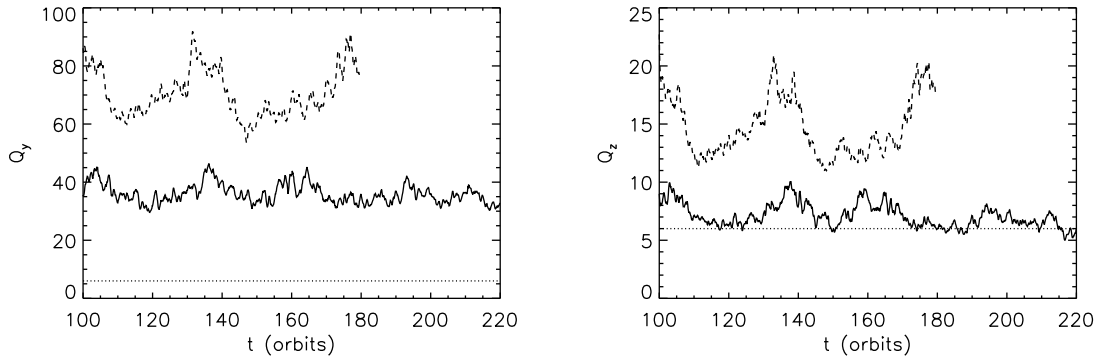


Fig. 5.10.— Quantitative measurement of how well resolved the MRI is in the toroidal ( $Q_y$ ; left plot) and vertical ( $Q_z$ ; right plot) directions as a function of time. The solid line corresponds to run 32Re1600Pm4 and the dashed line is 64Re1600pm4. The dotted horizontal line corresponds to  $Q = 6$ , below which the MRI is considered to be under-resolved (Sano et al. 2004).  $Q_i$  is calculated using the volume average of the magnetic energy and gas density for all  $x$  and  $y$  and for  $|z| \leq 0.5H$  (see text). The toroidal field MRI at both resolutions as well as the vertical field MRI at the higher resolution appear to be reasonably well-resolved. However, at the lower resolution, the vertical field MRI is only marginally resolved.

calculated as,

$$v_{Ai} = \sqrt{\frac{\langle B_i^2 \rangle}{\langle \rho \rangle}} \quad (5.21)$$

where the angled brackets denote a volume average for all  $x$  and  $y$  and for  $|z| \leq 0.5H$ . The figure suggests that the toroidal field MRI is quite well-resolved, but that the vertical MRI may be only marginally resolved for the lower resolution simulation. The higher resolution  $Q_y$  and  $Q_z$  are roughly a factor of 2 larger than the lower resolution  $Q$  values, which is simply a result of  $\Delta x_i$  decreasing by a factor of 2 for the higher resolution. Put another way, the turbulent saturation level is roughly the same between the two resolutions. This result coupled with the difference in how well resolved the vertical field MRI is between the two resolutions implies the vertical field MRI may not be playing a particularly significant role in setting the saturation level

in these simulations.

An alternate definition for the averaged Alfvén speed is

$$v_{Ai} = \left\langle \frac{|B_i|}{\sqrt{\rho}} \right\rangle. \quad (5.22)$$

That is, one can volume average the Alfvén speed calculated at each grid cell. We have produced the equivalent plots as those in Fig. 5.10 for the lower resolution and found that the  $Q$  values calculated via this method are a factor of  $\sim 1.3$  smaller than those calculated via Equation (5.21). While Equation (5.22) is more accurate than Equation (5.21), it is more computationally demanding to calculate  $v_A$  at every grid cell since it involves analyzing a large number of three-dimensional data sets. The Alfvén speed calculated via Equation (5.21), on the other hand, involves smaller files containing the one-dimensional, horizontally averaged data. We use Equation (5.21) in our calculation of the  $Q_i$  values for simplicity.

If this decay/regrowth is indeed a physical effect, what is its origin? In what follows, we carry out a number of diagnostics and experiments designed to answer this question. We first consider the space-time diagram of the horizontally averaged  $B_x$  and  $B_y$  components for several simulations. Fig. 5.11 shows this diagram for the first 200 orbits of 32Re1600Pm0.5. As can be seen from this figure (and Fig. 5.9), the turbulence level decreases dramatically from the beginning. This is not too surprising considering that the same  $Re$ ,  $P_m$  values give rapid decay of the turbulence in the unstratified case; the resistivity is large enough to quench the turbulence immediately. The space-time plots show that after this decay, there is a residual magnetic field left within the mid-plane region. In particular, within  $|z| \lesssim 0.5H$ , there is a net horizontally averaged  $B_x < 0$  and  $B_y < 0$  near  $t = 110$  orbits. The average  $B_x$  within this region remains constant for awhile, and  $B_y$  increases due to the shear of  $B_x$ ,

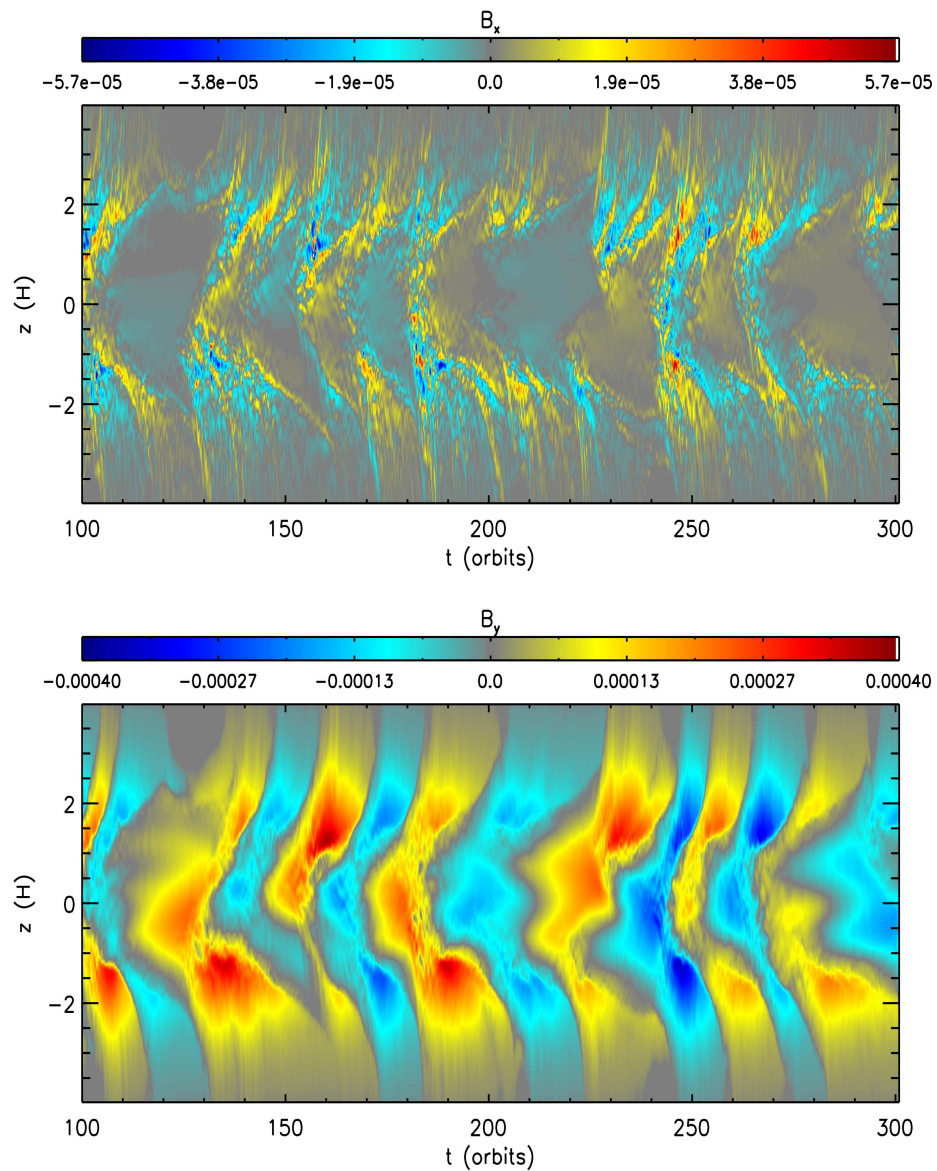


Fig. 5.11.— Space-time diagram of the horizontally averaged  $B_x$  (top panel) and  $B_y$  (bottom panel) for the first 200 orbits of 32Re1600Pm0.5. The turbulence initially decays, leaving a net  $B_x$  within the mid-plane region, which shears into toroidal field. This appears to eventually reenergize the MRI, but the large resistivity quickly quenches the turbulence again.

eventually flipping to  $B_y > 0$ . By  $t \sim 130$  orbits, the turbulence has reemerged, and the average  $B_y$  rises to larger  $|z|$ . The resistivity then kills off the MRI again, leading to another period of  $B_x$  shearing into  $B_y$  before the next outburst of active turbulence.

We now consider 32Re6400Pm0.5, which, as noted above, also experiences alternating states of MRI turbulence and decay. It is not immediately clear why the turbulence should decay at all for these dissipation parameters, since the equivalent unstratified run had sustained turbulence. We shall come back to this issue later, but for now, we focus on what causes the MRI to kick on after the fluid spends nearly 150 orbits in the non-turbulent state. Fig. 5.12 shows the space-time plot of  $B_x$  and  $B_y$  for a 300 orbit period in 32Re6400Pm0.5 during which the turbulence dies out and is then reenergized. For clarity, we also plot the volume-averaged horizontal field,  $\langle B_x \rangle$  and  $\langle B_y \rangle$ , where the average is done for all  $x$  and  $y$  and for  $|z| \leq 0.5H$ . When the MRI is shut off, there is a net radial field left in the mid-plane region, which then shears into  $B_y$ . Indeed, the lower right panel shows a linear response in  $\langle B_y \rangle$  to a constant  $\langle B_x \rangle$ ; see, e.g., 750-800 orbits.

From Figs. 5.11 and 5.12, it would seem that it is the growth of  $B_y$  that periodically reactivates the MRI. The most unstable wavelengths of the radial and vertical field MRI are very under-resolved;  $Q_x \lesssim 1$  and  $Q_z \lesssim 1$  during the non-turbulent states of both 32Re1600Pm0.5 and 32Re6400Pm0.5, where  $Q$  was calculated as a function of time using equations (5.20) and (5.21). Using these same equations to calculate  $Q_y$ , we find that the toroidal field MRI can reach marginal resolution in the non-turbulent states of these runs. Quantitatively,  $Q_y \sim 10 - 20$  in the non-turbulent states of 32Re1600Pm0.5, though occasionally  $Q_y = 6$ . The typical  $Q_y$  values for the non-turbulent states of 32Re6400Pm0.5 are similar but somewhat smaller. Also,  $Q_y$

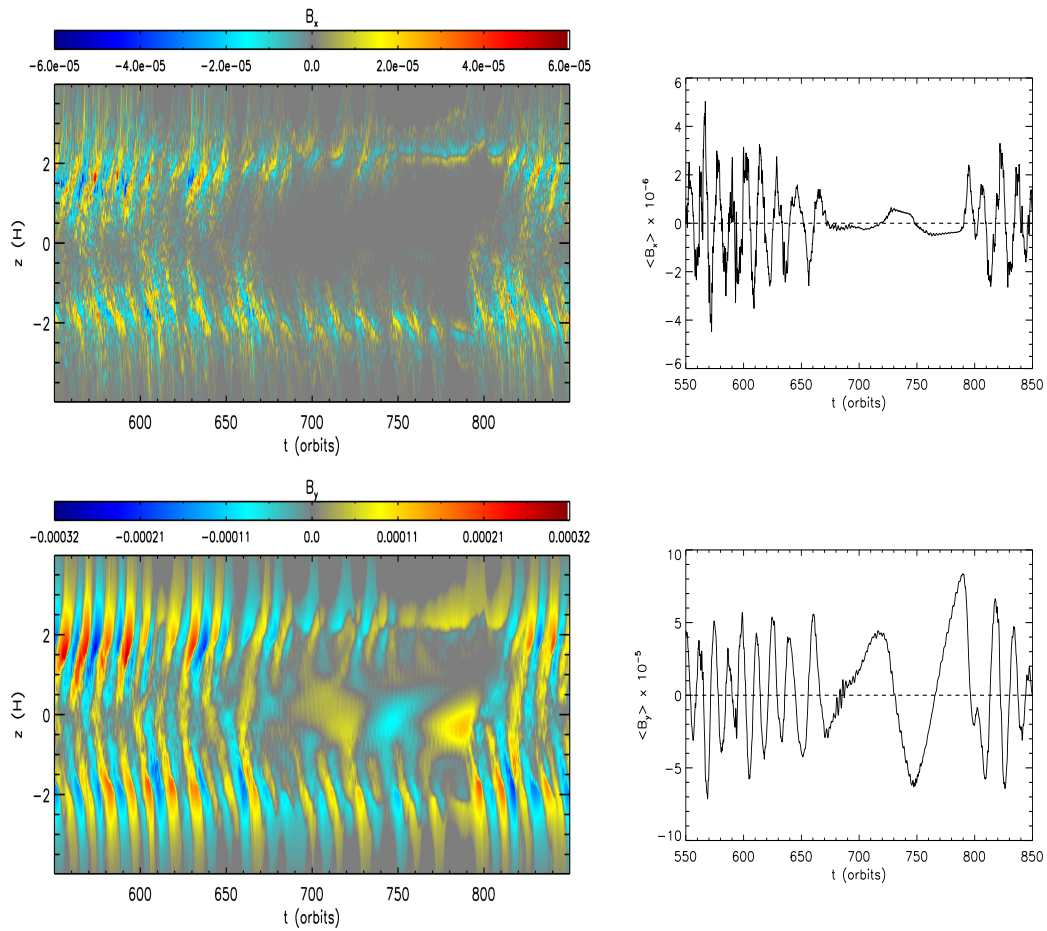


Fig. 5.12.— Space-time diagram of the horizontally averaged  $B_x$  (top left) and  $B_y$  (bottom left) for a 300 orbit period in 32Re6400Pm0.5, and the average of  $B_x$  (top right) and  $B_y$  (bottom right) over all  $x$  and  $y$  and for  $|z| \leq 0.5H$  as a function of time in orbits for the same 300 orbit period. During the period of no MRI turbulence, a net radial field still exists within the mid-plane region. This field appears to flip signs occasionally, leading to corresponding flips in  $B_y$  due to shear.

is well above the marginal resolution limit when the turbulence starts to decay.

To further test the hypothesis that the toroidal field is responsible for reactivating the MRI, we carry out two additional experiments. First, we take the state of the gas in 32Re1600Pm2 at  $t = 150$  orbits; at this point, the turbulence is in the process of decaying and the average of  $B_y$  within  $|z| \leq 0.5H$ ,  $\langle B_y \rangle = 5.9 \times 10^{-6}$ , is relatively small compared to the oscillation amplitude of  $\langle B_y \rangle$  in the turbulent state, which is  $\sim 5 \times 10^{-5}$ . We restart this simulation and add a net  $B_y = 8.9 \times 10^{-5}$  into the region  $|z| \leq 0.5H$ , which corresponds to a toroidal  $\beta \approx 126$  (using  $\beta$  defined with the initial mid-plane gas pressure  $P_o$ ). This run is 32Re1600Pm2\_By+ (see Table 5.2). Figure 5.13 shows the subsequent evolution of the stress along with the stress evolution of 32Re1600Pm2. Not only does the turbulence return, but the system undergoes episodic transitions between turbulent and non-turbulent states on  $\sim 100$  orbit time scales, as in 32Re6400Pm0.5.

In our second experiment, we initialize a stratified shearing box with all the same parameters as in 32Num but with the magnetic field initially consisting of a very weak radial field. Specifically, for  $|z| \leq 0.5H$ ,  $B_x = -\sqrt{2P_o/\beta_x}$  where  $\beta_x = 10^6$ . This field strength is very under-resolved; the Q value via equations (5.20) and (5.21) is 0.2, and the radial field MRI will not be activated during the evolution. Figure 5.14 shows the space-time diagrams of horizontally averaged  $B_x$  and  $B_y$ . The shearing of weak radial field leads to linear growth of toroidal field. Eventually, the toroidal field reaches a sufficient strength to activate the MRI. Once the MRI sets in, the subsequent behavior is very similar to the other vertically stratified MRI simulations; there are rising magnetic field structures, dominated by the toroidal component, and the period of oscillations in the mean field is  $\sim 10$  orbits.

These results all suggest that as long as there is a net radial field (even a weak

one) left within the mid-plane region, the MRI will eventually be reactivated through the creation of a sufficiently strong toroidal field. All of the simulations in which turbulence sets in after a period of decay show the presence of a net radial field within the mid-plane during the non-turbulent state. 32Re1600Pm2, however, is the only simulation that does not show the re-emergence of the MRI, despite over 1000 orbits of integration! An examination of the mid-plane region (up to  $|z| \lesssim H$ ) in the non-turbulent state of this run shows that the residual radial field is weaker than in the non-turbulent states of the other simulations. If this radial field would remain constant in time, the toroidal field would continually strengthen to the point of reactivating MRI. However,  $\langle B_x \rangle$  continues to change sign even in the absence of turbulence, though with a period of many hundreds of orbits. That is,  $\langle B_x \rangle$  oscillates about zero but with a very small amplitude, which lead to oscillations in  $\langle B_y \rangle$  due to shear.  $\langle B_y \rangle$  never reaches a sufficient amplitude to reactivate the MRI, and the simulation remains in the non-turbulent state.

Intriguingly,  $\langle B_x \rangle$  oscillates about zero in all of our simulations, even in the non-turbulent states. The cause of this behavior is unclear, but may be related to activity near  $|z| \sim 2H$  (see, e.g., Fig. 5.12). It is possible that the MRI is still active in this region (i.e., due to smaller  $\rho$ , the Alfvén speed may be sufficiently large to overcome resistive diffusion), or it could be some other mechanism at play. We will not pursue this issue further here but will address it in future work.

We now return to the issue of why the turbulence decays in the first place. As noted earlier and in Chapter 4, the critical  $Rm$  value below which the turbulence decays in unstratified shearing boxes is  $\sim 1000$ , but in these stratified shearing boxes, we have found that  $Rm$  can be as large as 3200 and the turbulence will still decay. One major difference between the stratified and unstratified simulations is that with

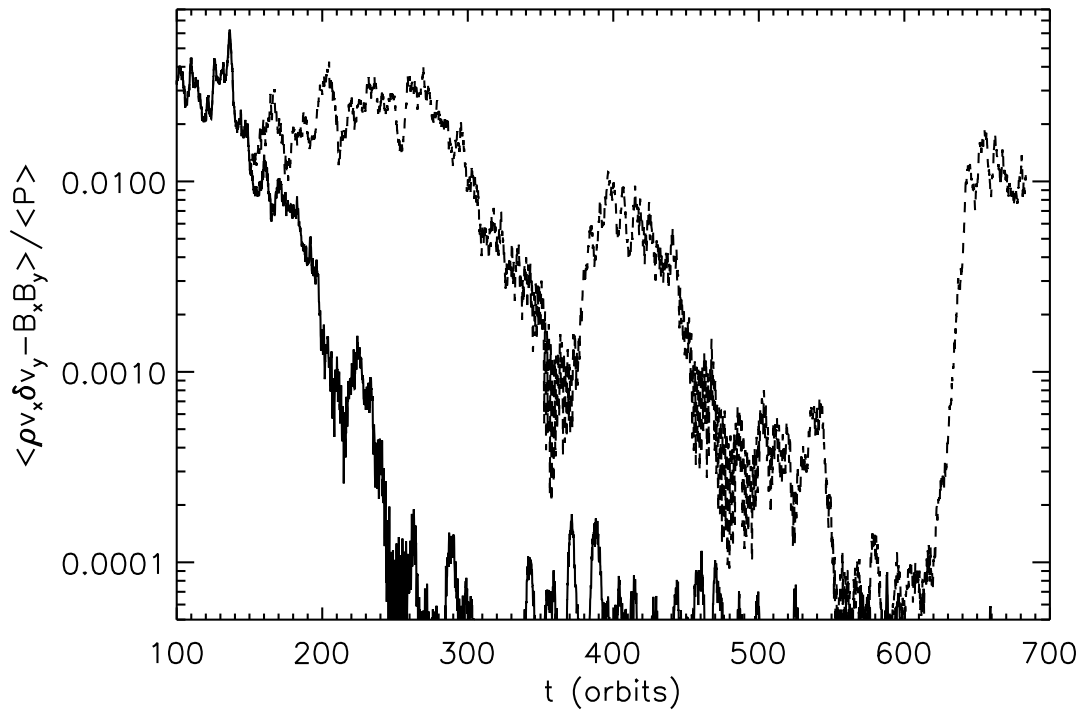


Fig. 5.13.— Volume-averaged Reynolds and Maxwell stresses normalized by the volume-averaged gas pressure as a function of time in orbits in 32Re1600Pm2 (solid line) and 32Re1600Pm2\_By+ (dashed line). The volume average is done over all  $x$  and  $y$  and for  $|z| \leq 2H$ . The run in which a net  $B_y$  is added into the mid-plane region (dashed line) has the MRI reactivated, followed by subsequent periods of decay and growth.

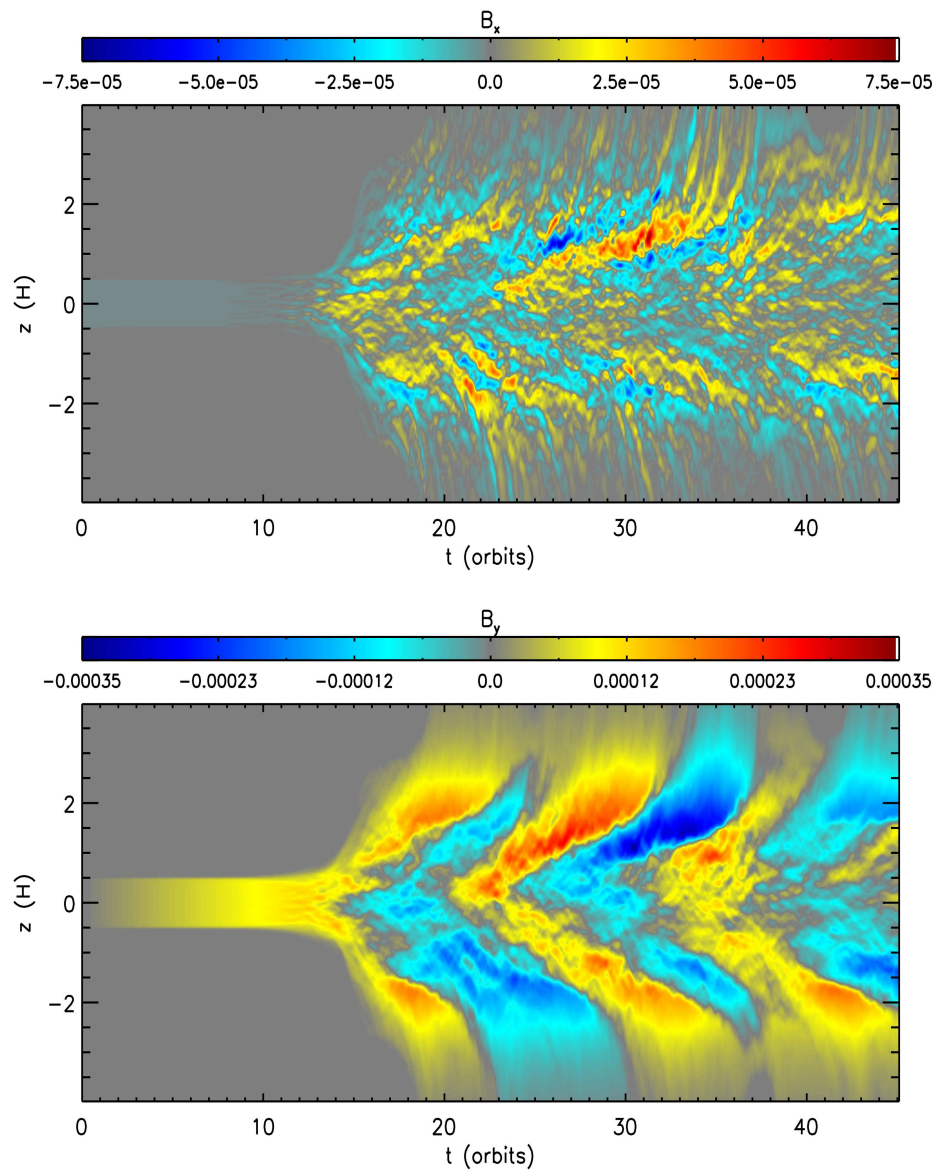


Fig. 5.14.— Space-time diagram of the horizontally averaged  $B_x$  (top panel) and  $B_y$  (bottom panel) for 32ShearBx. The uniform radial field that is present initially shears into toroidal field, which eventually becomes strong enough to launch the MRI.

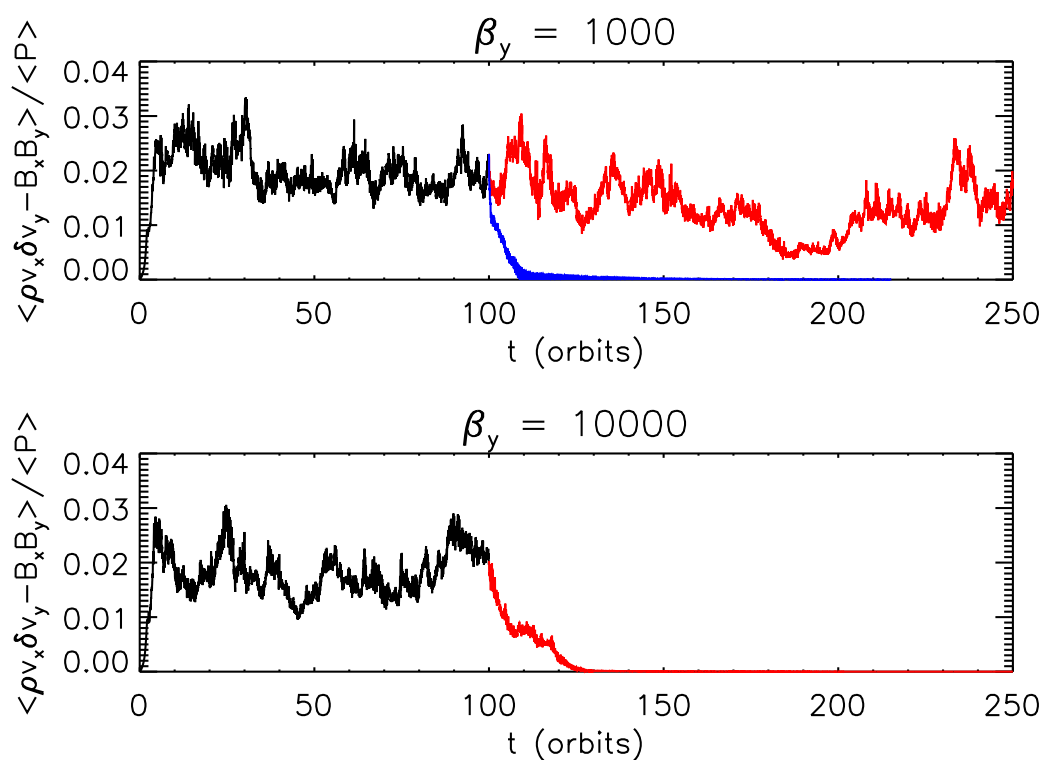


Fig. 5.15.— Volume-averaged total stress normalized by the volume-averaged gas pressure as a function of time in orbits for a series of unstratified shearing box simulations. The volume-average is done over the entire simulation domain. In each plot, the black line is from a simulation with only numerical dissipation. The colored lines are simulations with physical dissipation, initiated from the numerical dissipation run at orbit 100. The red lines correspond to  $Re = 1600$ ,  $P_m = 2$  and the blue line is  $Re = 1600$ ,  $P_m = 1$ . The top panel is initiated with a background toroidal field characterized by  $\beta = 1000$ , and the bottom panel has  $\beta = 10000$ . The weaker toroidal field appears to be killed off at a lower resistivity compared to the stronger background field.

vertical gravity, the net magnetic field within a localized region of the domain changes due to buoyancy.

What is the effect of changing the dissipation coefficients for different background field strengths? This question was discussed in the recent work of Longaretti & Lesur (2010); they found that the dependence of angular momentum transport on  $Rm$  and  $P_m$  became steeper for weaker background (vertical) fields in unstratified shearing boxes. We carry out similar (though less extensive) experiments here by first initializing two unstratified simulations with no physical dissipation and with a uniform, net toroidal field, one with  $\beta_y = 1000$  and the other with  $\beta_y = 10000$ . To shorten the time to MRI saturation, we also include a poloidal field loop of the exact same structure, size, and strength ( $\beta_p = 1600$ ) as present in 32FTNum. All other parameters, including resolution and initial conditions, are identical to those in 32FTNum, and these simulations are labeled as 32FTNum/ $\beta$ 1000 and 32FTNum/ $\beta$ 10000; see Table 5.1. These simulations were evolved for 100 orbits, and then we restarted with  $Re = 1600$  and with  $P_m = 1$  and 2.

The time history of the volume-averaged stresses for these simulations is shown in Fig. 5.15. For  $\beta_y = 1000$ , the turbulence survives at  $Rm = 3200$  but dies at  $Rm = 1600$ , whereas for  $\beta_y = 10000$ , the turbulence dies even at  $Rm = 3200$ . It would seem that for each increase in  $\beta_y$  by a factor of 10, the critical  $Rm$  value increases by roughly a factor of 2; it becomes easier to kill off the MRI with a lower resistivity as the background toroidal field is weakened. While Longaretti & Lesur (2010) did not address the issue of critical  $Rm$  values, their results with net vertical fields are generally consistent with ours. The resistivity seems to have a more profound effect on the turbulence for weaker background fields.

There is one caveat to this result worth mentioning. If we use equations (5.20)

and (5.21) (here, we volume average over the whole domain) to calculate the  $Q_y$  corresponding to the initial background field strengths we find that  $Q_y = 6.4$  and  $Q_y = 2$  for  $\beta_y = 1000$  and  $\beta_y = 10000$ , respectively; the toroidal field MRI is marginally resolved in the  $\beta_y = 1000$  simulation and under-resolved in the weakest field case. However, there are two additional issues to consider. First of all, despite these low  $Q_y$  values, the first 100 orbits, calculated without physical dissipation, show sustained turbulence, suggesting that at least some MRI modes are being resolved. It is only when resistivity is turned on that decaying turbulence is observed. The low  $Q_y$  values do introduce uncertainty on the values for the critical resistivity, but the effect of resistivity is unmistakable. Secondly, these unstratified simulations still serve as a guide for why the turbulence decays in the stratified simulations. That is, if the MRI is under-resolved in these unstratified runs, it will be equally under-resolved in the stratified simulations when the background toroidal field is weak enough.

How does this resistivity effect relate to the decay of turbulence in the vertically stratified simulations with  $Rm = 3200$ ? We know that the average toroidal field,  $\langle B_y \rangle$ , within the mid-plane region oscillates around zero with a period of 10 orbits. Thus, every 10 orbits or so,  $\langle B_y \rangle$  is conceivably weak enough for resistivity to kill the turbulence, but the turbulence remains sustained for many of these 10 orbit periods. Furthermore, averaging  $B_y$  within some vertical distance from the mid-plane erases information about the field structure there; e.g.,  $\langle B_y \rangle$  might be small but there could still be strong toroidal fields of opposite polarity close to  $z = 0$ . The point is, one cannot necessarily expect the turbulence to decay away strictly whenever  $\langle B_y \rangle$  drops below a certain (small) value.

As noted above, the  $\langle B_y \rangle$  oscillation amplitude appears to be modulated by a longer timescale, more on the order of  $\sim 100$  orbits (see, e.g., Fig. 5.5). This behavior

is present in all simulations with and without physical dissipation. It is interesting that this is roughly the same timescale over which the turbulence appears to decay and regrow in the  $Rm = 3200$  simulations. Comparing the time evolution of  $\langle B_y \rangle$  for  $|z| \leq 0.5H$  with the evolution of the total stress shows that the minima in the oscillation amplitude are generally correlated with the decay of turbulence. One exception is near 200 orbits in 32Re6400Pm0.5 in which  $\langle B_y \rangle$  becomes rather small, but the turbulence remains active, though relatively weak compared to the fully active state. This correlation implies that if the mean toroidal field near the mid-plane remains sufficiently small for some time, perhaps due to the longer timescale variability, resistivity can catch up with the MRI and cause eventual decay.

All of the results up to this point show that there exists a critical  $Rm$  below which the turbulence experiences this intermittency and that this critical value is  $Rm < 6000$ . We carry out two more stratified simulations with  $Rm \sim 6000$  but different  $P_m$  values in order to further test this hypothesis. The first simulation is 32Re800Pm8; thus,  $Rm = 6400$ , and  $P_m$  is relatively large. The turbulence is sustained over a long time, nearly 330 orbits, without any sign of decay. The dissipation coefficients of the second simulation, 32Re6250Pm1, are chosen to match the relatively high  $Rm$ , low  $P_m$  simulation that decays in the zero net flux shearing box (see Fromang et al. 2007, and Chapter 4). This simulation also remained sustained for nearly 330 orbits.

In summary, for sufficiently small  $Rm$ , stratified MRI turbulence can decay away, leaving a net radial field within the mid-plane region, which shears into toroidal field. Once this toroidal field reaches a sufficiently large amplitude, the MRI is reactivated, the turbulence is sustained for some duration and then decays again, repeating this pattern. This behavior appears to be independent of the  $P_m$  values we have probed, except for near  $Rm = 3200$ . In particular, 32Re800Pm4 has sustained turbulence,

whereas 32Re1600Pm2, 32Re1600Pm2\_By+, and 32Re6400Pm0.5 do not. In the higher resolution runs, 64Re800Pm4 and 64Re6400Pm0.5 show decay but 64Re1600Pm2 appears to be sustained (though again, these simulations were not integrated very far). While  $P_m$  may play a role here, the line between sustained and intermittent turbulence is unlikely to be hard and fast, and many factors probably contribute to the nature of the turbulence near this  $Rm$  value.

Is this the same mechanism responsible for the variability observed in the simulations of Davis et al. (2010)? First of all, the largest  $Rm$  used in their simulations was  $Rm = 3200$ , consistent with the largest critical  $Rm$  in our simulations. Secondly, an examination of the space-time data from their simulation with  $Re = 800$ ,  $P_m = 2$  (kindly provided by the authors) shows the same behavior as we have observed here; a net radial field remains within the mid-plane region after decay, shearing into toroidal field, from which the MRI is reactivated.

Lastly, we examine the magnetic field structure in the shearing box in the non-turbulent state. Figure 5.16 shows the equivalent information as Fig. 5.8, but for orbit 550 of 32Re1600Pm2\_By+. For  $|z| \gtrsim 2H$ , the field remains mainly toroidal but with some relatively large excursions, resembling the field structure in this region during fully active turbulence. Within  $2H$ , the field is almost completely toroidal, and any small radial (or vertical) field present within this region is not visible in this image. We also examined the azimuthally averaged poloidal field structure in several snapshots of this run. We found that the structure of the field was different, depending on which snapshot we examined. At some times, the poloidal field within  $2H$  is almost completely radial, with very little vertical field; at other times, the vertical and radial fields are comparable in size such that the field takes on a more loop-like structure.

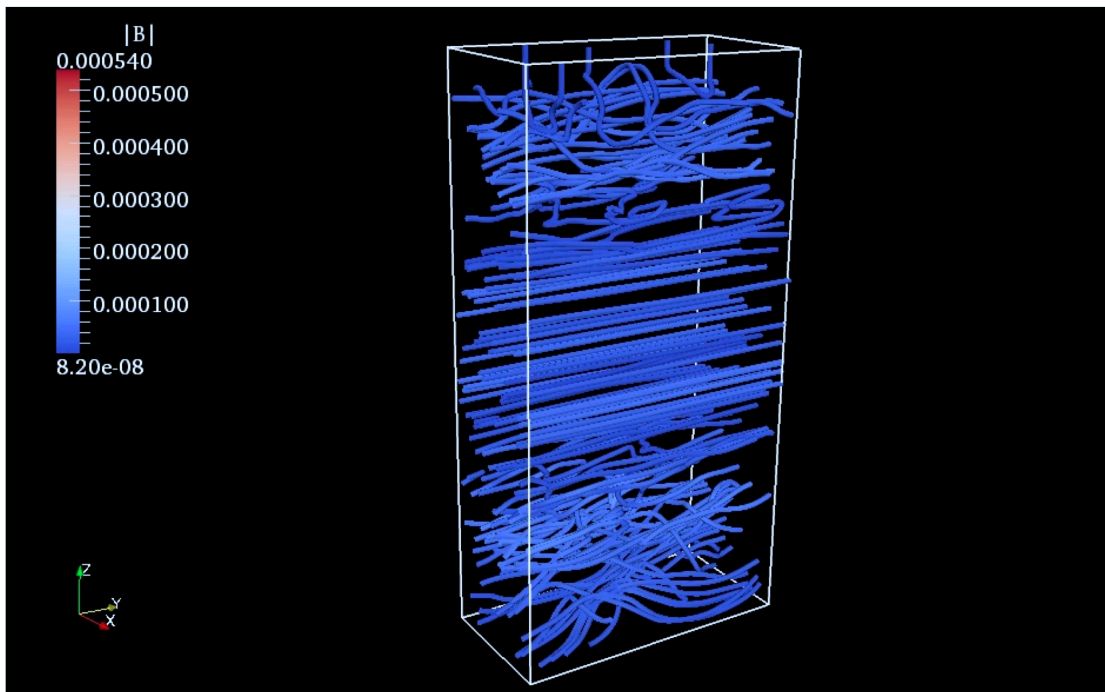


Fig. 5.16.— Magnetic field structure at  $t = 550$  orbits in  $32\text{Re}1600\text{Pm}2\text{.By}+$ , produced via a stream line integration. The field strength (in code units) is displayed via color and not the density of the field lines. The color scale is the same as that in Fig. 5.8 for comparison. This snapshot corresponds to a state in which the turbulence has decayed. The magnetic field is almost completely toroidal near the mid-plane but has a tangled structure in the upper  $|z|$  regions, more reminiscent of the active state.

### 5.4.3 The Prandtl Number Effect on Sustained Turbulence

In this section, we investigate how  $P_m$  affects angular momentum transport in sustained turbulence simulations. Does the same relationship between  $\alpha$  and  $P_m$  present in unstratified shearing boxes carry over to stratified simulations? The time evolution of the volume-averaged total stress divided by the volume-averaged gas pressure for the sustained turbulence simulations is shown in Fig. 5.17. The volume average is done for all  $x$  and  $y$  and for  $|z| \leq 2H$ . As the figure shows, there is a general increase in the turbulence levels with  $P_m$ , but there is also significant temporal variability in the stress. As a result, the curves overlap at certain times, much more so than for unstratified turbulence (see Fig. 5.2).

This feature is also shown by Fig. 5.18, which displays the  $\alpha$  parameter (as defined above) for the unstratified (left panel) and stratified simulations (right panel). The time average for the unstratified simulations is the same as in Fig. 5.3, from orbit 120 to the end of the calculation, and for the stratified simulations, this average is done from orbit 150 until the end of the simulation. The error bars denote one standard deviation about the temporal average. While there is a clear dependence of  $\alpha$  on  $P_m$  in the stratified simulations, the temporal variability is significantly larger relative to the trend with  $P_m$  than in the unstratified case. Taking a linear fit in log-log space, we again calculate  $\delta$  in  $\alpha \propto P_m^\delta$ ;  $\delta = 0.54$  for unstratified turbulence (from § 5.3), and  $\delta = 0.25$  for stratified calculations.

In Fig. 5.19, we show the vertical profile for the total stress in the sustained turbulence runs calculated via temporal and horizontal averaging. The time average was done from orbit 150 to the end of each simulation. Increasing  $P_m$  appears to increase the stress for nearly all  $z$ , and in all cases the stress drops off dramatically near  $|z| \sim 2H$ , consistent with the baseline simulations. Furthermore,  $32\text{Re}800\text{Pm}8$

appears to have a sharper peak in the stress profile near  $z = 0$ , whereas the other simulations have a flatter stress profile for  $|z| \lesssim 2H$ . Creating the same vertical stress profiles for different temporal averaging windows produces the same general results; the stress increases with  $P_m$  and 32Re800Pm8 has a sharper peak near the mid-plane. In some cases, however, the stress does not necessarily increase monotonically with  $P_m$  at  $|z| \gtrsim 2H$ . These results are generally consistent with the dependence of stress on  $P_m$  for unstratified simulations; where the MRI is at work, increasing  $P_m$  leads to an increase in stress.

Finally, we examined the vertical profile for the same quantities as in Fig. 5.7. We found that these profiles in the sustained turbulence simulations are all very similar to each other and to 32Num; the general vertical structure of the disk does not appear to be sensitive to  $P_m$ .

## 5.5 Summary and Discussion

We have carried out a series of shearing box simulations with the Athena code to characterize the behavior of MRI-driven turbulence in the presence of both vertical gravity and physical dissipation. Until the recent work of Davis et al. (2010), the role of physical dissipation in setting the level of angular momentum transport was studied solely in unstratified simulations. As Davis et al. (2010) has shown, however, this is an oversimplification; turbulence that decays in unstratified simulations is sustained in the presence of vertical gravity. These authors also observe intermittent turbulence in their simulations with physical dissipation; the turbulence decays away but then regrows on the timescale of  $\sim 100$  orbits.

Our primary goal in this study has been to understand the mechanism behind this behavior and determine its relevance to astrophysical disk systems. Our simulations

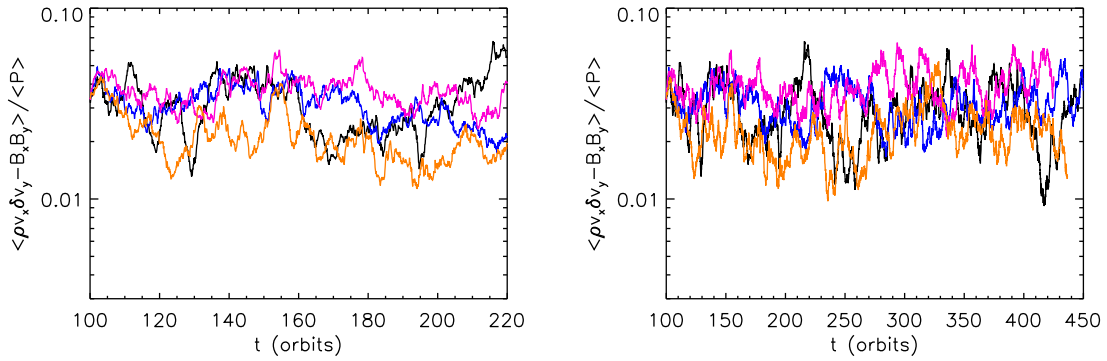


Fig. 5.17.— Volume-averaged total stress normalized by the volume-averaged gas pressure as a function of time in orbits in the lower resolution, vertically stratified simulations where turbulence remains sustained. The volume-average is done for all  $x$  and  $y$  and for  $|z| \leq 2H$ . The left plot is the first 120 orbits of the evolution, whereas the right plot is 350 orbits of the evolution. The black line corresponds to  $Re = 800$  and  $P_m = 4$ , dark blue is  $Re = 1600$  and  $P_m = 4$ , magenta is  $Re = 800$  and  $P_m = 8$ , and brown is  $Re = 6250$  and  $P_m = 1$ . The vertical axis has been chosen to match that of Fig. 5.2 for comparison.

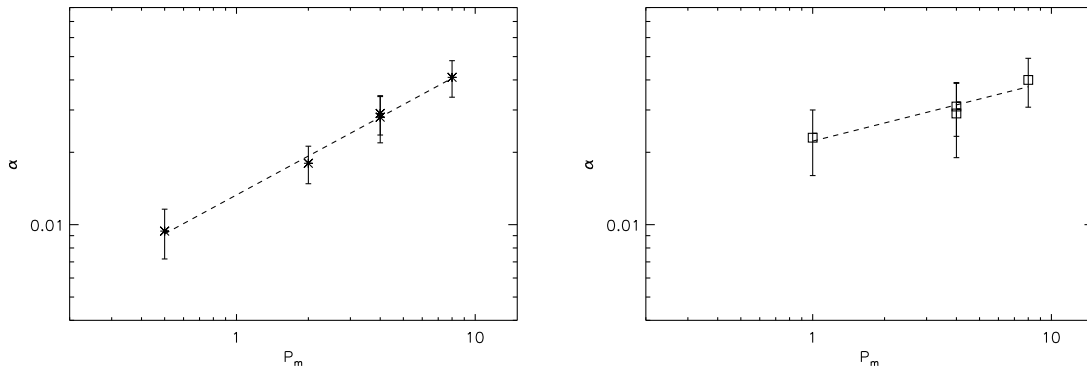


Fig. 5.18.— Time- and volume-averaged stress parameter  $\alpha$  as a function of  $P_m$  in the unstratified FT simulations (left plot) and the stratified simulations (right plot);  $\alpha \equiv \langle \langle \rho v_x \delta v_y - B_x B_y \rangle \rangle / \langle P \rangle$ . The average is calculated over the entire domain (all  $x$  and  $y$  and for  $|z| \leq 2H$ ) and from 120 (150) orbits to the end of the simulation for the unstratified (stratified) runs. The dashed lines are linear fits to the data in log-log space, and the error bars denote one standard deviation about the temporal average. Both cases show a clear  $P_m$  dependence. However, in the stratified runs, this dependence is less steep, and there is considerable temporal variability.

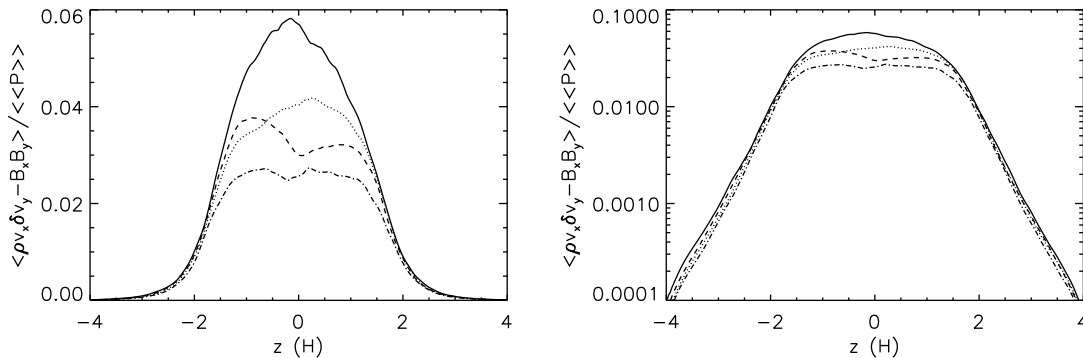


Fig. 5.19.— Time- and horizontally-averaged total stress as a function of  $z$  on a linear (left) and logarithmic (right) vertical scale. The stress is normalized by the time- and volume-averaged gas pressure, where the volume average is done for all  $x$  and  $y$  and for  $|z| \leq 2H$ . The time average is done from orbit 150 until the end of each simulation. The solid line corresponds to 32Re800Pm8, the dashed line is 32Re800Pm4, the dotted line is 32Re1600Pm4, and the dot-dashed line is 32Re6250Pm1. The stress appears to increase with  $P_m$  for nearly all  $z$ , and for all  $P_m$ , there is a sharp decrease in the stress for  $|z| \gtrsim 2H$ .

are thus an extension of those in Davis et al. (2010), but with several improvements. First, we have implemented more realistic, outflow boundary conditions in the vertical direction, whereas Davis et al. (2010) use vertically periodic boundaries. Second, in order to capture this intermittent turbulence, most of our simulations were run for significantly longer integration times than is usually done in shearing box calculations.

Given the long evolution times probed here, it was necessary to run these simulations at a resolution of 32 grid zones per  $H$ . Before running the vertically stratified simulations, we executed a series of unstratified calculations to determine the resolution at which the influence of physical dissipation on the MRI is resolved. We found that the effect of physical dissipation on MRI saturation is reasonably well converged at 32 zones per  $H$ :  $\alpha$  increases with  $P_m$  at this resolution, although with a steeper dependence than at higher resolution, and  $\alpha$  is roughly constant with resolution above 32 zones per  $H$  for a given set of  $Re$ ,  $Rm$ , and  $P_m$  values. This in itself is

an interesting result since it shows that the higher resolutions used in Fromang et al. (2007), Lesur & Longaretti (2007), and Chapter 4 may not be necessary to capture the general effects of physical dissipation.

We found that the inclusion of vertical gravity influences MRI turbulence and the resulting disk structure in several ways. First, for  $|z| \lesssim 2H$ , the time- and horizontally-averaged turbulent energy and stresses are roughly constant with height, the magnetic field is only marginally stable to buoyancy, and  $\beta > 1$ . In the upper regions of the disk, on the other hand, the turbulence is significantly weaker,  $\beta < 1$ , and the field is buoyantly unstable, rising away from the mid-plane at a faster rate than for  $|z| \lesssim 2H$ .

These results, which are consistent with the ZEUS-based results of Guan (2009), suggest that there are two separate vertical regions in these disks. For  $|z| \lesssim 2H$ , the disk is fully turbulent with enhanced Maxwell and Reynolds stresses and subthermal magnetic fields. Here, the MRI is fully at work and leads to occasional changes in the buoyant stability of the magnetic field such that predominantly toroidal field structures slowly rise away from the mid-plane. Outside of this region, the MRI appears to be stable, and the fluid is characterized by a superthermal field that rapidly rises out of the disk via buoyancy. These results suggest that to capture the behavior of the vertically stratified MRI, one need not go much beyond  $\pm 2H$  from the mid-plane. This is confirmed by a few additional simulations in which we extended the outer boundary to  $6H$  from the mid-plane instead of  $4H$ . We found no difference in the vertical structure of the disk, the volume averaged stress levels, or the temporal variability of the system.

The second major effect resulting from vertical gravity is considerable temporal variability: a strong 10 orbital period variability in the magnetic field within the

mid-plane region, which is modulated on timescales of tens to hundreds of orbits. The 10 orbit variability has been seen in many previous studies of vertically stratified shearing boxes (e.g., Stone et al. 1996; Hirose et al. 2006; Guan 2009; Shi et al. 2010; Gressel 2010; Davis et al. 2010) and originates from the buoyant rise of predominantly toroidal field from the mid-plane region; after this buoyant rise, a field of opposite sign takes its place at the mid-plane. We found that the evolution of this toroidal field is almost entirely controlled by the shearing of radial field and buoyancy.

The longer timescale variability, which appears in all of our simulations, is a new discovery. We do not know the origin of this variability, but there is evidence that it plays a role in the decay and subsequent regrowth of the MRI in sufficiently resistive disks, which occurs on a similar timescale. When the averaged mid-plane toroidal field remains relatively weak for a sufficiently long time, resistivity wins over turbulent MRI driving, and the turbulence decays. Any radial field left within the mid-plane region, even if weak, will shear into toroidal field; this mechanism is completely independent of physical dissipation. Once the toroidal field reaches a particular strength, the MRI is re-energized, and the disk becomes turbulent again.

This behavior is not particularly sensitive to  $P_m$  and is the same as that reported by Davis et al. (2010). Thus, it does not appear to be related to the dynamo issue of  $P_m \sim 1$  in zero net magnetic flux shearing boxes, which Davis et al. (2010) specifically investigated, and is instead a robust behavior that emerges whenever the disk is sufficiently resistive. The critical  $Rm$  below which the turbulence experiences these alternating periods of decay and active turbulence is  $3200 \lesssim Rm_c \lesssim 6000$ . If  $Rm > Rm_c$ , the turbulence remains sustained for the dissipation parameters explored here, and averaged stress levels increase with  $P_m$  for all  $z$ , though with a less steep dependence of  $\alpha$  on  $P_m$  compared to unstratified simulations.

What do these results imply for the MRI and its application to astrophysical disks? First, our analysis has shed light on the long-sought-after MRI dynamo. The cycles of activity and inactivity observed in our high-resistivity simulations in addition to our analysis of the temporal behavior of the horizontal field in our baseline runs directly demonstrate the important role played by the shearing of radial field into toroidal field. This orbital shear is a fundamental component to the behavior of the MRI and in the presence of vertical gravity, leads to significant temporal variability and allows the MRI to function even in highly resistive disks. The generation of radial field from toroidal can be modeled by a simple  $\alpha$  dynamo and is likely linked to the turbulence of the MRI itself. Furthermore, since this same behavior is observed in the zero net flux simulations of Davis et al. (2010), the MRI does appear to constitute a dynamo in vertically stratified local simulations.

The temporal variability present in the higher resistivity simulations could have potential observational implications for several types of accretion disks. Indeed, protoplanetary disks have large regions of low ionization gas, including the dead zone layer (Gammie 1996). Dwarf nova disks also contain regions of partial ionization, and it is intriguing that the  $Rm$  values in these systems (see Gammie & Menou 1998) are on the same order as the critical  $Rm \sim 10^3$  for the intermittent turbulence behavior observed in our simulations. Even some regions of AGN disks may have moderately high resistivity, though typical  $Rm$  values are probably larger than those in dwarf nova systems because of the larger disk scale height (Menou & Quataert 2001).

It is tempting to associate the peaks and dips of turbulent activity in our simulations with the outbursts and variability observed in these systems. Of course, there remains much work before such a connection can be formed. In particular, more realistic simulations will have  $\eta$  (and  $\nu$ ) depending on fluid quantities, such as

temperature and density, rather than being constant throughout the disk. Furthermore, the influence of other non-ideal MHD effects on the MRI needs more study. The Hall effect is often times just as important as Ohmic resistivity in astrophysical environments (Wardle 1999; Balbus & Terquem 2001; Balbus 2003), and while simulations including both Hall and Ohmic terms have been carried out by Sano & Stone (2002a) and Sano & Stone (2002b), there remains more parameter space to explore and physics to include. Lastly, we note that if  $\eta$  is so large that no MRI modes are present, the temporal variability we observe will likely not exist at all and the turbulence will be completely quenched.

What of the  $P_m$  effect when the resistivity is low and turbulence is continually sustained? This question holds relevance for hot, fully ionized disks, such as X-ray binaries. While our simulations show that angular momentum transport increases with  $P_m$  in sustained transport, the  $Re$  and  $Rm$  values of such disks are significantly larger than the values probed here. Whether or not the  $P_m$  effect continues into the large  $Re/Rm$  regime remains very much an open area of research.

Finally, one particular field geometry that has not been explored here or in most vertically stratified local simulations is that of a net vertical field. These simulations are quite challenging; the channel mode dominates the solution (Miller & Stone 2000; Latter et al. 2010), leading to very strongly magnetized regions of the disk that can often times cause the numerical integration techniques to fail (but see Suzuki & Inutsuka (2009), who produced a stable evolution).

In summary, we have explored the spatial and temporal behavior of the MRI in the presence of both vertical gravity and physical dissipation. We found that for moderately resistive simulations, the local domain cycles between states of turbulence and decay, and that orbital shear of radial field into toroidal field is essential to both

this behavior as well as the temporal variability of fully active turbulence. In addition, when sustained, turbulent stresses increase with  $P_m$ , in agreement with unstratified simulations. Our calculations are an important stepping stone towards more realistic simulations that include temperature-dependent  $\nu$  and  $\eta$ .

## Chapter 6

# Conclusions and Outlook

The MRI is currently the most promising candidate for angular momentum transport in magnetized accretion disks. All that is required is orbital shear and sufficient ionization to couple the gas to the magnetic field; the result is sustained turbulent outward angular momentum transport. The past two decades have firmly established this conclusion both analytically and in local and global simulations for many different magnetic field configurations and parameters.

Despite this tremendous progress, there has not yet been any direct connection made between observations and these theoretical models. This is partially the fault of observations, as our instruments are not sensitive enough to observe signatures of MRI-induced turbulence. But current simulations of this turbulence are equally lacking in that they cannot yet address aspects of MRI turbulence that could be connected with observations. The holy grail of accretion disk simulations is high resolution, global simulations of MRI turbulence with a realistic prescription for radiative transfer. One could then construct model observations from such simulations to compare to actual observations. Currently, however, such calculations are far from feasible.

Another approach is to construct a phenomenological disk evolution model, which captures the essential MRI physics in a sub-grid manner. The primary example of disk phenomenology is the  $\alpha$ -disk model of Shakura & Syunyaev (1973), which assumes that the turbulent stresses are determined by the gas and radiation pressure of the fluid, though it does not make any assumptions as to the source of this turbulence. But numerical studies of the MRI have shown that turbulent stress is *not* dependent on these pressures and the  $\alpha$  model is not quite the full picture. So then, what physical properties of the disk do play a role in setting the saturation amplitude of the MRI?

Recently, it has become evident that shear viscosity ( $\nu$ ) and Ohmic resistivity ( $\eta$ ) have a particularly strong influence over the MRI (e.g., Fromang et al. 2007; Lesur & Longaretti 2007), and in this thesis, we have carried out local shearing box simulations with Athena in order to obtain a deeper understanding of how the viscous and resistive dissipation scales affect MRI-driven turbulence. We first characterized the numerical dissipation of our code in the absence of vertical gravity, which is an essential step towards including more realistic prescriptions for dissipation. We then characterized the effect of  $\nu$ ,  $\eta$ , and  $P_m$  on the MRI, both in the presence and absence of vertical gravity.

Our primary conclusion is that the viscous and resistive dissipation scales do significantly affect the saturation level of the MRI for the (admittedly small) Reynolds numbers probed in these calculations. This is perhaps not surprising considering the work of Fromang & Papaloizou (2007), Fromang et al. (2007), and Lesur & Longaretti (2007), in which this dependence was first discovered. Our calculations, however, expand upon this preliminary work and elucidate several unresolved issues.

First, we found that the effective numerical  $P_m$  of Athena is  $\sim 2$  independent of

resolution and field geometry. This result shows that the decrease in MRI saturation with increasing resolution in the zero net flux model is *not* related to a change in numerical  $P_m$ . Furthermore, the numerical  $P_m$  and Reynolds numbers calculated from this analysis should lead to decay if they were equivalent to a physical  $P_m$  and Reynolds number. Instead, these simulations show sustained turbulence, which indicates that numerical dissipation *cannot* be equated to physical dissipation. Thus, to truly understand how the MRI operates in local simulations, one must include physical dissipation.

Second, the dependence of the turbulent saturation level on  $P_m$  is a robust effect, as it is present for Athena as well as for ZEUS, and it exists for net toroidal, net vertical, and zero net magnetic flux. However, in contrast to the zero net flux model,  $P_m < 1$  does not lead to decay if there is a net field penetrating the local domain. In the case of a net background field, only a sufficiently high resistivity can quench the turbulence.<sup>1</sup>

Third, the basic  $P_m$  effect remains when vertical gravity is included. However, if the turbulence is sustained, the dependence of stress on  $P_m$  is weaker and considerably more variable in time than in unstratified simulations. The critical parameter in these simulations is again resistivity; if  $\eta$  is large enough, the turbulence undergoes periods of decay followed by regrowth on timescales ranging from 10-100 orbits. The regrowth of the MRI is a direct result of the shearing of a weak radial field into a toroidal field. When this field reaches sufficient strength, the MRI is reactivated.

In summary, while  $P_m$  is an important parameter in determining the level of angular momentum transport, it may not be as critical as was once thought, i.e., in the simulations of Fromang et al. (2007). Decay of turbulence for  $P_m < 1$  appears

---

<sup>1</sup>We did not examine the net vertical field model in this work, but based upon the results of Fleming et al. (2000), we suspect that a sufficiently large  $\eta$  can quench turbulence in this case as well.

to occur only for unstratified, zero net field simulations, and these models are not particularly realistic. For more realistic models, resistivity is the more important parameter in determining whether or not the turbulence will decay. Furthermore, the actual dependence of the time- and volume-averaged stresses on  $P_m$  is relatively weak in the more realistic simulations that include vertical gravity and some form of net background field. It is also entirely possible that for sufficiently small  $\nu$  and  $\eta$ , the  $P_m$  dependence vanishes completely; there is even some hint of this in the calculations presented in Chapter 4. This would spell doom for models put forth to describe state transitions in fully ionized, black hole accretion disks via the steep temperature dependence of  $P_m$  (Balbus & Henri 2008).

However, more work remains before jumping to any such conclusions. For instance, a detailed Fourier analysis of the energy transfer between scales and magnetic/velocity fields could reveal the presence or absence of an inverse cascade that is enhanced as  $P_m$  increases. If such an inverse cascade does occur, one could then examine how this cascade changes as the dissipation scale is pushed towards larger wavenumbers. While we may not yet be able to resolve the  $\nu$  and  $\eta$  values of real astrophysical disks, this analysis could help us to extrapolate the  $P_m$  effect to significantly smaller  $\nu$  and  $\eta$ . This avenue of research is one of many that the author of this thesis plans to pursue.

If the  $P_m$  effect does indeed vanish for small  $\nu$  and  $\eta$ , there are many systems (e.g., dwarf nova and protostellar disks) where  $\eta$  is large enough to play a role in MRI evolution. Another task that I am very interested in pursuing is local simulations of the MRI with a more realistic prescription for  $\eta$ , such as one that is temperature-dependent. Coupled with the variability already observed in our constant  $\eta$  simulations, such a study could provide some very useful insights into the

observed variability and outburst behavior of these moderately resistive accretion systems.

As far as simulations go, we are now much closer to understanding what sets the saturation level of the MRI : background field strength and  $P_m$  matter. But is there anything else? There are, of course, other non-ideal MHD effects such as the Hall term and ambipolar diffusion, which have only barely been explored in the context of the MRI (e.g., Sano & Stone 2002a,b; Low et al. 1995). Another worthwhile endeavour, then, is to better understand the role that these additional effects play. Continued investigation of the interaction of radiation and MRI-driven turbulence is also called for; such work would be an extension of the excellent progress made by several groups (see, e.g., Turner 2004; Hirose et al. 2009).

Another issue in constructing a phenomenological disk model is that of thermodynamics. Does the assumption made by the  $\alpha$  model that turbulent heating and angular momentum transport are locally correlated hold true in MRI turbulence? The analytic work of Balbus & Papaloizou (1999) suggests that it should hold. In this thesis, we have carried out preliminary analyses to directly address this question in the context of numerical simulations. We found that the extraction of free energy from the shear flow by the MRI followed by the thermalization of this energy happens on a timescale much less than an orbit,  $\sim 0.2$  orbits. While this seems to support the idea of local turbulent heating, the simulations involved did not include physical dissipation or vertical gravity. An important extension to this work, then, would be a detailed study of disk heating in the context of more realistic physics, possibly even with temperature- and density-dependent dissipation.

It is clear that there remains much work to be done in studies of MRI-driven accretion. But progress has been excellent, and ever increasing computational facilities

allow more complex physics to be incorporated and higher resolutions to be achieved. Thus, the future will likely see continued progress, and accretion disk theory will no doubt remain an active and vibrant field for some time.

# References

- Balbus, S. A. 2003, *ARA&A*, 41, 555
- Balbus, S. A., & Hawley, J. F. 1991, *ApJ*, 376, 214
- . 1992, *ApJ*, 400, 610
- . 1998, *Reviews of Modern Physics*, 70, 1
- Balbus, S. A., Hawley, J. F., & Stone, J. M. 1996, *ApJ*, 467, 76
- Balbus, S. A., & Henri, P. 2008, *ApJ*, 674, 408
- Balbus, S. A., & Papaloizou, J. C. B. 1999, *ApJ*, 521, 650
- Balbus, S. A., & Terquem, C. 2001, *ApJ*, 552, 235
- Beckwith, K., Hawley, J. F., & Krolik, J. H. 2008a, *ApJ*, 678, 1180
- . 2008b, *MNRAS*, 390, 21
- Blackman, E. G., Penna, R. F., & Varnière, P. 2008, *New Astronomy*, 13, 244
- Bodo, G., Mignone, A., Cattaneo, F., Rossi, P., & Ferrari, A. 2008, *A&A*, 487, 1
- Brandenburg, A., Nordlund, A., Stein, R. F., & Torkelsson, U. 1995, *ApJ*, 446, 741
- Brandenburg, A., & Subramanian, K. 2005, *Phys. Rep.*, 417, 1

- Cargo, P., & Gallice, G. 1997, JCP, 136, 446
- Colella, P. 1990, JCP, 87, 171
- Colella, P., & Woodward, P. R. 1984, JCP, 54, 174
- Davis, S. W., Stone, J. M., & Pessah, M. E. 2010, ApJ, 713, 52
- Dzyurkevich, N., Flock, M., Turner, N. J., Klahr, H., & Henning, T. 2010, A&A, 515, 70
- Evans, C. R., & Hawley, J. F. 1988, ApJ, 332, 659
- Ferrarese, L., & Merritt, D. 2000, ApJ, 539, L9
- Fleming, T., & Stone, J. M. 2003, ApJ, 585, 908
- Fleming, T. P., Stone, J. M., & Hawley, J. F. 2000, ApJ, 530, 464
- Fromang, S. 2010, A&A, 514, L5
- Fromang, S., & Papaloizou, J. 2006, A&A, 452, 751
- . 2007, A&A, 476, 1113
- Fromang, S., Papaloizou, J., Lesur, G., & Heinemann, T. 2007, A&A, 476, 1123
- Gammie, C. F. 1996, ApJ, 457, 355
- Gammie, C. F., & Menou, K. 1998, ApJ, 492, L75
- Gardiner, T. A., & Stone, J. M. 2005a, MAGNETIC FIELDS IN THE UNIVERSE: From Laboratory and Stars to Primordial Structures. AIP Conference Proceedings, 784, 475

—. 2005b, JCP, 205, 509

—. 2008, JCP, 227, 4123

Gebhardt, K., Bender, R., Bower, G., Dressler, A., Faber, S. M., Filippenko, A. V., Green, R., Grillmair, C., Ho, L. C., Kormendy, J., Lauer, T. R., Magorrian, J., Pinkney, J., Richstone, D., & Tremaine, S. 2000, ApJ, 539, L13

Goodman, J., & Xu, G. 1994, ApJ, 432, 213

Gressel, O. 2010, MNRAS, 404

Guan, X. 2009, PhD thesis, University of Illinois at Urbana-Champaign

Guan, X., Gammie, C. F., Simon, J. B., & Johnson, B. M. 2009, ApJ, 694, 1010

Hartmann, L. 1998, *Accretion Processes in Star Formation* (Cambridge Astrophysics Ser. 32; Cambridge: Cambridge Univ. Press)

Hawley, J. F. 2001, ApJ, 554, 534

Hawley, J. F., & Balbus, S. A. 1991, ApJ, 376, 223

—. 1992, ApJ, 400, 595

Hawley, J. F., Balbus, S. A., & Winters, W. F. 1999, ApJ, 518, 394

Hawley, J. F., Gammie, C. F., & Balbus, S. A. 1995, ApJ, 440, 742

—. 1996, ApJ, 464, 690

Hirose, S., Krolik, J. H., & Blaes, O. 2009, ApJ, 691, 16

Hirose, S., Krolik, J. H., & Stone, J. M. 2006, ApJ, 640, 901

- Ilgner, M., & Nelson, R. P. 2008, *A&A*, 483, 815
- Johansen, A. 2009, in *IAU Symposium*, Vol. 259, *IAU Symposium*, 249–258
- Johnson, B. M., Guan, X., & Gammie, C. F. 2008, *ApJS*, 179, 553
- Käpylä, P. J., Brandenburg, A., Korpi, M. J., Snellman, J. E., & Narayan, R. 2010, arXiv, astro-ph.SR
- Komissarov, S. S. 2007, *MNRAS*, 382, 995
- Kretke, K. A., & Lin, D. N. C. 2007, *ApJ*, 664, L55
- Krolik, J. H., Hirose, S., & Blaes, O. 2007, *ApJ*, 664, 1045
- Latter, H. N., Fromang, S., & Gressel, O. 2010, *MNRAS*, 758
- Lesur, G., & Longaretti, P.-Y. 2005, *A&A*, 444, 25
- . 2007, *MNRAS*, 378, 1471
- Lesur, G., & Ogilvie, G. I. 2010, *MNRAS*, L43
- Longaretti, P.-Y., & Lesur, G. 2010, *A&A*, 516, 51
- Low, M.-M. M., Norman, M. L., Konigl, A., & Wardle, M. 1995, *ApJ*, 442, 726
- Masada, Y., & Sano, T. 2008, *ApJ*, 689, 1234
- Masset, F. 2000, *A&AS*, 141, 165
- Menou, K., & Quataert, E. 2001, *ApJ*, 552, 204
- Mignone, A. 2007, *JCP*, 225, 1427
- Miller, K. A., & Stone, J. M. 2000, *ApJ*, 534, 398

- Miyoshi, T., & Kusano, K. 2005, JCP, 208, 315
- Nelson, R. P., & Papaloizou, J. C. B. 2003, MNRAS, 339, 993
- . 2004, MNRAS, 350, 849
- Newcomb, W. A. 1961, PhFl, 4, 391
- Noble, S. C., Krolik, J. H., & Hawley, J. F. 2010, ApJ, 711, 959
- Oishi, J. S., & Low, M.-M. M. 2009, ApJ, 704, 1239
- Oishi, J. S., Low, M.-M. M., & Menou, K. 2007, ApJ, 670, 805
- Papaloizou, J. C. B., Nelson, R. P., & Snellgrove, M. D. 2004, MNRAS, 350, 829
- Papaloizou, J. C. B., & Terquem, C. 1997, MNRAS, 287, 771
- Pessah, M. E., & kwan Chan, C. 2008, ApJ, 684, 498
- Pessah, M. E., kwan Chan, C., & Psaltis, D. 2007, ApJ, 668, L51
- Roe, P. L. 1981, JCP, 43, 357
- Sano, T., & Inutsuka, S.-I. 2001, ApJ, 561, L179
- Sano, T., Inutsuka, S.-I., & Miyama, S. M. 1998, ApJ, 506, L57
- Sano, T., Inutsuka, S.-I., Turner, N. J., & Stone, J. M. 2004, ApJ, 605, 321
- Sano, T., & Stone, J. M. 2002a, ApJ, 570, 314
- . 2002b, ApJ, 577, 534
- Shakura, N. I., & Syunyaev, R. A. 1973, A&A, 24, 337

- Shen, Y., Stone, J. M., & Gardiner, T. A. 2006, *ApJ*, 653, 513
- Shi, J., Krolik, J. H., & Hirose, S. 2010, *ApJ*, 708, 1716
- Simon, J. B., & Hawley, J. F. 2009, *ApJ*, 707, 833
- Simon, J. B., Hawley, J. F., & Beckwith, K. 2009, *ApJ*, 690, 974
- Spitzer, L. 1962, *Physics of Fully Ionized Gases*
- Stone, J. M., & Balbus, S. A. 1996, *ApJ*, 464, 364
- Stone, J. M., & Gardiner, T. A. 2005, *MAGNETIC FIELDS IN THE UNIVERSE: From Laboratory and Stars to Primordial Structures*. AIP Conference Proceedings, 784, 16
- . 2010, *ApJS*, 189, 142
- Stone, J. M., Gardiner, T. A., Teuben, P., Hawley, J. F., & Simon, J. B. 2008, *ApJS*, 178, 137
- Stone, J. M., Hawley, J. F., Gammie, C. F., & Balbus, S. A. 1996, *ApJ*, 463, 656
- Stone, J. M., & Norman, M. L. 1992a, *ApJS*, 80, 753
- . 1992b, *ApJS*, 80, 791
- Suzuki, T. K., & Inutsuka, S.-I. 2009, *ApJ*, 691, L49
- Turner, N. J. 2004, *ApJ*, 605, L45
- Turner, N. J., Carballido, A., & Sano, T. 2010, *ApJ*, 708, 188
- Turner, N. J., & Sano, T. 2008, *ApJ*, 679, L131

Turner, N. J., Sano, T., & Dziourkevitch, N. 2007, *ApJ*, 659, 729

Wardle, M. 1999, *MNRAS*, 307, 849

Winters, W. F., Balbus, S. A., & Hawley, J. F. 2003, *MNRAS*, 340, 519

Yang, C.-C., Low, M.-M. M., & Menou, K. 2009, *ApJ*, 707, 1233

Ziegler, U., & Rüdiger, G. 2001, *A&A*, 378, 668